DISS. ETH NO. 23006

STRUCTURAL ANALYSIS OF THE INTERFACE BETWEEN NOGO-A-Δ20 AND SPHINGOSINE 1-PHOSPHATE RECEPTOR 2

A thesis submitted to
attain the degree of

DOCTOR OF SCIENCES of ETH ZURICH
(Dr. sc. ETH Zurich)

presented by

Michael Eduard Arzt
MSc Biology, ETH Zurich

born on 09.09.1984

citizen of Austria

accepted on the recommendation of

Prof. Dr. Martin E. Schwab, examiner
Prof. Dr. Ueli Suter, co-examiner
Prof. em. Dr. Peter Sonderegger, co-examiner

2015

SUMMARY

Neurons of the central nervous system (CNS) only possess very limited potential to restore disrupted networks upon stroke or spinal cord injury. This observation is in harsh contrast to the situation in the peripheral nervous system, where regeneration occurs to a much higher extent. Inhibitory molecules that are present in CNS myelin contribute profoundly to this difference and constitute an inherent obstacle for the recovery from CNS injuries. One of the best known examples is the myelin-associated neurite outgrowth inhibitory protein Nogo-A, or reticulon-4A. It restricts the elongation of regenerative fibers via two inhibitory domains, Nogo-A-Δ20 (residues 567-748 of human Nogo-A) and Nogo-66 (residues 1055-1120). Whereas Nogo-A-Δ20 is unique to Nogo-A, the Nogo-66 loop resides in the C-terminal reticulon homology domain that is also present in the isoforms Nogo-B and Nogo-C. A glycosylphosphatidylinositol-anchored receptor for Nogo-66 was identified shortly after the discovery of Nogo-A, and therefore termed Nogo-66 receptor 1 (NgR1). Via its associated co-receptors p75, Troy and Lingo-1, NgR1 triggers a signaling cascade involving the activation fo the small GTPase RhoA. This in turn leads to a destabilization of the actin cytoskeleton, finally resulting in collapse of the neuronal growth cone. Nogo-A-Δ20 exhibits similar inhibitory activity, and neutralizing antibodies that mask this region of Nogo-A have shown beneficial effects on neurite outgrowth *in vitro* and *in vivo* and on functional recovery from CNS injury *in vivo*. However, the molecular basis for Nogo-A-Δ20 signaling has long remained obscure, as no specific receptors for this domain have been known for a long time. We have recently identified sphingosine 1-phosphate receptor 2 (S1PR2) as a Nogo-A-Δ20-specific receptor. Via the G-protein G_{13} and the RhoGEF LARG, this G-protein coupled receptor causes the activation of RhoA, where Nogo-A-Δ20 and Nogo-66 signaling converge. The discovery of S1PR2 as the central receptor for Nogo-A-Δ20-induced inhibition became the foundation of this thesis.

Using a set of techniques ranging from genetic engineering to spectroscopy, my aim was to enhance our understanding of the interaction between Nogo-A-Δ20 and S1PR2 on a structural level. In addition, the relationship of Nogo-A-Δ20 and sphingosine 1-phosphate (S1P), the classically known agonist of S1PR2, should be determined. A rough mapping of the binding sites was conducted using microscale thermophoresis. Nogo-A-Δ20, but not Nogo-66, exhibited high binding affinity for isolated extracellular loops (ECLs) 2 and 3 of S1PR2. No tripartite complex of these two ECLs with Nogo-A-Δ20 could be detected, suggesting a common binding pocket on

Nogo-A-Δ20. An *in-silico* homology model of S1PR2 was obtained to assist in the selection of surface-accessible candidate residues for Nogo-A-Δ20 binding. Via site-directed mutagenesis, an S1PR2 mutant library was established containing alanine substitutions in the top 12 exposed amino acids, as well as in key known S1P-interacting residues. Functional evaluation of these mutants suggested an importance of the S1P-binding Arg108$^{3.28}$ for spreading inhibition imposed by Nogo-A-Δ20 on S1PR2-overexpressing fibroblasts.

To analyze the ligand-induced activation of S1PR2 in more detail, we have developed a new tool for S1PR2 research, S1PR2-FRET, a ratiometric intramolecular Förster resonance energy transfer (FRET) biosensor that allows live monitoring of the Å-level conformational changes that occur upon S1PR2 activation. The intracellular loop 3 (ICL3) of S1PR2 is deflected from the C-terminus in the activated state, resulting in a measurable attenuation of FRET efficiency between fluorophores inserted into these domains.

In structural studies, Nogo-A-Δ20 displayed intrinsically disordered properties as determined by nuclear magnetic resonance and circular dichroism spectroscopy. However, backbone assignment of 94 % of Nogo-A-Δ20 residues enabled us to identify three residual α-helices, ^{560}SEAIQESL^{567}, ^{639}EAMNVALKAL^{648}, and ^{695}YSEIAKFEKS^{704}. Interestingly, titration of isolated ECL2 or ECL3 of S1PR2 did not perturb the [^{1}H, ^{15}N]-heteronuclear single-quantum coherence spectrum of Nogo-A-Δ20 under a variety of conditions, which could be an indication for a fuzzy binding mechanism. We also worked toward a crystal structure of S1PR2 by comparing the expression levels of seven different orthologs. Murine S1PR2 exhibited highest expression in HEK293T cells and displayed only little aggregation as determined by fluorescence size-exclusion chromatography. To facilitate crystallization, T4 lysozyme was inserted into ICL3 of murine S1PR2 at various locations, and an increasing tolerance for insertion was observed at more C-terminal positions. We also detected N-linked glycosylation on all S1PR2 homologs analyzed and found differences in the glycosylation patterns of mammalian and *Xenopus tropicalis* S1PR2 variants.

Finally, in an *in vivo* collaborative project, we assessed the relevance of Nogo-A for cognitive processes by means of a genetically modified rat expressing a microRNA to silence Nogo-A. Preferential knockdown in neurons was observed, leading to enhanced synaptic plasticity and a schizophrenia-like phenotype.

Taken together, the findings presented in this thesis contribute to our knowledge of the architecture of Nogo-A-Δ20 and S1PR2, their physical interaction, and their relationship to S1P. Deeper structural insight into this signaling node will become invaluable for a more complete understanding of the multiple signaling mechanisms induced by Nogo-A, their neurobiological relevance, and the development of novel therapeutic interventions to enhance reparative processes after CNS damage.

ZUSAMMENFASSUNG

Die Fähigkeit von Neuronen des zentralen Nervensystems (ZNS), durchtrennte Verbindungen nach einem Schlaganfall oder einer Rückenmarksverletzung wiederherzustellen, ist in höchstem Masse eingeschränkt. Diese Beobachtung steht in einem starken Kontrast zum peripheren Nervensystem, wo Regeneration in viel grösserem Ausmass stattfinden kann. Inhibitorische Moleküle im Myelin des ZNS tragen entscheidend zu dieser Diskrepanz bei und stellen eine Hürde für die Genesung nach ZNS-Verletzungen dar. Eines der bekanntesten Beispiele ist das Myelin-assoziierte, Neuritenwachstum hemmende Protein Nogo-A, oder Reticulon-4A. Es blockiert das Auswachsen regenerativer Fasern durch zwei inhibitorische Domänen, Nogo-A-Δ20 (Aminosäuren 567-748 in humanem Nogo-A) und Nogo-66 (Aminosäuren 1055-1120). Während Nogo-A-Δ20 ausschliesslich in Nogo-A vorkommt, befindet sich Nogo-66 in der C-terminalen *reticulon homology domain*, welche auch Teil der Isoformen Nogo-B und Nogo-C ist. Ein Glycosylphosphatidylinositol-verankerter Rezeptor für Nogo-66 wurde bereits kurz nach der Entdeckung von Nogo-A gefunden und daher Nogo-66-Rezeptor 1 (NgR1) genannt. Über seine assoziierten Co-Rezeptoren p75, Troy und Lingo-1 verursacht NgR1 eine Signalkaskade, die die Aktivierung der kleinen GTPase RhoA zur Folge hat. Diese wiederum bewirkt eine Destabilisierung des Aktin-Zytoskeletts, was zum Kollaps des neuronalen Wachstumskegels führt. Nogo-A-Δ20 hat eine ähnlich inhibitorische Wirkung, und neutralisierende Antikörper, welche diese Region von Nogo-A maskieren, haben einen positiven Effekt auf Neuritenwachstum *in vitro* und *in vivo*, sowie auf die funktionelle Erholung von ZNS-Verletzungen *in vivo* gezeigt. Die molekulare Basis für die Signalwirkung von Nogo-A-Δ20 war jedoch lange unklar, da kein spezifischer Rezeptor für diese Domäne bekannt war. Erst vor kurzer Zeit haben wir Sphingosin-1-Phosphat-Rezeptor 2 (S1PR2) als Nogo-A-Δ20-spezifischen Rezeptor identifiziert. Dieser G-Protein-gekoppelte Rezeptor bewirkt über das G-Protein G_{13} und das RhoGEF LARG eine Aktivierung von RhoA, wo die Signalwege von Nogo-A-Δ20 und Nogo-66 konvergieren. Die Entdeckung von S1PR2 als zentralen Rezeptor für Nogo-A-Δ20-induzierte Inhibition stellt die Grundlage für diese Dissertation dar.

Mein Ziel war es unter Zuhilfenahme diverser Techniken, von gentechnischen Methoden bis hin zu spektroskopischen Verfahren, unser Verständnis der Interaktion zwischen Nogo-A-Δ20

und S1PR2 auf einer strukturellen Ebene zu erweitern. Darüber hinaus sollte die Beziehung zwischen Nogo-A-Δ20 und Sphingosin-1-Phosphat (S1P), dem klassisch bekannten Agonist für S1PR2 bestimmt werden. Eine grobe Kartierung der Bindungsstellen wurde mithilfe von *microscale thermophoresis* vorgenommen. Nogo-A-Δ20, aber nicht Nogo-66, zeigte eine hohe Bindungsaffinität für die isolierten extrazellulären Loops (ECLs) 2 und 3 von S1PR2. Kein dreiteiliger Komplex aus diesen beiden ECLs und Nogo-A-Δ20 konnte nachgewiesen werden, was eine gemeinsame Bindungsstelle auf Nogo-A-Δ20 nahelegt. Ein *in silico* Homologiemodell von S1PR2 wurde erstellt, welches die Auswahl oberflächenzugänglicher Aminosäuren als Kandidaten für Nogo-A-Δ20-Bindung erleichterte. Eine Mutations-Genbibliothek von S1PR2 wurde mittels zielgerichteter Mutagenese hergestellt, in der die Top 12 oberflächenzugänglichen Aminosäuren, sowie die wichtigsten bekannten S1P-bindenden Aminosäuren durch Alanin ersetzt wurden. Eine funktionelle Evaluation dieser Mutanten zeigte die Wichtigkeit der S1P-bindenden Aminosäure Arg108$^{3.28}$ für die Nogo-A-Δ20-vermittelte Ausbreitungsinhibition S1PR2-überexprimierender Fibroblasten.

Um die Liganden-induzierte Aktivierung von S1PR2 genauer untersuchen zu können, haben wir ein neuartiges Werkzeug für die S1PR2-Forschung entwickelt, S1PR2-FRET, einen ratiometrischen intramolekularen Förster-Resonanz-Energie-Transfer (FRET) Biosensor. Dieser erlaubt eine Live-Überwachung der Konformationsänderungen im Å-Massstab, die bei der Aktivierung von S1PR2 stattfinden. Der intrazelluläre Loop 3 (ICL3) von S1PR2 wird im aktivierten Zustand vom C-Terminus abgelenkt, was die FRET-Effizienz zwischen zwei eingebrachten Fluorophoren in diesen Domänen messbar dämpft.

In Struktur-Studien mittels Kernspinresonanz- (NMR-) und Circulardichroismus-Spektroskopie zeigte Nogo-A-Δ20 intrinsisch ungeordnete Eigenschaften. Die Zuordnung von 94 % der Aminosäuren in Nogo-A-Δ20 im NMR-Spektrum erlaubte es uns, drei restliche α-Helices zu identifizieren, ^{560}SEAIQESL^{567}, ^{639}EAMNVALKAL^{648} und ^{695}YSEIAKFEKS^{704}. Interessanterweise wurde ein [^{1}H, ^{15}N]-*heteronuclear single-quantum coherence*-Spektrum durch Titration isolierter ECL2 oder ECL3 unter verschiedenen Bedingungen nicht verändert, was als Indikation für eine *fuzzy* Bindung gewertet werden kann. Zusätzlich haben wir in Richtung einer Kristallstruktur von S1PR2 gearbeitet, indem wir die Expressionsniveaus sieben verschiedener Orthologe verglichen haben. Maus-S1PR2 zeigte die höchste Expression in HEK293T-Zellen bei nur schwacher Aggregation, wie wir mittels Fluoreszenz-Grössenausschlusschromatografie feststellen konnten. Um die Kristallisation zu unterstützen, wurde T4-Lysozym an verschiedenen Positionen in ICL3 von Maus-S1PR2 eingebracht, was eine erhöhte Insertionstoleranz für weiter C-terminale Positionen ergab. Ausserdem haben wir N-Glykosylierung auf allen analysierten S1PR2-Homologen festgestellt, wobei Unterschiede in den Glykosylierungsmustern von S1PR2 aus Säugetieren und *Xenopus tropicalis* beobachtet wurden.

Abschliessend haben wir in einem kollaborativen *in-vivo*-Projekt die Relevanz von Nogo-A für kognitive Prozesse anhand einer gentechnisch veränderten Ratte untersucht, die eine microRNA zum *silencing* von Nogo-A exprimiert. Ein präferenzieller *knockdown* in Neuronen wurde festgestellt, der zu erhöhter synaptischer Plastizität und zur Ausbildung eines Schizophrenie-ähnlichen Phänotyps führte.

Zusammengefasst tragen die Erkenntnisse dieser Dissertation zu unserem Verständnis der Architektur von Nogo-A-Δ20 und S1PR2 bei und gewähren Einblicke in deren physikalische Interaktion und ihr Verhältnis zu S1P. Weitergehende Untersuchungen zu diesem Signal-Knotenpunkt werden wertvoll für ein umfassenderes Verständnis der vielfältigen Signalmechanismen und der neurobiologischen Relevanz von Nogo-A werden. Dies ermöglicht die Entwicklung neuartiger therapeutischer Ansätze zur Verstärkung regenerativer Prozesse nach ZNS-Schädigungen.

CONTENTS

CONTEXT AND AIMS OF THIS THESIS

Injuries to the central nervous system (CNS) have detrimental effects on the quality of life of patients. In the US alone, more than five million people suffer from some form of paralysis, with stroke and spinal cord injury being the most frequent underlying causes (Gibson et al., 2009). Upon injury, neurons of the CNS need to grow their extensions through or around a lesion site in order to reach their former targets and restore disrupted connections. Alternatively, fibers of intact neurons could sprout and take over the control of downstream neuronal networks. However, the presence of inhibitory molecules in the CNS restricts such neuronal repair (Schwab and Caroni, 1988). The best-studied such molecule is the myelin-associated membrane protein Nogo-A, which inhibits fiber growth by causing the collapse of growth cones and by downregulating the neuronal growth machinery (Fig. 1) (Chen et al., 2000; GrandPre et al., 2000; Prinjha et al., 2000; Schwab and Strittmatter, 2014). Nogo-A exerts this effect via two separate domains, Nogo-A-Δ20 and Nogo-66 (Oertle et al., 2003). Whereas the receptor for Nogo-66, NgR1, was identified just one year after the discovery of Nogo-A (Fournier et al., 2001), the neuronal receptor for Nogo-A-Δ20 has remained elusive for over a decade. In an effort that is also part of my thesis, we have identified sphingosine 1-phosphate receptor 2 (S1PR2) as a Nogo-A-Δ20-

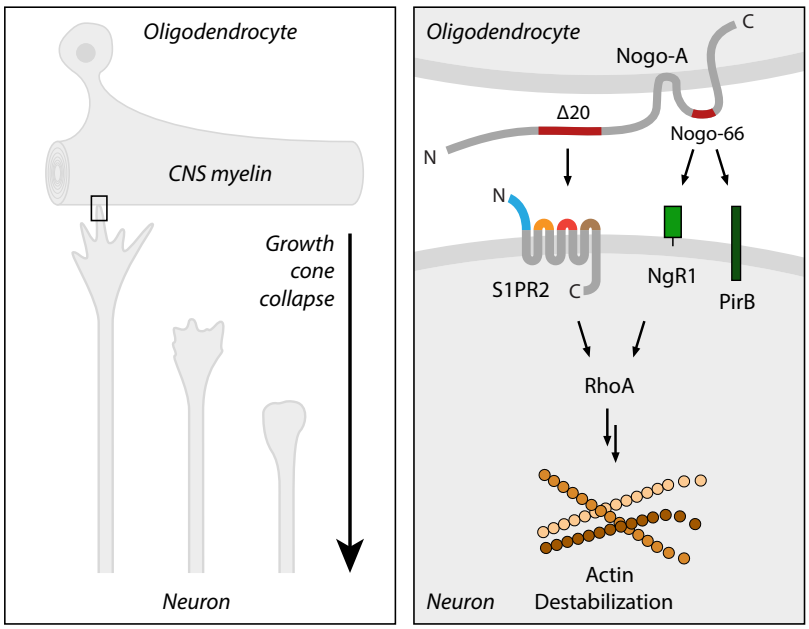

Fig. 1: The effect of Nogo-A on neurons. CNS myelin is non-permissive for neuronal outgrowth by causing a collapse of growth cones. Inhibitory molecules in CNS myelin, such as Nogo-A, are responsible for this effect. Nogo-A harbors two inhibitory domains, Nogo-A-Δ20 and Nogo-66, that each activate a different receptor complex (only directly interacting receptor components are shown). Signaling converges on the activation of RhoA, which causes destabilization of the actin cytoskeleton.

specific receptor (Kempf et al., 2014). This G-protein coupled receptor (GPCR) is best known for pleiotropic functions in response to its classic agonist sphingosine 1-phosphate (S1P) (Adada et al., 2013). Interestingly, S1P can also induce growth-cone collapse and is upregulated after spinal cord injury (Fincher et al., 2014; Kimura et al., 2007), suggesting synergistic effects caused by Nogo-A-Δ20 and S1P through S1PR2. However, the interdependence of signaling induced by these two ligands is not known.

Structural information on a protein can change our perspective on its functions and interactions profoundly. In recent years, this complementary approach has become available even for proteins that are difficult to express, including membrane proteins such as GPCRs (Piscitelli et al., 2015). The Nobel Prize in chemistry awarded to Brian Kobilka and Robert Lefkowitz in 2012 highlights the importance of such structural GPCR research (Kobilka, 2013; Lefkowitz, 2013). The aim of my thesis was to investigate the relationship between Nogo-A-Δ20 and S1P as agonists of S1PR2, and to establish a structural basis for this interaction. The three molecules involved exhibit remarkable structural differences: Nogo-A-Δ20 is a hydrophilic, intrinsically disordered protein domain, S1P is a small lysophospholipid, and S1PR2 consists of seven highly hydrophobic transmembrane domains typical for GPCRs. A multi-method approach was therefore followed by combining techniques of computational modeling, biochemistry, cell biology, genetic engineering, spectroscopy, and crystallography.

In chapter 1, I provide an overview of the current structural knowledge that is available for Nogo-A, as well as a comprehensive summary of its molecular interactors. A computer-aided mutagenesis approach to identify the amino acids on S1PR2 that interact with Nogo-A is detailed in chapter 2. Site-directed mutagenesis was also used to block binding of S1P, which gives us first insights on the importance of S1P for Nogo-A-Δ20 signaling. In chapter 3, I then present a FRET-based ratiometric biosensor that reports the activity state of S1PR2 in a live-cell imaging setup. The following two chapters describe our endeavors to gain structural information on Nogo-A-Δ20 and S1PR2. In chapter 4, we used NMR and CD spectroscopy to investigate residual structures present in Nogo-A-Δ20, as well as conformational alterations induced by binding of S1PR2 fragments. Chapter 5 summarizes our efforts toward crystallization of S1PR2, revealing N-linked glycosylation of the receptor. The foundation of this thesis is our discovery that S1PR2 acts as a receptor for Nogo-A-Δ20, which is provided in chapter 6. Finally, a collaborative project that was not directly related to our structural investigations is outlined in chapter 7, presenting a transgenic rat in which Nogo-A expression was attenuated by means of a microRNA.

LIST OF FIGURES

LIST OF TABLES

GLOSSARY

a. a.	amino acid
CD	circular dichroism
CFP	cyan fluorescent protein
CHS	cholesteryl hemisuccinate
CMV	cytomegalovirus
CNS	central nervous system
DDM	dodecyl maltoside
DMEM	Dulbecco's modified eagle medium
DTT	dithiothreitol
ECFP	enhanced cyan fluorescent protein
ECL	extracellular loop
EDTA	ethylenediaminetetraacetatic acid
ER	endoplasmic reticulum
FBS	fetal bovine serum
FRET	Förster resonance energy transfer
FSEC	fluorescence size exclusion chromatography
GFP	green fluorescent protein
GNT1	glucose N-acetyltransferase 1
GPCR	G-protein coupled receptor
HetNOE	heteronuclear NOE
HSQC	heteronuclear single-quantum coherence
ICL	intracellular loop
IDP	intrinsically disordered protein
I/O	input/output
KO	knockout
LED	light-emitting diode
LPAR	lysophosphatidic acid receptor
LTD	long-term depression
LTP	long-term potentiation
MEF	mouse embryonic fibroblast
MST	microscale thermophoresis
MW	molecular weight
miRNA	microRNA
NgR1	Nogo-66 receptor 1
NMR	nuclear magnetic resonance
NOE	nuclear Overhauser effect
ORF	open reading frame
PAGE	polyacrylamide gel electrophoresis
PBS	phosphate-buffered saline
PCR	polymerase chain reaction
PEI	polyethylenimine
PirB	paired immunoglobulin-like receptor B
PNGase F	peptide-N-glycosidase F
PPF	paired-pulse facilitation
ppm	parts per million
RHD	reticulon homology domain
RNAi	RNA interference
RT	room temperature
RTN	reticulon
S1P	sphingosine 1-phosphate
S1PR	sphingosine 1-phosphate receptor
SD	standard deviation
SDM	site-directed mutagenesis
SDS	sodium dodecyl sulfate
SEM	standard error of the mean
shRNA	small hairpin RNA
siRNA	small interfering RNA
SphK	sphingosine kinase
τ	time constant
T4L	T4 lysozyme
TMD	trans-membrane domain
TSPAN	tetraspanin
WT	wild-type
YFP	yellow fluorescent protein

CHAPTER 1

NOGO-A FROM ITS N- TO ITS C-TERMINUS: STRUCTURAL ASPECTS AND MOLECULAR INTERACTORS OF AN INHIBITOR OF NEURITE OUTGROWTH

Michael E. Arzt[1,2], Martin E. Schwab[1,3]

(unpublished manuscript)

M. E. A. conducted literature research, wrote the manuscript and prepared the figures.

[1] Brain Research Institute, University of Zurich, Switzerland
[2] Department of Biology, ETH Zurich, Switzerland
[3] Department of Health Sciences and Technology, ETH Zurich, Switzerland

Abstract

Neurons of the central nervous system (CNS) fail to re-grow fibers upon injury in part due to the presence of myelin-associated inhibitory molecules such as Nogo-A. Functional implications of the membrane protein Nogo-A for CNS regeneration, development, synaptic plasticity, and intracellular processes have been extensively studied *in vitro* and *in vivo*. A growing body of structural molecular information is available for Nogo-A which promotes our understanding of its molecular interactions and serves as an attractive starting point for rational drug design aiming to block or mimic Nogo-A actions. Though disordered over the majority of the protein, Nogo-A contains certain structural elements in both inhibitory domains: The biologically active Nogo-A-Δ20 region in the middle of the N-terminal extracellular domain includes three residual α-helices, and the second active site called Nogo-66 folds into a compact α-helical conformation in a membrane-like environment. Many interaction partners and several signal transducing receptor complexes for Nogo-A have been described which bind to different parts of the protein. Moving along the Nogo-A sequence from its N- to its C-terminus, we summarize the structural characteristics and functional binding sites of this biologically interesting and clinically important molecule.

Introduction

Nogo-A is a membrane protein of the central nervous system (CNS) that is best known for its inhibitory effect on the extension of neurites (Chen et al., 2000; GrandPre et al., 2000; Prinjha et al., 2000). Such non-permissive signals impede axon outgrowth in the context of CNS damage, thereby limiting the extent to which severed connections can be restored upon injury (Schwab and Strittmatter, 2014). Nogo-A, which is expressed by neuronal precursor cells, by subpopulations of neurons, and in the adult CNS primarily by oligodendrocytes and on myelin, is also implicated in CNS development and synaptic plasticity (Schwab, 2010; Schwab and Strittmatter, 2014). Intracellularly, Nogo proteins have been shown to influence the shape of the endoplasmic reticulum (ER), where their expression is especially high (GrandPre et al., 2000; Oertle et al., 2003b; Voeltz et al., 2006).

The *RTN4/Nogo* gene produces three major protein isoforms by alternative splicing and promoter usage, termed Nogo-A, Nogo-B, and Nogo-C (Oertle et al., 2003a). The C-terminal 188 amino acids (a. a.; unless marked differently, numbering of human Nogo-A is used throughout this review (Oertle et al., 2003a)), also referred to as the reticulon homology domain (RHD), are identical among the three isoforms, and are homologous to other members of the reticulon (RTN) family, to which Nogo also belongs (Oertle et al., 2003a). The N-termini that are linked to the RHD differ substantially from one another. While the very N-terminal 185 a. a. of Nogo-A and Nogo-B

are the same, Nogo-A features a unique 819 a. a. region between the shared N-terminal domain and the RHD. Nogo-C only contains an N-terminus of 11 a. a. that is generated by a second promoter.

Two domains of Nogo-A have been shown to exert inhibitory effects on neurite outgrowth and induce growth-cone collapse: the Nogo-A-Δ20 region (a. a. 567-748) within the Nogo-A-specific segment, and Nogo-66 (a. a. 1055-1120), a hydrophilic loop between the two hydrophobic stretches in the RHD (Fig. 1; Oertle et al., 2003b). Nogo-A-Δ20 and Nogo-66, both of which are exposed to the extracellular milieu on the cell surface, activate different neuronal receptors and intracellular cascades; however, signaling converges and leads to destabilization of the neuronal actin cytoskeleton and to downregulation of the cellular growth machinery (Fournier et al., 2001; Joset et al., 2010; Kempf et al., 2014; Schwab, 2010).

Antibodies targeted against Nogo-A have been used to neutralize its inhibitory effect *in vitro* and *in vivo*, and offer an attractive therapeutic strategy to promote axonal sprouting, regeneration and functional recovery after, e.g., spinal cord injury or stroke (Caroni and Schwab, 1988; Freund et al., 2006; Oertle et al., 2003b; Schnell and Schwab, 1990; Zorner and Schwab, 2010). In addition, soluble fragments of Nogo-A and of the Nogo-66 receptor NgR1 have been shown to abrogate neurite outgrowth inhibition (Fournier et al., 2002; GrandPre et al., 2002). However, structural information on ligand/receptor systems is essential for rational development of novel antagonists or agonists with therapeutic potential (Lescrinier, 2011). As a consequence, the architecture of Nogo-A and its receptors has been investigated by several groups, employing spectroscopic and other biochemical techniques. In this review, we aim to summarize the current knowledge on the structural biology of Nogo-A, with particular emphasis on the Nogo-A-specific region.

N-terminus (a. a. 1-185)

Nogo-A shares the first exon with its splicing isoform Nogo-B, encoding the very N-terminal 185 a. a. (Fig. 1) (Oertle et al., 2003a). In contrast, the N-terminus of Nogo-C only comprises 11 a. a. due to alternative promoter usage. Remarkably, none of the Nogo isoforms contain a typical N-terminal signal peptide expected for type I membrane proteins, mystifying the exact mechanism by which their extracellular regions reach the outside of the plasma membrane (Chen et al., 2000; von Heijne and Gavel, 1988). Multiple membrane topologies seem to exist, as the hydrophilic N-termini are found both extracellularly and in the cytosol (see RHD section). Within the N-terminus common to Nogo-A and Nogo-B, three proline-, glutamic acid-, serine- and threonine-rich (PEST) sequences are found, thought to confer short half-life to proteins by labeling them for degradation (Fig. 1B) (Oertle et al., 2003a; Rogers et al., 1986). There is a small stretch of high negative charge that almost exclusively contains glutamate and aspartate residues (a. a. 30-53), presumed to form weak interactions with Ca^{2+} ions (Oertle et al., 2003a). It is followed by a region

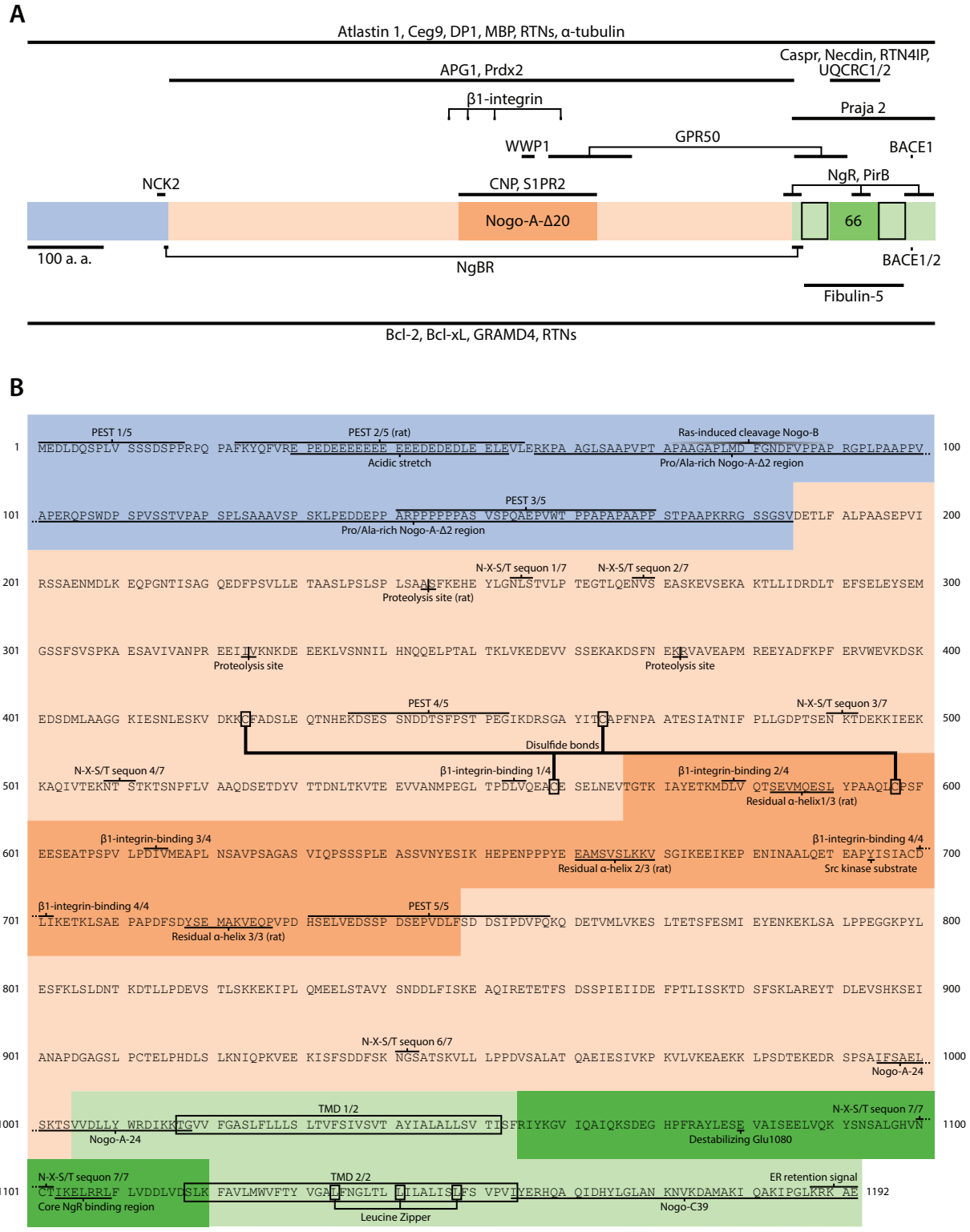

Fig. 1: Binding sites and structure of Nogo-A. A, Nogo-A is shown with its N-terminus shared with Nogo-B in blue, the Nogo-A-specific region in orange, and the RHD in green. The inhibitory regions Nogo-A-Δ20 and Nogo-66 (66) are accented, and TMDs are boxed. The binding sites of Nogo-A to other proteins are shown above, and those of Nogo-B below. **B**, Annotated sequence map of Nogo-A. Color labeling is identical to A.

enriched in proline and alanine (a. a. 57-185), suggesting a low degree of three-dimensional structure in this segment (Zander et al., 2007a). Indeed, the N-terminus shared by Nogo-A and Nogo-B is found to be intrinsically unstructured in nuclear magnetic resonance (NMR) and circular dichroism (CD) spectroscopy (Li and Song, 2007a). Nevertheless, a fragment of this region (rat a. a. 59-172, corresponding to human a. a. 57-185) exhibits inhibitory properties in a fibroblast spreading assay, though only minor effects on neurons are observed (Oertle et al., 2003b). Around a. a. 80, there is a proteolytic cleavage site that is cut in Nogo-B upon Ras-induced oncogenic transformation (Ahn et al., 2015). Proteolysis of Nogo-B then results in suppression of the interferon response in cancer cells, which is exploited by certain oncolytic viruses. Along the same lines, Nogo-B binds to Bcl-2 and Bcl-xL to attenuate their anti-apoptotic effect, and Nogo-C acts as a tumor suppressor by binding to B-Raf, though the binding regions of these interactions have not been established (Liu et al., 2014; Tagami et al., 2000). Several PxxP motifs are found in the proline/alanine-rich region that can act as SH3 ligands (Oertle et al., 2003a). In particular, a peptide containing PAAP at a. a. positions 173-176 has been shown to interact with the third SH3 domain of NCK2 (Liu et al., 2006). This cytoplasmic adapter protein is involved in reverse ephrin-B signaling and organization of the actin cytoskeleton, including axon guidance and cell motility (Buday et al., 2002; Li et al., 2001b; Li and She, 2000; McCarty, 1998). The classic role of NCK2 is to bind to phosphorylated tyrosines of cellular surface receptors with its SH2 domain and to use its three SH3 domains to recruit proline-rich effector proteins (Buday et al., 2002). The N-terminus of Nogo-A or Nogo-B would be recruited to the membrane and act as an effector in this scenario. However, the mutual influence of Nogo and NCK2 signaling is not fully understood.

As the shorter splicing isoform, Nogo-B does not possess any sequence that is absent in Nogo-A (Oertle et al., 2003a). Therefore, it seems logical that the binding site of the Nogo-B-specific receptor NgBR spans across the splicing junction that is only used for generation of Nogo-B (a. a. 181-200 of Nogo-B, or a. a. 181-185 and a. a. 1005–1019 of Nogo-A) (Miao et al., 2006). NgBR, which is composed of an intrinsically disordered ectodomain and an only partially folded cytoplasmic domain (Li and Song, 2007b), has been shown to play critical roles in angiogenesis (Teng et al., 2014; Zhao et al., 2010). NgBR is also involved in the production of dolichol monophosphate, a key molecule in N-linked glycosylation (Harrison et al., 2011; Park et al., 2014).

Nogo-A-specific region (a. a. 186-1004) including Nogo-A-Δ20

Primary structure

While the very N-termini of Nogo-B (a. a. 1-185) and Nogo-C (a. a. 1-11 originating from a different promoter) are directly linked to the RHD via alternative splicing, Nogo-A contains an additional, long, unique region (a. a. 186-1004), rendering it the longest Nogo isoform (Oertle et al., 2003a).

Interestingly, sequence alignment suggests that this segment originated evolutionarily from insertion of a neurocan-like sequence into an ancestor of Nogo-B (Shypitsyna et al., 2011). This part of the protein is also hydrophilic, but exhibits an a. a. composition typical for globular proteins (Fiedler et al., 2002; Zander et al., 2007a). Similarly to the N-terminus shared with Nogo-B, it contains two PEST sequences and several SH3 ligand motifs, though no SH3-bearing interaction partners have been identified to date (Oertle et al., 2003a). While human and rat Nogo-A each contain seven consensus sites for N-linked glycosylation (N-X-S/T), the bovine homolog harbors eight such motifs. Among these three species, only two sites are conserved in their position, namely one in the Nogo-A-specific region (human Asn490, rat Asn468, bovine Asn498) and one within Nogo-66 (human Asn1100, rat Asn1071, bovine Asn1110). A multitude of potential O-linked glycosylation sites are present in all three species (Steentoft et al., 2013). However, no glycan chains could be detected experimentally on bovine Nogo-A, and removal of putative sugars did not interfere with its inhibitory activity, thus calling the actual occupancy of glycosylation sites in question (Spillmann et al., 1998). A possible explanation for this is that Nogo-A, as an unconventionally trafficked membrane protein, could bypass the canonical ER/Golgi pathway, as is observed for α-integrin and cystic fibrosis trans-membrane conductance regulator (CFTR), as well as some soluble proteins (Chua et al., 2012; Schotman et al., 2008; Yoo et al., 2002).

Non-reducing SDS/PAGE has shown that a fragment derived from the Nogo-A-specific region (a. a. 334-966) exists in two disulfide isomers which migrate faster than their reduced equivalent, indicating a structural conformation induced by disulfide bonds (Zander et al., 2007a). It seems that four cysteines are involved in this disulfide bond formation, though their positions differ between species: Human Nogo-A contains six cysteines in the Nogo-A-specific region, of which four were shown to be important for folding of the protein (Cys424, Cys464, Cys559, Cys597; Fig. 1B) (Zander et al., 2007a). Though all of these cysteines are conserved in rat Nogo-A, only mutation of Cys443 (corresponding to human Cys464) led to diminished yields in recombinant expression, supporting the importance of cysteine in this position across species (Fiedler et al., 2002). Instead, the rat-specific Cys323 (corresponding to human Ser336) and Cys890 (corresponding to human His917) were found to be essential, along with Cys885 (corresponding to human Cys912) which is dispensable for human Nogo-A folding (Fiedler et al., 2002; Zander et al., 2007a). Interestingly, modification of cytoplasmic cysteines by sulfuhydryl reagents interfered with the function of Nogo-A in ER network formation (Voeltz et al., 2006). In addition, Cys424, Cys464, and Cys559 were claimed to be crucial for the neuroprotective role of Nogo-A against reactive oxygen species, which was attributed to an interaction of the Nogo-A-specific region with peroxiredoxin 2 (Prdx2) (Mi et al., 2012). The a. a. residues 290-562 have been shown to be essential for this function, and were sufficient to impose a protective effect on HT22 hippocampal neurons (Guo et al., 2013; Mi et al., 2012). Similarly, heat shock protein APG1 interacts with the

Nogo-A-specific region, and a co-regulation of the two proteins was observed under hypoxic and oxidative stress in hippocampal neurons (Kern et al., 2013).

Within the Nogo-A-specific segment, the Nogo-A-Δ20 domain (a. a. 567-748) has been shown to exert inhibitory activity on fibroblast spreading and neurite outgrowth (Oertle et al., 2003b). We have recently identified the G-protein coupled receptor (GPCR) sphingosine 1-phosphate receptor 2 (S1PR2) as a receptor for this domain (Kempf et al., 2014). Via the G protein G_{13} and the RhoGEF LARG, it causes activation of RhoA, resulting in destabilization of the actin cytoskeleton. However, S1PR2 does not seem to be the only protein that interacts with Nogo-A-Δ20; of particular interest are the tetraspanin protein Tspan-3 and the heparin sulfate proteoglycans syndecan-3 and -4, which can act as co-receptors and subunits of a multisubunit receptor complex in conjunction with S1PR2 (Thiede-Stan et al., 2015; Kempf et al., unpublished observations). Three out of four highly conserved β1-integrin-binding motifs are located in this region (a. a. 578-580, 613-615 and 700-702), and the fourth is positioned in close N-terminal proximity (a. a. 553-555) (Shypitsyna et al., 2011). Indeed, the Nogo-A-specific region inhibits adhesion-promoting signaling of β1-integrin, though a direct physical interaction seems to be weak and might require additional molecular components (Hu and Strittmatter, 2008). A protein microarray interaction study has found cyclic nucleotide phosphodiesterase (CNP) to interact with Nogo-A-Δ20, though this cytosolic protein is much more likely to be involved in intracellular functions of Nogo-A (Sumiyoshi et al., 2010). Similarly, the cytoplasmic C-terminus of G-protein coupled receptor 50 (GPR50) interacts with Nogo-A at the C-terminal boundary of Nogo-A-Δ20 (a. a. 685-794) and at the first hydrophobic stretch (a. a. 1008-1077), and the two proteins co-localize in the post-synaptic density (Grunewald et al., 2009). Nogo-A is not only inhibitory to neurite outgrowth by an interaction *in trans*, but could also impose a similar effect by expression in neurons (Mingorance et al., 2004; Montani et al., 2009). To this end, Nogo-A and GPR50 seem to have opposing roles, as GPR50 overexpression promoted neurite extension (Grunewald et al., 2009). A PPxY WW-ligand sequence motif found within Nogo-A-Δ20 (a. a. 656-659) is recognized by the NEDD4-like E3 ubiquitin ligase WWP1, which presumably regulates ubiquitination and proteasomal degradation of Nogo-A (Oertle et al., 2003a; Qin et al., 2008). NEDD4 itself was also found to interact with Nogo-A in a phage display screen, though this interaction has not been validated to date (Kurakin and Bredesen, 2002). Finally, Nogo-A-Δ20 contains the only phosphorylated tyrosine of Nogo-A, Tyr-694, which is phosphorylated by Src family kinases (Yokoyama et al., 2006). However, the consequences of this modification remain elusive.

A fragment at the very C-terminus of the Nogo-A-specific region called Nogo-A-24 (a. a. 995-1018) has been reported to bind to NgR1 at a high affinity without imposing an inhibitory effect (Hu et al., 2005; Huebner et al., 2011; Lauren et al., 2007). However, this direct interaction between the Nogo-A-specific region and NgR1 could not be reproduced in a spot array (Zander et al., 2007b).

Secondary/tertiary structure

Already shortly after the discovery of Nogo-A, it became obvious that this protein harbors large unstructured regions, as it contains many prolines and alanines and is very sensitive to proteolytic degradation (Chen et al., 2000; Fiedler et al., 2002; Li et al., 2004; Li and Song, 2007a; Spillmann et al., 1998; Zander et al., 2007a). The N-terminus of the Nogo-A-specific region contains a proteolytic hotspot, and cleavage of the recombinant protein has been observed to occur before Ser233 in rat Nogo-A (corresponding to human Ser245) and before Val325 and Arg373 in the human homolog (Fig. 1B) (Fiedler et al., 2002; Zander et al., 2007a). Another early indication for a lack of structural elements was that full-length Nogo-A and its recombinant fragments display an aberrant migration profile in SDS-PAGE gels, producing bands of much higher apparent molecular weights than expected from their sequences (Chen et al., 2000; Li et al., 2004; Li and Song, 2007a; Zander et al., 2007a). This observation represents a hallmark feature of intrinsically disordered proteins that has been attributed to their lower capacity to bind SDS (Tompa, 2002). However, a. a. composition and presence of disulfide bonds suggested a globular structure of the Nogo-A-specific region, which is why it was chosen as an antigen for the neutralizing IgM antibody IN-1 (Fiedler et al., 2002). For this antibody, no linear epitope could be identified in a spot assay, suggesting a discontinuous antigenic determinant and thus implying the presence of structural elements in this region (Zander et al., 2007b). This notion is further supported by the finding that incomplete trypsin digestion of a Nogo-A-specific fragment produced discrete bands, presumably reflecting structural domains (Zander et al., 2007a). Indeed, it seems that the Nogo-A-specific region, while being an intrinsically unstructured segment (Li and Song, 2007a), does contain some residual structural elements (see Chapter 4; Li et al., 2004; Zander et al., 2007a).

Due to the high biological relevance of the inhibitory Nogo-A-Δ20 domain, its structural properties have been an important focus of research. Whereas other parts of the intrinsically disordered N-terminus of Nogo-A could be regarded as flexible linkers with no rigid structure, this functional domain was initially expected to be structurally folded, in line with the classic "lock and key" model of ligand-receptor interaction (Fiedler et al., 2002). In surprising contrast, Nogo-A-Δ20 was also shown to be intrinsically disordered (see Chapter 4; Li and Song, 2007a). Structural flexibility can be advantageous to proteins, as it increases the surface area available for binding to molecular interactors, thereby contributing to both potential specificity but also promiscuity (Berlow et al., 2015; Tompa, 2003; Uversky and Dunker, 2013). For a protein like Nogo-A, which is implicated in various cellular processes presumably via different compositions of interacting receptor complexes (Schwab, 2010), structural disorder can therefore be an important feature. On the other hand, residual structures are often found in intrinsically disordered proteins and can serve as molecular recognition motifs forming initial contact between an intrinsically disordered protein and its binding partner (Fuxreiter et al., 2004; Song et al., 2008; Tsai et al., 2001; Zhang et

al., 2012). For Nogo-A-Δ20, CD spectroscopy and *in-silico* prediction suggest a slight α-helical propensity, which can be somewhat enhanced by addition of Zn^{2+} (Li et al., 2004; Li and Song, 2007a). We have recently confirmed by NMR spectroscopy that biologically active rat Nogo-A-Δ20, while being an intrinsically disordered region, contains three residual α-helices at the positions a. a. 560-567, 639-648, and 695-704 (corresponding to human a. a. 583-590, 661-670, and 718-727; see Chapter 4). Imitating a membrane-like environment by addition of phosphocholines did not induce pronounced folding of Nogo-A-Δ20 as observed for Nogo-66 (see Chapter 4 and RHD section; Vasudevan et al., 2010). Of the four cysteines found to be essential for folding of a larger Nogo-A-specific fragment (Zander et al., 2007a), only Cys597 is located within Nogo-A-Δ20. This implies that a disulfide bridge with a cysteine outside of Nogo-A-Δ20 is formed in the full-length protein, indicating the presence of additional structural properties that are not observable in the fragment alone. Unfortunately, studying the entire Nogo-A-specific region with NMR spectroscopy has failed due to low expression yields (Li and Song, 2007a). It is of note that addition of S1PR2 extracellular loops 2 and 3, shown to individually bind to Nogo-A-Δ20 at high affinity (Kempf et al., 2014), did not perturb the heteronuclear single quantum coherence spectrum of Nogo-A-Δ20 (see Chapter 4). While this might be indicative of a so-called fuzzy binding mechanism, i.e., retention of full flexibility even in the bound state (Fuxreiter and Tompa, 2012), additional structural data are required to solidify this notion.

Quarternary structure

The question whether Nogo-A oligomerizes to exert its inhibitory activity has long been on debate. Surface staining of Nogo-A produces a punctuate pattern in various cell types, which suggests that clustering occurs in the plasma membrane (Dodd et al., 2005). Nogo-A associates with Nogo-B and Nogo-C, and molecular interactions with other RTNs have been observed (Dodd et al., 2005; Liu et al., 2014; Qi et al., 2003). Analogously, dimerization of Nogo-A-Δ20 drastically enhanced its inhibitory effect especially in assays where it was administered in solution (Fournier et al., 2001; Oertle et al., 2003b). Gel permeation chromatography of a fragment of the Nogo-A-specific region (a. a. 334-966) indicated a large molecular weight consistent with oligomerization (Zander et al., 2007a). However, the same study reported this fragment to appear as a monomer in analytical ultracentrifugation and dynamic light scattering experiments. Whether Nogo-A oligomerizes *in vivo* therefore remains elusive.

Reticulon homology domain (a. a. 1005-1192) including Nogo-66

Whereas Nogo-A, Nogo-B, and Nogo-C differ in their N-termini, they share a common C-terminal region encoded by exons 4-9 (a. a. 1005-1192 in Nogo-A) (Oertle et al., 2003a). This part of the

protein is the defining feature of a family of four reticulons (RTNs), and is therefore referred to as the reticulon homology domain (RHD, Fig. 1) (Di Sano et al., 2012). It consists of two hydrophobic regions (a. a. 1017-1052 and a. a. 1118-1154) that flank a 66 a. a. hydrophilic loop (Oertle et al., 2003a). In Nogo, which is also referred to as RTN4, this loop is called Nogo-66 (a. a. 1055-1120) and exhibits inhibitory activity towards axonal outgrowth, causing collapse of the neuronal growth cone (Fournier et al., 2001; GrandPre et al., 2000; Oertle et al., 2003b). This is achieved via the leucine-rich repeat protein Nogo-66 receptor (NgR1), which is a glycosylphosphatidylinositol-anchored membrane protein (Fournier et al., 2001). As such, it requires co-receptors to transduce the Nogo-66-elicited signal to the interior of the cell, where S1PR2- and NgR1-mediated signaling converge on the activation of RhoA (Schwab, 2010). Spot array and mutagenesis experiments have identified a. a. 1103-1109 of Nogo-A (a. a. 49-55 within Nogo-66) as the core residues for NgR1 binding (Li et al., 2008; Zander et al., 2007b). This position is situated within "peptide 4" (a. a. 1085-1109, or a. a. 31-55 within Nogo-66), the least conserved region of Nogo-66 that is sufficient to induce growth-cone collapse and inhibit neurite outgrowth (GrandPre et al., 2000). However, surrounding elements also seem to play a pivotal role, as the potency of "peptide 4" is lower compared to full-length Nogo-66. NgR1 binding seems to be further enhanced by the regions directly outside of the two trans-membrane domains, i.e., Nogo-A-24 (a. a. 995-1018) in the Nogo-A-specific region and Nogo-C39 (a. a. 1154-1192) at the C-terminus (Hu et al., 2005; Lauren et al., 2007). A fragment of Nogo-A containing all three NgR1-interacting regions was markedly more inhibitory in a growth cone collapse assay than Nogo-66 alone, implying a cooperative trivalent binding mode of the membrane-proximal regions of Nogo-A to NgR1 (Huebner et al., 2011). Interestingly, NEP1-40 (a. a. 1055-1094 or a. a. 1-40 within Nogo-66), a peptide that partially overlaps "peptide 4" but misses the central inhibitory part, acts as an antagonist of NgR1 and enhances functional recovery after spinal cord injury (GrandPre et al., 2002). The structural characteristics of NgR1 have been thoroughly reviewed by Saha et al. (2014).

In addition to this classic receptor complex, paired immunoglobin-like receptor B (PirB) has been shown to function as a receptor for Nogo-66 (Atwal et al., 2008). PirB is a glycoprotein that is tethered to the membrane by a conventional trans-membrane domain, and contains six Ig-like domains in its extracellular N-terminus and four immunoreceptor tyrosine-based inhibition motif (ITIM) domains in its intracellular C-terminus (Nakamura et al., 2011; Takai, 2005). Similarly to NgR1, the affinity of Nogo-66 to PirB is enhanced by Nogo-A-24 and Nogo-C39 (Huebner et al., 2011).

Intracellularly, three mitochondrial proteins were found to interact with Nogo-66 in a yeast two-hybrid screen, i.e., ubiquinol-cytochome c reductase core proteins 1 and 2 (UQCRC1/2) and a novel protein designated Nogo-interacting mitochondrial protein (NIMP) (Hu et al., 2002). The latter, which is also called reticulon 4 interacting protein 1 (RTN4IP1), has been shown to exert a tumor-suppressive effect (Rahbari et al., 2013) and has been successfully crystallized in complex

with NADPH (PDB entry 2VN8). However, as Nogo-A is not physiologically present in mitochondria, the nature of these interactions is unclear and might only be relevant in the context of lesion-induced cell disruption (Hu et al., 2002). Another cancer-related molecule, the extracellular matrix glycoprotein Fibulin-5, is transported from the ER to the plasma membrane by Nogo-B via an interaction between the RHD and the sixth cbEGF domain of Fibulin-5 (Zhou et al., 2010). Nogo-B is also involved in the trafficking of TLR9 in the innate immune response, a function that is counteracted by direct binding of GRAM domain containing 4 protein (GRAMD4) to Nogo-B (Kimura et al., 2015). Spanning the first hydrophobic stretch and the N-terminal portion of Nogo-66 is the second binding site of Nogo-A for neurite outgrowth-promoting GPR50 (a. a. 1008-1077, see Nogo-A-specific part section) (Grunewald et al., 2009). Neuronal Nogo-66 also sequesters Necdin from the nucleus by binding to its central a. a. 95-290, which impedes the pro-outgrowth effect of Necdin (Liu et al., 2009). At paranodes, a Nogo-66-mediated Nogo-A/Caspr interaction has been described that seems to interact with voltage-dependent potassium channels Kv1.1 and Kv1.2 at early myelination stages of CNS development (Nie et al., 2003). The importance of Nogo-A in myelination is further highlighted by the finding that it interacts with myelin basic protein (MBP) and α-tubulin in mature oligodendrocytes, though positional information on the binding sites is lacking (Taketomi et al., 2002).

The structure of Nogo-66 is relatively well studied. Similarly to the rest of the Nogo-A sequence, recombinant Nogo-66 was found to be disordered in an aqueous solution by means of CD and NMR spectroscopy (Vasudevan et al., 2010). However, this region of the protein is unique in that it folds into a dense bundle of five α-helices in the presence of membrane-mimicking phosphocholines, and an NMR-derived protein structure could be determined (Vasudevan et al., 2010). The importance of a membrane-like environment for Nogo-66 structure is rationalized by the finding that Glu1080 (position 26 within Nogo-66) destabilizes folding of this domain if not neutralized by a counter-ion such as phosphocholine (Alhoshani et al., 2014). The obtained structure is a confirmation of earlier reports showing that fragments of Nogo-66 also had α-helical propensities, and folded into an α-helical structure in trifluoroethanol (Li et al., 2006a; Li et al., 2004; Vasudevan et al., 2010). NgR1-binding "peptide 4" corresponds to one of four exposed positive patches discovered in an NMR-derived structure of a smaller Nogo-66 fragment and is very accessible in the full-length Nogo-66 crystal structure (GrandPre et al., 2000; Li et al., 2006b; Vasudevan et al., 2010). Also, it should be possible to further truncate the N-terminus of NEP1-40 without a loss of its antagonistic activity, since only a. a. 1082-1094 (a. a. 28-40 within Nogo-66) appear accessible to a receptor (Vasudevan et al., 2010).

Membrane topology of Nogo has long been a matter of debate. The two hydrophobic stretches flanking Nogo-66 are 36 a. a. and 37 a. a. in length, respectively (Oertle et al., 2003a). Given that average trans-membrane domains consist of about 20 a. a., this is exceptionally long for a single-pass trans-membrane domain, but also too short for a complete bi-pass structure spanning both

leaflets. In order to interact with receptors on Nogo-A-responsive cells, the inhibitory domains have to be displayed toward the extracellular space. Both the N-terminus of Nogo-A and Nogo-66 were detected on the surface of oligodendrocytes, though at comparably low levels (GrandPre et al., 2000;Oertle et al., 2003b). This is supported by the presence of disulfide bonds in the Nogo-A-specific region, the formation of which requires the oxidizing milieu of extracellular and luminal compartments (Fiedler et al., 2002; Zander et al., 2007a). The finding that NgR1 is not only bound by Nogo-66 but also by the directly adjacent regions of the N- and C-terminal parts of Nogo-A, i.e., Nogo-A-24 and Nogo-C39, suggests a topology in which all three hydrophilic domains face the extracellular space (Hu et al., 2005; Lauren et al., 2007). On the other hand, the bulk of Nogo-A is found at intracellular membranes, where its N-terminus is detected on the cytosolic side (Kern et al., 2013; Mi et al., 2012; Oertle et al., 2003b; Taketomi et al., 2002; Yokoyama et al., 2006). Both hydrophobic regions of the RHD have been found to form short hairpins in the outer leaflet of the ER membrane, presenting the N-terminus, Nogo-66, and the C-terminus to the cytosol (Voeltz et al., 2006). Here, the structure of Nogo-A is directly connected to its ER-shaping function, as monotopic anchoring selectively increases the area of the cytosolic leaflet of the ER membrane, thus contributing to high membrane curvature. Oligomerization can further amplify this effect, since Nogo-A associates in the ER with RTN3 and DP1, a non-reticulon protein closely resembling the two long trans-membrane domains of the RHD (Shibata et al., 2008; Voeltz et al., 2006; Zurek et al., 2011). Strikingly, extending the hydrophobic regions of the Nogo RHD to the length of a typical bi-pass trans-membrane domain obstructs exclusive partitioning into ER tubules, and interferes with ER-shaping effects attributed to Nogo (Zurek et al., 2011). The mechanistic origin of these different membrane topologies remains elusive (Oertle et al., 2003b). As Nogo-A is inserted into the membrane by a non-conventional pathway, there might exist individual insertion mechanisms for each topology. Post-translational insertion has been observed for a group of so-called tail-anchored proteins which, reminiscent of Nogo-A, lack an N-terminal signal peptide but contain a trans-membrane domain about 30 a. a. before their C-termini (Borgese et al., 2007). After their biosynthesis at free ribosomes, these proteins are targeted to specific membranes by a rapid direct insertion mechanism that can induce translocation of the short C-termini (Kutay et al., 1993). Depending on the hydrophobicity of the trans-membrane domain, this process can occur spontaneously or require the assistance of chaperones (Johnson et al., 2013). An alternative model explaining the co-existence of several membrane topologies is interconversion (Bowie, 2013). Though topology flipping of hydrophilic domains through the lipid bilayer seems energetically unfavorable, such a mechanism has been observed for EmrE (Seppala et al., 2010) and aquaporin 1 (Lu et al., 2000). In addition, topology flipping of lactose permease is observed even in the absence of any putative chaperone proteins (Wang et al., 2002), and is controlled by the lipid composition of the membrane (Dowhan and Bogdanov, 2009). It is therefore possible

that the different topologies of Nogo-A on the cell surface and in the ER are determined by differences in the lipid contents of the plasma and ER membranes.

The trans-membrane domains of Nogo-A also seem to be important interactive regions of the protein. Atlastin 1 (ATL1), an ER-associated integral membrane GTPase that has been found mutated in hereditary spastic paraplegia, binds to the RHD of Nogo-A and RTN3C, and to DP1 (Hu et al., 2009). These interactions seem to occur within the hydrophobic segments, as DP1 only contains a very short loop between its two trans-membrane domains. In addition, binding of ATL1 to RTN3C could be abolished by deletion of trans-membrane domains in either of the proteins. Recently, it has been shown that Ceg9, an Icm/Dot translocated substrate (IDTS) protein of the intracellular pathogen *Legionella pneumophila*, also binds to Nogo-A and Nogo-B, forming a tripartite complex with ATL1 (Haenssler et al., 2015). This bacterium hijacks the host cell vesicular system to propagate inside a replication vacuole by interactions with host proteins, such as Nogo-A. The second hydrophobic stretch in the RHD is the most highly conserved part of this protein across phyla (Yang and Strittmatter, 2007). This region contains a leucine-zipper-like motif which is critical for Nogo-B-mediated induction of apoptosis (Li et al., 2001a; Oertle et al., 2003a).

Eventually, a short hydrophilic C-terminus is present in Nogo (a. a. 1155-1192) (Oertle et al., 2003a). This part of the protein, also referred to as Nogo-C39 (a. a. 1154-1192), is intrinsically unstructured and binds to NgR1 (Lauren et al., 2007; Li and Song, 2007a). Nogo-A binds to β-amyloid converting enzyme 1 (BACE1) and interferes with BACE1-driven production of amyloid-β (He et al., 2004; Wojcik et al., 2007). Since also Nogo-B, Nogo-C, and RTN3 exhibit this interaction, a binding region inside the RHD seems likely (Murayama et al., 2006). Indeed, BACE1 was shown to bind to the C-terminus of RTN3, requiring a Gln-Ile-Asp motif that is conserved among reticulons (a. a. 1161-1163 in Nogo-A) (He et al., 2006). As stated above, proteolytic turnover of Nogo-A seems to be regulated by WWP1 and NEDD4 E3 ubiquitin ligases that bind to Nogo-A-Δ20 (Kurakin and Bredesen, 2002; Qin et al., 2008). Additionally, the RING-type E3 ligase Praja 2 (PJA2) binds to the RHD and ubiquitinates Nogo-A in neurons (Sepe et al., 2014). The final five a. a. at the C-terminus constitute a classic di-lysine signal for ER membrane retention, which is in line with the finding that a large portion of cellular Nogo-A molecules remain associated to intracellular membranes (Chen et al., 2000; GrandPre et al., 2000; Oertle et al., 2003a; Oertle et al., 2003b; Prinjha et al., 2000; van de Velde et al., 1994).

Conclusion

Visualization is a key element of human problem solving, both in everyday life and in science. As we tackle the complex biological phenomena around us, we depend on fairly limited capabilities of our senses, particularly eyesight. It is for this reason that the invention of microscopes has

Interactor				Nogo-A					
Alias	Full name	Interaction site	Residues	Interaction site	Residues	K_D	Evidence	Function	References
APG1	Heat shock protein APG1	n.d.	n.d.	Nogo-A-specific region	174-979 (rat)	n.d.	MS, Co-IP, PLA	Hypoxic and oxidative stress	Kern et al., 2013
ATL1	Atlastin 1	C-terminus* (TMDs)	448-558*	RHD (TMDs)	n.d.	n.d.	MS, Co-IP	ER shaping	Hu et al., 2009
BACE1	β-amyloid converting enzyme 1	C-terminus*	n.d.	C-terminus*	1161-1163*	n.d.	Co-IP	β-secretase in Alzheimer's disease	Wojcik et al., 2007; He et al., 2006
Caspr	Contactin-associated protein	n.d.	n.d.	Nogo-66	1055-1120	n.d.	Co-IP, CBA	Myelin formation	Nie et al., 2003
CD29	β1-integrin	n.d.	n.d.	Nogo-A-specific region Nogo-A-Δ20 Nogo-A-Δ20 Nogo-A-Δ20	553-555 578-580 613-615 700-702	n.d.	Co-IP, Seq	Cell-cell and Cell-ECM interactions	Hu & Strittmatter, 2008; Shypitsyna et al., 2011
Ceg9	Ceg9 (*Legionella pneumophila*)	N-terminal half*	1-120*	n.d.	n.d.	n.d.	MS, Co-IP	*Legionella pneumophila* replication vacuole	Haenssler et al., 2015
CNP	Cyclic nucleotide phosphodiesterase	n.d.	n.d.	Nogo-A-Δ20	567-748	n.d.	PMA, Co-IP	Membrane anchor for tubulin in oligodendrocytes	Sumiyoshi et al., 2010
DP1	Deleted in polyposis 1	n.d.	n.d.	n.d.	n.d.	n.d.	MS, Co-IP	ER shaping	Voeltz et al., 2006
GPR50	G-protein coupled receptor 50	Intracellular C-terminus	292-617	Nogo-A-specific region RHD	685-794 1008-1077	n.d. n.d.	Y2H, Co-IP	Neurite extension	Grünewald et al., 2009
MBP	Myelin basic protein	n.d.	n.d.	n.d.	n.d.	n.d.	Co-IP	Myelin formation	Taketomi et al., 2002
NCK2	Cytoplasmic NCK2	Third SH3 domain	199-257	N-terminus	171-181	low-μM	NMR, ITC	Adapter protein	Liu et al., 2006
NDN	Necdin	Central region	95-290	Nogo-66	1055-1120	n.d.	Y2H, Co-IP	Nuclear protein, promotes neurite outgrowth	Liu et al., 2009
NgR	Nogo-66 receptor 1	LRR (concave center)	various	Nogo-66 Nogo-A-24 Nogo-C39	1085-1109 995-1018 1154-1192	low-nM low-nM low-nM	CBA CBA CBA	Neurite outgrowth inhibition, growth cone collapse Enhances binding of Nogo-66 to NgR Enhances binding of Nogo-66 to NgR	Fournier et al., 2001; Schimmele et al., 2005; Lauren et al., 2007 Hu et al., 2005; Lauren et al., 2007 Lauren et al., 2007
PirB	Paired immunoglobin-like receptor B	Extracellular N-terminus n.d. n.d.	n.d. n.d. n.d.	Nogo-66 Nogo-A-24 Nogo-C39	1085-1109 995-1018 1154-1192	low-nM low-nM low-nM	EC, CBA CBA CBA	Neurite outgrowth inhibition Enhances binding of Nogo-66 to PirB Enhances binding of Nogo-66 to PirB	Atwal et al., 2008; Huebner et al., 2011 Huebner et al., 2011 Huebner et al., 2011
PJA2	Praja 2	C-terminal half	531-708	RHD	1005-1192	n.d.	Co-IP	Ubiquitination/degradation	Sepe et al., 2014
Prdx2	Peroxiredoxin 2	n.d.	n.d.	Nogo-A-specific region	186-1004	n.d.	PDA	Peroxidase	Mi et al., 2012
RTN4A	Nogo-A	n.d.	n.d.	n.d.	n.d.	n.d.	GPC	Nogo clustering	Zander, Hettich et al., 2007
RTN4B	Nogo-B	n.d.	n.d.	n.d.	n.d.	n.d.	Co-IP	Nogo clustering	Dodd et al., 2005
RTN4C	Nogo-C	n.d.	n.d.	n.d.	n.d.	n.d.	Co-IP	Nogo clustering	Dodd et al., 2005
RTN4IP1	Reticulon 4 interacting protein 1	n.d.	n.d.	Nogo-66	1055-1120	n.d.	Y2H, Co-IP	Mitochondrial protein, tumor suppression	Hu et al., 2002; Rahbari et al., 2013
S1PR2	Sphingosine 1-phosphate receptor 2	ECL1 ECL2 ECL3	92-105 171-192 251-269	Nogo-A-Δ20	544-725 (rat)	low-μM mid-nM mid-nM	Y2H, Co-IP, BLI, MST	Neurite outgrowth inhibition, growth cone collapse, fibroblast spreading inhibition	Kempf et al., 2014
TUBA	α-tubulin	n.d.	n.d.	n.d.	n.d.	n.d.	Co-IP	Microtubule constituent	Taketomi et al., 2002
UQCRC1	Ubiquinol-cytochome c reductase core protein 1	n.d.	n.d.	Nogo-66	1055-1120	n.d.	Y2H, Co-IP	Mitochondrial respiratory chain	Hu et al., 2002
UQCRC2	Ubiquinol-cytochome c reductase core protein 2	n.d.	n.d.	Nogo-66	1055-1120	n.d.	Y2H, Co-IP	Mitochondrial respiratory chain	Hu et al., 2002
WWP1	NEDD4-like E3 ubiquitin-protein ligase	WW domain 1 WW domain 2 WW domain 3 WW domain 4	346-385 380-417 453-491 494-531	Nogo-A-Δ20	650-666	low-μM low-μM low-μM low-μM	T7PD, PDA, Co-IP, CD, NMR, ITC, Seq	Ubiquitination/degradation	Qin et al., 2008

Interactor				Nogo-B					
Alias	Full name	Interaction site	Residues	Interaction site	Residues	KD	Evidence	Function	References
BACE1	β-amyloid converting enzyme 1	C-terminus	444-501	C-terminus*	342-344*	n.d.	MS, Co-IP	β-secretase in Alzheimer's disease	He et al., 2004; He et al., 2006; Murayama et al., 2006; Wojcik et al., 2007
BACE2	β-amyloid converting enzyme 2	n.d.	n.d.	n.d.	n.d.	n.d.	Co-IP	β-secretase in Alzheimer's disease	Murayama et al., 2006
Bcl-2	B-cell lymphoma 2	n.d.	n.d.	n.d.	n.d.	n.d.	Y2H, Co-IP	Anti-apoptotic	Tagami et al., 2000
Bcl-xL	B-cell lymphoma-extra large	n.d.	n.d.	n.d.	n.d.	n.d.	Y2H, Co-IP	Anti-apoptotic	Tagami et al., 2000
Ceg9	*Ceg9* (*Legionella pneumophila*)	N-terminal half	1-120	n.d.	n.d.	n.d.	MS, Co-IP	*Legionella pneumophila* replication vacuole	Haenssler et al., 2015
FBLN5	Fibulin 5	Sixth cbEGF domain	288-333	RHD	202-332	n.d.	Y2H, PDA, Co-IP, SPB	Tumor migration	Zhou et al., 2010
GRAMD4	GRAM domain containing protein 4	n.d.	n.d.	n.d.	n.d.	n.d.	MS, Co-IP	Immune response, pro-apoptotic	Kimura et al., 2015
NgBR	Nogo-B Receptor	N-terminus	n.d.	N-terminus/RHD	181-200	low-nM	cDNA, CBA	Angiogenesis	Miao et al., 2006
RTN3	Reticulon 3	RHD	48-139, 157-218	n.d.	n.d.	n.d.	Y2H, Co-IP	Apoptosis	Qi et al., 2003
RTN4C	Nogo-C	n.d.	n.d.	n.d.	n.d.	n.d.	MS, Co-IP	Nogo clustering	Liu et al., 2014

Interactor				Nogo-C					
Alias	Full name	Interaction site	Residues	Interaction site	Residues	KD	Evidence	Function	References
BACE1	β-amyloid converting enzyme 1	n.d.	n.d.	n.d.	n.d.	n.d.	Co-IP	β-secretase in Alzheimer's disease	Murayama et al., 2006
BRAF	B-Raf	n.d.	n.d.	n.d.	n.d.	n.d.	MS, Co-IP	Growth, proliferation, migration	Liu et al., 2014
RTN4B	Nogo-B	n.d.	n.d.	n.d.	n.d.	n.d.	MS, Co-IP	Nogo clustering	Liu et al., 2014

Table 1: Interacting proteins of Nogo-A (top), Nogo-B (middle) and Nogo-C (bottom). Screening hits are only included if independently validated by a second experiment. Information derived from studies with other reticulons is marked with an asterisk. RTN4IP1 is also called NIMP. BLI, Biolayer interferometry; CBA, Cell binding assay; cDNA, cDNA screening; Co-IP: Co-immunoprecipitation; EC, Expression cloning; ECM, Extracellular matrix; GPC, Gel permeation chromatography; ITC, Isothermal titration calorimetry; MS, Mass spectrometry; MST, Microscale thermophoresis; PDA, Pull-down assay; PLA, Proximity ligation assay; PMA, Protein microarray; Seq, Consensus sequence in Nogo-A; SPB, Solid phase binding assay; T7PD, T7 phage display; Y2H, yeast 2-hybrid.

spawned some of the most remarkable discoveries in several scientific disciplines. X-ray crystallography and NMR spectroscopy have pushed the border even further, enabling us to envision objects much smaller than the wavelength of visible light, e.g., proteins. To date, more than 100'000 protein structures are deposited in the Protein Data Bank, serving as puzzle pieces for our understanding of complex signaling and structural networks (www.rcsb.org and (Berman et al., 2000)).

At the same time, one has to be cautious when interpreting data from an atomic level with a mind designed to deal with objects in the range of millimeters to kilometers, as certain phenomena cannot be extrapolated from one scale to another. The finding that proteins do not require stable folding to engage in specific molecular interactions is a good example of such a caveat. Intrinsically disordered proteins are found in all three domains of life, i.e., Archaea, Eukaryota, and Bacteria, where they contribute to various cellular processes (Dunker et al., 2015). Structural ambiguity allows each part of an intrinsically disordered protein to interact with different molecules depending on context, maximizing its capabilities to act as a signaling hub (Berlow et al., 2015; Tompa, 2003; Uversky and Dunker, 2013). In addition to this "moonlighting" function, a high degree of flexibility increases the interaction surface with binding partners, thus enhancing specificity.

In Nogo-A, the majority of the sequence is intrinsically disordered, including the potent inhibitory domain Nogo-A-Δ20. To execute its various functions in CNS development and rewiring, synaptic plasticity, ER shaping and other processes (Schwab, 2010), Nogo-A interacts with numerous other proteins (Table 1). Structural disorder of Nogo-A therefore increases the surface area available for binding to different combinations of interacting molecules in each setting. If the huge N-terminus of Nogo-A is indeed flipped across the membrane to switch between topologies, flexibility would be imagined to facilitate this process. Strikingly, Nogo-66 appeared as an unstructured domain in solution but folded into a stable conformation as phosphocholine was added to mimic a membrane-like environment (Vasudevan et al., 2010). This indicates that the molecular surrounding critically influences the transition between ordered and disordered states, a phenomenon that could also be imagined for other domains of Nogo-A. It is of note that intrinsic order seems to be a common feature among myelin proteins (Han et al., 2013). For example, reminiscent of Nogo-66, MBP also belongs to the family of intrinsically disordered proteins when in solution, but assumes secondary structure in the presence of lipids (Harauz et al., 2009; Stadler et al., 2014). Given the unusually high lipid content of the myelin membrane, folding of myelin proteins could therefore be particularly susceptible to changes in their lipidic environment (Boggs and Moscarello, 1978; Inouye and Kirschner, 1988).

Structural biology is an invaluable complementary approach enhancing our knowledge about the nature of protein conformations and interactions. A better understanding of the architecture

of ligands and receptors involved in Nogo signaling will serve as an important template for the development of novel therapeutic agents.

References

Ahn, D.G., T. Sharif, K. Chisholm, D.M. Pinto, S.A. Gujar, and P.W. Lee. 2015. Ras transformation results in cleavage of reticulon protein Nogo-B that is associated with impairment of IFN response. *Cell Cycle*. 14:2301-2310.

Alhoshani, A., R. Vithayathil, J. Bandong, K.M. Chrunyk, G.O. Moreno, G.A. Weiss, and M.J. Cocco. 2014. Glutamate provides a key structural contact between reticulon-4 (Nogo-66) and phosphocholine. *Biochimica et biophysica acta*. 1838:2350-2356.

Atwal, J.K., J. Pinkston-Gosse, J. Syken, S. Stawicki, Y. Wu, C. Shatz, and M. Tessier-Lavigne. 2008. PirB is a functional receptor for myelin inhibitors of axonal regeneration. *Science*. 322:967-970.

Berlow, R.B., H.J. Dyson, and P.E. Wright. 2015. Functional advantages of dynamic protein disorder. *FEBS letters*.

Berman, H.M., J. Westbrook, Z. Feng, G. Gilliland, T.N. Bhat, H. Weissig, I.N. Shindyalov, and P.E. Bourne. 2000. The Protein Data Bank. *Nucleic acids research*. 28:235-242.

Boggs, J.M., and M.A. Moscarello. 1978. Structural organization of the human myelin membrane. *Biochimica et biophysica acta*. 515:1-21.

Borgese, N., S. Brambillasca, and S. Colombo. 2007. How tails guide tail-anchored proteins to their destinations. *Current opinion in cell biology*. 19:368-375.

Bowie, J.U. 2013. Structural biology. Membrane protein twists and turns. *Science*. 339:398-399.

Buday, L., L. Wunderlich, and P. Tamas. 2002. The Nck family of adapter proteins: regulators of actin cytoskeleton. *Cellular signalling*. 14:723-731.

Caroni, P., and M.E. Schwab. 1988. Antibody against myelin-associated inhibitor of neurite growth neutralizes nonpermissive substrate properties of CNS white matter. *Neuron*. 1:85-96.

Chen, M.S., A.B. Huber, M.E. van der Haar, M. Frank, L. Schnell, A.A. Spillmann, F. Christ, and M.E. Schwab. 2000. Nogo-A is a myelin-associated neurite outgrowth inhibitor and an antigen for monoclonal antibody IN-1. *Nature*. 403:434-439.

Chua, C.E., Y.S. Lim, M.G. Lee, and B.L. Tang. 2012. Non-classical membrane trafficking processes galore. *Journal of cellular physiology*. 227:3722-3730.

Di Sano, F., P. Bernardoni, and M. Piacentini. 2012. The reticulons: guardians of the structure and function of the endoplasmic reticulum. *Experimental cell research*. 318:1201-1207.

Dodd, D.A., B. Niederoest, S. Bloechlinger, L. Dupuis, J.P. Loeffler, and M.E. Schwab. 2005. Nogo-A, -B, and -C are found on the cell surface and interact together in many different cell types. *The Journal of biological chemistry*. 280:12494-12502.

Dowhan, W., and M. Bogdanov. 2009. Lipid-dependent membrane protein topogenesis. *Annual review of biochemistry*. 78:515-540.

Dunker, A.K., S.E. Bondos, F. Huang, and C.J. Oldfield. 2015. Intrinsically disordered proteins and multicellular organisms. *Seminars in cell & developmental biology*. 37:44-55.

Fiedler, M., C. Horn, C. Bandtlow, M.E. Schwab, and A. Skerra. 2002. An engineered IN-1 F(ab) fragment with improved affinity for the Nogo-A axonal growth inhibitor permits immunochemical detection and shows enhanced neutralizing activity. *Protein engineering*. 15:931-941.

Fournier, A.E., G.C. Gould, B.P. Liu, and S.M. Strittmatter. 2002. Truncated soluble Nogo receptor binds Nogo-66 and blocks inhibition of axon growth by myelin. *The Journal of neuroscience : the official journal of the Society for Neuroscience*. 22:8876-8883.

Fournier, A.E., T. GrandPre, and S.M. Strittmatter. 2001. Identification of a receptor mediating Nogo-66 inhibition of axonal regeneration. *Nature*. 409:341-346.

Freund, P., E. Schmidlin, T. Wannier, J. Bloch, A. Mir, M.E. Schwab, and E.M. Rouiller. 2006. Nogo-A-specific antibody treatment enhances sprouting and functional recovery after cervical lesion in adult primates. *Nature medicine*. 12:790-792.

Fuxreiter, M., I. Simon, P. Friedrich, and P. Tompa. 2004. Preformed structural elements feature in partner recognition by intrinsically unstructured proteins. *Journal of molecular biology*. 338:1015-1026.

Fuxreiter, M., and P. Tompa. 2012. Fuzzy complexes: a more stochastic view of protein function. *Advances in experimental medicine and biology*. 725:1-14.

GrandPre, T., S. Li, and S.M. Strittmatter. 2002. Nogo-66 receptor antagonist peptide promotes axonal regeneration. *Nature*. 417:547-551.

GrandPre, T., F. Nakamura, T. Vartanian, and S.M. Strittmatter. 2000. Identification of the Nogo inhibitor of axon regeneration as a Reticulon protein. *Nature*. 403:439-444.

Grunewald, E., H.L. Kinnell, D.J. Porteous, and P.A. Thomson. 2009. GPR50 interacts with neuronal NOGO-A and affects neurite outgrowth. *Molecular and cellular neurosciences*. 42:363-371.

Guo, F., H. Wang, L. Li, H. Zhou, H. Wei, W. Jin, Q. Wang, and L. Xiong. 2013. A novel domain of amino-Nogo-A protects HT22 cells exposed to oxygen glucose deprivation by inhibiting NADPH oxidase activity. *Cellular and molecular neurobiology*. 33:443-452.

Haenssler, E., V. Ramabhadran, C.S. Murphy, M.I. Heidtman, and R.R. Isberg. 2015. Endoplasmic Reticulum Tubule Protein Reticulon 4 Associates with the Legionella pneumophila Vacuole and with Translocated Substrate Ceg9. *Infection and immunity*. 83:3479-3489.

Han, H., M. Myllykoski, S. Ruskamo, C. Wang, and P. Kursula. 2013. Myelin-specific proteins: a structurally diverse group of membrane-interacting molecules. *Biofactors*. 39:233-241.

Harauz, G., V. Ladizhansky, and J.M. Boggs. 2009. Structural polymorphism and multifunctionality of myelin basic protein. *Biochemistry*. 48:8094-8104.

Harrison, K.D., E.J. Park, N. Gao, A. Kuo, J.S. Rush, C.J. Waechter, M.A. Lehrman, and W.C. Sessa. 2011. Nogo-B receptor is necessary for cellular dolichol biosynthesis and protein N-glycosylation. *The EMBO journal*. 30:2490-2500.

He, W., X. Hu, Q. Shi, X. Zhou, Y. Lu, C. Fisher, and R. Yan. 2006. Mapping of interaction domains mediating binding between BACE1 and RTN/Nogo proteins. *Journal of molecular biology*. 363:625-634.

He, W., Y. Lu, I. Qahwash, X.Y. Hu, A. Chang, and R. Yan. 2004. Reticulon family members modulate BACE1 activity and amyloid-beta peptide generation. *Nature medicine*. 10:959-965.

Hu, F., B.P. Liu, S. Budel, J. Liao, J. Chin, A. Fournier, and S.M. Strittmatter. 2005. Nogo-A interacts with the Nogo-66 receptor through multiple sites to create an isoform-selective subnanomolar agonist. *The Journal of neuroscience : the official journal of the Society for Neuroscience*. 25:5298-5304.

Hu, F., and S.M. Strittmatter. 2008. The N-terminal domain of Nogo-A inhibits cell adhesion and axonal outgrowth by an integrin-specific mechanism. *The Journal of neuroscience : the official journal of the Society for Neuroscience*. 28:1262-1269.

Hu, J., Y. Shibata, P.P. Zhu, C. Voss, N. Rismanchi, W.A. Prinz, T.A. Rapoport, and C. Blackstone. 2009. A class of dynamin-like GTPases involved in the generation of the tubular ER network. *Cell*. 138:549-561.

Hu, W.H., O.N. Hausmann, M.S. Yan, W.M. Walters, P.K. Wong, and J.R. Bethea. 2002. Identification and characterization of a novel Nogo-interacting mitochondrial protein (NIMP). *Journal of neurochemistry*. 81:36-45.

Huebner, E.A., B.G. Kim, P.J. Duffy, R.H. Brown, and S.M. Strittmatter. 2011. A multi-domain fragment of Nogo-A protein is a potent inhibitor of cortical axon regeneration via Nogo receptor 1. *The Journal of biological chemistry*. 286:18026-18036.

Inouye, H., and D.A. Kirschner. 1988. Membrane interactions in nerve myelin: II. Determination of surface charge from biochemical data. *Biophysical journal*. 53:247-260.

Johnson, N., K. Powis, and S. High. 2013. Post-translational translocation into the endoplasmic reticulum. *Biochimica et biophysica acta*. 1833:2403-2409.

Joset, A., D.A. Dodd, S. Halegoua, and M.E. Schwab. 2010. Pincher-generated Nogo-A endosomes mediate growth cone collapse and retrograde signaling. *The Journal of cell biology*. 188:271-285.

Kempf, A., B. Tews, M.E. Arzt, O. Weinmann, F.J. Obermair, V. Pernet, M. Zagrebelsky, A. Delekate, C. Iobbi, A. Zemmar, Z. Ristic, M. Gullo, P. Spies, D. Dodd, D. Gygax, M. Korte, and M.E. Schwab. 2014. The sphingolipid receptor S1PR2 is a receptor for Nogo-a repressing synaptic plasticity. *PLoS biology*. 12:e1001763.

Kern, F., R.I. Stanika, B. Sarg, M. Offterdinger, D. Hess, G.J. Obermair, H. Lindner, C.E. Bandtlow, L. Hengst, and R. Schweigreiter. 2013. Nogo-A couples with Apg-1 through interaction and co-ordinate expression under hypoxic and oxidative stress. *The Biochemical journal*. 455:217-227.

Kimura, T., S. Endo, M. Inui, S. Saitoh, K. Miyake, and T. Takai. 2015. Endoplasmic Protein Nogo-B (RTN4-B) Interacts with GRAMD4 and Regulates TLR9-Mediated Innate Immune Responses. *J Immunol*. 194:5426-5436.

Kurakin, A., and D. Bredesen. 2002. Target-assisted iterative screening reveals novel interactors for PSD95, Nedd4, Src, Abl and Crk proteins. *Journal of biomolecular structure & dynamics*. 19:1015-1029.

Kutay, U., E. Hartmann, and T.A. Rapoport. 1993. A class of membrane proteins with a C-terminal anchor. *Trends in cell biology*. 3:72-75.

Lauren, J., F. Hu, J. Chin, J. Liao, M.S. Airaksinen, and S.M. Strittmatter. 2007. Characterization of myelin ligand complexes with neuronal Nogo-66 receptor family members. *The Journal of biological chemistry*. 282:5715-5725.

Lescrinier, E. 2011. Structural biology in drug development. *Verhandelingen - Koninklijke Academie voor Geneeskunde van Belgie*. 73:65-78.

Li, M., Y. Li, X. Liao, J. Liu, H. Qin, Z.C. Xiao, and J. Song. 2008. Rational design, solution conformation and identification of functional residues of the soluble and structured Nogo-54, which mimics Nogo-66 in inhibiting the CNS neurite outgrowth. *Biochemical and biophysical research communications*. 373:498-503.

Li, M., J. Liu, X. Ran, M. Fang, J. Shi, H. Qin, J.M. Goh, and J. Song. 2006a. Resurrecting abandoned proteins with pure water: CD and NMR studies of protein fragments solubilized in salt-free water. *Biophysical journal*. 91:4201-4209.

Li, M., J. Liu, and J. Song. 2006b. Nogo goes in the pure water: solution structure of Nogo-60 and design of the structured and buffer-soluble Nogo-54 for enhancing CNS regeneration. *Protein science : a publication of the Protein Society*. 15:1835-1841.

Li, M., J. Shi, Z. Wei, F.Y. Teng, B.L. Tang, and J. Song. 2004. Structural characterization of the human Nogo-A functional domains. Solution structure of Nogo-40, a Nogo-66 receptor antagonist enhancing injured spinal cord regeneration. *European journal of biochemistry / FEBS*. 271:3512-3522.

Li, M., and J. Song. 2007a. The N- and C-termini of the human Nogo molecules are intrinsically unstructured: bioinformatics, CD, NMR characterization, and functional implications. *Proteins*. 68:100-108.

Li, M., and J. Song. 2007b. Nogo-B receptor possesses an intrinsically unstructured ectodomain and a partially folded cytoplasmic domain. *Biochemical and biophysical research communications*. 360:128-134.

Li, Q., B. Qi, K. Oka, M. Shimakage, N. Yoshioka, H. Inoue, A. Hakura, K. Kodama, E.J. Stanbridge, and M. Yutsudo. 2001a. Link of a new type of apoptosis-inducing gene ASY/Nogo-B to human cancer. *Oncogene*. 20:3929-3936.

Li, W., J. Fan, and D.T. Woodley. 2001b. Nck/Dock: an adapter between cell surface receptors and the actin cytoskeleton. *Oncogene*. 20:6403-6417.

Li, W., and H. She. 2000. The SH2 and SH3 adapter Nck: a two-gene family and a linker between tyrosine kinases and multiple signaling networks. *Histology and histopathology*. 15:947-955.

Liu, J., M. Li, X. Ran, J.S. Fan, and J. Song. 2006. Structural insight into the binding diversity between the human Nck2 SH3 domains and proline-rich proteins. *Biochemistry*. 45:7171-7184.

Liu, X., S.J. Cui, S.J. Zhu, D.C. Geng, and L. Yu. 2014. Nogo-C contributes to HCC tumorigenesis via suppressing cell growth and its interactome analysis with comparative proteomics research. *International journal of clinical and experimental pathology*. 7:2044-2055.

Liu, X., Y. Wang, Y. Zhang, W. Zhu, X. Xu, M. Niinobe, K. Yoshikawa, C. Lu, and C. He. 2009. Nogo-A inhibits necdin-accelerated neurite outgrowth by retaining necdin in the cytoplasm. *Molecular and cellular neurosciences*. 41:51-61.

Lu, Y., I.R. Turnbull, A. Bragin, K. Carveth, A.S. Verkman, and W.R. Skach. 2000. Reorientation of aquaporin-1 topology during maturation in the endoplasmic reticulum. *Molecular biology of the cell*. 11:2973-2985.

McCarty, J.H. 1998. The Nck SH2/SH3 adaptor protein: a regulator of multiple intracellular signal transduction events. *BioEssays : news and reviews in molecular, cellular and developmental biology*. 20:913-921.

Mi, Y.J., B. Hou, Q.M. Liao, Y. Ma, Q. Luo, Y.K. Dai, G. Ju, and W.L. Jin. 2012. Amino-Nogo-A antagonizes reactive oxygen species generation and protects immature primary cortical neurons from oxidative toxicity. *Cell death and differentiation*. 19:1175-1186.

Miao, R.Q., Y. Gao, K.D. Harrison, J. Prendergast, L.M. Acevedo, J. Yu, F. Hu, S.M. Strittmatter, and W.C. Sessa. 2006. Identification of a receptor necessary for Nogo-B stimulated chemotaxis and morphogenesis of endothelial cells. *Proceedings of the National Academy of Sciences of the United States of America*. 103:10997-11002.

Mingorance, A., X. Fontana, M. Sole, F. Burgaya, J.M. Urena, F.Y. Teng, B.L. Tang, D. Hunt, P.N. Anderson, J.R. Bethea, M.E. Schwab, E. Soriano, and J.A. del Rio. 2004. Regulation of Nogo and Nogo receptor during the development of the entorhino-hippocampal pathway and after adult hippocampal lesions. *Molecular and cellular neurosciences*. 26:34-49.

Montani, L., B. Gerrits, P. Gehrig, A. Kempf, L. Dimou, B. Wollscheid, and M.E. Schwab. 2009. Neuronal Nogo-A modulates growth cone motility via Rho-GTP/LIMK1/cofilin in the unlesioned adult nervous system. *The Journal of biological chemistry*. 284:10793-10807.

Murayama, K.S., F. Kametani, S. Saito, H. Kume, H. Akiyama, and W. Araki. 2006. Reticulons RTN3 and RTN4-B/C interact with BACE1 and inhibit its ability to produce amyloid beta-protein. *The European journal of neuroscience*. 24:1237-1244.

Nakamura, Y., Y. Fujita, M. Ueno, T. Takai, and T. Yamashita. 2011. Paired immunoglobulin-like receptor B knockout does not enhance axonal regeneration or locomotor recovery after spinal cord injury. *The Journal of biological chemistry*. 286:1876-1883.

Nie, D.Y., Z.H. Zhou, B.T. Ang, F.Y. Teng, G. Xu, T. Xiang, C.Y. Wang, L. Zeng, Y. Takeda, T.L. Xu, Y.K. Ng, C. Faivre-Sarrailh, B. Popko, E.A. Ling, M. Schachner, K. Watanabe, C.J. Pallen, B.L. Tang, and Z.C. Xiao. 2003. Nogo-A at CNS paranodes is a ligand of Caspr: possible regulation of K(+) channel localization. *The EMBO journal*. 22:5666-5678.

Oertle, T., C. Huber, H. van der Putten, and M.E. Schwab. 2003a. Genomic structure and functional characterisation of the promoters of human and mouse nogo/rtn4. *Journal of molecular biology*. 325:299-323.

Oertle, T., M.E. van der Haar, C.E. Bandtlow, A. Robeva, P. Burfeind, A. Buss, A.B. Huber, M. Simonen, L. Schnell, C. Brosamle, K. Kaupmann, R. Vallon, and M.E. Schwab. 2003b. Nogo-A inhibits neurite outgrowth and cell spreading with three discrete regions. *The Journal of neuroscience : the official journal of the Society for Neuroscience*. 23:5393-5406.

Park, E.J., K.A. Grabinska, Z. Guan, V. Stranecky, H. Hartmannova, K. Hodanova, V. Baresova, J. Sovova, L. Jozsef, N. Ondruskova, H. Hansikova, T. Honzik, J. Zeman, H. Hulkova, R. Wen, S. Kmoch, and W.C. Sessa. 2014. Mutation of Nogo-B receptor, a subunit of cis-prenyltransferase, causes a congenital disorder of glycosylation. *Cell metabolism*. 20:448-457.

Prinjha, R., S.E. Moore, M. Vinson, S. Blake, R. Morrow, G. Christie, D. Michalovich, D.L. Simmons, and F.S. Walsh. 2000. Inhibitor of neurite outgrowth in humans. *Nature*. 403:383-384.

Qi, B., Y. Qi, A. Watari, N. Yoshioka, H. Inoue, Y. Minemoto, K. Yamashita, T. Sasagawa, and M. Yutsudo. 2003. Pro-apoptotic ASY/Nogo-B protein associates with ASYIP. *Journal of cellular physiology*. 196:312-318.

Qin, H., H.X. Pu, M. Li, S. Ahmed, and J. Song. 2008. Identification and structural mechanism for a novel interaction between a ubiquitin ligase WWP1 and Nogo-A, a key inhibitor for central nervous system regeneration. *Biochemistry*. 47:13647-13658.

Rahbari, R., M. Kitano, L. Zhang, S. Bommareddi, and E. Kebebew. 2013. RTN4IP1 is down-regulated in thyroid cancer and has tumor-suppressive function. *The Journal of clinical endocrinology and metabolism*. 98:E446-454.

Rogers, S., R. Wells, and M. Rechsteiner. 1986. Amino acid sequences common to rapidly degraded proteins: the PEST hypothesis. *Science*. 234:364-368.

Saha, N., M. Kolev, and D.B. Nikolov. 2014. Structural features of the Nogo receptor signaling complexes at the neuron/myelin interface. *Neuroscience research*. 87:1-7.

Schnell, L., and M.E. Schwab. 1990. Axonal regeneration in the rat spinal cord produced by an antibody against myelin-associated neurite growth inhibitors. *Nature*. 343:269-272.

Schotman, H., L. Karhinen, and C. Rabouille. 2008. dGRASP-mediated noncanonical integrin secretion is required for Drosophila epithelial remodeling. *Developmental cell*. 14:171-182.

Schwab, M.E. 2010. Functions of Nogo proteins and their receptors in the nervous system. *Nature reviews. Neuroscience*. 11:799-811.

Schwab, M.E., and S.M. Strittmatter. 2014. Nogo limits neural plasticity and recovery from injury. *Current opinion in neurobiology*. 27:53-60.

Sepe, M., L. Lignitto, M. Porpora, R. Delle Donne, L. Rinaldi, G. Belgianni, G. Colucci, O. Cuomo, D. Viggiano, A. Scorziello, C. Garbi, L. Annunziato, and A. Feliciello. 2014. Proteolytic control of neurite outgrowth inhibitor NOGO-A by the cAMP/PKA pathway. *Proceedings of the National Academy of Sciences of the United States of America*. 111:15729-15734.

Seppala, S., J.S. Slusky, P. Lloris-Garcera, M. Rapp, and G. von Heijne. 2010. Control of membrane protein topology by a single C-terminal residue. *Science*. 328:1698-1700.

Shibata, Y., C. Voss, J.M. Rist, J. Hu, T.A. Rapoport, W.A. Prinz, and G.K. Voeltz. 2008. The reticulon and DP1/Yop1p proteins form immobile oligomers in the tubular endoplasmic reticulum. *The Journal of biological chemistry*. 283:18892-18904.

Shypitsyna, A., E. Malaga-Trillo, A. Reuter, and C.A. Stuermer. 2011. Origin of Nogo-A by domain shuffling in an early jawed vertebrate. *Molecular biology and evolution*. 28:1363-1370.

Song, J., L.W. Guo, H. Muradov, N.O. Artemyev, A.E. Ruoho, and J.L. Markley. 2008. Intrinsically disordered gamma-subunit of cGMP phosphodiesterase encodes functionally relevant transient secondary and tertiary structure. *Proceedings of the National Academy of Sciences of the United States of America*. 105:1505-1510.

Spillmann, A.A., C.E. Bandtlow, F. Lottspeich, F. Keller, and M.E. Schwab. 1998. Identification and characterization of a bovine neurite growth inhibitor (bNI-220). *The Journal of biological chemistry*. 273:19283-19293.

Stadler, A.M., L. Stingaciu, A. Radulescu, O. Holderer, M. Monkenbusch, R. Biehl, and D. Richter. 2014. Internal nanosecond dynamics in the intrinsically disordered myelin basic protein. *Journal of the American Chemical Society*. 136:6987-6994.

Steentoft, C., S.Y. Vakhrushev, H.J. Joshi, Y. Kong, M.B. Vester-Christensen, K.T. Schjoldager, K. Lavrsen, S. Dabelsteen, N.B. Pedersen, L. Marcos-Silva, R. Gupta, E.P. Bennett, U. Mandel, S. Brunak, H.H. Wandall, S.B. Levery, and H. Clausen. 2013. Precision mapping of the human O-GalNAc glycoproteome through SimpleCell technology. *The EMBO journal*. 32:1478-1488.

Sumiyoshi, K., S. Obayashi, H. Tabunoki, K. Arima, and J. Satoh. 2010. Protein microarray analysis identifies cyclic nucleotide phosphodiesterase as an interactor of Nogo-A. *Neuropathology : official*

journal of the Japanese Society of Neuropathology. 30:7-14.

Tagami, S., Y. Eguchi, M. Kinoshita, M. Takeda, and Y. Tsujimoto. 2000. A novel protein, RTN-XS, interacts with both Bcl-XL and Bcl-2 on endoplasmic reticulum and reduces their anti-apoptotic activity. *Oncogene*. 19:5736-5746.

Takai, T. 2005. Paired immunoglobulin-like receptors and their MHC class I recognition. *Immunology*. 115:433-440.

Taketomi, M., N. Kinoshita, K. Kimura, M. Kitada, T. Noda, H. Asou, T. Nakamura, and C. Ide. 2002. Nogo-A expression in mature oligodendrocytes of rat spinal cord in association with specific molecules. *Neuroscience letters*. 332:37-40.

Teng, R.J., U. Rana, A.J. Afolayan, B. Zhao, Q.R. Miao, and G.G. Konduri. 2014. Nogo-B receptor modulates angiogenesis response of pulmonary artery endothelial cells through eNOS coupling. *American journal of respiratory cell and molecular biology*. 51:169-177.

Thiede-Stan, N.K., B. Tews, D. Albrecht, Z. Ristic, H. Ewers, and M.E. Schwab. 2015. Tetraspanin-3 is an organizer of the multi-subunit Nogo-A signaling complex. *Journal of cell science*.

Tompa, P. 2002. Intrinsically unstructured proteins. *Trends in biochemical sciences*. 27:527-533.

Tompa, P. 2003. The functional benefits of protein disorder. *Journal of Molecular Structure: THEOCHEM*. 666–667:361-371.

Tsai, C.J., B. Ma, Y.Y. Sham, S. Kumar, and R. Nussinov. 2001. Structured disorder and conformational selection. *Proteins*. 44:418-427.

Uversky, V.N., and A.K. Dunker. 2013. The case for intrinsically disordered proteins playing contributory roles in molecular recognition without a stable 3D structure. *F1000 biology reports*. 5:1.

van de Velde, H.J., A.J. Roebroek, N.H. Senden, F.C. Ramaekers, and W.J. Van de Ven. 1994. NSP-encoded reticulons, neuroendocrine proteins of a novel gene family associated with membranes of the endoplasmic reticulum. *Journal of cell science*. 107 (Pt 9):2403-2416.

Vasudevan, S.V., J. Schulz, C. Zhou, and M.J. Cocco. 2010. Protein folding at the membrane interface, the structure of Nogo-66 requires interactions with a phosphocholine surface. *Proceedings of the National Academy of Sciences of the United States of America*. 107:6847-6851.

Voeltz, G.K., W.A. Prinz, Y. Shibata, J.M. Rist, and T.A. Rapoport. 2006. A class of membrane proteins shaping the tubular endoplasmic reticulum. *Cell*. 124:573-586.

von Heijne, G., and Y. Gavel. 1988. Topogenic signals in integral membrane proteins. *European journal of biochemistry / FEBS*. 174:671-678.

Wang, X., M. Bogdanov, and W. Dowhan. 2002. Topology of polytopic membrane protein subdomains is dictated by membrane phospholipid composition. *The EMBO journal*. 21:5673-5681.

Wojcik, S., W.K. Engel, R. Yan, J. McFerrin, and V. Askanas. 2007. NOGO is increased and binds to BACE1 in sporadic inclusion-body myositis and in A beta PP-overexpressing cultured human muscle fibers. *Acta neuropathologica*. 114:517-526.

Yang, Y.S., and S.M. Strittmatter. 2007. The reticulons: a family of proteins with diverse functions. *Genome biology*. 8:234.

Yokoyama, K., T. Tezuka, N. Hoshina, T. Nakazawa, and T. Yamamoto. 2006. Phosphorylation at Tyr-694 of Nogo-A by Src-family kinases. *Biochemical and biophysical research communications*. 349:1401-1405.

Yoo, J.S., B.D. Moyer, S. Bannykh, H.M. Yoo, J.R. Riordan, and W.E. Balch. 2002. Non-conventional trafficking of the cystic fibrosis transmembrane conductance regulator through the early secretory pathway. *The Journal of biological chemistry*. 277:11401-11409.

Zander, H., E. Hettich, K. Greiff, L. Chatwell, and A. Skerra. 2007a. Biochemical characterization of the recombinant human Nogo-A ectodomain. *The FEBS journal*. 274:2603-2613.

Zander, H., U. Reineke, J. Schneider-Mergener, and A. Skerra. 2007b. Epitope mapping of the neuronal growth inhibitor Nogo-A for the Nogo receptor and the cognate monoclonal antibody IN-1 by means of the SPOT technique. *Journal of molecular recognition : JMR*. 20:185-196.

Zhang, W., D. Ganguly, and J. Chen. 2012. Residual structures, conformational fluctuations, and electrostatic interactions in the synergistic folding of two intrinsically disordered proteins. *PLoS computational biology*. 8:e1002353.

Zhao, B., C. Chun, Z. Liu, M.A. Horswill, K. Pramanik, G.A. Wilkinson, R. Ramchandran, and R.Q. Miao. 2010. Nogo-B receptor is essential for angiogenesis in zebrafish via Akt pathway. *Blood*. 116:5423-5433.

Zhou, S., W. Xiao, Q. Wan, C. Yi, F. Xiao, Y. Liu, and Y. Qi. 2010. Nogo-B mediates HeLa cell adhesion and motility through binding of Fibulin-5. *Biochemical and biophysical research communications*. 398:247-253.

Zorner, B., and M.E. Schwab. 2010. Anti-Nogo on the go: from animal models to a clinical trial. *Annals of the New York Academy of Sciences*. 1198 Suppl 1:E22-34.

Zurek, N., L. Sparks, and G. Voeltz. 2011. Reticulon short hairpin transmembrane domains are used to shape ER tubules. *Traffic*. 12:28-41.

CHAPTER 2

NOGO-A AND SPHINGOSINE 1-PHOSPHATE: TWO STRUCTURALLY DISTINCT AGONISTS OF SPHINGOSINE 1-PHOSPHATE RECEPTOR 2 MODULATE EACH OTHER'S SIGNALING

Michael E. Arzt[1,2], Xavier Deupi[3,4], Björn Tews[5], Gebhard F. X. Schertler[2,3], Martin E. Schwab[1,6]

(unpublished manuscript)

M. E. A. designed, conducted, analyzed, and interpreted the experiments, wrote the manuscript, and prepared the figures.

[1] Brain Research Institute, University of Zurich, Switzerland
[2] Department of Biology, ETH Zurich, Switzerland
[3] Laboratory of Biomolecular Research, Paul Scherrer Institute, Villigen, Switzerland
[4] Condensed Matter Theory Group, Paul Scherrer Institute, Villigen, Switzerland
[5] Schaller Research Group, Division of Molecular Mechanisms of Tumor Invasion, University of Heidelberg and German Cancer Research Center, Heidelberg, Germany
[6] Department of Health Sciences and Technology, ETH Zurich, Switzerland

Abstract

G-protein coupled receptors respond to a broad variety of stimuli, such as photons, hormones, lipids, or proteins. Sphingosine 1-phosphate receptor 2 (S1PR2), known to be activated by the small lysophospholipid sphingosine 1-phosphate (S1P), was recently found to bind to and be activated by the myelin-associated membrane protein Nogo-A. The Nogo-A/S1PR2 interaction is thought to be highly relevant in the context of repair processes after lesions in the central nervous system (CNS), as activation of S1PR2 causes intracellular signaling cascades that result in the collapse of neuronal growth cones, thus restricting regeneration and plasticity of injured and spared CNS fibers. Here, we show that a single site within Nogo-A-Δ20 is responsible for binding to the extracellular loops 2 and 3 of S1PR2. We obtained an *in-silico* homology model of S1PR2 that was used as a template for selection of surface-accessible residues. An S1PR2 mutation library was established in which the key S1P-binding residues and the top 12 surface-accessible amino acids were substituted by alanine. The role of S1P for Nogo-A/S1PR2 signaling was studied using fibroblast spreading assays. Mutation of the central S1P-binding Arg108$^{3.28}$ of S1PR2 greatly attenuated the Nogo-A-Δ20-induced cell spreading inhibition, pointing to an importance of S1P as a positive modulator of Nogo-A signaling. However, additional experiments are required to consolidate this finding, and to determine the exact S1PR2 residues involved in the interaction with Nogo-A-Δ20.

Introduction

Injured fibers in the lesioned central nervous system trying to regenerate encounter a complex molecular environment inhibiting their growth and rewiring. Myelin-associated inhibitory proteins such as Nogo-A act as non-permissive substrates and growth inhibitors for neurite outgrowth, thereby restricting the functional recovery after, e.g., spinal cord injury (Schwab and Strittmatter, 2014). On the other hand, small molecules such as the lysophospholipid sphingosine 1-phosphate (S1P) can also cause the collapse of neuronal growth cones (Fincher et al., 2014). Nogo-A and S1P are both upregulated after spinal cord injury, imposing an even stronger inhibitory effect on disrupted networks (Kimura et al., 2007; Wang et al., 2015). We have recently found a new link between these structurally very distinct molecules by identifying S1P receptor 2 (S1PR2) as a neuronal receptor for the inhibitory Nogo-A-Δ20 domain (Kempf et al., 2014). Via interactions with the extracellular loops (ECLs) of this G-protein coupled receptor (GPCR), Nogo-A-Δ20 activates S1PR2, which in turn initiates intracellular signaling via the G protein G_{13} and the Rho GEF LARG (Kempf et al., 2014). Finally, the small GTPase RhoA is activated, which triggers a signaling cascade resulting in actin filament destabilization (Kempf et al., 2014; Schwab, 2010). Nogo-66, the second inhibitory domain of Nogo-A that is recognized by the Nogo-66

receptor 1 (NgR1), also elicits activation of RhoA, leading to a convergence of Nogo-A-induced signaling.

S1P and Nogo-A-Δ20 both act as agonists for S1PR2, but the exact relationship of these two ligands on S1PR2 activation is not understood. Here, we aimed to decipher possible mutual interactions of S1P and Nogo-A-Δ20 in each other's signaling through S1PR2. We used microscale thermophoresis (MST) to show that a single binding pocket on Nogo-A-Δ20 incorporates two ECLs of S1PR2. We then employed a computational homology model of S1PR2 to predict which amino acids are exposed on the surface and are therefore good candidates for an interaction with Nogo-A-Δ20. A mutation library of S1PR2 was established, carrying alanine substitutions in key S1P-interacting and most surface-accessible positions.

Materials and Methods

Microscale Thermophoresis (MST)

Recombinant rat Nogo-A-Δ20 (a. a. 544-725) was expressed in *E. coli* and purified, and MST experiments were conducted as described previously (Kempf et al., 2014; Oertle et al., 2003). Briefly, fluorescence labeling of Nogo-A-Δ20 was achieved using the Amine Reactive Protein labeling kit RED (L001, NanoTemper Technologies GmbH). The extracellular domains of S1PR2 were synthesized as unlabeled peptides [JPT Peptide Technologies, sequences: N-terminus, MGGLYSEYLNPEKVQEHYNYTKETLDMQETPSRK; ECL1, LSGHVTLSLTPVQW; ECL2, NCLNQLEAC-STVLPLYAKHYVL; ECL3, SILLLDSTCPVRACPVLYK; ECL1-scrambled negative control (ECL1-scr), VGLSQVWTSLPTLH]. For determination of affinity constants, a serial dilution of extracellular domains in measurement buffer (0.025% Tween-20 in PBS, pH 7.4) was prepared and added to a constant concentration of Nogo-A-Δ20 (~40 nM) in measurement buffer. Complexes were allowed to equilibrate for 5 min at RT and loaded into hydrophilic glass capillaries (K004, NanoTemper Technologies GmbH). MST measurements were then performed on a Monolith NT.115 (NanoTemper Technologies GmbH) at RT with an LED intensity of 60% and infrared LASER power of 20%. Baseline-corrected MST data were used for non-linear regression assuming a Hill coefficient of 1.0, and K_D values were determined (GraphPad Prism).

For competition experiments, fluorophore-labeled Nogo-A-Δ20 (~40 nM) was saturated with 5 μM ECL2 or ECL3 at RT for 5 min, and a serial dilution of the other ECL was prepared and added. After 5 min of complex formation at RT, MST measurements were conducted as described above.

In-silico homology modeling of S1PR2

A computational homology model of murine S1PR2 based on the crystal structure of human S1PR1 (PDB entry 3V2Y) was obtained using SWISS-MODEL (Biasini et al., 2014; Hanson et al., 2012). Briefly, sequence alignment between S1PR1 and S1PR2 was performed to identify conserved residues (Altschul et al., 1990). The sequence of S1PR2 was then threaded onto the crystal structure of S1PR1, replacing homologous amino acids as determined by the sequence alignment. Minimal energy minimization was performed to eliminate spatial clashes or gaps. The position of S1PR2 in the membrane was determined using the PPM server (Lomize et al., 2012). The model was visualized using the PyMOL Molecular Graphics System, Version 1.3 Schrödinger, LLC.

The S1PR2 homology model was then used to calculate per-residue surface accessibilities on the VADAR platform (Willard et al., 2003). All amino acids that appeared in the extracellular space or maximally two amino acids inside the plasma membrane in the model were considered for mutagenesis and ranked by their surface accessibility.

Amino acid numbering

The Ballesteros-Weinstein numbering scheme for GPCRs is provided in superscript for all relevant amino acids (Ballesteros and Weinstein, 1995). In each trans-membrane domain (TMD), the most conserved amino acid is determined by sequence alignment and designated X.50, where X is the number of the respective TMD (Fig. 3F). Other amino acid positions are then given relatively to the closest such residue, e. g., Arg108$^{3.28}$ is located at TMD3, 22 residues before the most conserved residue, Arg130$^{3.50}$. For mutations, standard single-letter codes are used, e.g., R3.28A.

Site-directed mutagenesis (SDM)

Alanine substitutions were created for the key S1P-interacting amino acids, as well as for the top 12 surface-accessible residues. Similarly, in order to create knockdown (KD)-resistant constructs, the short hairpin RNA (shRNA)-binding site of *S1PR2* was mutated in every position possible without affecting the amino acid sequence. An optimized Quikchange protocol was employed for SDM (Zheng et al., 2004). For each mutagenesis, a pair of mutagenic primers was designed by the following rules: (i), include 5 or more template-homologous nucleotides flanking each side of the mutation; (ii), extend the 3'-end of each primer by at least 8 template-homologous nucleotides; (iii), end with one or two G or C nucleotides at the 3'-terminus. Forward and reverse primers were only homologous to each other in the part outlined by rule (i). Due to their 3'-extensions from rule (ii), affinity to the template was higher than to the other primer, thus favoring hybridization with the template over primer dimerization (Fig. 4A) (Zheng et al., 2004). Primers were ordered as

desalted oligonucleotides (Microsynth); a complete SDM primer list is provided in Table 1. All PCR amplifications were carried out with Phusion Hot Start DNA polymerase (Life Technologies). 50 µl PCR reactions were prepared containing 100 ng murine S1PR2-WT-encoding template plasmid, 200 µM each dNTP, 0.5 µM each mutagenic primer, and 0.02 U/µl Phusion Hot Start DNA polymerase in 1x Phusion HF buffer. Plasmid DNA was initially denatured at 98°C for 30 s, amplified by 16 cycles of 98°C for 8 s, T_a for 20 s, and 72°C for 20 s/kb, and finally extended at 72°C for 8 min. The annealing temperature T_a was chosen well above the melting temperature for primer dimerization $T_{m,\,dimer}$ (Table 1). A 5 µl aliquot of the reaction mix was separated as undigested control, and 1 µl *Dpn*I (New England Biolabs) was added to the rest of the PCR product in PCR buffer and incubated at 37°C for 1 h. Success of PCR and of *Dpn*I digestion was evaluated by gel electrophoresis in 1% agarose/TAE. 3 µl of the digested PCR product were transformed into 50 µl One Shot TOP10 chemically competent *E. coli* (Thermo Fisher Scientific) according to the manufacturer's protocol, streaked out on LB (Sigma Aldrich) / agar (AppliChem) plates containing 100 µg/ml ampicillin (Sigma Aldrich), and incubated at 37°C. The next day, single colonies were transferred to 3 ml of liquid LB/ampicillin and incubated at 250 rpm and 37°C overnight. Plasmid DNA was purified with the GenElute Plasmid Miniprep Kit (Sigma Aldrich). Presence of inserted restriction sites was evaluated by control digestion with the corresponding restriction endonuclease (New England Biolabs, Table 1) according to the manufacturer's protocol. Positive clones were verified by DNA sequencing of the entire open reading frame (Microsynth).

Cell culture

Silencing of *S1PR2* was achieved by retroviral transduction of 3T3 fibroblasts with an shRNA construct that targeted 5'-ACC AAG GAG ACG CTG GAC ATG-3' as described previously (Kempf et al., 2014). Resultant S1PR2-KD cells were maintained in fibroblast media [Dulbecco's modified eagle medium (DMEM) containing 25 mM glucose and GlutaMAX (Thermo Fisher Scientific) supplemented with 10% neonatal calf serum (Thermo Fisher Scientific)] at 37 °C and 5 % CO_2.

Mouse embryonic fibroblasts (MEF) were prepared from *S1PR2*$^{-/-}$ (B6.129S6-S1pr2^{tm1Rlp}) or littermate wild-type (WT) E14-E16 embryos (Kono et al., 2004). The mother was sacrificed by cervical dislocation, and embryos were isolated. The head and dark organs were removed and used for genotyping, and the rest of the embryos was minced thoroughly using a scalpel blade. Tissue was enzymatically digested in 15 ml conical tubes by 5 ml per embryo 0.05 % trypsin/EDTA (Thermo Fisher Scientific) at 37 °C for 30 min with occasional inversion. Digestion was terminated by transfer to 30 ml fibroblast media, supplemented with 1 % penicillin/ streptomycin (Thermo Fisher Scientific). Trypsin was removed by centrifugation at 300 g for 5 min and aspiration of the supernatant. The pellet was resuspended in fresh media with

antibiotics, and pipetted through a 40 µm cell strainer (BD Biosciences) to obtain single cells. MEF cells were expanded, and 10^7 cells were frozen per cryotube in 1 ml antibiotics-free media containing 10 % DMSO and 20 % neonatal calf serum. Thawed aliquots were cultured in fibroblast media without antibiotics.

Fibroblast spreading assay

S1PR2-KD 3T3 fibroblasts or MEF cells were co-transfected with constructs from the S1PR2 mutation library and pmaxGFP (Lonza) using Lipofectamine 3000 (Life Technologies) or a 4D-Nucleofector (Lonza) according to the manufacturers' protocols. The next day, an amount of Nogo-A-Δ20 in PBS corresponding to IC_{50} of the batch used was added to 4-well dishes, and incubated at 4°C overnight for coating (Greiner BioOne). 48 h post-transfection, coated plates were washed three times with PBS, and transfected cells were briefly trypsinized. 7'000 cells were then added to each well and incubated at 37°C and 5 % CO_2 for 1 h. Cells were fixed with warm 4 % paraformaldehyde (Sigma Aldrich) in PBS for 20 min and washed three times with PBS. They were then incubated with blocking buffer [2 % normal goat serum (Jackson Laboratories), 0.3 % Triton X-100 (AppliChem), 0.004 % fish skin gelatin (Sigma Aldrich) in PBS, pH 7.4] at RT for 30 min, followed by DAPI (1:1000, Life Technologies) and Alexa Fluor 594-labeled phalloidin (1:100, Life Technologies) in blocking buffer at RT for 30 min for staining of nuclei and actin, respectively. Cells were then washed three times with PBS and coverslipped in fluorescence mounting medium (Dako). Leica DM5500 or Zeiss Axioskop 2 mot plus epifluorescence microscopes with motorized stages were used to image the entire wells. Single cells were analyzed with ImageJ (Schneider et al., 2012) or CellProfiler (Kamentsky et al., 2011). Only non-clumped, transfected cells were included for quantification of the cell size.

Results

ECL2 and ECL3 of S1PR2 bind to the same region on Nogo-A-Δ20

We used microscale thermophoresis (MST) to determine the domains of S1PR2 involved in binding to Nogo-A-Δ20. Synthesized peptides of the N-terminus or ECLs of S1PR2, or ECL1-scrambled control (ECL1-scr) were titrated to a constant concentration of fluorophore-labeled

Fig. 1: Nogo-A-Δ20 primarily binds to ECL2 and ECL3 of S1PR2. A, S1PR2 fragments were titrated to a constant concentration of fluorophore-labeled Nogo-A-Δ20, and the mix was transferred into glass capillaries. **B**, In the Monolith MST instrument, the capillaries are focally heated with an infrared (IR) LASER, and fluorescence of the labeled molecule is measured in the LASER focus. **C-G**, MST data from one measurement per fragment are shown in the left panels. Upon LASER activation (On), labeled Nogo-A-Δ20 migrated out of the LASER focus, thereby causing a decrease in fluorescence that recovered partially after LASER shutdown (Off). Single curves represent individual concentrations of S1PR2 fragments, from low (light grey) to high (black). Data from triplicate measurements are shown as dose-response curves in the right panels (means ± SD). This data set has been used for determination of affinity constants between Nogo-A-Δ20 and the S1PR2 extracellular domains (Kempf et al., 2014).

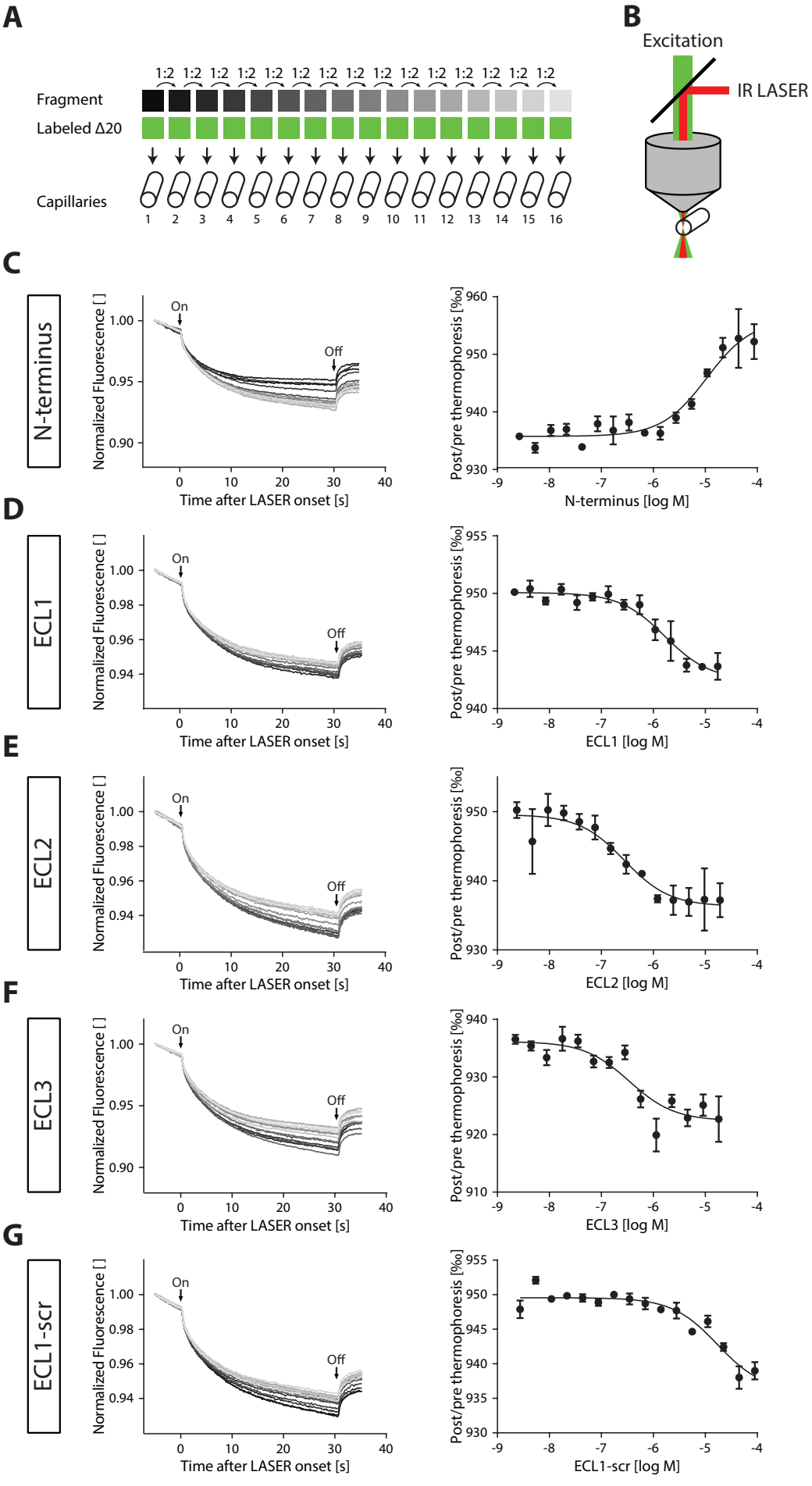
A
1:2 1:2 1:2 1:2 1:2 1:2 1:2 1:2 1:2 1:2 1:2 1:2 1:2 1:2 1:2
Fragment
Labeled Δ20
Capillaries
1 2 3 4 5 6 7 8 9 10 11 12 13 14 15 16
B
Excitation
IR LASER
C
N-terminus
Normalized Fluorescence [ ]
On
Off
Time after LASER onset [s]
Post/pre thermophoresis [‰]
N-terminus [log M]
D
ECL1
Normalized Fluorescence [ ]
On
Off
Time after LASER onset [s]
Post/pre thermophoresis [‰]
ECL1 [log M]
E
ECL2
Normalized Fluorescence [ ]
On
Off
Time after LASER onset [s]
Post/pre thermophoresis [‰]
ECL2 [log M]
F
ECL3
Normalized Fluorescence [ ]
On
Off
Time after LASER onset [s]
Post/pre thermophoresis [‰]
ECL3 [log M]
G
ECL1-scr
Normalized Fluorescence [ ]
On
Off
Time after LASER onset [s]
Post/pre thermophoresis [‰]
ECL1-scr [log M]

Nogo-A-Δ20 and loaded into glass capillaries (Fig. 1A). The MST instrument then focally heated the sample with an infrared LASER beam, thereby creating a slight temperature gradient (Fig. 1B). Due to the Ludwig-Soret effect (Ludwig, 1856), Nogo-A-Δ20 moved away from the heat, causing a measurable drop of fluorescence in the LASER focus upon activation (Fig. 1C-G, left panels). Fluorescence recovered partially after switching off the LASER, indicating that the signal loss was not caused by bleaching. Importantly, the velocity of this motion depends directly on the size, charge and hydration shell of the molecule and can therefore be used as a proxy for complex formation (Jerabek-Willemsen et al., 2011). Accordingly, thermophoretic mobility of Nogo-A-Δ20 correlated with the concentration of titrated fragments, yielding sigmoidal dose response curves (Fig. 1C-G, right panels). Interestingly, whereas binding of ECLs accelerated thermophoretic mobility of Nogo-A-Δ20, the opposite effect was observed upon binding of the N-terminus. The respective affinity constants indicated that Nogo-A-Δ20 primarily binds to ECL2 and ECL3, and to a lesser extent to ECL1 (Kempf et al., 2014). In contrast, affinity of the N-terminus of S1PR2 to Nogo-A-Δ20 was comparable to that of the negative control ECL1-scr.

We next wondered whether ECL2 and ECL3 bind to independent sites on Nogo-A-Δ20. For this purpose, we employed an MST-based competition assay. Nogo-A-Δ20 was saturated with a constant, high concentration of one ECL, and the other ECL was titrated to the complex as described above (Fig. 2A). Independent binding of the two ECLs to separate sites of Nogo-A-Δ20 should result in a tripartite complex, whereas binding at the same site would be expected to cause an equilibrium state where only one of the ECLs is bound to Nogo-A-Δ20 at a time (Fig. 2B). We hypothesized that such tripartite and bipartite complexes would exhibit different thermophoretic motion velocities, and therefore be distinguishable by MST (Fig. 2C). Indeed, though ECL2 and ECL3 both bound to Nogo-A-Δ20 individually (Fig. 2D,E, left panels), titration of ECL3 to ECL2-saturated Nogo-A-Δ20 did not induce a further change in thermophoretic mobility (Fig. 2D, right panel). Reciprocal titration of ECL2 to Nogo-A-Δ20 saturated with ECL3 yielded the same result, suggesting mutually exclusive binding of ECL2 or ECL3 to a putative common region on Nogo-A-Δ20 (Fig. 2E, right panel).

In-silico homology modeling of S1PR2

In search of the amino acids of S1PR2 that directly interact with Nogo-A-Δ20 upon binding, we hypothesized that such residues should be located on the surface of the receptor. In order to

Fig. 2: ECL2 and ECL3 of S1PR2 bind to a common region on Nogo-A-Δ20. A, Fluorophore-labeled Nogo-A-Δ20 was pre-incubated with a high concentration of one ECL, and the other ECL was titrated. **B**, Independent binding of the other ECL would lead to a tripartite complex, whereas competition would result in an equilibrium with only one of the ECLs bound at a time. **C**, Bipartite and tripartite complexes should be distinguishable in MST by different thermophoretic properties. Titration of any of the ECLs individually shifts the thermophoretic motion to another plateau. Titration of one ECL to Nogo-A-Δ20 saturated with the other ECL should result in an observable shift to a third plateau if binding occurs independently. **D**, Saturation of Nogo-A-Δ20 with ECL2 abolishes observable binding of ECL3, supporting the competition model. **E**, Vice versa experiment of D, leading to the same result.

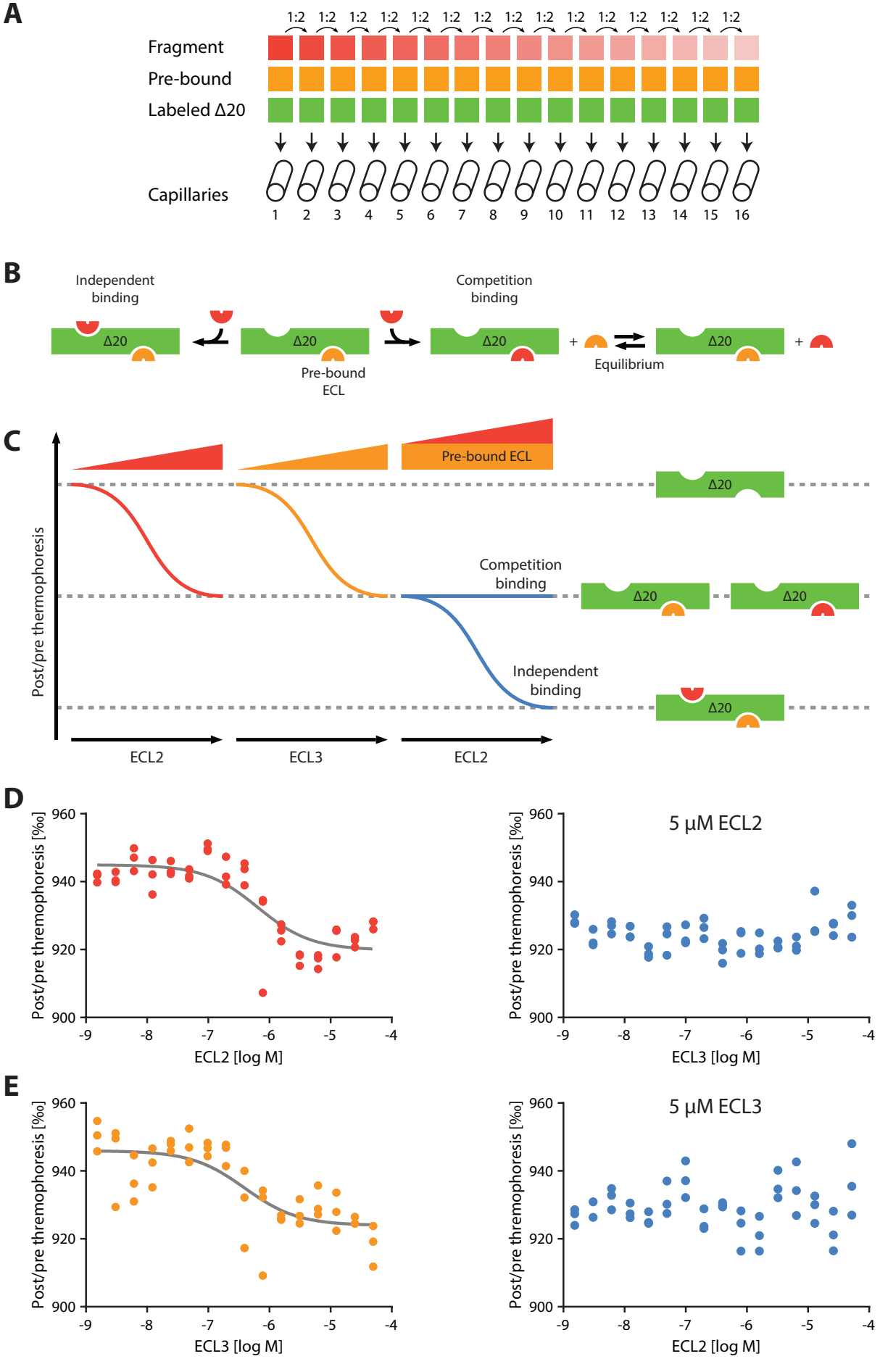
A
1:2
Fragment
Pre-bound
Labeled Δ20
Capillaries
1 2 3 4 5 6 7 8 9 10 11 12 13 14 15 16
B
Independent binding
Competition binding
Δ20
Pre-bound ECL
Equilibrium
C
Pre-bound ECL
Competition binding
Independent binding
Post/pre thermophoresis
ECL2
ECL3
ECL2
D
Post/pre thermophoresis [‰]
ECL2 [log M]
5 µM ECL2
ECL3 [log M]
E
Post/pre thermophoresis [‰]
ECL3 [log M]
5 µM ECL3
ECL2 [log M]

Fig. 3: Homology model of S1PR2. A, Side view of S1PR2 colored from its N-terminus (blue) to its C-terminus (red). Note the N-terminal helical cap. The extracellular and intracellular boundaries of the plasma membrane are indicated in red and blue, respectively. **B**, Conserved residues interacting with S1P are located inside the receptor. The N-terminal helix has been omitted for clarity. **C**, S1P is shown with three phosphate-interacting residues and three amino acids that bind its lipidic tail. **D**, Surface-accessible residues of S1PR2. The top 12 solvent-exposed residues that were mutated in this study are labeled. **E**, Ranking of top 12 surface-accessible residues. **F**, S1PR2 mutant library. Residues interacting with the S1P phosphate group are indicated in red, those binding to the lipidic tail are colored orange. The top 12 surface-accessible residues are marked in blue. The most highly conserved residues in each TMD, used for Ballesteros-Weinstein numbering, are labeled in black.

choose candidate residues for mutagenesis, a crystal structure of S1PR2 would be desirable as a template. However, since no such structure is available at present, a computational homology model of S1PR2 was obtained (Fig. 3A) that was based on the recently solved crystal structure of S1PR1 (Hanson et al., 2012). In the S1PR2 homology model, the conserved key S1P-interacting residues are found at locations analogous to those in the S1PR1 crystal structure (Fig. 3B,C). In particular, the amino acids which interact with the S1P polar head group, Arg108$^{3.28}$ and Glu109$^{3.29}$ (Valentine et al., 2011), are highly conserved and located inside the seven TMDs (Fig. 3B). Likewise, Leu116$^{3.36}$, Val120$^{3.40}$, and Trp246$^{6.48}$, which are thought to interact with the lipidic tail of S1P (Fujiwara et al., 2007), are positioned deeper inside the receptor. Lys269$^{7.34}$, also shown to interact with the phosphate of S1P (Valentine et al., 2011), is found at the cleft between TMD1 and TMD7 that is thought to be the lateral entry site for S1P (Hanson et al., 2012). Quantitative evaluation of the S1PR2 homology model further identified the amino acids that exhibit the highest surface accessibility on the extracellular side (Fig. 3D,E). These residues were therefore subjected to alanine substitution, along with the key S1P-binding amino acids (Fig. 3F).

Site-directed mutagenesis of S1P-interacting and surface-accessible S1PR2 residues

S1P and Nogo-A-Δ20 are both agonists of S1PR2 (Kempf et al., 2014). In order to study the relationship and putative interdependence of S1P- and Nogo-A-Δ20-induced signaling, we created S1PR2 mutants carrying alanine substitutions in key S1P-interacting residues. In addition, the top 12 surface-accessible amino acids of S1PR2 were mutated to alanine to map the Nogo-A-Δ20 binding site. Open reading frames of S1PR2 and of the lysophosphatidic acid receptor LPAR1 were amplified from murine brain tissue and cloned into pcDNA5/FRT. SDM of S1PR2 was performed with mutagenic primers that only overlapped partially, therefore favoring full-length hybridization to the template DNA over primer dimerization (Fig. 4A) (Zheng et al., 2004). After amplification, the PCR product was incubated with the restriction endonuclease *Dpn*I, which selectively digests methylated template plasmid while leaving un-methylated PCR product intact (Fig. 4A,B). Indeed, the DNA band originating from the SDM PCR was still evident after *Dpn*I digestion, whereas the template DNA was cleaved into shorter fragments (Fig. 4B). Mutagenic primers did not only include the mutations necessary for alanine substitution, but also a silent

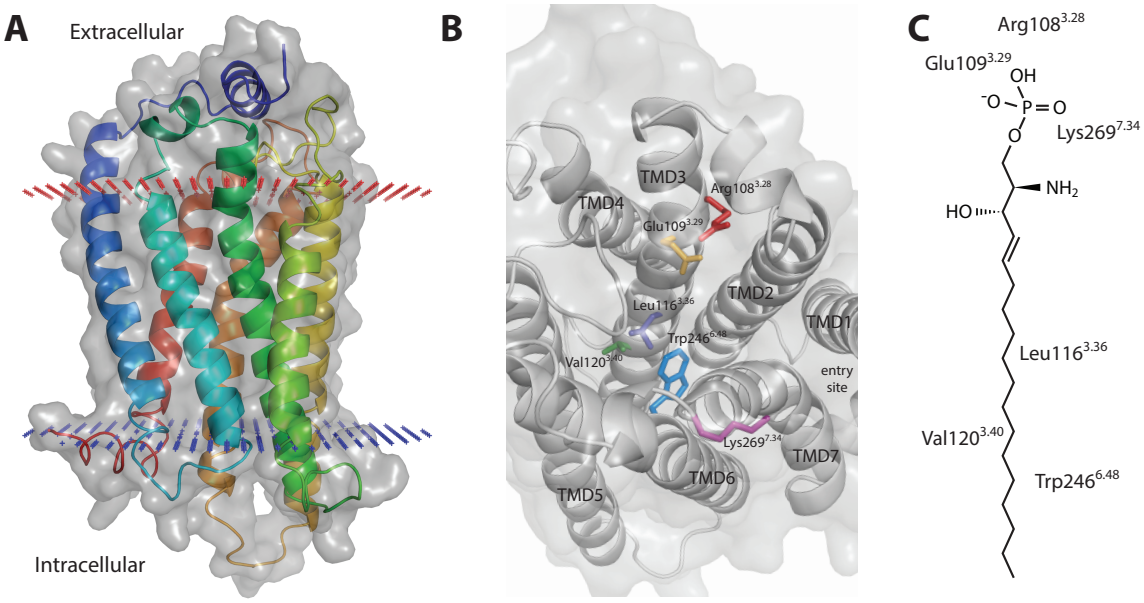

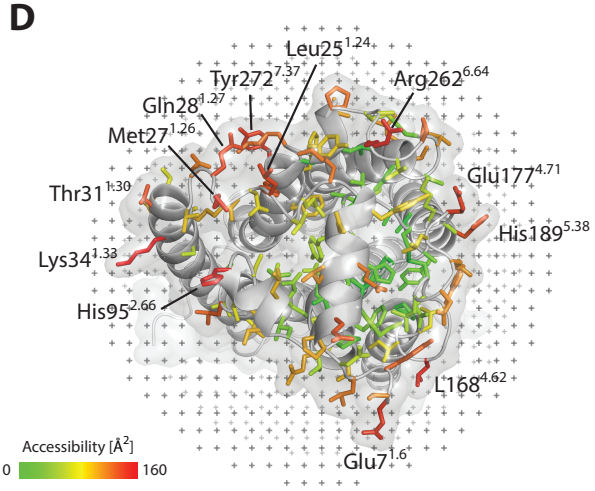

E

Rank	Residue	Surface accessibility [Å^2]
1	Lys34$^{1.33}$	159.3
2	His95$^{2.66}$	150.0
3	Arg262$^{6.64}$	143.2
4	Leu168$^{4.62}$	141.7
5	Met27$^{1.26}$	140.9
6	Glu7$^{1.6}$	139.5
7	Tyr272$^{7.37}$	135.3
8	Glu177$^{4.71}$	129.8
9	Gln28$^{1.27}$	128.8
10	Leu25$^{1.24}$	120.0
11	Thr31$^{1.30}$	114.9
12	His189$^{5.38}$	114.7

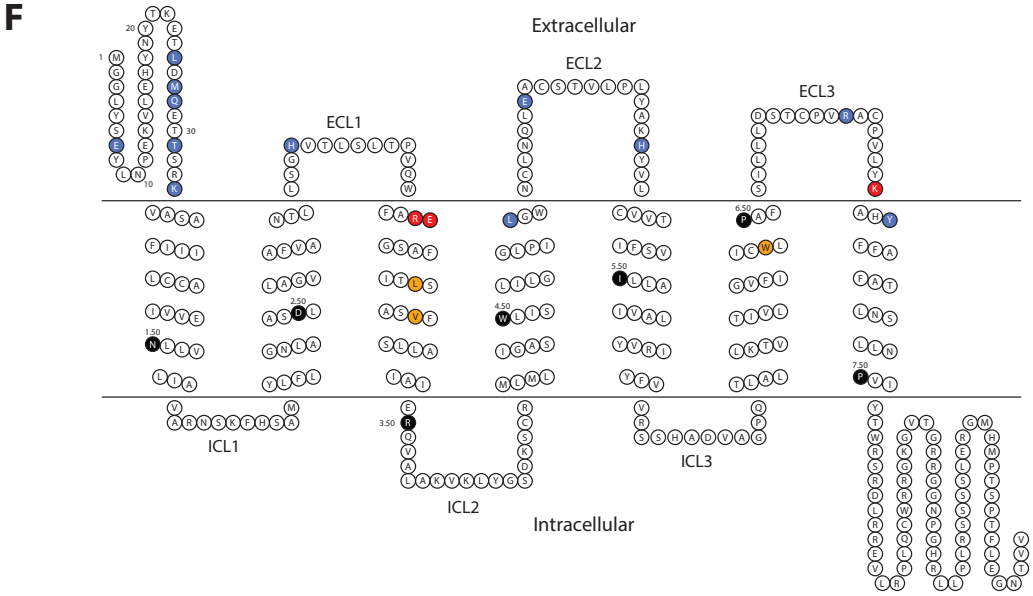

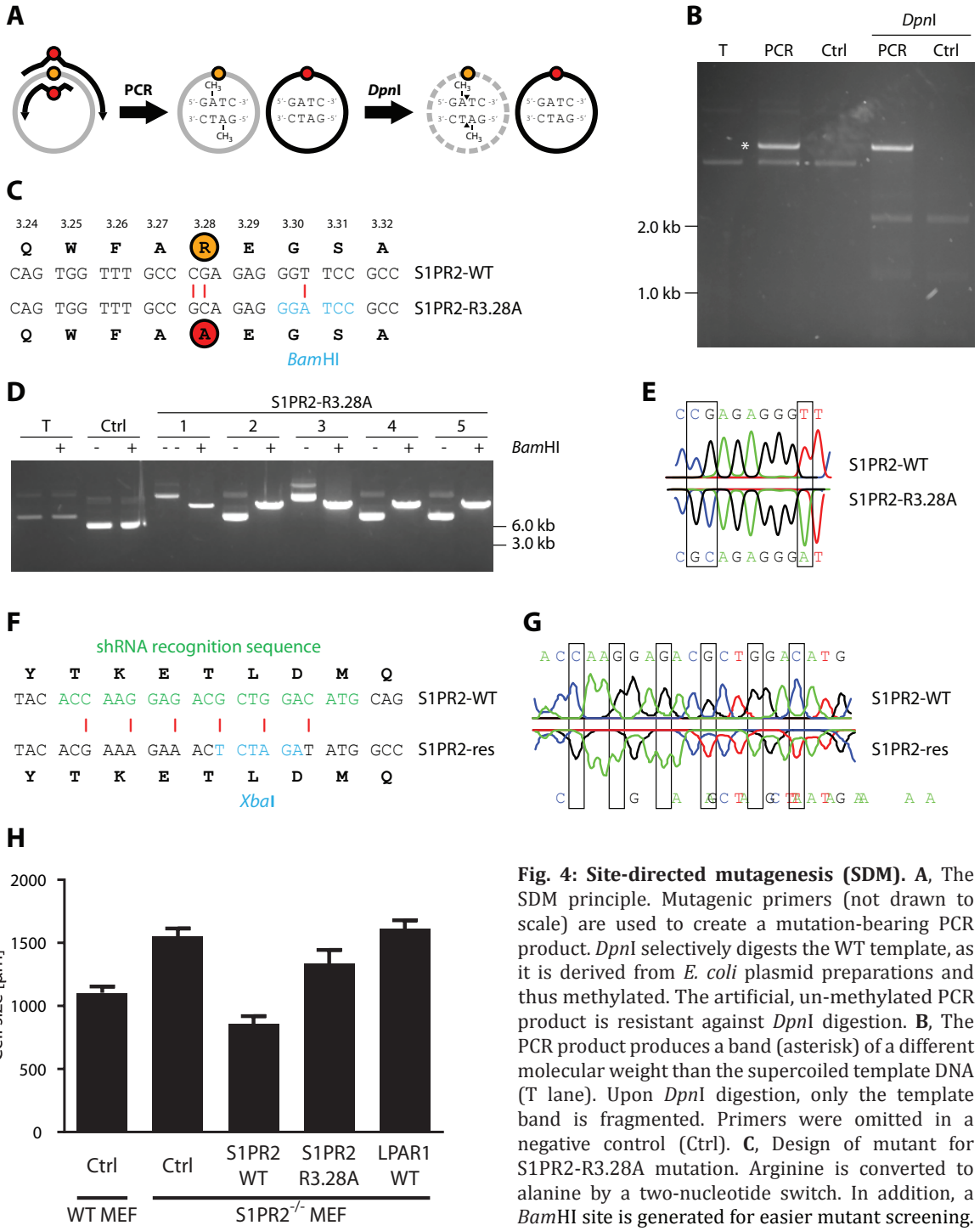

Fig. 4: Site-directed mutagenesis (SDM). A, The SDM principle. Mutagenic primers (not drawn to scale) are used to create a mutation-bearing PCR product. *Dpn*I selectively digests the WT template, as it is derived from *E. coli* plasmid preparations and thus methylated. The artificial, un-methylated PCR product is resistant against *Dpn*I digestion. **B**, The PCR product produces a band (asterisk) of a different molecular weight than the supercoiled template DNA (T lane). Upon *Dpn*I digestion, only the template band is fragmented. Primers were omitted in a negative control (Ctrl). **C**, Design of mutant for S1PR2-R3.28A mutation. Arginine is converted to alanine by a two-nucleotide switch. In addition, a *Bam*HI site is generated for easier mutant screening. **D**, Control digests with *Bam*HI show linearization of all mutants, but not of the template or control (Ctrl) plasmids, which do not contain *Bam*HI sites. **E**, Sanger sequencing result of D demonstrates successful mutagenesis. **F**, The recognition sequence of an shRNA targeting S1PR2 was mutated to render the construct knockdown-resistant (S1PR2-res). **G**, Sanger sequencing result of F. **H**, Fibroblast spreading assay on Nogo-A-Δ20. S1PR2$^{-/-}$ MEF cells spread better on Nogo-A-Δ20 than WT MEF cells. Overexpression of S1PR2-WT, but not S1PR2-R3.28A reverses this effect. LPAR1 overexpression does not alter spreading behavior compared to empty pcDNA5/FRT vector control (Ctrl).

Table 1: Mutagenic primers used for SDM of S1PR2. Mutations are indicated in lowercase, inserted restriction sites in bold type. 3'-extensions unique to each primer are underlined. Some nucleotides correspond to shRNA-resistant S1PR2 (italics). N-term, N-terminus; RE, restriction endonuclease; Tm, melting temperature.

		Mutation	Location	Mutagenic primers (5'→3')	$T_{m,\ template}$	$T_{m,\ dimer}$	RE site
S1P-binding residues	Phosphate interacting	R3.28A	TMD3	fwd TTGCCgcAGAG**GGaTCC**GCCTTCATCACGCTC	70.2 °C	63.3 °C	*Bam* HI
				rev GC**GGAtCC**CTCTgcGGCAAACCACTGCACG	70.6 °C		
		E3.29A	TMD3	fwd CCCGAGcG**GGaTCC**GCCTTCATCACGCTC	70.2 °C	62.3 °C	*Bam* HI
				rev GC**GGAtCC**CgCTCGGGCAAACCACTGC	70.7 °C		
		E3.29Q	TMD3	fwd CCCGAcAG**GGaTCC**GCCTTCATCACGCTC	68.5 °C	58.8 °C	*Bam* HI
				rev GC**GGAtCC**CTgTCGGGCAAACCACTGC	68.8 °C		
		K7.34	TMD7	fwd TCTACgcAGCCCACTATTTTTTTGCCTTTGCCACCCT**gAAtTC**ACTGCTCAATCC	70.0 °C	68.5 °C	*Eco* RI
				rev AGT**GAaTTc**AGGGTGGCAAAGGCAAAAAAATAGTGGGCTgcGTAGAGGACAGG	70.1 °C		
	Lipidic tail-interacting	L3.36A	TMD3	fwd TCACG**gctagc**GCCTCGGTCTTTAGCCTCCTGG	70.3 °C	57.8 °C	*Nhe* I
				rev GAGGC**gctagc**CGTGATGAAGGCGGAACCCTC	70.2 °C		
		L3.36Q	TMD3	fwd CACGCaaTCC**GCtagc**GTCTTTAGCCTCCTGG	67.4 °C	60.2 °C	*Nhe* I
				rev AAGAC**gctaGC**GGAttGCGTGATGAAGGCG	66.7 °C		
		V3.40	TMD3	fwd TCC**GCtagc**GcCTTTAGCCTCCTGGCCATCG	70.3 °C	53.4 °C	*Nhe* I
				rev TAAAGgC**gctaGC**GGAGAGCGTGATGAAGGCGGAACC	70.3 °C		
		W6.48	TMD6	fwd TCTGCgcGCTGCCGGCTTTTAGCATCCTTCTtcTAGACTCCACCTG	71.3 °C	69.0 °C	*Xba* I
				rev GTCTAgaAGAAGGATGCTAAAAGCCGGCAGCgcGCAGAGCAGATGATG	70.1 °C		
Surface-accessible residues	Rank 1	K1.33A	N-term	fwd CCCGCgcGGTGGCCTCGGCCTTC	86.7 °C	67.4 °C	none
				rev CCACCgcGCGGGAGGTGGTCTC	81.2 °C		
	Rank 2	H2.66A	ECL1	fwd CAGGGgcTGTCACTCTGTCCTTAAC	70.0 °C	49.6 °C	none
				rev TGACAgcCCCTGAGAGTAAGGTG	68.9 °C		
	Rank 3	R6.64A	ECL3	fwd CCGTTgcGGCCTGCCCTGTCCTC	81.4 °C	59.4 °C	none
				rev AGGCCgcAACGGGACAGGTGGAG	79.4 °C		
	Rank 4	L4.62A	TMD4	fwd CCATCgcGGGCTGGAATTGTCTG	77.0 °C	59.3 °C	none
				rev AGCCCgcGATGGGCAAGCCACC	81.7 °C		
	Rank 5	M1.26A	N-term	fwd TAGATgcGCAGGAGACCACCTC	70.0 °C	46.8 °C	none
				rev CCTGCgcATCTAGAGTTTCTTTC	65.4 °C		
	Rank 6	E1.6A	N-term	fwd CTCAGcGTACCTCAATCCTGAG	65.4 °C	36.3 °C	none
				rev GGTACgCTGAGTATAAGCCGC	65.0 °C		
	Rank 7	Y7.37A	TMD7	fwd CCCACgcTTTTTTTGCCTTTGC	72.1 °C	48.0 °C	none
				rev AAAAAgcGTGGGCTTTGTAGAG	65.6 °C		
	Rank 8	E4.71A	ECL2	fwd GCTGGcGGCCTGCTCCACCGTG	82.2 °C	56.2 °C	none
				rev AGGCCgCCAGCTGGTTCAGAC	74.1 °C		
	Rank 9	Q1.27A	N-term	fwd ATATGgcGGAGACCACCTCCCG	73.9 °C	44.2 °C	none
				rev TCTCCgcCATATCTAGAGTTTC	61.6 °C		
	Rank 10	L1.24A	N-term	fwd AAACTgcAGATATGCAGGAGAC	62.6 °C	32.0 °C	none
				rev TATCTgcAGTTTCTTTCGTGTAATTG	64.3 °C		
	Rank 11	T1.30A	N-term	fwd AGACCgCCTCCCGCAAGGTG	75.0 °C	46.7 °C	none
				rev GGAGGcGGTCTCCTGCATATCTAGAG	71.5 °C		
	Rank 12	H5.38A	ECL2	fwd CTAAGgcCTACGTGCTCTGC	64.3 °C	40.5 °C	none
				rev CGTAGgcCTTAGCATAGAGAGG	63.3 °C		
RNAi site		several (silent)	N-term	fwd TACACgAAaGAaAC**tCTaGA**tATGCAGGAGACCACCTCC	64.1 °C	53.8 °C	*Xba* I
				rev TGCATa**TCtAGa**GTtTCtTTcGTGTAATTGTAGTGTTCCAGAACC	63.0 °C		

mutation generating a nearby restriction site, which facilitated colony screening for S1PR2 mutants (Table 1). In the case of S1PR2-R3.28A mutagenesis, a *Bam*HI site was introduced that was absent in the S1PR2-WT template (Fig. 4C). Indeed, *Bam*HI digestion selectively linearized plasmid DNA from all five SDM colonies, whereas the S1PR2-WT template and a control plasmid retained several supercoiling isoforms (Fig. 4D). This indicates that a *Bam*HI site was successfully inserted into all five clones of S1PR2, presumably along with its adjacent alanine substitution. Sanger sequencing confirmed the presence of both the artificial *Bam*HI site and the substitution necessary for S1PR2-R3.28A (Fig. 4E).

Using this approach, we established a mutation library of S1PR2 containing alanine substitutions in the key S1P-interacting positions. In addition, the 12 most surface-accessible residues were mutated as an independent starting point for a residue-level analysis of the Nogo-A-Δ20 binding pocket. Due to high efficiency of mutagenesis, restriction endonuclease-based pre-screening was omitted in the generation of surface-accessible residue mutants.

Arg108$^{3.28}$ is required for S1PR2-mediated spreading inhibition on Nogo-A-Δ20

The inhibitory effect of Nogo-A-Δ20 on fibroblast spreading (Oertle et al., 2003) was used to evaluate functional consequences of S1PR2 mutations. A 3T3 fibroblast cell line stably expressing an shRNA against endogenous S1PR2 that has been described earlier (Kempf et al., 2014) was used to isolate the effect of overexpressed S1PR2 mutants. Hence, the shRNA binding site in the mutation library was saturated with silent mutations in order to shield the exogenous receptors from silencing (Fig. 4F,G). However, only low overexpression levels were observed in this cell type (not shown), prompting us to switch to MEF cells from S1PR2$^{-/-}$ mice, instead. S1PR2$^{-/-}$ MEF cells showed enhanced spreading on Nogo-A-Δ20 compared to WT MEFs (Fig. 4H). Overexpression of S1PR2 inversed this effect, resulting in even stronger inhibition of S1PR2-transfected S1PR2$^{-/-}$ MEF cells than control-transfected WT MEFs. Strikingly, this sensitizing influence of S1PR2 overexpression was lost in the S1PR2-R3.28A mutant. Overexpression of a close S1PR2 relative, LPAR1, was comparable to control transfections. These results indicate an important functional role of Arg108$^{3.28}$ and probably S1P for Nogo-A-Δ20-induced activation of S1PR2.

Discussion

Our MST data indicate that Nogo-A-Δ20 binds primarily to ECL2 and ECL3 of S1PR2. In contrast to ECL1 and the N-terminus, ECL2 and ECL3 each contain two conserved cysteines which have been shown to form intra-loop disulfide bridges in the S1PR1 crystal structure (Hanson et al., 2012). It is therefore possible that the synthesized ECL2 and ECL3 peptides contained an oxidized population, which could have contributed to native-like folding and thus enhanced affinity (Lopes et al., 2013). Similarly, it cannot be excluded that the N-terminus of S1PR2 contributes to the binding of Nogo-A-Δ20 under physiological conditions, as the synthesized fragment might not adequately mimic its rigid helical conformation observed in the S1PR1 crystal structure (Hanson et al., 2012). Interestingly, thermophoretic mobility of Nogo-A-Δ20 increased upon binding of any of the ECLs or ECL1-scr, but decreased when the N-terminus bound at very high concentrations. This observation can be explained by the fact that thermophoretic motion does not only depend on the size of a molecular complex but also on other parameters, such as charge and the hydration shell (Jerabek-Willemsen et al., 2011). Binding of a small ECL might therefore elicit changes in the exposed charges or hydration of Nogo-A-Δ20 that increase its thermophoretic mobility. These effects could be outweighed by the higher molecular mass of the N-terminal peptide, causing an opposite effect.

In our competition experiments, no evidence for a tripartite complex comprising Nogo-A-Δ20 and ECL2 and ECL3 of S1PR2 was found. This observation could be explained by two different models. Either, the two ECLs compete for a common binding site on Nogo-A-Δ20, or binding of

one ECL induces structural changes to Nogo-A-Δ20 that block binding of the other ECL. Considering that the ECLs are in close proximity inside S1PR2, and given that Nogo-A-Δ20 is intrinsically disordered even upon titration of ECLs (see Chapter 4; Li and Song, 2007), a shared binding region seems more likely. In the full-length receptor, where the spatial relationship of the ECLs is controlled by tightly packed TMDs, the ECLs probably bind cooperatively to directly adjacent regions on Nogo-A-Δ20. However, the loose termini of the synthetic ECL peptides could occlude these neighboring sites and therefore account for the competition observed. To this end, truncation experiments of ECLs would give more insight into the exact binding modes. This approach could also be used to rule out the unlikely possibility that a tripartite complex exhibits the same thermophoretic mobility as a bipartite complex.

A homology model of murine S1PR2 was used for prediction of the surface-accessible amino acids. The choice of human S1PR1 as the template crystal structure for S1PR2 modeling was obvious, as these receptors share ~50 % sequence identity. For comparison, even the closely related human LPAR1, the crystal structure of which was not available at the time of these experiments, only shares ~35 % identity with S1PR2. A major limitation of our homology model stems from the presence of an antagonist in the S1PR1 crystal structure (Hanson et al., 2012). This is common practice in GPCR crystallization, as it prevents the overexpressed receptor from signaling in the cell culture, yielding higher expression levels (Ghosh et al., 2015; Piscitelli et al., 2015). In addition, the presence of a ligand can stabilize the GPCR in one conformational state, which facilitates crystallization (Deupi et al., 2012). However, the consequence of this method is that the S1PR1 crystal structure represents the inactive conformation of the receptor, which might expose different residues to the surface than those encountered by Nogo-A-Δ20 in the physiological situation. The closest GPCR for which agonist-bound, partial agonist-bound, inverse agonist-bound or even ligand-free crystal structures are available is the β1-adrenergic receptor from *Meleagris gallopavo* (Isberg et al., 2014), which is only ~25 % identical to S1PR2. The S1PR1 crystal structure therefore remains the most adequate template for an S1PR2 homology model despite its limitations.

We have constructed silencing-resistant S1PR2 constructs for use in S1PR2-KD 3T3 fibroblasts by introducing six evenly spaced mismatches over the 21 nucleotide shRNA recognition sequence. Nevertheless, only very low expression levels of these constructs were observed in S1PR2-KD 3T3 fibroblasts. It is unlikely that these mRNAs still get downregulated by the shRNA, as even single mismatches have been shown to block RNA interference, particularly in the 5'-region of the sequence (Amarzguioui et al., 2003; Birmingham et al., 2006; Du et al., 2005). An alternative explanation might stem from the observation that the CMV promoter can get downregulated in 3T3 fibroblasts when grown to confluence (Wiederkehr and Caroni, 1995). This is difficult to avoid in GPCR overexpression, which typically requires 48 h culturing after transfection.

Like 3T3 fibroblasts, MEFs from wild-type mice are inhibited in cell spreading when plated on a Nogo-A-Δ20 substrate. In S1PR2$^{-/-}$ MEF cells, spreading on Nogo-A-Δ20 was markedly enhanced compared to WT MEFs. Sensitivity of S1PR2$^{-/-}$ MEF cells to Nogo-A-Δ20 could be restored by overexpression of S1PR2. In fact, S1PR2$^{-/-}$ MEF cells transfected with S1PR2 appeared even less spread than WT MEF cells transfected with control plasmids, probably owing to strong CMV promoter-driven overexpression. Mutation of Arg108$^{3.28}$ to alanine abolished the sensitizing effect of S1PR2 overexpression on fibroblast spreading inhibition. This residue, which is conserved among all five S1PRs, has been shown by *in-silico* modeling and mutation experiments to interact with the phosphate group of S1P (Pham et al., 2008; Valentine et al., 2011). Importantly, the homologous S1PR1-R3.28A mutant was reported to be expressed at levels comparable to those of S1PR1-WT, and to be similarly localized to the plasma membrane, at least in RH7777 cells (Parrill et al., 2000). Arg108$^{3.28}$ is located inside the receptor in the S1PR1 crystal structure, obstructed from extracellular access by an N-terminal helix that folds onto the ECLs (Hanson et al., 2012). It has been speculated that S1P first inserts into the membrane with its lipidic tail before it diffuses laterally into the receptor, presumably through an opening between TMD1 and TMD7 (Hanson et al., 2012). For a large, hydrophilic protein domain such as Nogo-A-Δ20, such a binding mode can hardly be imagined. However, the S1PR1 crystal structure is only a snapshot of the antagonist-bound protein, and GPCRs are known to sample various conformational states (Kobilka and Deupi, 2007; Preininger et al., 2013). It is therefore quite possible that the N-terminus contains flexible domains that allow transient opening of the receptor. Alternatively, the blocking cap could be a specific feature of S1PR1. In the recently solved crystal structure of LPAR1, a close relative of S1PRs, the N-terminus is more flexible than in the S1PR1 structure, allowing ligand access from the extracellular space (Chrencik et al., 2015). In LPAR1, the gap between TMD1 and TMD7 is closed, supporting that the occlusion by a rigid N-terminus found in S1PR1 necessitates an alternative ligand entry site. Indeed, loading of retinal into opsin and anandamide entry into cannabinoid receptors seems to follow a similar mechanism (Hurst et al., 2010; Schadel et al., 2003). However, direct binding of Nogo-A-Δ20 to Arg108$^{3.28}$ is not necessary in order to explain the loss of function in the mutant. It is more likely that Nogo-A- and S1P-induced signaling are linked to each other, and that Nogo-A-Δ20 requires pre-sensitization of S1PR2 by S1P in order to elicit a signal. Mutation of the key S1P-interacting residues would then block binding of S1P, and thus inhibit putative conformational changes of S1PR2 that allow modulation of the signal by Nogo-A-Δ20. Indeed, allosteric modulation is becoming an increasingly important concept in GPCR signaling (Christopoulos, 2014; Conn et al., 2009; Gentry et al., 2015).

Some control experiments are still missing to verify the importance of Arg108$^{3.28}$ for Nogo-A-Δ20-induced signaling. First, equal expression and localization of the mutant needs to be demonstrated in S1PR2$^{-/-}$ MEF cells. Second, fibroblast spreading on a control substrate will be

necessary to rule out the possibility that the observed differences in cell size represent an S1PR2-mediated effect independent of Nogo-A-Δ20.

Unfortunately, issues with cell culture and transfection efficiency have obstructed the evaluation of S1PR2 surface mutants. It is therefore our next priority to optimize this assay and determine the Nogo-A-Δ20 binding pocket on S1PR2. The top 12 surface-accessible residues from our computational model are evenly distributed over the three-dimensional extracellular landscape of S1PR2. However, most of these amino acids belong to the N-terminus of S1PR2, which exhibited only weak affinity to Nogo-A-Δ20 in MST binding experiments. Keeping in mind that MST data represent synthetic fragments of the receptor that do not necessarily reflect native conformations, SDM is an elegant complementary method for precise mapping of the binding sites. It is for this reason that we chose to include N-terminal exposed residues in the candidate list. The relatively big size of the unstructured Nogo-A-Δ20 domain in comparison to the spatially confined extracellular domains of S1PR2 could allow binding to multiple sites of the receptor. If an attenuation of Nogo-A-Δ20 signaling is observed in an S1PR2 mutant, this position can be used as a seed for systematic mutagenesis of its environment. Further optimization of this assay is therefore required to gain a residue-level understanding of the Nogo-A-Δ20/S1PR2 interaction.

Acknowledgments

MST measurements were conducted at the laboratory of Prof. Dr. J. Seelig, Biocenter Basel, University of Basel, Switzerland. We thank Tien Chau Nguyen and Dr. Zorica Ristic for excellent technical assistance.

References

Altschul, S.F., W. Gish, W. Miller, E.W. Myers, and D.J. Lipman. 1990. Basic local alignment search tool. *Journal of molecular biology*. 215:403-410.

Amarzguioui, M., T. Holen, E. Babaie, and H. Prydz. 2003. Tolerance for mutations and chemical modifications in a siRNA. *Nucleic acids research*. 31:589-595.

Ballesteros, J.A., and H. Weinstein. 1995. Integrated methods for the construction of three-dimensional models and computational probing of structure-function relations in G protein-coupled receptors. *In* Receptor Molecular Biology. Vol. 25. S.C. Sealfon, editor. Academic Press. 366.

Biasini, M., S. Bienert, A. Waterhouse, K. Arnold, G. Studer, T. Schmidt, F. Kiefer, T.G. Cassarino, M. Bertoni, L. Bordoli, and T. Schwede. 2014. SWISS-MODEL: modelling protein tertiary and quaternary structure using evolutionary information. *Nucleic acids research*. 42:W252-258.

Birmingham, A., E.M. Anderson, A. Reynolds, D. Ilsley-Tyree, D. Leake, Y. Fedorov, S. Baskerville, E. Maksimova, K. Robinson, J. Karpilow, W.S. Marshall, and A. Khvorova. 2006. 3' UTR seed matches, but not overall identity, are associated with RNAi off-targets. *Nature methods*. 3:199-204.

Chrencik, J.E., C.B. Roth, M. Terakado, H. Kurata, R. Omi, Y. Kihara, D. Warshaviak, S. Nakade, G. Asmar-Rovira, M. Mileni, H. Mizuno, M.T. Griffith, C. Rodgers, G.W. Han, J. Velasquez, J. Chun, R.C. Stevens, and M.A. Hanson. 2015. Crystal Structure of Antagonist Bound Human Lysophosphatidic Acid Receptor 1. *Cell*. 161:1633-1643.

Christopoulos, A. 2014. Advances in G protein-coupled receptor allostery: from function to structure. *Molecular pharmacology*. 86:463-478.

Conn, P.J., A. Christopoulos, and C.W. Lindsley. 2009. Allosteric modulators of GPCRs: a novel approach for the treatment of CNS disorders. *Nature reviews. Drug discovery*. 8:41--54.

Deupi, X., X.D. Li, and G.F. Schertler. 2012. Ligands stabilize specific GPCR conformations: but how? *Structure*. 20:1289-1290.

Du, Q., H. Thonberg, J. Wang, C. Wahlestedt, and Z. Liang. 2005. A systematic analysis of the silencing effects of an active siRNA at all single-nucleotide mismatched target sites. *Nucleic acids research*. 33:1671-1677.

Fincher, J., C. Whiteneck, and E. Birgbauer. 2014. G-protein-coupled receptor cell signaling pathways mediating embryonic chick retinal growth cone collapse induced by lysophosphatidic acid and sphingosine-1-phosphate. *Developmental neuroscience*. 36:443-453.

Fujiwara, Y., D.A. Osborne, M.D. Walker, D.A. Wang, D.A. Bautista, K. Liliom, J.R. Van Brocklyn, A.L. Parrill, and G. Tigyi. 2007. Identification of the hydrophobic ligand binding pocket of the S1P1 receptor. *The Journal of biological chemistry*. 282:2374-2385.

Gentry, P.R., P.M. Sexton, and A. Christopoulos. 2015. Novel Allosteric Modulators of G Protein-coupled Receptors. *The Journal of biological chemistry*. 290:19478-19488.

Ghosh, E., P. Kumari, D. Jaiman, and A.K. Shukla. 2015. Methodological advances: the unsung heroes of the GPCR structural revolution. *Nature reviews. Molecular cell biology*. 16:69-81.

Hanson, M.A., C.B. Roth, E. Jo, M.T. Griffith, F.L. Scott, G. Reinhart, H. Desale, B. Clemons, S.M. Cahalan, S.C. Schuerer, M.G. Sanna, G.W. Han, P. Kuhn, H. Rosen, and R.C. Stevens. 2012. Crystal structure of a lipid G protein-coupled receptor. *Science*. 335:851-855.

Hurst, D.P., A. Grossfield, D.L. Lynch, S. Feller, T.D. Romo, K. Gawrisch, M.C. Pitman, and P.H. Reggio. 2010. A lipid pathway for ligand binding is necessary for a cannabinoid G protein-coupled receptor. *The Journal of biological chemistry*. 285:17954-17964.

Isberg, V., B. Vroling, R. van der Kant, K. Li, G. Vriend, and D. Gloriam. 2014. GPCRDB: an information system for G protein-coupled receptors. *Nucleic acids research*. 42:D422-425.

Jerabek-Willemsen, M., C.J. Wienken, D. Braun, P. Baaske, and S. Duhr. 2011. Molecular interaction studies using microscale thermophoresis. *Assay and drug development technologies*. 9:342-353.

Kamentsky, L., T.R. Jones, A. Fraser, M.A. Bray, D.J. Logan, K.L. Madden, V. Ljosa, C. Rueden, K.W. Eliceiri, and A.E. Carpenter. 2011. Improved structure, function and compatibility for CellProfiler: modular high-throughput image analysis software. *Bioinformatics*. 27:1179-1180.

Kempf, A., B. Tews, M.E. Arzt, O. Weinmann, F.J. Obermair, V. Pernet, M. Zagrebelsky, A. Delekate, C. Iobbi, A. Zemmar, Z. Ristic, M. Gullo, P. Spies, D. Dodd, D. Gygax, M. Korte, and M.E. Schwab. 2014. The sphingolipid receptor S1PR2 is a receptor for Nogo-a repressing synaptic plasticity. *PLoS biology*. 12:e1001763.

Kimura, A., T. Ohmori, R. Ohkawa, S. Madoiwa, J. Mimuro, T. Murakami, E. Kobayashi, Y. Hoshino, Y. Yatomi, and Y. Sakata. 2007. Essential roles of sphingosine 1-phosphate/S1P1 receptor axis in the migration of neural stem cells toward a site of spinal cord injury. *Stem cells*. 25:115-124.

Kobilka, B.K., and X. Deupi. 2007. Conformational complexity of G-protein-coupled receptors. *Trends in pharmacological sciences*. 28:397-406.

Kono, M., Y. Mi, Y. Liu, T. Sasaki, M.L. Allende, Y.P. Wu, T. Yamashita, and R.L. Proia. 2004. The sphingosine-1-phosphate receptors S1P1, S1P2, and S1P3 function coordinately during embryonic angiogenesis. *The Journal of biological chemistry*. 279:29367-29373.

Li, M., and J. Song. 2007. The N- and C-termini of the human Nogo molecules are intrinsically unstructured: bioinformatics, CD, NMR characterization, and functional implications. *Proteins*. 68:100-108.

Lomize, M.A., I.D. Pogozheva, H. Joo, H.I. Mosberg, and A.L. Lomize. 2012. OPM database and PPM web server: resources for positioning of proteins in membranes. *Nucleic acids research*. 40:D370-376.

Lopes, D.D., R.F. Vieira, L. Malavolta, E.F. Poletti, S.I. Shimuta, A.C. Paiva, S. Schreier, L. Oliveira, and C.R. Nakaie. 2013. Short peptide constructs mimic agonist sites of AT(1)R and BK receptors. *Amino acids*. 44:835-846.

Ludwig, C. 1856. Diffusion zwischen ungleich erwärmten Orten gleich zusammengesetzter Lösungen. *Sitzungsber Akad Wiss Wien Math-Naturwiss Kl*. 20:539.

Oertle, T., M.E. van der Haar, C.E. Bandtlow, A. Robeva, P. Burfeind, A. Buss, A.B. Huber, M. Simonen, L. Schnell, C. Brosamle, K. Kaupmann, R. Vallon, and M.E. Schwab. 2003. Nogo-A inhibits neurite outgrowth and cell spreading with three discrete regions. *The Journal of neuroscience : the official journal of the Society for Neuroscience*. 23:5393-5406.

Parrill, A.L., D. Wang, D.L. Bautista, J.R. Van Brocklyn, Z. Lorincz, D.J. Fischer, D.L. Baker, K. Liliom, S. Spiegel, and G. Tigyi. 2000. Identification of Edg1 receptor residues that recognize sphingosine 1-phosphate. *The Journal of biological chemistry*. 275:39379-39384.

Pham, T.C., J.I. Fells, Sr., D.A. Osborne, E.J. North, M.M. Naor, and A.L. Parrill. 2008. Molecular recognition in the sphingosine 1-phosphate

receptor family. *Journal of molecular graphics & modelling*. 26:1189-1201.

Piscitelli, C.L., J. Kean, C. de Graaf, and X. Deupi. 2015. A Molecular Pharmacologist's Guide to G Protein-Coupled Receptor Crystallography. *Molecular pharmacology*. 88:536-551.

Preininger, A.M., J. Meiler, and H.E. Hamm. 2013. Conformational flexibility and structural dynamics in GPCR-mediated G protein activation: a perspective. *Journal of molecular biology*. 425:2288-2298.

Schadel, S.A., M. Heck, D. Maretzki, S. Filipek, D.C. Teller, K. Palczewski, and K.P. Hofmann. 2003. Ligand channeling within a G-protein-coupled receptor. The entry and exit of retinals in native opsin. *The Journal of biological chemistry*. 278:24896-24903.

Schneider, C.A., W.S. Rasband, and K.W. Eliceiri. 2012. NIH Image to ImageJ: 25 years of image analysis. *Nature methods*. 9:671-675.

Schwab, M.E. 2010. Functions of Nogo proteins and their receptors in the nervous system. *Nature reviews. Neuroscience*. 11:799-811.

Schwab, M.E., and S.M. Strittmatter. 2014. Nogo limits neural plasticity and recovery from injury. *Current opinion in neurobiology*. 27:53-60.

Valentine, W.J., V.I. Godwin, D.A. Osborne, J. Liu, Y. Fujiwara, J. Van Brocklyn, R. Bittman, A.L. Parrill, and G. Tigyi. 2011. FTY720 (Gilenya) phosphate selectivity of sphingosine 1-phosphate receptor subtype 1 (S1P1) G protein-coupled receptor requires motifs in intracellular loop 1 and transmembrane domain 2. *The Journal of biological chemistry*. 286:30513-30525.

Wang, J.W., J.F. Yang, Y. Ma, Z. Hua, Y. Guo, X.L. Gu, and Y.F. Zhang. 2015. Nogo-A expression dynamically varies after spinal cord injury. *Neural regeneration research*. 10:225-229.

Wiederkehr, A., and P. Caroni. 1995. Widely used enhancer of eukaryotic expression vectors is strongly and differentially regulated in fibroblast, myoblast, and teratocarcinoma cell lines. *Experimental cell research*. 219:664-670.

Willard, L., A. Ranjan, H. Zhang, H. Monzavi, R.F. Boyko, B.D. Sykes, and D.S. Wishart. 2003. VADAR: a web server for quantitative evaluation of protein structure quality. *Nucleic acids research*. 31:3316-3319.

Zheng, L., U. Baumann, and J.L. Reymond. 2004. An efficient one-step site-directed and site-saturation mutagenesis protocol. *Nucleic acids research*. 32:e115.

CHAPTER 3

AN INTRAMOLECULAR FRET BIOSENSOR FOR LIVE MONITORING OF SPHINGOSINE 1-PHOSPHATE RECEPTOR 2 (S1PR2) ACTIVITY

Michael E. Arzt[1,2], Martin E. Schwab[1,3]

(unpublished manuscript)

M. E. A. designed, conducted, analyzed, and interpreted the experiments, wrote the manuscript, and prepared the figures.

[1] Brain Research Institute, University of Zurich, Switzerland
[2] Department of Biology, ETH Zurich, Switzerland
[3] Department of Health Sciences and Technology, ETH Zurich, Switzerland

Abstract

Due to their involvement in various physiological and pathophysiological processes, G-protein coupled receptors (GPCRs) have been an important subject of biological and pharmacological research. The GPCR sphingosine 1-phosphate receptor 2 (S1PR2) has important biological roles in fibrotic diseases, cancer, and injuries of the central nervous system; antagonists for S1PR2 would therefore be of high interest as novel therapeutic agents. Reliable, high-throughput-compatible assays that report the activation of S1PR2 are required for the development of such pharmacological modulators. Here, we present S1PR2-FRET, a FRET-based biosensor that reports the activity state of S1PR2 at the receptor level. YFP was inserted into the intracellular loop 3 of S1PR2, and CFP was fused to the C-terminus. The occurrence of FRET between the two fluorophores was confirmed by acceptor photobleaching in a live-cell imaging setup. Strikingly, FRET efficiency decreased upon application of S1P and recovered when the competitive antagonist JTE-013 was added, indicating that the intracellular loop 3 is displaced from the C-terminus upon activation. S1PR2-FRET can therefore be used as a biosensor for time-resolved measurement of S1PR2 activity.

Introduction

Sphingosine 1-phosphate receptor 2 (S1PR2) is one of five G-protein coupled receptors (GPCRs) that sense the small signaling lysophospholipid sphingosine 1-phosphate (S1P) (Blaho and Hla, 2014). S1PR2 exhibits a broad expression pattern and plays diverse roles in different tissues, including immune cells, kidney, liver, muscles, neuronal progenitors, adult neurons, and pancreas (Adada et al., 2013). Accordingly, S1PR2 also has broad relevance in the pathology and therapy of several diseases, including cancer and atherosclerosis (Maceyka et al., 2012). We have recently demonstrated a novel role of S1PR2 as a receptor for the inhibitory Nogo-A-Δ20 domain of the myelin-associated neurite outgrowth inhibitory protein Nogo-A (Kempf et al., 2014). Blockade of the interaction between Nogo-A and S1PR2 provides a novel strategy to enhance regeneration after lesions of the central nervous system (CNS). A neutralizing antibody that binds to Nogo-A and promotes functional recovery upon spinal cord injury or stroke in rodents is currently being evaluated in clinical trials (Zorner and Schwab, 2010). JTE-013, a blocker of S1PR2, mimics several important plasticity- and regeneration-enhancing effects of Nogo-A blockade (Kempf et al., 2014). Although very specific in their target recognition, therapeutic antibodies have particular pharmacokinetic limitations, and their delivery to the CNS is restricted by the blood-brain barrier (Chames et al., 2009; Yu and Watts, 2013). Therefore, small molecules that cross the blood-brain barrier and specifically interrupt Nogo-A-Δ20-induced signaling through S1PR2 would be a promising new pharmacological avenue. S1PR2 antagonists have also been suggested for the

treatment of cancer and certain fibrotic diseases (Kusumi et al., 2015; Li et al., 2015). The most widely used S1PR2 antagonist, JTE-013, is highly lipophilic, leading to accumulation in CNS myelin and severely restricted penetration into the CNS compartment even after intrathecal application (unpublished observations). In addition, JTE-013 is fairly unstable *in vivo* and exhibits a debatable specificity, which requires further optimization of the lead compound (Adada et al., 2013; Li et al., 2015). Therefore, novel antagonists for S1PR2 are urgently sought after (Kusumi et al., 2015). Current high-throughput screening assays primarily rely on GPCR-induced signaling at the G-protein or effector molecule levels as a readout (Thomsen et al., 2005). Since downstream signaling of S1PR2 is shared with a multitude of other GPCRs, this approach imposes specificity problems. In addition, the physiological response to activation of S1PR2 depends largely on the cell type, presumably due to different G-protein compositions (Adada et al., 2013). New tools are therefore essential that allow live monitoring of S1PR2 activation at the receptor level.

An elegant way to observe the activation of a GPCR is monitoring its conformational changes by means of Förster resonance energy transfer (FRET) (Förster, 1948). FRET describes a phenomenon by which an excited donor fluorophore transfers some of its energy to an acceptor fluorophore if the donor emission and the acceptor absorption spectra overlap (Fig. 1A). Importantly, the FRET efficiency E_{FRET} is inversely proportional to the sixth power of the separation distance *r* between the fluorophores,

$$E_{FRET} = \frac{R_0^6}{R_0^6 + r^6}$$

where R_0 is the Förster distance of the FRET pair used, i.e., the distance at which half of the energy is transferred (Arai and Nagai, 2013). The ECFP and Venus variants of CFP and YFP that were used in this study exhibit an R_0 of 50 Å (Lam et al., 2012). Upon excitation at 427 nm, CFP therefore transfers some of its energy to YFP only if the molecules are closer than ~100 Å, resulting in quenched CFP emission at 472 nm and enhanced YFP emission at 542 nm (Fig. 1B). E_{FRET} can therefore be used as a proxy of the distance between these molecules.

A popular application of FRET is to attach the donor and acceptor fluorophores to two interacting molecules, which results in intermolecular FRET upon complex formation. In GPCR research, this approach has been used to detect receptor oligomerization, as well as interactions with ligands, β-arrestins or other intracellular mediators (Oueslati et al., 2015; Pfleger and Eidne, 2005). Alternatively, attachment of a FRET pair to the intracellular loop (ICL) 3 and the C-terminus of a GPCR allows sensitive monitoring of conformational changes by intramolecular FRET (Fig. 1C,D) (Vilardaga et al., 2003). Here, we used an analogous approach to create a conformation-dependent S1PR2-FRET biosensor.

Materials and Methods

Molecular Cloning

Multiple sequence alignment was conducted using CLUSTAL 2.1 (Larkin et al., 2007) to compare the fluorophore insertion sites of GPCR-FRET probes from α_{2A}-adrenergic receptor (Vilardaga et al., 2003), β_1-adrenergic receptor (Rochais et al., 2007), M_1 acetylcholine receptor (Jensen et al., 2009), and B_2 bradykinin receptor (Chachisvilis et al., 2006). The Venus variant (Nagai et al., 2002) of EYFP was introduced to ICL3 of murine S1PR2 (between Val223 and Ala224), and ECFP was fused to the C-terminus of the receptor by seamless fusion cloning (Fig. 1E) (Matsumura, 2013). Briefly, the open reading frames (ORFs) of Venus and ECFP, as well as the two moieties of the S1PR2 ORF from the N-terminus to Val223 and from Ala224 to the C-terminus were amplified individually by PCR with Phusion Hot Start II DNA polymerase (Life Technologies). Primers used were: S1PR2-N-FWD, 5'-CGT TTA AAC TTA AGC TTG CCA CCA TGG-3'; S1PR2-N-REV, 5'-AAC ATC CGC GTG GCT G-3'; Venus-FWD, 5'-<u>CAG CCA CGC GGA TGT T</u>GT GAG CAA GGG CGA GGA-3'; Venus-REV, 5'-<u>GCT AGC GTC TGA GGA CCA GC</u>C TTG TAC AGC TCG TCC ATG C-3'; S1PR2-C-FWD, 5'-GCT GGT CCT CAG ACG CTA GC-3'; S1PR2-C-REV, 5'-GAC CAC TGT GTT ACC CTC CAG A-3'; ECFP-FWD, 5'-<u>TCT GGA GGG TAA CAC AGT GGT C</u>GT GAG CAA GGG CGA GGA-3'; ECFP-REV, 5'-*GGT TTA AAC GGG CCC TCT AGA CTC GAG TCA* CTT GTA CAG CTC GTC CAT GC-3'. Venus-FWD and Venus-REV contained 5'-extensions (underlined) that were homologous to the S1PR2 sequence upstream and downstream to the desired junction site in ICL3, thus flanking the Venus fragment with the adjacent S1PR2 sequence. Likewise, the ECFP-FWD introduced a 5'-flanking sequence that was homologous to the C-terminal portion of the S1PR2 ORF. The 5'-extension of ECFP-REV was designed to match the sequence of pcDNA5, the desired destination vector (italics). After PCR purification using the MinElute PCR Purification Kit (Qiagen), equimolar amounts of the N-terminal S1PR2 moiety and of the flanked Venus ORF were combined, and the S1PR2-homologous extension on the Venus fragment acted as a primer in another PCR reaction, resulting in the desired fusion construct (Fig. 1E, fusion 1). After 15 cycles, S1PR2-N-FWD and Venus-REV were added to favor amplification of the fusion construct. Likewise, the C-terminal moiety of S1PR2 was fused to ECFP, adding S1PR2-C-FWD and ECFP-REV after 15 cycles (Fig. 1E, fusion 2). The fusion products were analyzed on a 1% agarose/TAE gel and purified using the GenElute Gel Extraction Kit (Sigma Aldrich), and fusion of the final construct was achieved by combining equimolar amounts and repeating the seamless fusion cloning protocol (Fig. 1E, fusion 3), adding terminal primers after 15 cycles (Total-FWD, 5'-CGT TTA AAC TTA AGC TTG CCA CCA TGG; Total-REV, 5'-GGT TTA AAC GGG CCC TCT AGA CTC G-3'). The resulting total PCR product was ligated into the toxic *eco47IR* gene of pJET1.2 (Life Technologies), which ensures that only insert-bearing ligation products yield viable colonies after transformation of OneShot TOP10

chemically competent *E. coli* (Life Technologies). Plasmid DNA was isolated from individual bacterial colonies and sequenced, and a clone containing the desired fusion construct was sub-cloned into pcDNA5/FRT for CMV-driven overexpression. The final plasmid was again sequenced, and designated pS1PR2-FRET.

Live-Cell Imaging

HEK293T cells were briefly trypsinized and seeded to 6-well plates at a density of $5x10^5$ cells per well. The next day, cells were 70-90% confluent and were transfected with pS1PR2-FRET using Lipofectamine 2000 (Life Technologies). After 3 h, media were replaced with fresh full growth media. One day later, cells were detached with 2 mM EDTA/PBS and re-plated to a 24-well plate containing poly-L-lysine-coated 12 mm coverslips at $1.5x10^5$ cells per well. 48 hours after transfection, coverslips were placed in a Ludin chamber for live-cell imaging and transferred to a temperature-controlled Leica DMI 6000 inverted microscope at 37 °C equipped with a 63x oil immersion objective. CFP was excited at 427 ± 10 nm, and CFP and YFP emission were recorded simultaneously at 472 ± 30 nm and 542 ± 27 nm, respectively. Cells with apparent high surface expression of S1PR2-FRET were chosen for analysis, and CFP and YFP emission were recorded simultaneously every 5 s in measurement buffer [137 mM NaCl, 5 mM KCl, 1 mM $CaCl_2$, 1 mM $MgCl_2$, 20 mM HEPES, 0.1% (w/v) BSA, pH 7.4]. A gravity flow perfusion system was used to superfuse cells with 1 µM sphingosine 1-phosphate (Sigma Aldrich) or 1 µM JTE-013 (Tocris), which both were diluted in measurement buffer. FRET was measured as the YFP to CFP emission ratio of single cells. For acceptor photobleaching, several cells were measured and averaged over time. Image analysis was conducted in ImageJ (Schneider et al., 2012), and non-linear regression was performed in GraphPad Prism assuming a mono-exponential relationship.

Results

Design and molecular cloning of the S1PR2-FRET sensor

The correct choice of insertion sites for CFP and YFP is critical in order to obtain a GPCR-FRET probe that reports conformational changes upon activation (Krasel and Hoffmann, 2010). For construction of S1PR2-FRET, sequence alignment of its ICL3 with five functional and published GPCR-FRET constructs was performed (Fig. S1). Among these, human B_2 bradykinin receptor shared a similar ICL3 length with S1PR2. The insertion site for YFP was therefore chosen at an analogous position, placing YFP inside ICL3 and CFP at the C-terminus (Fig. 1C,D). Seamless fusion cloning was used for generation of S1PR2-FRET (Fig. 1E). In short, the open reading frames of individual fragments from S1PR2, Venus, and ECFP were amplified by PCR, flanking them with

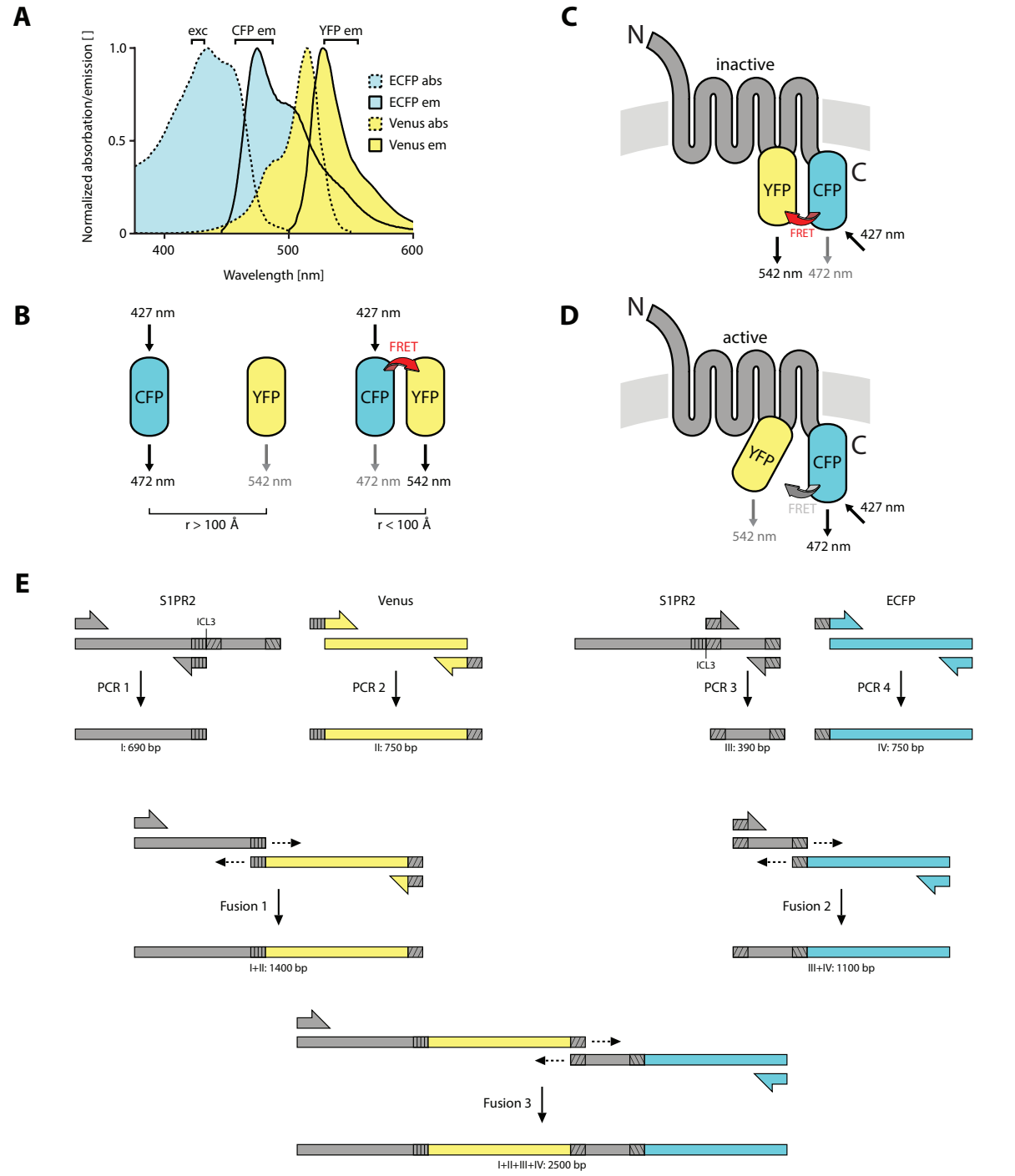
A
exc
CFP em
YFP em
Normalized absorbation/emission [ ]
1.0
0.5
0
400
500
600
Wavelength [nm]
ECFP abs
ECFP em
Venus abs
Venus em
B
427 nm
CFP
472 nm
YFP
542 nm
r > 100 Å
FRET
r < 100 Å
C
N
inactive
YFP
CFP
C
FRET
427 nm
542 nm
472 nm
D
N
active
YFP
CFP
C
FRET
427 nm
542 nm
472 nm
E
S1PR2
ICL3
PCR 1
I: 690 bp
Venus
PCR 2
II: 750 bp
Fusion 1
I+II: 1400 bp
S1PR2
ICL3
PCR 3
III: 390 bp
ECFP
PCR 4
IV: 750 bp
Fusion 2
III+IV: 1100 bp
Fusion 3
I+II+III+IV: 2500 bp
F
I
II
III
IV
bp
1000
750
500
250
G
I+II
III+IV
bp
1500
1000
750
500
250
H
I+II+III+IV
bp
3000
2500
2000
1500
1000

Fig. 1: Design and molecular cloning of S1PR2-FRET. A, Absorption (abs) and emission (em) spectra of ECFP and the YFP variant Venus. ECFP emission and Venus absorption overlap, giving rise to FRET. Wavelengths of the excitation (ex) and emission (em) filters used in live-cell microscopy are given above the spectra. Spectra were obtained from http://searchlight.semrock.com. **B**, FRET efficiency depends on the distance between fluorophores. If CFP and YFP are further apart than ~100 Å, excitation of CFP at 427 nm primarily causes CFP emission at 472 nm. If the fluorophores are closer together, energy of excited CFP is transferred to YFP via FRET, which quenches CFP and causes YFP emission at 542 nm. **C**, In the inactive state of the FRET sensor, CFP and YFP are in close proximity, giving rise to an observable FRET signal. **D**, Upon activation, conformational changes in the GPCR cause a displacement of YFP from CFP, resulting in an attenuation of FRET. **E**, Seamless fusion cloning. Venus and ECFP primers carry 5'-overhangs homologous to adjacent S1PR2 sequence (gray). These flanking regions act as primers in the fusion PCR steps, enabling seamless fusion of individual fragments. **F**, PCR products from PCR 1-4 in E. **G**, PCR products from fusions 1-2 in E. Bands corresponding to the fusion product are marked with asterisks. **H**, PCR product from fusion 3 in E. The final S1PR2-FRET construct is marked with an asterisk.

sequence from adjacent fragments by 5'-extended primers (Fig. 1E, PCR1-4). All fragments were readily amplified to their expected molecular weights (Fig. 1F). In a subsequent round of fusion PCRs connecting adjacent fragment pairs, the flanking regions of one fragment acted as primers on the other, causing fusion of the fragments (Fig. 1E, fusion 1-2). Indeed, bands corresponding to the lengths of the fusion constructs could be observed after this PCR (Fig. 1G). These fusion products were then further fused to obtain the final S1PR2-FRET construct (Fig. 1E, fusion 3). Though the resulting fusion band was very faint (Fig. 1H), it was successfully cloned into a CMV-driven expression vector and designated pS1PR2-FRET.

Acceptor photobleaching

S1PR2-FRET was overexpressed in HEK293T cells, and CFP and YFP emissions were recorded simultaneously in a live-cell microscopy setup. Signals could be observed in both channels upon CFP excitation, and a large intracellular pool of S1PR2-FRET was evident (Fig. 2B). Photobleaching of the FRET acceptor YFP resulted in an amplified CFP emission (Fig. 2B,C). This demonstrates that prior to YFP photobleaching, some of the CFP energy was transferred to YFP, thus confirming the occurrence of FRET in the sensor (Fig. 2A).

The FRET probe is responsive to S1P-induced activation of S1PR2

We next wondered whether the observed FRET signal in the S1PR2-FRET probe could be modulated by addition of an agonist. A permanent superfusion system was used to apply ligand compounds to S1PR2-FRET-overexpressing HEK293T cells during live-cell imaging. Indeed, upon addition of 1 µM S1P, a reduction of the YFP/CFP emission ratio by ~8 % could be observed (Fig. 2D,E). Strikingly, this effect could be completely abolished when, after 2 min, S1P was replaced by 1 µM JTE-013, a selective competitive antagonist of S1PR2 binding to the same site as S1P. Withdrawal of JTE-013 and reapplication of S1P again resulted in an attenuation of the FRET signal. Interestingly, the time constants (τ) of the FRET response to these ligands differed substantially (Fig. 2E): while the reduction of FRET upon initial S1P application was very rapid

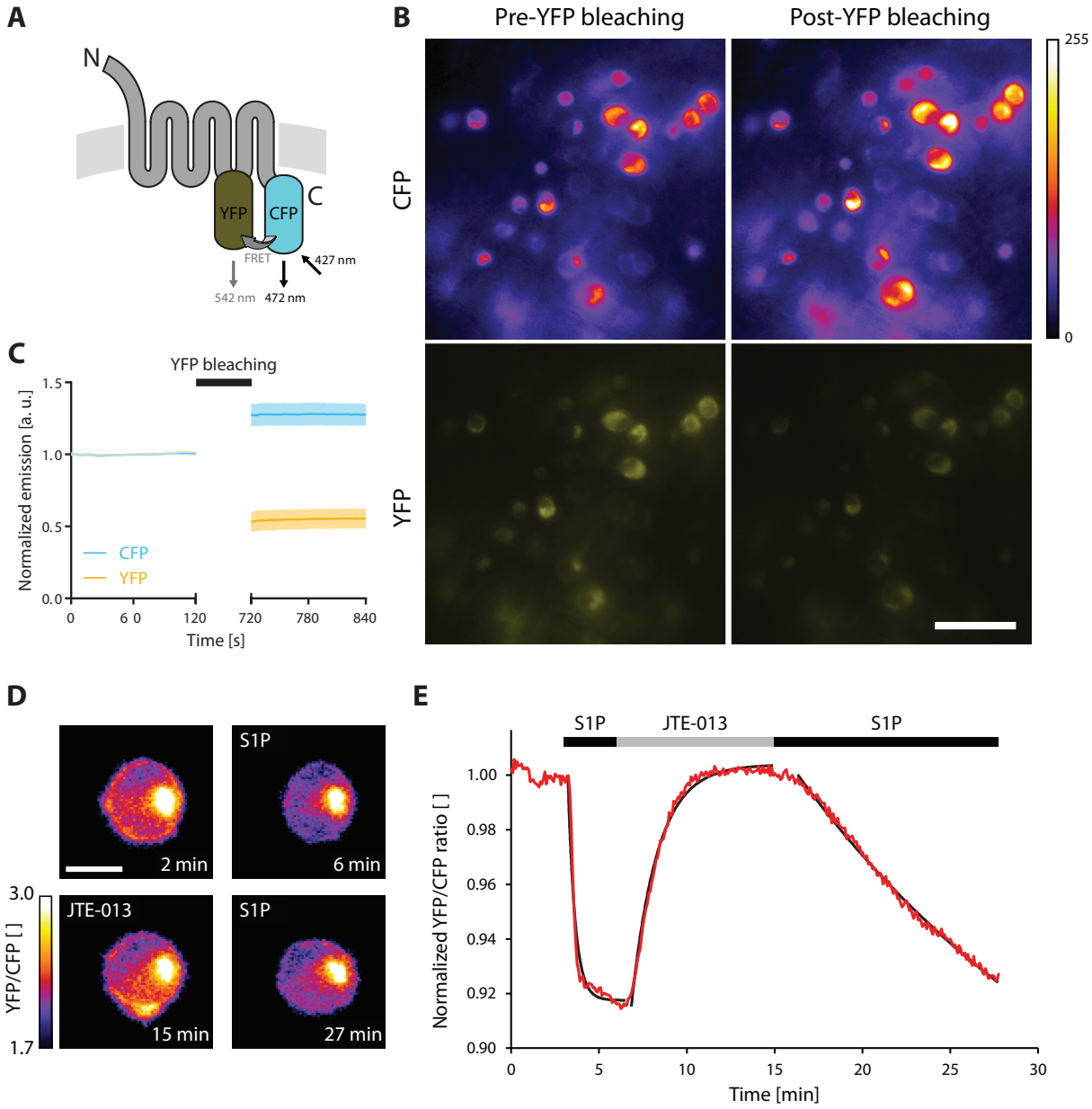

Fig. 2: Live-cell imaging of S1PR2-FRET. A, After photobleaching of the YFP acceptor, less energy can be transferred from CFP to YFP by FRET. CFP emission should therefore be enhanced after YFP photobleaching. **B**, Indeed, CFP emission increases after YFP photobleaching. The scale bar corresponds to 50 µm. **C**, Quantification of B, reporting means ±SD from seven cells within the field of view shown in B. **D**, Upon addition of the agonist S1P, FRET efficiency is attenuated. The competitive antagonist JTE-013 reverses this effect. The scale bar corresponds to 10 µm. **E,** Quantificatino of C. Mono-exponential regression curves are shown in black. Note the different time constants of the responses.

(τ = 24.08 s), FRET recovery by JTE-013 occurred at a slower rate (τ = 1.47 min). Finally, when JTE-013 was replaced by S1P, the observed FRET response appeared even slower (τ = 19.79 min). The intracellular pool of S1PR2-FRET was not modulated by S1P or JTE-013. Taken together, these results indicate that the S1PR2-FRET probe can be used in live-cell microscopy to monitor the conformational switch between active and inactive states of this receptor.

Discussion

The design of FRET-based biosensors can be very challenging. The distance and orientation of the fluorophores have to be chosen such that the active and inactive conformations of the host protein lead to physical distance changes between the two fluorophores, thus exerting distinguishable FRET efficiencies. As outlined above, the dynamic range of FRET is below 100 Å for CFP and YFP, requiring precise relative positioning of these fluorophores. Additionally, insertion sites have to be chosen such that they do not interfere with the native structure of the host protein. As a result, multiple insertion sites usually have to be screened in order to obtain a conformation-responsive FRET probe. We exploited homology of S1PR2 with other published GPCR-FRET probes in order to predict a functional insertion site (Chachisvilis et al., 2006; Jensen et al., 2009; Rochais et al., 2007; Vilardaga et al., 2003). We used seamless fusion cloning to insert YFP to ICL3, and CFP to the C-terminus of S1PR2. In contrast to conventional restriction endonuclease-based cloning methods, this PCR-based procedure does not introduce any unwanted restriction sites to the junctions of the fusion construct (Matsumura, 2013).

Indeed, the first S1PR2-FRET construct that we cloned exhibited FRET as seen in the acceptor photobleaching experiment. Importantly, the FRET efficiency could be modulated by addition of S1P, resulting in ~8 % attenuation of the signal. This amplitude probably even underestimates the real effect, as large intracellular pools of the sensor were evident in microscopy that may not have responded readily to the exogenous agonist and therefore retained a high FRET efficiency even in the presence of S1P. The S1P-mediated attenuation of FRET efficiency indicates that ICL3 of S1PR2 is deflected from the C-terminus upon activation. A similar conformational change has been observed in other GPCRs, where it has been attributed to a displacement of trans-membrane domain (TMD) 6 (Hoffmann et al., 2008; Vilardaga et al., 2003). Addition of the competitive antagonist JTE-013 restored the FRET efficiency of S1PR2-FRET to baseline levels, but not beyond. This was surprising, as the presence of endogenous S1P was expected to contribute to a partial activation in the baseline recordings. Therefore, either the FRET efficiency was saturated at the baseline and after JTE-013 administration, or S1P was low or absent from our cell culture during baseline measurements. Interestingly, the time constants of the conformational changes were pretty slow compared to other GPCR-FRET probes (Vilardaga et al., 2003). Slow saturation even in the excess of S1P has been observed before and has been attributed to an unusual entry mechanism of S1P into the receptor (Hanson et al., 2012; Rosen et al., 2009). In the crystal structure of S1PR1, an N-terminal helix blocks direct access to the internal S1P binding site (Hanson et al., 2012). It has therefore been suggested that S1P first inserts into the membrane with its lipophilic tail and reaches its binding pocket by lateral diffusion through an opening between TMD1 and TMD7. Such limited access explains the slow saturation of S1P at initial application. Signal recovery by JTE-013 was an even slower process, in line with S1P displacement

through a narrow opening. Interestingly, the conformational change upon S1P was much slower when S1PR2-FRET had been saturated with JTE-013, supporting the idea that ligand replacement is the rate-limiting step in the interplay between agonist and antagonist.

CFP and YFP are the most commonly used FRET pair due to their strong spectral overlap (Day and Davidson, 2012). However, such genetically encoded fluorophores are relatively big, which can interfere with the folding and interactions of the host protein (Hoffmann et al., 2005). In S1PR2-FRET, which contains fluorophore insertions both in ICL3 and at the C-terminus, intracellular coupling to G-proteins and other cytosolic signal transducers is likely to be affected. As a consequence, the suitability of the biosensor to detect conformational changes upon binding of intracellular proteins is limited. This problem can be minimized by covalently linking small organic dyes like fluorescein arsenical hairpin binder (FlAsH) to tetracysteine motifs that are introduced into the GPCR (Hoffmann et al., 2005). However, ensuring labeling specificity can be a challenge, which is never an issue with genetically encoded fluorophores. In addition, the gain of function caused by strong overexpression of wild-type GPCRs often elicits cytotoxicity, which is a bottleneck in producing high GPCR yields (Ghosh et al., 2015). The presence of bulky fluorophores sterically masking the intracellular signaling domain can therefore have a beneficial effect on S1PR2-FRET expression levels, which enhances the signal-to-noise ratio.

Many potential applications of the S1PR2-FRET system can be imagined. We intend to quantify S1PR2 activation in a multi-well format to assess the interdependence of its two agonists, the small-MW lysophospholipid S1P and the high-MW membrane protein Nogo-A or its soluble fragment Nogo-A-Δ20. Solubilization of S1PR2-FRET may be used to release the intracellular pool and thus enhance the responsiveness of the system. These methodological adaptations will further expand the applicability of S1PR2-FRET, providing a high-throughput platform for compound screens of putative S1PR2 modulators. In addition, S1PR2-FRET may be utilized for spatio-temporal detection of S1PR2 activation in migrating cells, as well as *in-vivo* FRET imaging in small organisms (Johnsson et al., 2014; Langenhan et al., 2015; Lohse, 2015; van Unen et al., 2015).

Acknowledgments

Venus and ECFP plasmids were kind gifts of Dr. Stella Kramer and Dr. Darcie Moore. Thanks to Dr. Alok Kumar Behara and Dr. José María Mateos Melero for assistance with microscopy. Live-cell imaging experiments were conducted with equipment maintained by the Center for Microscopy and Image Analysis, University of Zurich.

References

Adada, M., D. Canals, Y.A. Hannun, and L.M. Obeid. 2013. Sphingosine-1-phosphate receptor 2. *The FEBS journal*. 280:6354-6366.

Arai, Y., and T. Nagai. 2013. Extensive use of FRET in biological imaging. *Microscopy (Oxf)*. 62:419-428.

Blaho, V.A., and T. Hla. 2014. An update on the biology of sphingosine 1-phosphate receptors. *Journal of lipid research*. 55:1596-1608.

Chachisvilis, M., Y.L. Zhang, and J.A. Frangos. 2006. G protein-coupled receptors sense fluid shear stress in endothelial cells. *Proceedings of the National Academy of Sciences of the United States of America*. 103:15463-15468.

Chames, P., M. Van Regenmortel, E. Weiss, and D. Baty. 2009. Therapeutic antibodies: successes, limitations and hopes for the future. *British journal of pharmacology*. 157:220-233.

Day, R.N., and M.W. Davidson. 2012. Fluorescent proteins for FRET microscopy: monitoring protein interactions in living cells. *BioEssays : news and reviews in molecular, cellular and developmental biology*. 34:341-350.

Förster, T. 1948. Zwischenmolekulare Energiewanderung und Fluoreszenz. *Annalen der Physik*. 437:55-75.

Ghosh, E., P. Kumari, D. Jaiman, and A.K. Shukla. 2015. Methodological advances: the unsung heroes of the GPCR structural revolution. *Nature reviews. Molecular cell biology*. 16:69-81.

Hanson, M.A., C.B. Roth, E. Jo, M.T. Griffith, F.L. Scott, G. Reinhart, H. Desale, B. Clemons, S.M. Cahalan, S.C. Schuerer, M.G. Sanna, G.W. Han, P. Kuhn, H. Rosen, and R.C. Stevens. 2012. Crystal structure of a lipid G protein-coupled receptor. *Science*. 335:851-855.

Hoffmann, C., G. Gaietta, M. Bunemann, S.R. Adams, S. Oberdorff-Maass, B. Behr, J.P. Vilardaga, R.Y. Tsien, M.H. Ellisman, and M.J. Lohse. 2005. A FlAsH-based FRET approach to determine G protein-coupled receptor activation in living cells. *Nature methods*. 2:171-176.

Hoffmann, C., A. Zurn, M. Bunemann, and M.J. Lohse. 2008. Conformational changes in G-protein-coupled receptors-the quest for functionally selective conformations is open. *British journal of pharmacology*. 153 Suppl 1:S358-366.

Jensen, J.B., J.S. Lyssand, C. Hague, and B. Hille. 2009. Fluorescence changes reveal kinetic steps of muscarinic receptor-mediated modulation of phosphoinositides and Kv7.2/7.3 K+ channels. *The Journal of general physiology*. 133:347-359.

Johnsson, A.K., Y. Dai, M. Nobis, M.J. Baker, E.J. McGhee, S. Walker, J.P. Schwarz, S. Kadir, J.P. Morton, K.B. Myant, D.J. Huels, A. Segonds-Pichon, O.J. Sansom, K.I. Anderson, P. Timpson, and H.C. Welch. 2014. The Rac-FRET mouse reveals tight spatiotemporal control of Rac activity in primary cells and tissues. *Cell reports*. 6:1153-1164.

Kempf, A., B. Tews, M.E. Arzt, O. Weinmann, F.J. Obermair, V. Pernet, M. Zagrebelsky, A. Delekate, C. Iobbi, A. Zemmar, Z. Ristic, M. Gullo, P. Spies, D. Dodd, D. Gygax, M. Korte, and M.E. Schwab. 2014. The sphingolipid receptor S1PR2 is a receptor for Nogo-a repressing synaptic plasticity. *PLoS biology*. 12:e1001763.

Krasel, C., and C. Hoffmann. 2010. Using Intramolecular Fluorescence Resonance Energy Transfer to Study Receptor Conformation. *In* G Protein-Coupled Receptors. Wiley-Blackwell. 133-146.

Kusumi, K., K. Shinozaki, T. Kanaji, H. Kurata, A. Naganawa, K. Otsuki, T. Matsushita, T. Sekiguchi, A. Kakuuchi, and T. Seko. 2015. Discovery of novel S1P2 antagonists. Part 1: discovery of 1,3-bis(aryloxy)benzene derivatives. *Bioorganic & medicinal chemistry letters*. 25:1479-1482.

Lam, A.J., F. St-Pierre, Y. Gong, J.D. Marshall, P.J. Cranfill, M.A. Baird, M.R. McKeown, J. Wiedenmann, M.W. Davidson, M.J. Schnitzer, R.Y. Tsien, and M.Z. Lin. 2012. Improving FRET dynamic range with bright green and red fluorescent proteins. *Nature methods*. 9:1005-1012.

Langenhan, T., M.M. Barr, M.R. Bruchas, J. Ewer, L.C. Griffith, I. Maiellaro, P.H. Taghert, B.H. White, and K.R. Monk. 2015. Model Organisms in G Protein-Coupled Receptor Research. *Molecular pharmacology*. 88:596-603.

Larkin, M.A., G. Blackshields, N.P. Brown, R. Chenna, P.A. McGettigan, H. McWilliam, F. Valentin, I.M. Wallace, A. Wilm, R. Lopez, J.D. Thompson, T.J. Gibson, and D.G. Higgins. 2007. Clustal W and Clustal X version 2.0. *Bioinformatics*. 23:2947-2948.

Li, M.H., R. Swenson, M. Harel, S. Jana, E. Stolarzewicz, T. Hla, L.H. Shapiro, and F. Ferrer. 2015. Antitumor activity of a novel S1P2 antagonist, AB1, in neuroblastoma. *The Journal of pharmacology and experimental therapeutics*.

Lohse, M. 2015. In Vivo-Studies of GPCR Conformational Changes using Fluorescence-Based Assays. *Biophysical journal*. 108:358a.

Maceyka, M., K.B. Harikumar, S. Milstien, and S. Spiegel. 2012. Sphingosine-1-phosphate signaling and its role in disease. *Trends in cell biology*. 22:50-60.

Matsumura, I. 2013. A quarter century of reaping what we SOE. *BioTechniques*. 54:127-128.

Nagai, T., K. Ibata, E.S. Park, M. Kubota, K. Mikoshiba, and A. Miyawaki. 2002. A variant of yellow fluorescent protein with fast and efficient maturation for cell-biological applications. *Nature biotechnology*. 20:87-90.

Oueslati, N., C. Hounsou, A. Belhocine, T. Rodriguez, E. Dupuis, J.M. Zwier, E. Trinquet, J.P. Pin, and T. Durroux. 2015. Time-resolved FRET strategy to screen GPCR ligand library. *Methods Mol Biol*. 1272:23-36.

Pfleger, K.D., and K.A. Eidne. 2005. Monitoring the formation of dynamic G-protein-coupled receptor-protein complexes in living cells. *The Biochemical journal*. 385:625-637.

Rochais, F., J.P. Vilardaga, V.O. Nikolaev, M. Bunemann, M.J. Lohse, and S. Engelhardt. 2007. Real-time optical recording of beta1-adrenergic receptor activation reveals supersensitivity of the Arg389 variant to carvedilol. *The Journal of clinical investigation*. 117:229-235.

Rosen, H., P.J. Gonzalez-Cabrera, M.G. Sanna, and S. Brown. 2009. Sphingosine 1-phosphate receptor signaling. *Annual review of biochemistry*. 78:743-768.

Schneider, C.A., W.S. Rasband, and K.W. Eliceiri. 2012. NIH Image to ImageJ: 25 years of image analysis. *Nature methods*. 9:671-675.

Thomsen, W., J. Frazer, and D. Unett. 2005. Functional assays for screening GPCR targets. *Current opinion in biotechnology*. 16:655-665.

van Unen, J., J. Woolard, A. Rinken, C. Hoffmann, S. Hill, J. Goedhart, M. Bruchas, M. Bouvier, and M. Adjobo-Hermans. 2015. A Perspective on Studying GPCR Signaling with RET Biosensors in Living Organisms. *Molecular pharmacology*.

Vilardaga, J.P., M. Bunemann, C. Krasel, M. Castro, and M.J. Lohse. 2003. Measurement of the millisecond activation switch of G protein-coupled receptors in living cells. *Nature biotechnology*. 21:807-812.

Yu, Y.J., and R.J. Watts. 2013. Developing therapeutic antibodies for neurodegenerative disease. *Neurotherapeutics : the journal of the American Society for Experimental NeuroTherapeutics*. 10:459-472.

Zorner, B., and M.E. Schwab. 2010. Anti-Nogo on the go: from animal models to a clinical trial. *Annals of the New York Academy of Sciences*. 1198 Suppl 1:E22-34.

Supplement

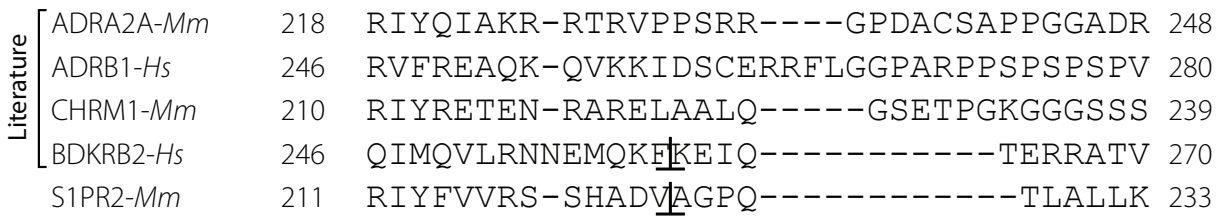

Fig. S1: Multiple sequence alignment of ICL3 from S1PR2. Other GPCRs from the literature used as ICL3/C-terminus FRET probes were used as templates for YFP insertion. BDKRB2 lacks similar amino acids in ICL3 as S1PR2 (dashes). The YFP insertion site for S1PR2 was therefore chosen in an analogous position as the insertion site in BDKRB2 (inverted T). ADRA2A-*Mm*, murine α_{2A}-adrenergic receptor; ADRB1-*Hs*, human β_1-adrenergic receptor; CHRM1-*Mm*, murine M_1 acetylcholine receptor; S1PR2-*Mm*, murine sphingosine 1-phosphate receptor 2; BDKRB2-*Hs*, human B_2 bradykinin receptor.

CHAPTER 4

THE NEURITE OUTGROWTH INHIBITORY NOGO-A-Δ20 REGION IS AN INTRINSICALLY DISORDERED SEGMENT HARBOURING THREE STRETCHES WITH HELICAL PROPENSITY

Viviane Zelenay[1¶], Michael E. Arzt[2,3¶], Stefan Bibow[1], Martin E. Schwab[2,4], Roland Riek[1*]

(unpublished manuscript)

M. E. A. designed, conducted, analyzed, and interpreted the experiments, wrote the manuscript, and prepared the figures.

* Corresponding author. E-Mail: roland.riek@phys.chem.ethz.ch
¶ These authors contributed equally to this work.
[1] Department of Physical Chemistry, ETH Zurich, Switzerland
[2] Brain Research Institute, University of Zurich, Switzerland
[3] Department of Biology, ETH Zurich, Switzerland
[4] Department of Health Sciences and Technology, ETH Zurich, Switzerland

Abstract

Functional recovery from central neurotrauma, such as spinal cord injury, is limited by myelin-associated inhibitory proteins. The most prominent example, Nogo-A, imposes an inhibitory cue for nerve fibre growth via two independent domains: Nogo-A-Δ20 (residues 544-725 of the rat Nogo-A sequence) and Nogo-66 (residues 1026-1091). Whereas the helical conformation of Nogo-66 has been studied extensively, only little structural information is available for the Nogo-A-Δ20 region. We used nuclear magnetic resonance (NMR) spectroscopy to assess potential residual structural propensities of the intrinsically disordered Nogo-A-Δ20. Triple resonance experiments resulted in the sequential backbone assignment of 94 %. While secondary structure analysis and relaxation measurements highlighted the intrinsically disordered character of Nogo-A-Δ20, three stretches comprising residues ^{560}SEAIQESL^{567}, ^{639}EAMNVALKAL^{648}, and ^{695}YSEIAKFEKS^{704} form transient α-helical structures. Interestingly, ^{560}SEAIQESL^{567} is located in direct juxtaposition with one of the most conserved regions of Nogo-A-Δ20 (residues 554-559) that harbours a β1-integrin binding motif. Similarly, ^{639}EAMNVALKAL^{648} partially overlaps with the binding epitope for the Nogo-A-neutralizing antibody 11C7 (residues 630-640) that has been shown to enhance recovery from spinal cord injury. Surprisingly, interaction between the isolated extracellular loops 2 and 3 of sphingosine 1-phosphate receptor 2 (S1PR2), which have previously been shown to bind to Nogo-A-Δ20, could not be observed on Nogo-A-Δ20 by chemical shift perturbation experiments.

Introduction

Neurons in the central nervous system (CNS) exhibit very limited capacity to regrow upon neurotrauma, preventing them from restoring disrupted networks after a spinal cord or brain injury. This is contrary to the situation in the peripheral nervous system (PNS), where regrowth of nerve fibres can occur to a much higher extent (David and Aguayo, 1981; Schwab and Thoenen, 1985). CNS-specific myelin-associated inhibitory molecules that actively prevent the outgrowth of neurons are an important factor accounting for this discrepancy (Schwab and Caroni, 1988). One of the most prominent members of these inhibitory molecules is the 1192 residues long membrane protein Nogo-A, also referred to as reticulon 4-A (Chen et al., 2000; GrandPre et al., 2000; Prinjha et al., 2000). Nogo-A is expressed on the surface of oligodendrocytes where it exhibits an inhibitory signal for neurite growth (Dodd et al., 2005; Oertle et al., 2003). Nogo-A acts as a stabilizer for the highly complex CNS wiring; it restricts synaptic plasticity and influences various intracellular processes such as shaping of the endoplasmic reticulum (ER), where particularly high Nogo-A levels are found (Schwab, 2010; Tews et al., 2013; Voeltz et al., 2006). Two domains of Nogo-A have been identified that impose inhibitory effects on neurite growth and cell migration: Nogo-A-Δ20 and Nogo-66 (Oertle et al., 2003). The Nogo-A-Δ20 domain, which

contains 182 residues, is located in the middle of the 803 residues long Nogo-A-specific segment. In contrast, the 66 residues long Nogo-66 domain is situated between two long hydrophobic stretches at the C-terminus that Nogo-A shares with its much smaller isoforms Nogo-B and Nogo-C, as well as with other reticulon proteins. Neurons express distinct receptors for each of these inhibitory domains, i.e., sphingosine 1-phosphate receptor 2 (S1PR2) together with tetraspanin-3 for Nogo-A-Δ20 and Nogo receptor 1 (NgR1) in association with co-receptors p75, Troy and Lingo-1 (Fournier et al., 2001; Kempf et al., 2014; Mi et al., 2004; Park et al., 2005; Shao et al., 2005; Thiede-Stan et al., 2015; Wang et al., 2002). Both receptor complexes lead to an activation of RhoA in the neuronal cytoplasm, which in turn causes destabilisation of the actin cytoskeleton and thus collapse of the neuronal growth cone as well as a general downregulation of the neuronal growth machinery (Schwab, 2010).

Structural analysis at atomic resolution is a powerful approach to gain insight into the structure-activity relationship of proteins. To date, Nogo-66 is the only inhibitory domain of Nogo for which a structure has been determined (Vasudevan et al., 2010). Nogo-A-Δ20 exhibits an unstructured conformation according to nuclear magnetic resonance (NMR) spectroscopy (Li and Song, 2007). In contrast, circular dichroism (CD) spectroscopy data suggests residual secondary structure for Nogo-A-Δ20 (Li et al., 2004). This is supported by secondary structure prediction indicating the presence of residual conformations within the Nogo-A-Δ20 sequence (Jones, 1999; Li and Song, 2007). Furthermore, the addition of Zn^{2+} to Nogo-A-Δ20 induced a higher degree of α-helical content in circular dichroism (Li et al., 2004).

Only little is known about the structural aspects of the interaction between Nogo-A-Δ20 and its G-protein coupled receptor S1PR2. Binding affinities of individual extracellular loops (ECLs) of S1PR2 to Nogo-A-Δ20 have been found to be in the nanomolar range in the case of ECL2 and ECL3 (Kempf et al., 2014). However, the exact binding mode and amino acid residues involved in this interaction remain elusive.

Here, we report on the residue-specific investigation of Nogo-A-Δ20 structure using NMR spectroscopy. The backbone of Nogo-A-Δ20 was assigned to a completeness of 94% using various triple resonance experiments, revealing three sites of marked α-helical propensity. In addition, we investigated by chemical shift perturbation the interaction of S1PR2 with Nogo-A-Δ20 by titrating ECL2 and ECL3 of S1PR2 to Nogo-A-Δ20 without success.

Results

Structural Propensities for Nogo-A-Δ20

Nogo-A-Δ20 was expressed as ^{13}C- and/or ^{15}N-labelled recombinant protein in *E. coli* to study its structural characteristics using CD and NMR spectroscopy. The CD spectrum of Nogo-A-Δ20 with

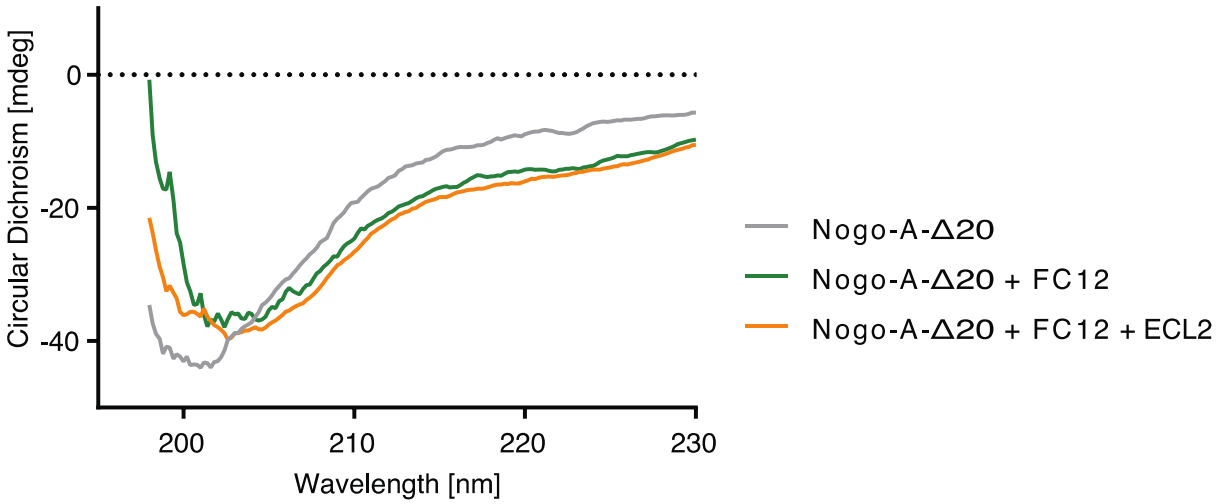

Fig. 1: CD spectroscopy of Nogo-A-Δ20 at 25 °C. Recombinant Nogo-A-Δ20 exhibits a spectrum typical for unstructured proteins. Addition of FC12, thought to mimic a membrane environment, slightly enhances the structural composition of the protein. However, the observed changes are negligible compared to the α-helical structure reported for Nogo-66 upon FC12 addition (Vasudevan et al., 2010). Addition of ECL2 to Nogo-A-Δ20 in a membrane-mimicking environment does not lead to folding, either.

its minimum at 203 nm suggests a high proportion of unstructured regions, although not a completely random coiled structure (Fig. 1). Addition of FC12, which is required for structuring of Nogo-66 (Vasudevan et al., 2010), led to minor changes in the CD spectrum of Nogo-A-Δ20, indicating the absence of FC12 induced significant structural rearrangements.

In accordance with the CD spectrum observed for Nogo-A-Δ20 without FC12, initial NMR measurements using a 2D [^{15}N,^{1}H]-HSQC spectrum confirmed the intrinsically disordered character of Nogo-A-Δ20, as deduced from the low chemical shift dispersion in the ^{1}H dimension (Fig. 2A). In order to obtain sequence-specific conformational and structural information, a backbone assignment was conducted. Standard pulse programs (HNCA, HNCACB) and non-standard experiments (HNN and HCAN) were recorded on [^{13}C, ^{15}N]-Nogo-A-Δ20. The low dispersion in the proton dimension, present in HNCA, HNCACB, and HNN spectra, together with many proline residues present in the sequence (13 %, 23 prolines of 182 residues), interrupted the sequential assignment and posed a severe challenge. To overcome the discontinuity of the spectra along the backbone caused by proline residues, an HCAN spectrum was recorded. Here, the magnetisation is transferred from ^{1}H$^{\alpha}$ to ^{13}C$^{\alpha}$ and further on to N_i and N_{i+1}, enabling a connection of a proline to its following residue (Gal et al., 2011) and allowing a sequential assignment through prolines. With this set of NMR experiments 94 % of the non-proline ^{13}C$^{\alpha}$ and ^{13}C$^{\beta}$ and 83 % of proline ^{13}C$^{\alpha}$- and ^{13}C$^{\beta}$-frequencies in Nogo-A-Δ20 were assigned (Fig. 2B). An unambiguous assignment was impossible for the residue stretches ^{575}PSFE^{578} and ^{678}LIKETK^{683} due to severe peak overlap (Fig S1).

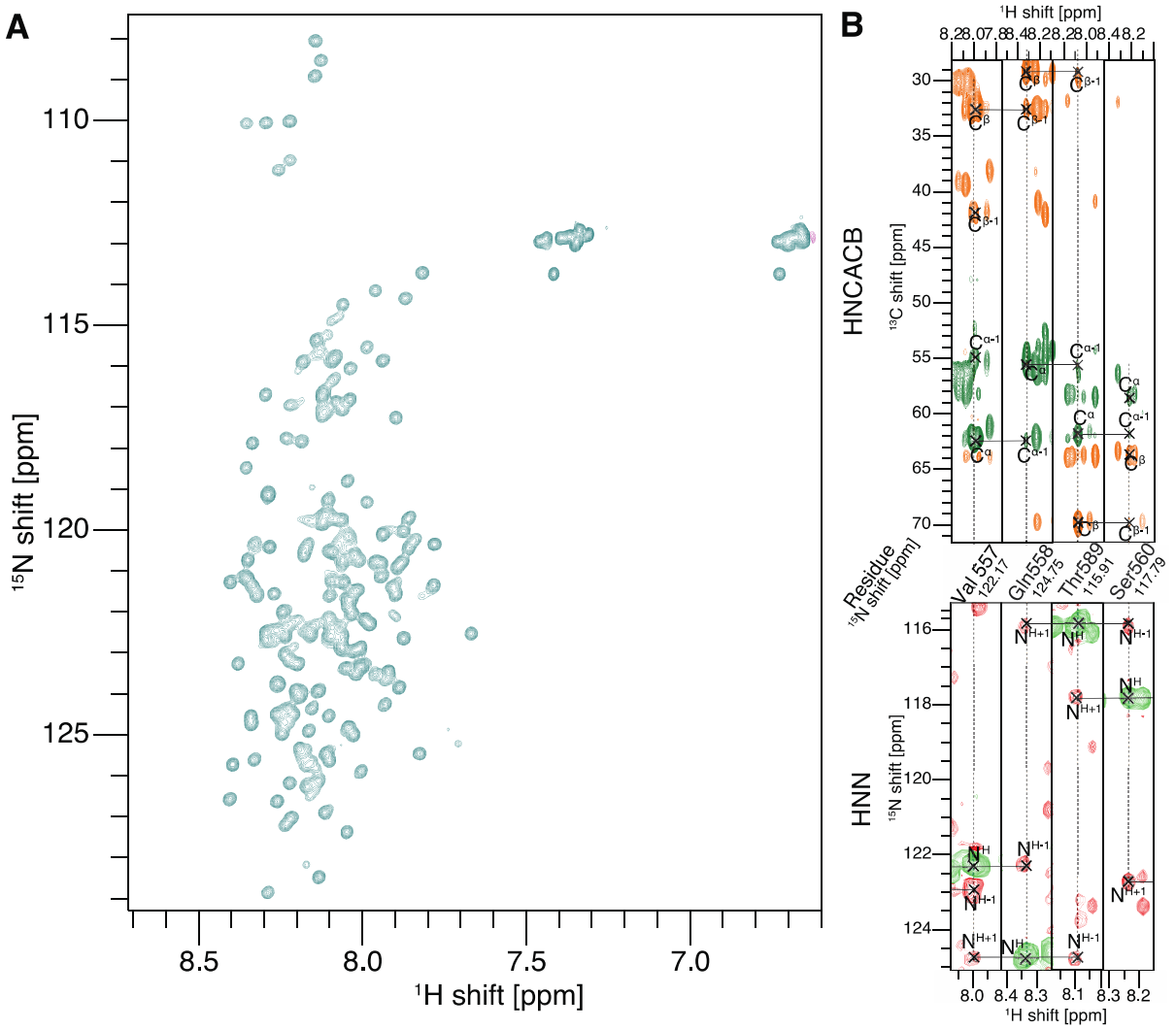

Fig. 2: 2D [^{15}N, ^{1}H]-HSQC and some strips of 3D triple resonance experiments used for the sequential assignment of Nogo-A-Δ20. A, [^{15}N, ^{1}H]-HSQC of Nogo-A-Δ20. The narrow chemical shift dispersion is a common feature of IDPs. **B**, At the top strips of the 3D HNCACB spectrum is shown with green and orange contours indicating positive and negative cross peaks, respectively. At the bottom strips of the 3D HNN spectrum is shown with red and green contours indicating positive and negative cross peaks, respectively. In the HNCACB, cross peaks belonging to C^{α}, $C^{\alpha-1}$, C^{β} and $C^{\beta-1}$ are indicated, while in the HNN spectrum, the N_i, N_{i-1} and N_{i+1} are labelled. The HNCACB spectrum was recorded at a 600 MHz and the HNN spectrum was recorded at a 700 MHz NMR spectrometer at 6 °C and pH 7.4.

The sequential assignment enables secondary structure analysis using secondary chemical shifts of $\Delta\delta^{13}C^{\alpha}$ and $\Delta\delta^{13}C^{\beta}$, which are the difference between the observed chemical shifts and corresponding random coil chemical shifts (Fig. S2) (Wishart and Sykes, 1994) If $\Delta\delta^{13}C^{\alpha}$ values are positive and $\Delta\delta^{13}C^{\beta}$ values are negative for several consecutive residues, these residues are in an α-helical conformation. Conversely, negative $\Delta\delta^{13}C^{\alpha}$ in combination with positive $\Delta\delta^{13}C^{\beta}$ indicate the formation of a β-strand. The two measures can be combined by subtracting the $\Delta\delta13C^{\beta}$ from $\Delta\delta^{13}C^{\alpha}$, resulting in a combined statistically more relevant value denoted [$\Delta\delta^{13}C^{\alpha}$ - $\Delta\delta^{13}C^{\beta}$] in Fig. 3A (Spera and Bax, 1991). Its analysis of Nogo-A-Δ20 show that all the residues show values close to zero (Fig. 3A), indicating a random coil-like structure without fully formed secondary structural elements (Mittag and Forman-Kay, 2007; Novacek et al., 2014; Rezaei-Ghaleh et al., 2012). However, the two segments ^{560}SEAIQESL^{567} and ^{639}EAMNVALKAL^{648} contain

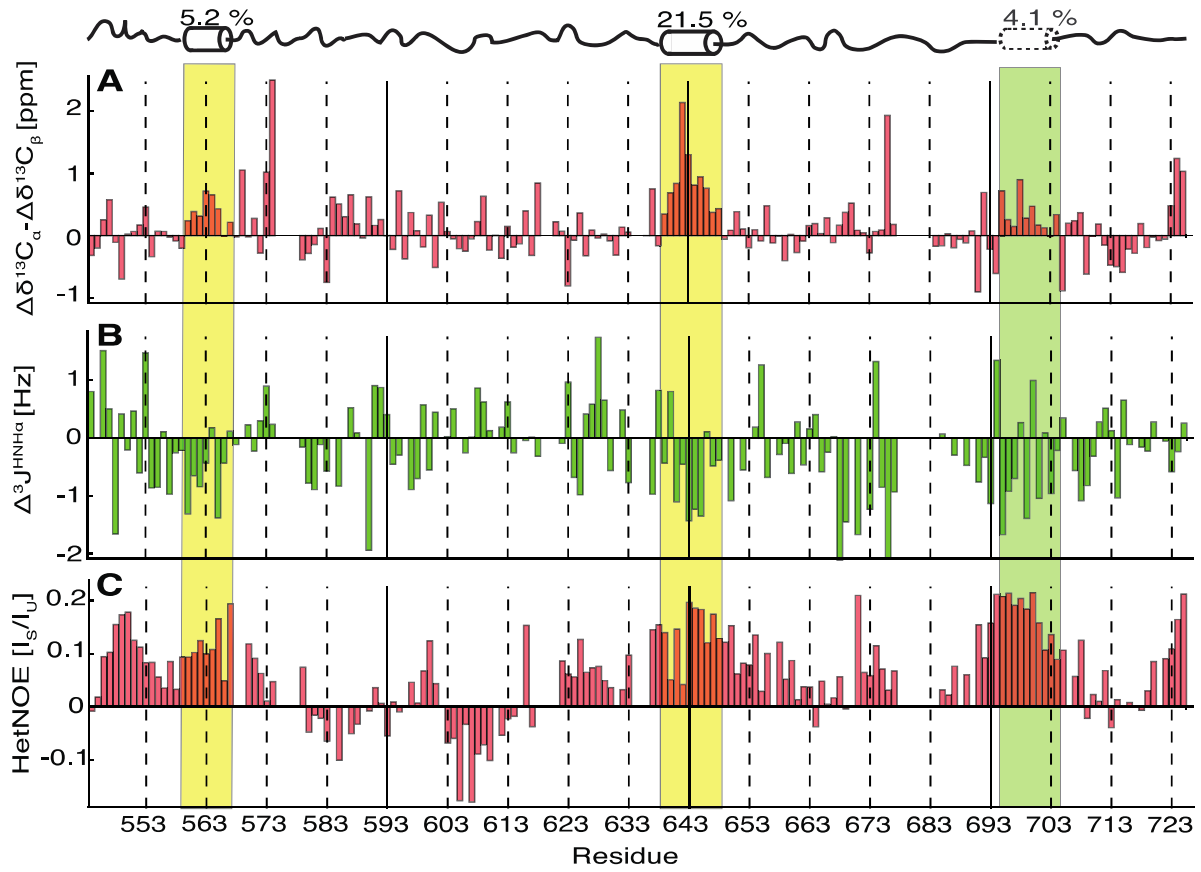

Fig. 3: Secondary structure and flexibility analysis of Nogo-A-Δ20. A, Combined secondary chemical shifts of $^{13}C^{\alpha}$ and $^{13}C^{\beta}$ denoted [$\Delta\delta^{13}C^{\alpha}$-$\Delta\delta^{13}C^{\beta}$]. Values exceeding ± 2 ppm over several consecutive residues indicate a fully formed secondary structure (Tanja Mittag & Forman-Kay, 2007). Here, all values but two (Pro574, Asn642) are smaller than ± 2 ppm. B: $\Delta^3J_{HNH\alpha}$ derived from the difference between $^3J_{HNH\alpha}$ measured from intensity modulated [^{15}N,^1H]-HSQC experiments and corresponding random coil values. Negative Δ3JHNHα indicate an α-helical while positive values indicate an extended conformation, respectively. C: $^{15}N\{^1H\}$-HetNOEs. A value near 1 indicates a fully rigid conformation; smaller values indicate a more flexible structure, values close to zero indicate the presence of ~1 ns dynamics, while negative values indicate the presence of even faster motion. Most of the values are positive between the ratios 0.1-0.2. Only two consecutive strands between the residues 580-588 and 603-614 have negative values. The locations and secondary structure propensity of α-helices as determined by NMR (see text) are indicated above the diagrams. The dotted cylinder/green box indicates a possible helical secondary structure that is only weakly supported by the NMR data such us a segment of only slightly positive [$\Delta\delta^{13}C^{\alpha}$-$\Delta\delta^{13}C^{\beta}$] values. Residues belonging to the affinity tags flanking Nogo-A-Δ20 are not plotted.

small positive [$\Delta\delta^{13}C^{\alpha}$ -$\Delta\delta^{13}C^{\beta}$] values for several consecutive residues indicating a significant α-helical propensity. Those two stretches relate well to two α-helices that were predicted *in silico* by PSIPRED 3.3V (Jones, 1999) (residues 561-567 and 637-648) (Fig. S3). For the third α-helix predicted with high confidence (comprising residues 695-704), only slightly positive combined [$\Delta\delta^{13}C^{\alpha}$-$\Delta\delta^{13}C^{\beta}$] values are found supporting partly the presence of a residual helical structure of residues ^{695}YSEIAKFEKS^{704}. To estimate the secondary structure propensity of the three structural helical elements, the observed secondary chemical shifts were normalised to corresponding values determined from regular secondary structure. By doing so, helix segment 1 is proposed to be 5.2% populated, helix segment 2 21.5% and helix segment 3 4.1%, respectively (Fig. 3).

In order to strengthen the proposed helical propensity of the three segments the scalar couplings $^3J_{HNH\alpha}$ were measured. Secondary scalar couplings, $\Delta^3J_{HNH\alpha}$, were calculated by subtracting random-coil values (Plaxco et al., 1997) from the experimentally measured $^3J_{HNH\alpha}$ data.

While positive $\Delta^3J_{HNH\alpha}$ values show a tendency for β-sheets, negative values indicate turns or α-helical propensities (Lam and Hsu, 2003). All the three stretches ^{560}SEAIQESL^{567}, ^{639}EAMNVALKAL^{648}, and ^{95}YSEIAKFEKS^{704} proposed to be α-helical according to the combined secondary chemical shift values, have negative $\Delta^3J_{HNH\alpha}$ values, supporting the presence of transient α-helices in these segments (Fig. 3B).

An independent measure of both disorder and secondary structure can be obtained by ^{15}N{^{1}H}-heteronuclear NOEs (HetNOE). While positive values close to 1 indicate structural rigidity of the backbone ^{15}N-^{1}H moieties, values close to zero indicate a dynamic in the range of ~ 1ns, and ^{15}N-^{1}H moieties with negative values are highly flexible (with a dynamic faster than ~ 1 ns) (Clore et al., 1990; Eliezer et al., 1998). Most of the values of Nogo-A-Δ20 are slightly positive between 0.1 and 0.2, and extended runs of positive values were especially found at the locations of all three proposed α-helical stretches. Overall, the HetNOE data indicate a highly flexible state for Nogo-A-Δ20, as commonly found in intrinsically disordered polypeptides (IDPs) (Mukrasch et al., 2009; Oldfield and Dunker, 2014).

Titration of S1PR2 Fragments to Nogo-A-Δ20

It has been shown that Nogo-A-Δ20 binds to isolated extracellular loops (ECL) 2 and 3 of sphingosine 1-phosphate receptor 2 (S1PR2) with affinities in the nanomolar range for ECL2 and ECL3 (Kempf et al., 2014). In order to identify the interaction between ECL peptides and Nogo-A-Δ20 at atomic resolution ligand titration studies were investigated by NMR spectroscopy.

First, ECL2 was titrated to ^{15}N-labeled Nogo-A-Δ20 at different molar ratios. A [^{15}N, ^{1}H]-HSQC spectrum with a resolution of was measured for each titration step at 6 °C and pH 7.4 including the reference without any addition of ECL2 (Fig. 4 and Fig. S4). Even with a threefold excess of ECL2, no cross peak shifts were detected when compared with the corresponding spectrum in absence of ECL2 (Fig. 4C and Fig. S4C). Normalized chemical shift changes of Nogo-A-Δ20 on average of 0.001 ppm were observed. These values are below the detection resolution of 0.02 pm, indicating that no conformational changes were detected upon ECL2 addition. Since pronounced chemical shift changes were observed for several peaks of Nogo-A-Δ20 upon decreased pH (Fig. S5), it was assumed that a lower pH might be necessary for binding. However, a reduction of pH from 7.4 to 6.4 did not result in any peak shifts upon ECL2 titration (Fig. 4B and Fig. S4B). Furthermore, a temperature increase from 6 °C to 15 °C to match the conditions of a previously published binding studies more closely (Kempf et al., 2014) did not result in any peak shifts upon ECL2 titration (Fig. 4D and Fig. S4D). Subsequently, Nogo-A-Δ20 was investigated upon ECL3 titration. Again, no peak shifts could be detected (Fig. 4E and Fig. S6A). Since the presence of zinc ions increases the α-helical content of Nogo-A-Δ20 (Li et al., 2004), up to 4 mM zinc ions were added to the sample. However, no changes in the spectra could be detected upon ECL3 addition,

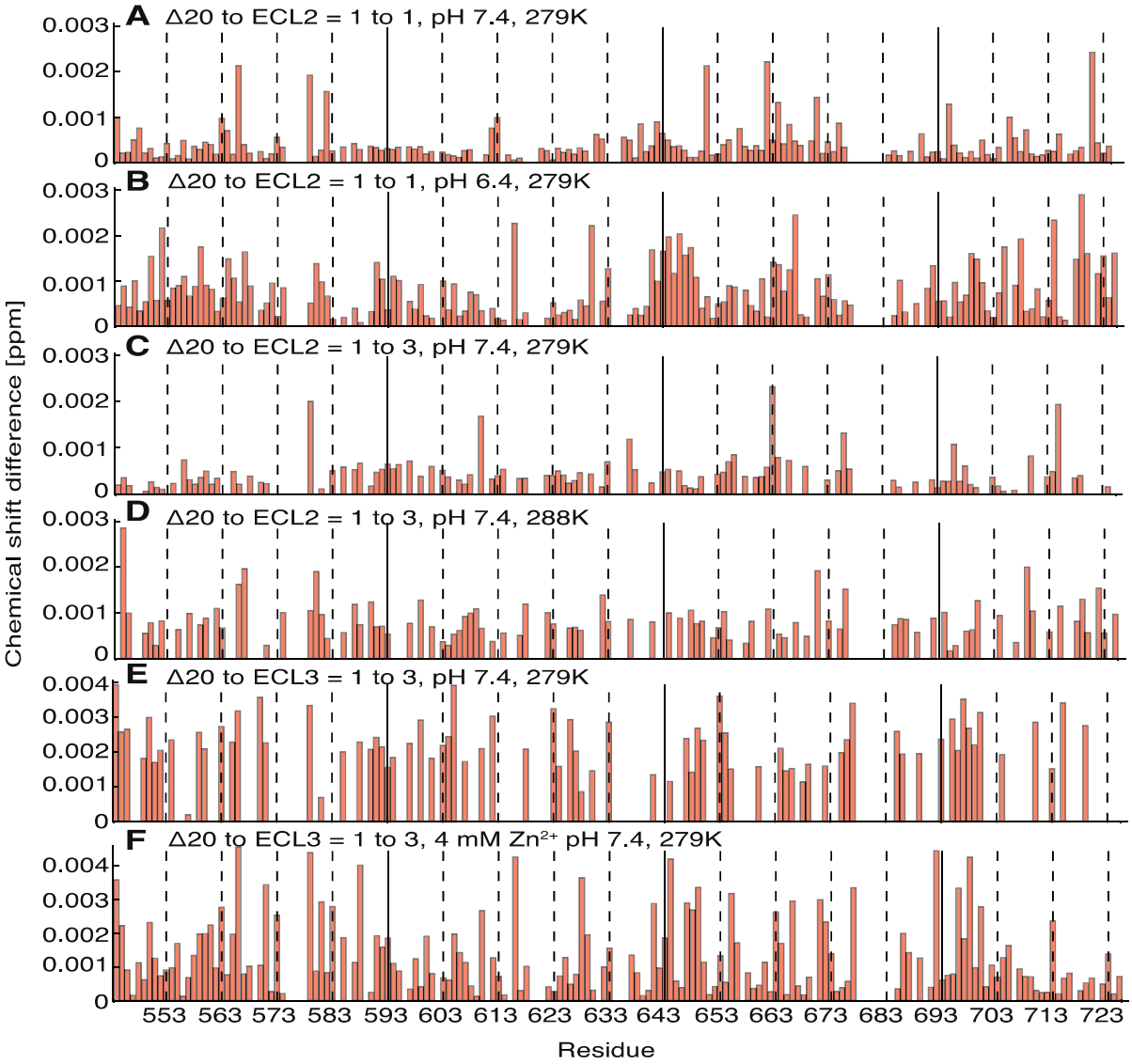

Fig. 4: Chemical shift perturbations upon titration of ECLs of S1PR2 to Nogo-A-Δ20. A, Nogo-A-Δ20 chemical shift difference (CSD) between free Nogo-A-Δ20 and Nogo-A-Δ20 in presence of equimolar ECL2: 1 to 1 ratio (ECL2) at pH 7.4 and 6 °C. **B**, 1 to 1 ratio (ECL2) at pH 6.4 and 6 °C. **C**, 1 to 3 ratio (ECL2) at pH 7.4 and 6 °C. **D**, 1 to 3 ratio (ECL2) at pH 7.4 and 15 °C. **E**, 1 to 3 ratio (ECL3) at pH 7.4 and 6 °C. **F**, 1 to 3 ratio (ECL3) at pH 7.4 and 6 °C in the presence of 4 mM zinc ions Zn^{2+}. The average chemical shift difference is around 0.001 ppm indicating no chemical shift changes of Nogo-A-Δ20 protein upon ligand titration.

indicating that zinc ions do not facilitate ECL binding (Fig. 4F and Fig. S6B). Finally, as FC12 is required for folding of Nogo-66 (Vasudevan et al., 2010), we explored the possibility whether Nogo-A-Δ20 only binds to ECL2 in the presence of FC12. However, no changes in the Nogo-A-Δ20 CD spectrum were observed in the presence of ECL2 (Fig. 1). The missing shifts of [^{15}N,^{1}H]-HSQC peaks might be explained by an intermediate exchange of the bound and unbound state. In this time regime, decreases of intensities of the amino acid residues participating in an interaction are anticipated. Therefore, the intensity ratio of Nogo-A-Δ20 in the presence vs. absence of ECL2 and ECL3 was calculated for each residue (Fig. 5). The intensity ratios at pH 7.4 at 6 °C were found to have a random distribution near 1 for the Nogo-A-Δ20 to ECL2 ratios of 1 to 1 and 1 to 3, indicating

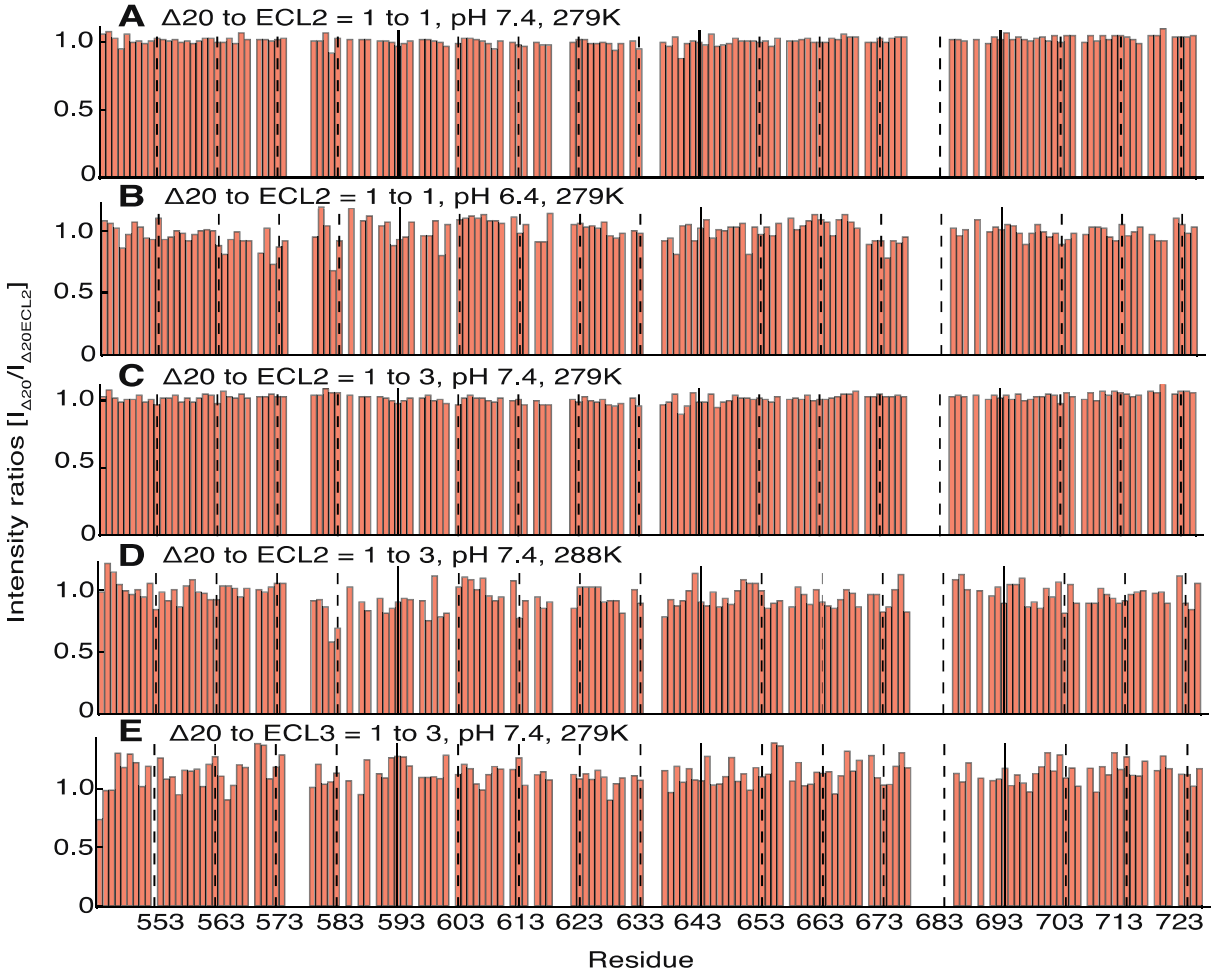

Fig. 5: Intensity ratios between Nogo-A-Δ20 in the presence vs. absence of ECLs. A, 1 to 1 ratio (ECL2) at pH 7.4 and 6 °C. **B**, 1 to 1 ratio (ECL2) at pH 6.4 and 6 °C. **C**, 1 to 3 ratio (ECL2) at pH 7.4 and 6 °C. **D**, 1 to 3 ratio (ECL2) at pH 7.4 and 15 °C. **E**, 1 to 3 ratio (ECL3) at pH 7.4 and 6 °C. The values are corrected for the volume decrease upon ligand titration. The average intensity ratios of A and B are near 1, while for B and D the average has a larger deviation from 1, which might be explained by imperfectly tuned pH and temperature.

no intermediate exchange. Intensity ratios at pH 6.4 at 6 °C and at pH 7.4 at 15 °C upon addition of ECL2 and the intensity ratio at pH 7.4 at 6 ° upon addition of ECL3 have a larger deviation from the value 1, which might be rather attributed to an imperfect adjustment of pH and temperature than ECL binding.

Cellular Activity Assay for Nogo-A-Δ20

In order to confirm that the obtained structural data correspond to a biologically active protein, and in order to exclude that the lack of peak shifts upon ECL titration was due to misfolding of Nogo-A-Δ20, we performed a 3T3 fibroblast spreading assay (Fig. 6). Fibroblast spreading was markedly inhibited on isotopically labelled Nogo-A-Δ20 substrate, confirming intact inhibitory activity of the protein. Importantly, the IC50 value was ~40 pmol/cm^2, which is a typical potency for Nogo-A-Δ20-induced inhibition of 3T3 fibroblast spreading (Schmandke et al., 2013).

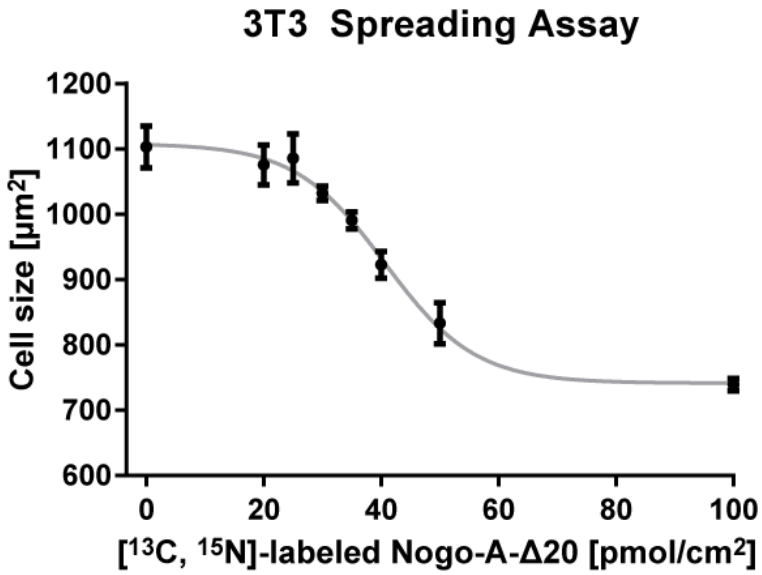

Fig. 6: Activity assay of [^{13}C, ^{15}N]-labelled Nogo-A-Δ20. 3T3 fibroblasts were plated on Nogo-A-Δ20 or control substrate for 1 h and fixed with paraformaldehyde. Non-linear regression reveals an IC_{50} value of ~40 pmol/cm^2. Mean cell size ± standard deviation from three wells is shown for each concentration.

In summary, the Nogo-A-Δ20 segment is an intrinsically disordered domain as indicated by CD data, [^{15}N, ^{1}H]-HSQC peak dispersion, secondary chemical shift analysis and dynamic studies. Within the disordered region, three contiguous segments of α-helical stretches are found. All agree well with those indicated by a computational algorithm. While titration of ECL2 and ECL3 to Nogo-A-Δ20 did not induce pronounced peak shifts in [^{15}N,^{1}H]-HSQC spectra, the used batch of Nogo-A-Δ20 was found to be active in a 3T3 fibroblast spreading assay.

Discussion

We investigated Nogo-A-Δ20 using CD and NMR spectroscopy. We were able to obtain high-quality NMR spectra for backbone assignment, which enabled us to obtain structural data with atomic resolution. Our data show a high degree of disorder within the neurite growth and cell spreading inhibitory Nogo-A-Δ20 region. The largely random coil CD spectrum and narrow proton dispersion in [^{15}N, ^{1}H]-HSQC spectra confirm previous observations (Li and Song, 2007) and are extended by the experimentally obtained secondary structure analysis of $\Delta\delta^{13}C^{\alpha}$ and $\Delta\delta^{13}C^{\beta}$ secondary chemical shifts, $^{3}J_{HNH\alpha}$ scalar coupling, as well as the high degree of flexibility indicated by HetNOE measurements. Importantly, despite the lack of fully structured regions, isotopically labelled and thrombin-cleaved Nogo-A-Δ20 exerted its typical inhibitory activity in a 3T3 fibroblast spreading assay.

Structural flexibility imposes a variety of advantages on proteins, ranging from an enlarged interaction surface and thus higher binding specificity to an elevated promiscuity towards binding partners (Berlow et al., 2015; Tompa, 2003; Uversky, 2013). As a consequence, IDPs are involved in a multitude of signalling pathways and appear in all three domains of life, i.e., Archaea, Bacteria,

and Eukarya (Dunker et al., 2015). The intrinsically disordered Nogo-A-Δ20 has been shown to interact with various binding partners, such as S1PR2, heparan sulfate proteoglycans, tetraspanin-3 and β1-integrins (Hu and Strittmatter, 2008; Kempf, 2013; Kempf et al., 2014; Shypitsyna et al., 2011; Thiede-Stan et al., 2015). In addition, clustering of N-terminal Nogo-A fragments including Nogo-A-Δ20 has been described to enhance their inhibitory potency (Fournier et al., 2001; Hu and Strittmatter, 2008). A high degree of flexibility might therefore represent an important structural feature of this domain, increasing its surface area available for binding molecular target proteins and homodimerisation. Additionally, Nogo-A is a multifaceted player implicated in neurite outgrowth inhibition, CNS development, synaptic plasticity, ER membrane morphology, and several other processes by interacting with several binding partners and multisubunit receptors (Kempf and Schwab, 2013; Schwab, 2010; Schwab and Strittmatter, 2014). Structural disorder could therefore allow different sets of interacting molecules to bind to the same sites within Nogo-A-Δ20 depending on the context, a model referred to as functional moonlighting (Tompa et al., 2005).

Although no fully structured regions were found, we present three regions within Nogo-A-Δ20 that appear to form transient and dynamical α-helical structures: ^{560}SEAIQESL^{567}, ^{639}EAMNVALKAL^{648}, and ^{695}YSEIAKFEKS^{704}. Significant residual secondary structures are commonly found in IDPs, and they often resemble structural characteristics present in the bound state (Fuxreiter et al., 2004; Song et al., 2008; Tompa, 2005; Tsai et al., 2001; Zhang et al., 2012). It has therefore been suggested that these residual structures are involved in initial molecular recognition (Fuxreiter et al., 2004; Tsai et al., 2001). One could speculate that the α-helical structures found in Nogo-A-Δ20 also serve as such recognition sparks, forming initial contact with binding partners. Adjacent unstructured regions could then confer higher specificity to the interaction. Strikingly, ^{560}SEAIQESL^{567} is located in direct juxtaposition with one of the most conserved domains of Nogo-A-Δ20 (residues 554-559) that harbours a β1-integrin binding motif (Fig. S1)) (Shypitsyna et al., 2011). Similarly, ^{639}EAMNVALKAL^{648} partially overlaps with the binding epitope for the Nogo-A-neutralizing antibody 11C7 (residues 630-640) that has been shown to enhance recovery from spinal cord injury in rats and macaques (Freund et al., 2006; Liebscher et al., 2005).

No peak perturbations could be observed upon titration of ECL2 or ECL3. This is surprising, as the two peptides have been shown to bind Nogo-A-Δ20 with K_D values of ~280 nM and ~350 nM, respectively (Kempf et al., 2014). These affinities were determined with both binding partners in solution using microscale thermophoresis (MST), which should closely resemble sample conditions in the NMR experiments. In contrast to NMR spectroscopy, MST determines the diffusion coefficient of a labelled molecule as a function of the concentration of its binding partner. The diffusion coefficient is susceptible to various parameters such as buffer composition or size, charge, hydration shell or conformation of a molecule (Jerabek-Willemsen et al., 2011). Therefore,

not only molecular interactions are measured via MST, but also conformational changes or charge variations upon slight changes in the buffer conditions within the titration experiment such as pH, which do not have to be induced by ligand binding.

However, there are also experimentally studied IDPs which remain completely disordered even when bound to their molecular targets (Mittag et al., 2008; Pometun et al., 2004; Sigalov et al., 2004; Simon et al., 2008). These IDPs are thought to only form transient contacts with their respective binding partners, which do not lead to folding (Fuxreiter and Tompa, 2012). The same might be the case for Nogo-A-Δ20 when bound to the ECLs. The observation of no distinguishable peak shifts might be explained by unspecific binding, or by a large population difference between bound and unbound states in a slow conformational exchange, only with peaks observable for the large population, e.g. unbound state. None of the aforementioned cases would produce observable peak shifts in the NMR spectra.

It should be noted that isolated ECLs might not represent the physiologically relevant conformation, where their structure is likely to be influenced by adjacent hydrophobic regions. Likewise, disulphide bonds are found between Nogo-A-Δ20 and other parts of Nogo-A (Fiedler et al., 2002; Zander et al., 2007), suggesting that additional structural components might be needed for a native overall structure. Therefore, it cannot be ruled out that ECL2 and ECL3 do not bind to Nogo-A-Δ20 in the NMR setup.

In conclusion, we have shown that biologically active Nogo-A-Δ20, while unstructured in the majority of its sequence, contains three stretches with α-helical propensity. Whereas α-helices could be involved in initial recognition and presentation of disordered regions, structural flexibility of Nogo-A-Δ20 might be essential for specific interactions with a plethora of binding partners in cellular membranes, neuritic growth cones, at CNS synapses and in the ER. In addition, we could not detect any structural changes of Nogo-A-Δ20 upon titration of ECL2 or ECL3 by NMR. Whether this observation is based on a fuzzy binding or just the absence of binding in the NMR setup will have to be investigated by further studies. It will be fascinating to gain more insight on the structural basis of this clinically highly relevant molecule.

Material and Methods

Expression of Isotopically Labelled Nogo-A-Δ20

Rat Nogo-A-Δ20 (residues 544-725) was cloned into the pET28 vector containing a His_6-tag at each terminus and a T7-tag between the N-terminal His_6-tag and Nogo-A-Δ20 (Oertle et al., 2003). ^{15}N- or ^{13}C,^{15}N-labelled Nogo-A-Δ20 was expressed in One Shot BL21 (DE3) strain of *E. coli* in M9 minimal medium with max. 4 g/L D–glucose-$^{13}C_6$ (^{13}C > 99 %) or 8 g/L D-glucose-$^{12}C_6$ and 1 g/L ^{15}N-ammonium chloride ($^{15}NH_4Cl$, ^{15}N > 98 %) purchased from Sigma-Aldrich (Buchs,

Switzerland). Bacteria were grown at 37 °C at 100 rpm until the OD_{590} reached 1.2, transferred to 30 °C and induced with 1 mM IPTG. The fusion protein was expressed for 8 hours and cells were harvested by centrifugation. The wet pellet was stored at -80 °C.

Purification of Nogo-A-Δ20

All of the following purification steps were performed at 4 °C. A frozen pellet of 1 L of bacterial culture was thawed on ice and resuspended in 50 mL lysis buffer (20 mM NaH_2PO_4, 500 mM NaCl, 20 mM imidazole, pH 7.4). 0.5 mg/mL lysozyme, 0.5 mM PMSF, and 1 protease inhibitory tablet (Roche Diagnostics GmbH, Mannheim, Germany) were added. The lysate was stirred for 20 min. Cells were further disrupted by passing twice through a 110S microfluidizer (Microfluidics, Newton, Massachusetts, USA) at 40 PSI. The suspension was centrifuged at 40'000 rpm (125171 g) for 30 min (Optima L-90K Ultracentrifuge, rotor Ti-45, Beckman Coulter International, S.A., Nyon, Switzerland) to pellet cellular debris (cite Oertle:2003fj). The supernatant of the centrifugation was bound to 3 ml Ni-NTA Agarose from Qiagen (Merck KGaA, Darmstadt, Germany) via batch mode during 2 h. The Ni-NTA was washed with 30 ml lysis buffer, eluted with ca. 5 ml elution buffer (20 mM NaH_2PO_4, 500 mM NaCl, 500 mM imidazole, pH 7.4) via gravity flow and collected in 0.5 ml fractions. The elution buffer was exchanged to PBS buffer with a pre-packed and disposable PD-10 desalting column (GE Healthcare Life Sciences, Buckinghamshire, UK). To remove the N-terminal His_6-tag, bovine thrombin (Sigma-Aldrich, Buchs, Switzerland) was added to the desalted sample with the ratio of 2 NIH units of thrombin per ca. 1 mg desalted Nogo-A-Δ20 for 1 hour. The cleaved fusion protein was purified on a Highload™ 26/60, Superdex™ 75 column using an Äkta FPLC system (prep grade, GE Healthcare, Uppsala, Sweden).

To exclude batch-to-batch variations, 6 L of ^{15}N-labelled Nogo-A-Δ20 were expressed, purified, shock frozen in aliquots, and finally stored at -80 °C until usage for ECL titration.

CD spectroscopy

CD measurements were carried out on a Jasco J815. The spectra were scanned from 260-198 nm at 20 nm/min with 1 nm band-pass, 4 seconds integration and averaged over 2 repetitions. The measurements of Nogo-A-Δ20 were executed in PBS at 25 °C with a concentration of 10 µM. FC12 and ECL2 were added to final concentrations of 6.67 mM and 10 µM, respectively.

NMR spectroscopy

The concentration of isotopically labelled Nogo-A-Δ20 for the NMR measurements was between 80-400 µM in PBS buffer containing 95 % H_2O and 5 % D_2O at pH 7.4. The experiments were recorded on 600 MHz and 700 MHz Bruker NMR spectrometers (Bruker BioSpin AG, Faellanden,

Switzerland) equipped with either TCI or TXI cryoprobes. For the amino acid sequence assignment, a [^{15}N, ^{1}H]-HSQC and a set of four triple-resonance experiments were measured at 6 °C. The chemical shifts of the amide proton, the amide nitrogen, the $^{13}C^{\alpha}$ and $^{13}C^{\beta}$ were obtained using the triple-resonance experiments HNCA (80[F3] × 80[F2] × 1024[F1] complex data points, 16 number of scans, 0.8 s relaxation delay, WATERGATE for water suppression and gradient pulses) (Kay et al., 1990) and HNCACB (100[F3] × 80[F2] × 1024[F1] complex data points, 32 number of scans, 1 ms relaxation delay, preservation of equivalent path (PEP) sensitivity enhancement and gradient pulses) (Grzesiek and Bax, 1992). Additionally, an HNN spectrum was recorded connecting N_i to N_{i-1} and N_{i+1} (1024[F3] × 144[F2] × 256[F1] complex data points, 16 number of scans, 1 s relaxation delay with gradient enhancement) (Panchal et al., 2001). To correlate $^{1}H_{\alpha}$ to $^{13}C_{\alpha}$ and to N_i and N_{i-1}, a HCAN spectrum (124[F3] × 114[F2] × 1024[F1] complex data points, 16 number of scans, 1 s relaxation delay) using PEP was recorded (Gal et al., 2011), enabling assignment through proline residues.

The difference of the chemical shifts of the measured $\delta^{13}C^{\alpha}$ and $\delta^{13}C^{\beta}$ and random coil values (Kjaergaard and Poulsen, 2011) were calculated for the secondary chemical shift analysis. Combined [$\Delta\delta^{13}C^{\alpha}$-$\Delta\delta C^{\beta}$] values were calculated by subtracting the $\Delta\delta^{13}C^{\beta}$ from $\Delta\delta^{13}C^{\alpha}$. To estimate the secondary structure propensity of structural elements in Nogo-A-Δ20, the observed $\Delta\delta^{13}C^{\alpha}$ were normalised by the empirically determined secondary chemical shift of $\Delta\delta^{13}C^{\alpha}$ in regular secondary structure, summed up and normalised by the number of residues.

An intensity modulated [^{15}N, ^{1}H]-HSQC (Permi et al., 2000) was measured to obtain the $^{3}J_{HNH?}$ scalar couplings (16 number of scans, 1 s relaxation delay, 2τ = time for evolution of $^{3}J_{HNH?}$: 18 ms). The intensity ratios of the relation $I_m/I_d = \cos(\pi(^{3}J_{HNH?})2\,\tau)$ were used for the calculation of the coupling constant $^{3}J_{HNH?}$, I_m being the intensity of the modulated spectra and I_d that of decoupled ones. The experimentally obtained $^{3}J_{HNH?}$ was multiplied by a correction coefficient of the magnitude of 1.06 due to the different relaxation properties of the in- and antiphase magnetisation of the H^N compared to the H^{α} (Permi et al., 2000). The secondary scalar couplings, $\Delta^{3}J_{HNH\alpha}$, were calculated by subtracting the corresponding random-coil values (Plaxco et al., 1997) from the experimentally measured $^{3}J_{HNH\alpha}$ data.

The dynamics of Nogo-A-Δ20 were examined with a ^{15}N{^{1}H}-HetNOE experiment (8 number of scans, 6 s relaxation delay) (Clore et al., 1990). The HetNOE was calculated estimated by dividing I_S, the intensity of the saturated spectrum, by I_U, the intensity of the corresponding peak in the unsaturated spectrum, respectively.

For the ECL titration [^{15}N,^{1}H]-HSQC experiments were measured with a resolution of 124 [F2] × 1024 [F1] with a maximal evolution time of 140 ms and 210 ms for ^{15}N and ^{1}H frequency, respectively, yielding a resolution of 0.1 ppm and 0.007 ppm, respectively. The sequence of ECL2 is NCLNQLEACSTVLPLYAKHYVL and for ECL3 is SILLLDSTCPVRACPVLYK (purchased from JPT Peptide Technologies GmbH, Berlin, Germany). The concentration used for ^{15}N-labeled Nogo-A-Δ20

was 88 µM or 120 µM and the following ratios were measured: Nogo-A-Δ20 : ECL2: 1 : 1 and 1 : 3, Nogo-A-Δ20 : ECL3: 1:3. The sample for ECL2 titration was measured at different pH values (pH 7.4 and 6.4) and different temperatures (6 °C and 15 °C) in the presence or absence of the ligand. The sample for the ECL3 titration was measured at pH 7.4 at 6 °C in the presence or absence of 4 mM $ZnCl_2$ and the ligand. The chemical shift differences between the peaks of Nogo-A-Δ20 alone and those in presence of an ECL in the [^{15}N, ^{1}H]-HSQC were calculated using the following equation (Williamson, 2013):

$$CSD = \sqrt{0.5 \times \left[\left({}^{1}H_A - {}^{1}H_T \right)^2 + 0.14 \times \left({}^{15}N_A - {}^{15}N_T \right)^2 \right]}$$

where $^{1}H_A$ and $^{1}H_T$ are the ^{1}H chemical shifts of Nogo-A-Δ20 alone and in the presence of ECL, and $^{15}N_A$ and $^{15}N_T$ are the ^{15}N chemical shifts of Nogo-A-Δ20 alone and in the presence of ECL. The spectra were processed with Topspin 3.1 (Bruker) before analysis. The amino acid residue assignment was accomplished using the CcpNmr software (Vranken et al., 2005).

3T3 Fibroblast Spreading Assay

Four-well plates (Greiner BioOne GmbH, Frickenhausen, Germany) were coated overnight at 4 °C with a dilution series of [^{13}C, ^{15}N]-labelled Nogo-A-Δ20 in PBS, ranging from 0 to 100 pmol per cm^2 growth area. The next day, wells were washed three times with PBS. NIH 3T3 fibroblasts (ATCC, Wesel, Germany) were briefly trypsinised, plated on Nogo-A-Δ20 or plastic control substrate at 7'000 cells per cm^2, and incubated for 1 h at 37 °C and 5% CO_2. Cells were fixed with warm 4% paraformaldehyde (Sigma-Aldrich, Buchs, Switzerland) in PBS for 20 min at RT, and washed three times with PBS at RT. Permeabilisation/blocking buffer [2% normal goat serum (Jackson Laboratories, ME, USA), 0.2 % Triton-X100 (AppliChem, Damstadt, Germany), 0.004 % fish skin gelatine (Sigma-Aldrich, Buchs, Switzerland) in PBS at pH 7.4] was added for permeabilisation at 4 °C overnight. Cells were then incubated with DAPI (1:1000, Life Technologies, Carlsbad, CA, USA) and Alexa Fluor 488-labelled phalloidin (1:100, Life Technologies, Carlsbad, CA, USA) in permeabilisation/blocking buffer for 1 h at RT to stain nuclei and the actin cytoskeleton, respectively. Finally, cells were washed three times with PBS and coverslipped in fluorescence mounting medium (Dako Schweiz AG, Baar, Switzerland). An Axioskop 2 mot plus fluorescence microscope (Carl Zeiss AG, Feldbach, Switzerland) was used for automatic acquisition of DAPI and phalloidin images for 28 positions in each well. CellProfiler software was employed to measure the sizes of only non-clumped cells (Kamentsky et al., 2011). Finally, non-linear regression was performed in GraphPad Prism.

Acknowledgements

We thank Dr. Zorica Ristic for her expertise on Nogo-A-Δ20 expression and Dr. Jason Greenwald for assistance with the CD spectrometer.

References

Berlow, R.B., H.J. Dyson, and P.E. Wright. 2015. Functional advantages of dynamic protein disorder. *FEBS letters*.

Chen, M.S., A.B. Huber, M.E. van der Haar, M. Frank, L. Schnell, A.A. Spillmann, F. Christ, and M.E. Schwab. 2000. Nogo-A is a myelin-associated neurite outgrowth inhibitor and an antigen for monoclonal antibody IN-1. *Nature*. 403:434-439.

Clore, G.M., P.C. Driscoll, P.T. Wingfield, and A.M. Gronenborn. 1990. Analysis of the backbone dynamics of interleukin-1 beta using two-dimensional inverse detected heteronuclear 15N-1H NMR spectroscopy. *Biochemistry*. 29:7387--7401.

David, S., and A.J. Aguayo. 1981. Axonal elongation into peripheral nervous system "bridges" after central nervous system injury in adult rats. *Science*. 214:931-933.

Dodd, D.A., B. Niederoest, S. Bloechlinger, L. Dupuis, J.P. Loeffler, and M.E. Schwab. 2005. Nogo-A, -B, and -C are found on the cell surface and interact together in many different cell types. *The Journal of biological chemistry*. 280:12494-12502.

Dunker, A.K., S.E. Bondos, F. Huang, and C.J. Oldfield. 2015. Intrinsically disordered proteins and multicellular organisms. *Seminars in cell & developmental biology*. 37:44-55.

Eliezer, D., J. Yao, H.J. Dyson, and P.E. Wright. 1998. Structural and dynamic characterization of partially folded states of apomyoglobin and implications for protein folding. *Nature structural biology*. 5:148-155.

Fiedler, M., C. Horn, C. Bandtlow, M.E. Schwab, and A. Skerra. 2002. An engineered IN-1 F(ab) fragment with improved affinity for the Nogo-A axonal growth inhibitor permits immunochemical detection and shows enhanced neutralizing activity. *Protein engineering*. 15:931-941.

Fournier, A.E., T. GrandPre, and S.M. Strittmatter. 2001. Identification of a receptor mediating Nogo-66 inhibition of axonal regeneration. *Nature*. 409:341-346.

Freund, P., E. Schmidlin, T. Wannier, J. Bloch, A. Mir, M.E. Schwab, and E.M. Rouiller. 2006. Nogo-A-specific antibody treatment enhances sprouting and functional recovery after cervical lesion in adult primates. *Nature medicine*. 12:790-792.

Fuxreiter, M., I. Simon, P. Friedrich, and P. Tompa. 2004. Preformed structural elements feature in partner recognition by intrinsically unstructured proteins. *Journal of molecular biology*. 338:1015-1026.

Fuxreiter, M., and P. Tompa. 2012. Fuzzy complexes: a more stochastic view of protein function. *Advances in experimental medicine and biology*. 725:1-14.

Gal, M., K.A. Edmonds, A.G. Milbradt, K. Takeuchi, and G. Wagner. 2011. Speeding up direct (15)N detection: hCaN 2D NMR experiment. *J Biomol NMR*. 51:497--504.

GrandPre, T., F. Nakamura, T. Vartanian, and S.M. Strittmatter. 2000. Identification of the Nogo inhibitor of axon regeneration as a Reticulon protein. *Nature*. 403:439-444.

Grzesiek, S., and A. Bax. 1992. An efficient experiment for sequential backbone assignment of medium-sized isotopically enriched proteins. *Journal of Magnetic Resonance (1969)*. 99:201 - 207.

Hu, F., and S.M. Strittmatter. 2008. The N-terminal domain of Nogo-A inhibits cell adhesion and axonal outgrowth by an integrin-specific mechanism. *The Journal of neuroscience : the official journal of the Society for Neuroscience*. 28:1262-1269.

Jerabek-Willemsen, M., C.J. Wienken, D. Braun, P. Baaske, and S. Duhr. 2011. Molecular interaction studies using microscale thermophoresis. *Assay and drug development technologies*. 9:342-353.

Jones, D.T. 1999. Protein secondary structure prediction based on position-specific scoring matrices. *Journal of molecular biology*. 292:195-202.

Kamentsky, L., T.R. Jones, A. Fraser, M.A. Bray, D.J. Logan, K.L. Madden, V. Ljosa, C. Rueden, K.W. Eliceiri, and A.E. Carpenter. 2011. Improved structure, function and compatibility for CellProfiler: modular high-throughput image analysis software. *Bioinformatics*. 27:1179-1180.

Kay, L.E., M. Ikura, R. Tschudin, and A. Bax. 1990. Three-dimensional triple-resonance \NMR\ spectroscopy of isotopically enriched proteins. *Journal of Magnetic Resonance (1969)*. 89:496 - 514.

Kempf, A. 2013. Identification and characterization of a nogo-A-specific receptor complex. ETH, Zèurich. 1 Band.

Kempf, A., and M.E. Schwab. 2013. Nogo-A represses anatomical and synaptic plasticity in the central nervous system. *Physiology*. 28:151-163.

Kempf, A., B. Tews, M.E. Arzt, O. Weinmann, F.J. Obermair, V. Pernet, M. Zagrebelsky, A. Delekate, C. Iobbi, A. Zemmar, Z. Ristic, M. Gullo, P. Spies, D. Dodd, D. Gygax, M. Korte, and M.E. Schwab. 2014. The sphingolipid receptor S1PR2 is a receptor for Nogo-a repressing synaptic plasticity. *PLoS biology*. 12:e1001763.

Kjaergaard, M., and F.M. Poulsen. 2011. Sequence correction of random coil chemical shifts: correlation between neighbor correction factors and changes in the Ramachandran distribution. *J Biomol NMR*. 50:157--165.

Lam, S.L., and V.L. Hsu. 2003. NMR identification of left-handed polyproline type II helices. *Biopolymers*. 69:270--281.

Li, M., J. Shi, Z. Wei, F.Y. Teng, B.L. Tang, and J. Song. 2004. Structural characterization of the human Nogo-A functional domains. Solution structure of Nogo-40, a Nogo-66 receptor antagonist enhancing injured spinal cord regeneration. *European journal of biochemistry / FEBS*. 271:3512-3522.

Li, M., and J. Song. 2007. The N- and C-termini of the human Nogo molecules are intrinsically unstructured: bioinformatics, CD, NMR characterization, and functional implications. *Proteins*. 68:100-108.

Liebscher, T., L. Schnell, D. Schnell, J. Scholl, R. Schneider, M. Gullo, K. Fouad, A. Mir, M. Rausch, D. Kindler, F.P. Hamers, and M.E. Schwab. 2005. Nogo-A antibody improves regeneration and locomotion of spinal cord-injured rats. *Annals of neurology*. 58:706-719.

Mi, S., X. Lee, Z. Shao, G. Thill, B. Ji, J. Relton, M. Levesque, N. Allaire, S. Perrin, B. Sands, T. Crowell, R.L. Cate, J.M. McCoy, and R.B. Pepinsky. 2004. LINGO-1 is a component of the Nogo-66 receptor/p75 signaling complex. *Nature neuroscience*. 7:221-228.

Mittag, T., and J.D. Forman-Kay. 2007. Atomic-level characterization of disordered protein ensembles. *Current opinion in structural biology*. 17:3--14.

Mittag, T., S. Orlicky, W.Y. Choy, X. Tang, H. Lin, F. Sicheri, L.E. Kay, M. Tyers, and J.D. Forman-Kay. 2008. Dynamic equilibrium engagement of a polyvalent ligand with a single-site receptor. *Proceedings of the National Academy of Sciences of the United States of America*. 105:17772-17777.

Mukrasch, M.D., S. Bibow, J. Korukottu, S. Jeganathan, J. Biernat, C. Griesinger, E. Mandelkow, and M. Zweckstetter. 2009. Structural polymorphism of 441-residue tau at single residue resolution. *PLoS biology*. 7:e34.

Novacek, J., L. Zidek, and V. Sklenar. 2014. Toward optimal-resolution NMR of intrinsically disordered proteins. *J Magn Reson*. 241:41--52.

Oertle, T., M.E. van der Haar, C.E. Bandtlow, A. Robeva, P. Burfeind, A. Buss, A.B. Huber, M. Simonen, L. Schnell, C. Brosamle, K. Kaupmann, R. Vallon, and M.E. Schwab. 2003. Nogo-A inhibits neurite outgrowth and cell spreading with three discrete regions. *The Journal of neuroscience : the official journal of the Society for Neuroscience*. 23:5393-5406.

Oldfield, C.J., and A.K. Dunker. 2014. Intrinsically disordered proteins and intrinsically disordered protein regions. *Annual review of biochemistry*. 83:553-584.

Panchal, S.C., N.S. Bhavesh, and R.V. Hosur. 2001. Improved 3D triple resonance experiments, HNN and HN(C)N, for HN and 15N sequential correlations in (13C, 15N) labeled proteins: application to unfolded proteins. *J Biomol NMR*. 20:135--147.

Park, J.B., G. Yiu, S. Kaneko, J. Wang, J. Chang, X.L. He, K.C. Garcia, and Z. He. 2005. A TNF receptor family member, TROY, is a coreceptor with Nogo receptor in mediating the inhibitory activity of myelin inhibitors. *Neuron*. 45:345-351.

Permi, P., I. Kilpelainen, A. Annila, and S. Heikkinen. 2000. Intensity modulated HSQC and HMQC: two simple methods to measure 3J(HNH)alpha in proteins. *J Biomol NMR*. 16:29--37.

Plaxco, K.W., C.J. Morton, S.B. Grimshaw, J.A. Jones, M. Pitkeathly, I.D. Campbell, and C.M. Dobson. 1997. The effects of guanidine hydrochloride on the 'random coil' conformations and NMR chemical shifts of the peptide series GGXGG. *J Biomol NMR*. 10:221--230.

Pometun, M.S., E.Y. Chekmenev, and R.J. Wittebort. 2004. Quantitative observation of backbone disorder in native elastin. *The Journal of biological chemistry*. 279:7982--7987.

Prinjha, R., S.E. Moore, M. Vinson, S. Blake, R. Morrow, G. Christie, D. Michalovich, D.L. Simmons, and F.S. Walsh. 2000. Inhibitor of neurite outgrowth in humans. *Nature*. 403:383-384.

Rezaei-Ghaleh, N., M. Blackledge, and M. Zweckstetter. 2012. Intrinsically disordered proteins: from sequence and conformational properties toward drug discovery. *Chembiochem : a European journal of chemical biology*. 13:930--950.

Schmandke, A., A. Schmandke, M.A. Pietro, and M.E. Schwab. 2013. An open source based high content screening method for cell biology laboratories investigating cell spreading and adhesion. *PloS one*. 8:e78212.

Schwab, M.E. 2010. Functions of Nogo proteins and their receptors in the nervous system. *Nature reviews. Neuroscience*. 11:799-811.

Schwab, M.E., and P. Caroni. 1988. Oligodendrocytes and CNS myelin are nonpermissive substrates for neurite growth and fibroblast spreading in vitro. *The Journal of neuroscience : the official journal of the Society for Neuroscience*. 8:2381-2393.

Schwab, M.E., and S.M. Strittmatter. 2014. Nogo limits neural plasticity and recovery from injury. *Current opinion in neurobiology*. 27:53-60.

Schwab, M.E., and H. Thoenen. 1985. Dissociated neurons regenerate into sciatic but not optic nerve explants in culture irrespective of neurotrophic factors. *The Journal of neuroscience : the official journal of the Society for Neuroscience*. 5:2415-2423.

Shao, Z., J.L. Browning, X. Lee, M.L. Scott, S. Shulga-Morskaya, N. Allaire, G. Thill, M. Levesque, D. Sah, J.M. McCoy, B. Murray, V. Jung, R.B. Pepinsky, and S. Mi. 2005. TAJ/TROY, an orphan TNF receptor family member, binds Nogo-66 receptor 1 and regulates axonal regeneration. *Neuron*. 45:353-359.

Shypitsyna, A., E. Malaga-Trillo, A. Reuter, and C.A. Stuermer. 2011. Origin of Nogo-A by domain shuffling in an early jawed vertebrate. *Molecular biology and evolution*. 28:1363-1370.

Sigalov, A., D. Aivazian, and L. Stern. 2004. Homooligomerization of the cytoplasmic domain of the T cell receptor zeta chain and of other proteins containing the immunoreceptor tyrosine-based activation motif. *Biochemistry*. 43:2049-2061.

Simon, S.M., F.J. Sousa, R. Mohana-Borges, and G.C. Walker. 2008. Regulation of Escherichia coli SOS mutagenesis by dimeric intrinsically disordered umuD gene products. *Proceedings of the National Academy of Sciences of the United States of America*. 105:1152-1157.

Song, J., L.W. Guo, H. Muradov, N.O. Artemyev, A.E. Ruoho, and J.L. Markley. 2008. Intrinsically disordered gamma-subunit of cGMP phosphodiesterase encodes functionally relevant transient secondary and tertiary structure. *Proceedings of the National Academy of Sciences of the United States of America*. 105:1505-1510.

Spera, S., and A. Bax. 1991. Empirical correlation between protein backbone conformation and C.alpha. and C.beta. 13C nuclear magnetic resonance chemical shifts. *Journal of the American Chemical Society*. 113:5490-5492.

Tews, B., K. Schonig, M.E. Arzt, S. Clementi, M.S. Rioult-Pedotti, A. Zemmar, S.M. Berger, M. Schneider, T. Enkel, O. Weinmann, H. Kasper, M.E. Schwab, and D. Bartsch. 2013. Synthetic microRNA-mediated downregulation of Nogo-A in transgenic rats reveals its role as regulator of synaptic plasticity and cognitive function. *Proceedings of the National Academy of Sciences of the United States of America*. 110:6583-6588.

Thiede-Stan, N.K., B. Tews, D. Albrecht, Z. Ristic, H. Ewers, and M.E. Schwab. 2015. Tetraspanin-3 is an organizer of the multi-subunit Nogo-A signaling complex. *Journal of cell science*.

Tompa, P. 2003. The functional benefits of protein disorder. *Journal of Molecular Structure: THEOCHEM*. 666–667:361-371.

Tompa, P. 2005. The interplay between structure and function in intrinsically unstructured proteins. *FEBS letters*. 579:3346-3354.

Tompa, P., C. Szasz, and L. Buday. 2005. Structural disorder throws new light on moonlighting. *Trends in biochemical sciences*. 30:484-489.

Tsai, C.J., B. Ma, Y.Y. Sham, S. Kumar, and R. Nussinov. 2001. Structured disorder and conformational selection. *Proteins*. 44:418-427.

Uversky, V.N. 2013. Intrinsic disorder-based protein interactions and their modulators. *Current pharmaceutical design*. 19:4191-4213.

Vasudevan, S.V., J. Schulz, C. Zhou, and M.J. Cocco. 2010. Protein folding at the membrane interface, the structure of Nogo-66 requires interactions with a phosphocholine surface. *Proceedings of the National Academy of Sciences of the United States of America*. 107:6847-6851.

Voeltz, G.K., W.A. Prinz, Y. Shibata, J.M. Rist, and T.A. Rapoport. 2006. A class of membrane proteins shaping the tubular endoplasmic reticulum. *Cell*. 124:573-586.

Vranken, W.F., W. Boucher, T.J. Stevens, R.H. Fogh, A. Pajon, M. Llinas, E.L. Ulrich, J.L. Markley, J. Ionides, and E.D. Laue. 2005. The CCPN data model for NMR spectroscopy: development of a software pipeline. *Proteins*. 59:687--696.

Wang, K.C., J.A. Kim, R. Sivasankaran, R. Segal, and Z. He. 2002. P75 interacts with the Nogo receptor as a co-receptor for Nogo, MAG and OMgp. *Nature*. 420:74-78.

Williamson, M.P. 2013. Using chemical shift perturbation to characterise ligand binding. *Prog Nucl Magn Reson Spectrosc*. 73:1--16.

Wishart, D.S., and B.D. Sykes. 1994. The 13C chemical-shift index: a simple method for the identification of protein secondary structure using 13C chemical-shift data. *J Biomol NMR*. 4:171--180.

Zander, H., E. Hettich, K. Greiff, L. Chatwell, and A. Skerra. 2007. Biochemical characterization of the recombinant human Nogo-A ectodomain. *The FEBS journal*. 274:2603-2613.

Zhang, W., D. Ganguly, and J. Chen. 2012. Residual structures, conformational fluctuations, and electrostatic interactions in the synergistic folding of two intrinsically disordered proteins. *PLoS computational biology*. 8:e1002353.

Supplement

560 567

527 GSHm asmtggqqmg RGS**TGTKIAY ETKV*DLV*QTS EAIQESL**YPT 570

571 **AQLC**PSFE**EA EATPSPVLP*D IV*MEAPLNSL LPSAGASVVQ PSVSPLEA**PP 620

639 648

621 **PVSYDSIKLE PEN**PP**PYEEA MNVALKAL**GT **KEGIKEPESF NAAVQETEAP** 670

695 704

671 **YISIAC*D***LIK ETK**LSTEPSP DFSNYSEIAK FEKS**VPEHAE **LVEDSSPESE** 720

721 **PVDLF**LEhhhhhh

Fig. S1: Sequential backbone assignment of Nogo-A-Δ20. Assigned residues are designated in black, unassigned ones in grey. Bold type indicates the Nogo-A-Δ20 segment; the His_6-tag and the T7-tag are indicated in lowercase. 94 % of the non-proline δC^{α} frequencies of 182 amino acid residues long protein were assigned. Residues with transient α-helical conformations according to the combined secondary chemical shift values [$\Delta\delta^{13}C^{\alpha}$-$\Delta\delta^{13}C^{\beta}$] are highlighted in yellow, those predicted to have α-helical conformation with only small positive combined $\Delta\delta^{13}C^{\alpha}$ and $\Delta\delta^{13}C^{\beta}$ chemical shift values are highlighted in green. Amino acid residues are numbered as found in the rat Nogo-A protein.

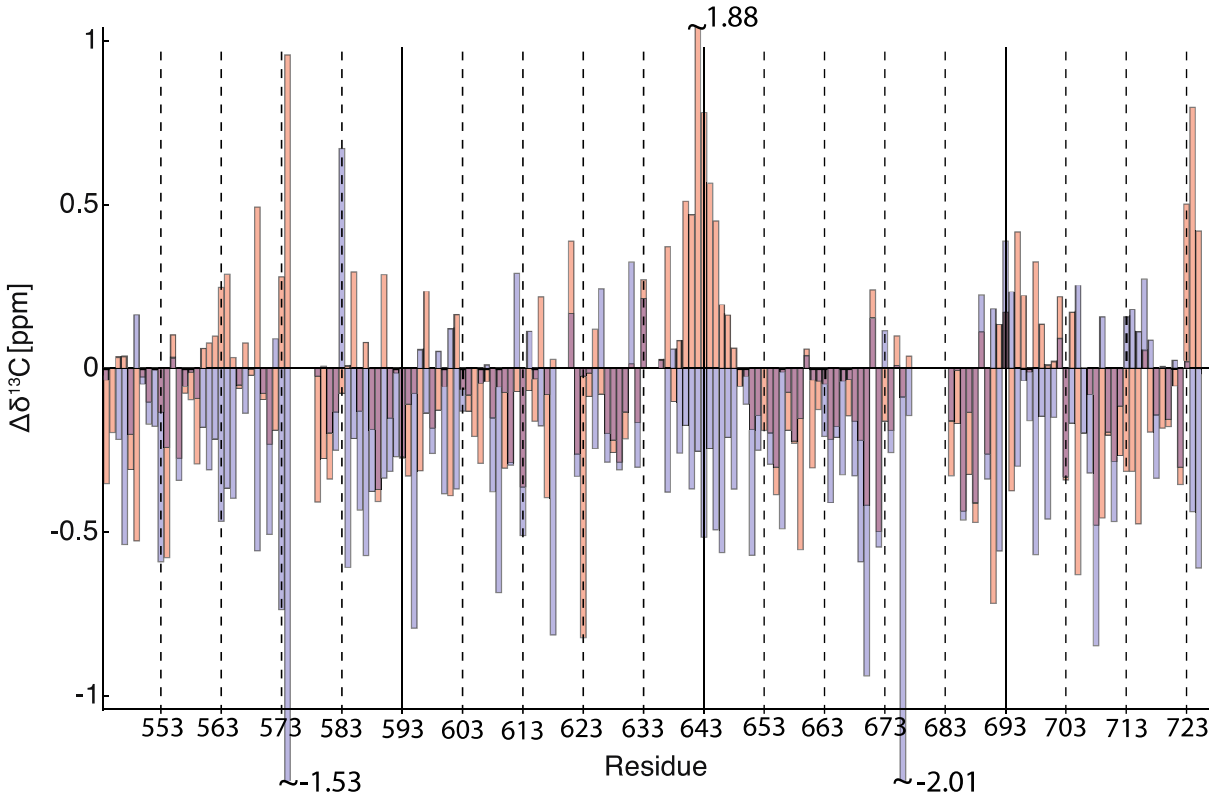

Fig. S2: Secondary chemical shift analysis. $\Delta\delta^{13}C^{\alpha}$ and $\Delta\delta^{13}C^{\beta}$ are shown individually in red and blue. Stretches of α-helical propensity are found at residues 560-567, 639-648, and possibly 695-704.

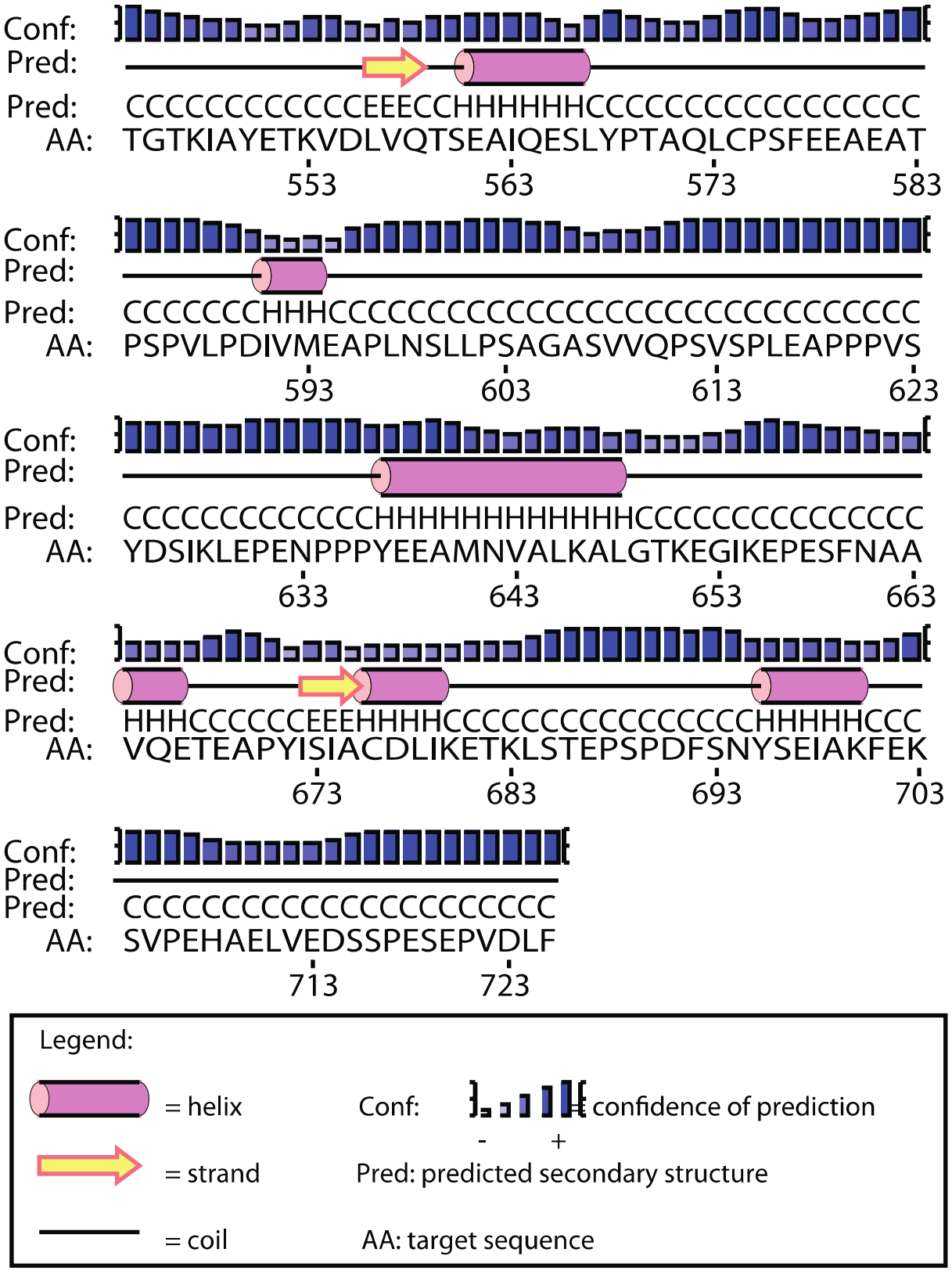

Fig. S3: PSIPRED 3.3V secondary structure prediction for Nogo-A-Δ20. Several α-helical domains and two β-strands are predicted with different confidence scores. Especially the α-helices around amino acid residues 563, 643 and 697 have elevated likeliness to occur.

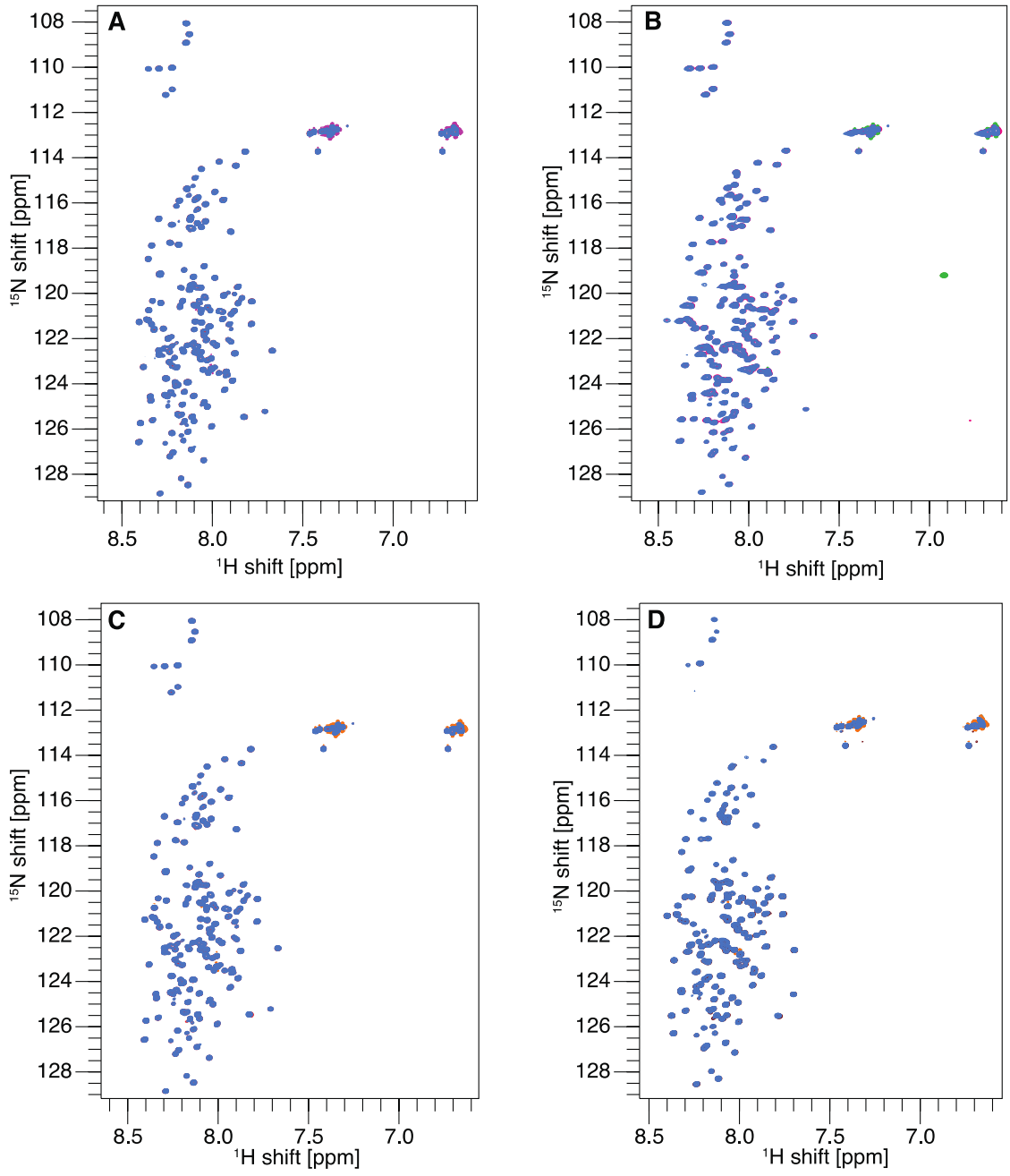

Fig. S4: [^{15}N, ^{1}H]-HSQC spectra of 88 µM Nogo-A-Δ20 alone and in the presence of ECL2 at different pH values and temperatures. For each subfigure the spectrum of Nogo-A-Δ20alone is shown in red contours, while the spectrum upon addition of an ECL fragment is color coded in blue. **A**: Nogo-A-Δ20 to ECL2 ratio of 1 to 1 at pH 7.4 and 6 °C. **B**: Nogo-A-Δ20 to ECL2 ratio of 1 to 1 at pH 6.4 and 6 °C. **C**: Nogo-A-Δ20 to ECL2 ratio of 1 to 3 at pH 7.4 and 6 °C. **D**: Nogo-A-Δ20 to ECL2 ratio of 1 to 3 at pH 7.4 and 15 °C. No significant peak shifts occurred upon ECL2 titration.

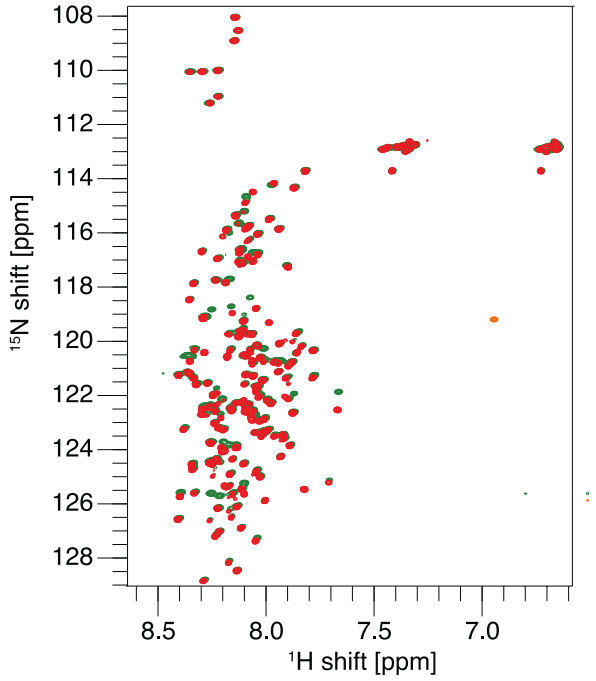

Fig. S5: [^{15}N, ^{1}H]-HSQC of Nogo-A-Δ20 at pH 7.4 and 6.4 at 6 °C. Red spectrum corresponds to Nogo-A-Δ20 at pH 7.4 and the green spectrum at pH 6.4. When comparing the spectra at pH 7.4 and 6.4 pronounced chemical shifts are observable.

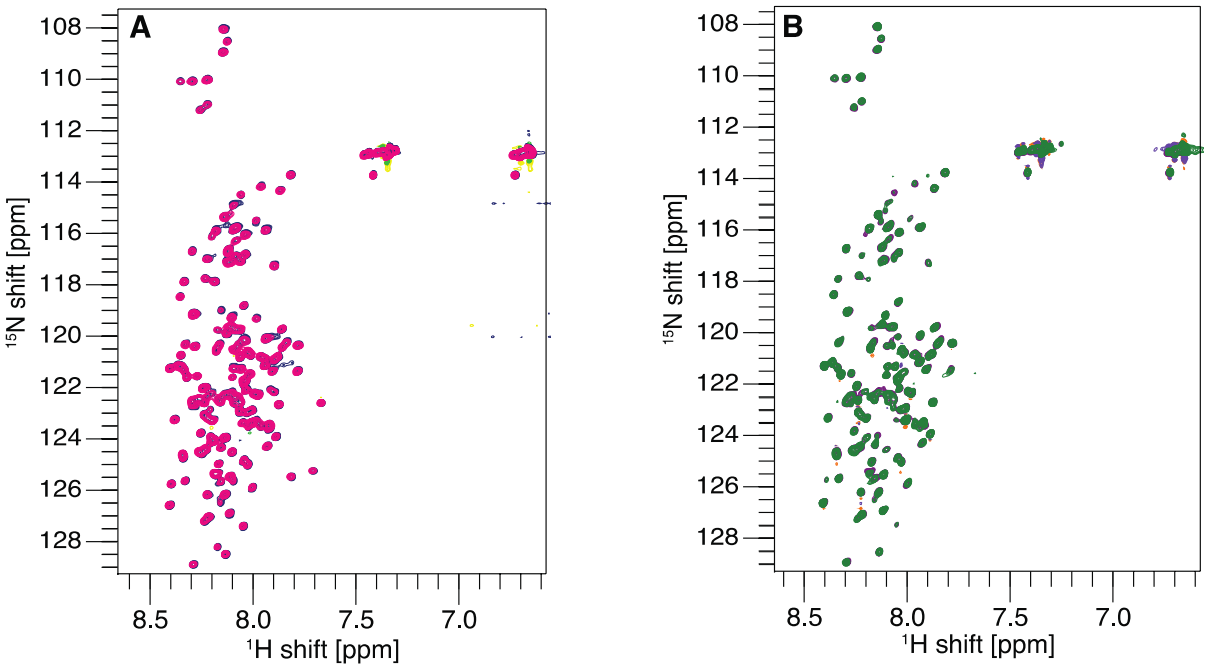

Fig. S6: [^{15}N, ^{1}H]-HSQC of 120 µM Nogo-A-Δ20 alone and in the presence of ECL3 at pH 7.4 and 6 °C. A. Nogo-A-Δ20 to ECL3 ratio of 1 to 3 at pH 7.4 and 6 °C. **B**, Nogo-A-Δ20 to ECL3 ratio of 1 to 3 at pH 7.4 and 6 °C in the presence of 4 mM Zn2+. Pink and green spectrum: Nogo-A-Δ20 alone and in the presence of zinc, respectively; blue and purple spectrum: Nogo-A-Δ20 in the presence of ECL2 and additionally zinc. No significant peak shifts occurred upon ECL3 titration in the presence or absence of zinc ions.

CHAPTER 5

TOWARD CRYSTALLIZATION OF SPHINGOSINE1-PHOSPHATE RECEPTOR 2

Michael E. Arzt[1,2], Chayne L. Piscitelli[3], Martin E. Schwab[1,4], Gebhard F. X. Schertler[2,3]

(unpublished manuscript)

M. E. A. designed, conducted, analyzed, and interpreted the experiments, wrote the manuscript, and prepared the figures.

[1] Brain Research Institute, University of Zurich, Switzerland
[2] Department of Biology, ETH Zurich, Switzerland
[3] Laboratory of Biomolecular Research, Paul Scherrer Institute, Villigen, Switzerland
[4] Department of Health Sciences and Technology, ETH Zurich, Switzerland

Abstract

G-protein coupled receptors (GPCRs) have attracted a lot of interest by basic biological research as well as by the pharmaceutical industry, as they are key regulators of many physiological and pathophysiological processes. Recent methodological advances have overcome former bottlenecks in GPCR structural biology, leading to an expanding list of solved crystal structures. Sphingosine 1-phosphate receptor 2 (S1PR2) is a pleiotropic class A GPCR that, among many other cellular roles, acts as a neuronal receptor for the neurite growth inhibitory protein Nogo-A. We aimed to crystallize S1PR2, adopting a published workflow that had led to the crystal structure of its close relative S1PR1 (Hanson et al., 2012). A homology screen of seven S1PR2 variants revealed that murine S1PR2 is expressed at highest levels with only moderate aggregation. N-linked glycosylation was observed on all S1PR2 homologs, resulting in two co-existing N-glycosylation isoforms in the mammalian variants. To facilitate S1PR2 crystallization, T4 lysozyme (T4L) was inserted at various positions within the third intracellular loop (ICL3). Interestingly, expression levels correlated with the site of insertion, exhibiting higher tolerance for T4L in more C-terminal positions of ICL3. However, no crystallization could be attempted up to now due to a marked heterogeneity of S1PR2 complex compositions.

Introduction

G-protein coupled receptors (GPCRs) are a large family of 7-transmembrane domain (TMD) proteins that comprise about 800 members in the human genome (Fredriksson et al., 2003; Fredriksson and Schioth, 2005). While this only makes up about 3% of all genes, GPCRs account for 40% of current pharmacological drug targets, and some pharma companies focus exclusively on these receptors (Filmore, 2004; Overington et al., 2006). Cells use GPCRs to sense a broad variety of external stimuli, ranging from photons to proteins (Dohlman, 2015). Activation of GPCRs elicits conformational changes in their cytoplasmic domains which then interact with intracellular heterotrimeric G proteins to propagate the signal (Rosenbaum et al., 2009). They trigger amplification cascades involving second messengers such as 3'-5'-cyclic adenosine monophosphate, diacylglycerol, or Ca^{2+}, leading to a diverse spectrum of cellular responses (Marinissen and Gutkind, 2001).

Sphingosine 1-phosphate receptor 2 (S1PR2) is a rhodopsin-like GPCR that exhibits very broad tissue distribution (Aarthi et al., 2011; Adada et al., 2013). It is best known as one of five GPCRs that are activated by sphingosine 1-phosphate (S1P), a ubiquitous sphingolipid that is involved in many cellular processes such as inflammation, proliferation, migration, and angiogenesis (Kim et al., 2009). We have recently identified S1PR2 as a novel receptor for Nogo-A, a myelin-associated inhibitory protein that prevents neurite growth and regeneration after spinal

cord injury or stroke (Kempf et al., 2014; Schwab, 2010). This interaction is the target of a neutralizing antibody blocking the inhibitory signal of Nogo-A which enhances fiber growth and promotes functional recovery after spinal cord injury in rats and macaques (Liebscher et al., 2005; Freund et al., 2007). Clinical trials are currently ongoing to test the concept of therapeutic anti-Nogo-A antibodies as a treatment in humans (Zörner et al., 2010).

Structural information about a molecule can serve as an invaluable template for rational drug design (Lescrinier, 2011). However, crystallization and structure determination of GPCRs has long been regarded almost impossible. From a crystallographic standpoint, an ideal protein would express to large quantities, be easy to purify, assume a relatively uniform conformation and cystallize into highly regular patterns. In contrast, GPCRs typically have low expression levels, are deeply embedded in the plasma membrane, and retain a high degree of conformational ambiguity, imposing several obstacles on GPCR crystallography. It is only with modern cell culture systems, sophisticated solubilization methods and protein engineering that these difficulties can be circumvented (Ghosh et al., 2015). The results are a total of 130 crystal structures from 31 different GPCRs that have been published to date (Isberg et al., 2014).

The structural characteristics of S1PR2 are widely unknown. In the absence of a crystal structure, architectural information can only be deduced from homology models built on the known structures of other GPCRs (Cavasotto and Phatak, 2009). Combination of such a model with mutagenesis experiments has located the binding pocket for S1P buried inside the seven TMDs of S1PR2 (Pham et al., 2008; Valentine et al., 2011). In contrast, the large Nogo-A-Δ20 domain seems to bind to the extracellular loops (ECLs) of the receptor (Kempf et al., 2014).

In 2012, the group of Ray Stevens successfully determined the crystal structure of S1PR1 (Hanson et al., 2012). As the conserved binding pocket of S1P is occluded by an α-helix in the N-terminus of S1PR1, it seems that S1P first inserts into the membrane and then diffuses laterally into the receptor. Whereas a similar mechanism could be imagined for binding of S1P to S1PR2, the structural features of the interaction between Nogo-A-Δ20 and this receptor are unknown. We therefore sought to crystallize S1PR2, adhering closely to the protocol described for S1PR1. First, a homolog library of S1PR2 from seven different species was established and tested for expression. Then, bacteriophage T4 lysozyme (T4L) was inserted into the intracellular loop 3 (ICL3) of S1PR2 for stabilization.

Materials and Methods

Bioinformatics

Multiple sequence alignment of S1PR2 homologs was achieved by CLUSTAL 2.1 (Larkin et al., 2007), and sequence comparison of S1PR1 and S1PR2 was performed using BLASTP (Altschul et

al., 1990). For visualization of S1PR1-T4L, coordinates were taken from PDB entry 3V2Y (Hanson et al., 2012), and a model was constructed in the PyMOL Molecular Graphics System, Version 1.3 Schrödinger, LLC.

Molecular Cloning of S1PR2 and S1PR2-T4L Libraries

Coding sequences of S1PR2 were cloned directly from murine brain tissue and human blood. In addition, the following homologs of S1PR2 were ordered as synthesized genes (Genewiz): *Bos taurus*, *Callithrix jacchus*, *Canis familiaris*, *Sus scrofa*, *Xenopus tropicalis*. All open reading frames (ORFs) were transferred to pCGFP-EU for CMV-driven overexpression with a C-terminal green fluorescent protein (GFP) tag (Fig. S1).

A cysteine-free mutant (C54T, C97A) of bacteriophage T4L lacking the initiation methionine and C-terminal three amino acids was inserted into ICL3 of murine S1PR2 by seamless fusion cloning (Matsumura, 2013). Briefly, T4L and the N-terminal and C-terminal moieties of S1PR2 were amplified by PCR with Phusion Hot Start II DNA polymerase (Life Technologies). For the S1PR2-T4LΔH220 construct, T4L from Asn2 to Tyr161 was inserted between Ser219 and Ala221 by use of the following primers: S1PR2-N-FWD, 5'-GCG CGA GCT CTC GAG A-3'; S1PR2-N-REV, 5'-GCT GGA GCG GAC TAC AAA GTA G-3'; T4L-FWD, 5'-CTA CTT TGT AGT CCG CTC CAG CAA TAT CTT CGA GAT GCT CCG C-3'; T4L-REV, 5'-GGA CCA GCA ACA TCC GCG TAG GCA TCC CAG GTG CC-3'; S1PR2-C-FWD, 5'-GCG GAT GTT GCT GGT CC-3'; S1PR2-C-REV, 5'-AGT CCT GCG TCG ACG AC-3'. T4L primers contained 5'-extensions that were complementary to the adjacent S1PR2 sequence in the desired fusion construct (underlined). These flanking regions acted as primers in a second round of PCR, where equimolar amounts of all three PCR products were combined without any additional primers. Only after 15 cycles, S1PR2-N-FWD and S1PR2-C-REV were added to favor amplification of the full-length construct. S1PR2-T4Lchim was constructed analogously, but included the sequence of ICL3 from S1PR1 in T4L-REV (italics): 5'-*GCT CTT CTC GCT GCT ACG GCT GGC* GTA GGC ATC CCA GGT GCC-3'. Accordingly, S1PR2-C-FWD was adapted with a 5'-extension (underlined) to act as a primer on the modified ICL3: 5'-CCG TAG CAG CGA GAA GAG CCT AGC CCT GCT CAA GAC GG-3'. The result was a chimeric construct comprising S1PR2 from its N-terminus to Ser219, T4L from Asn2 to Tyr161, Ala244 to Ser251 of S1PR1, and the C-terminal moiety of S1PR2 starting at Leu229 (S1PR2-T4Lchim). Full-length constructs were ligated into pJET2.1, transformed into One Shot TOP10 chemically competent *E. coli* (Life Technologies), and colonies were screened for a DNA insert of the correct size. ORFs were then sub-cloned into pCGFP-EU and sequenced.

T4L was further repositioned within ICL3 by site-directed mutagenesis (SDM) (Zheng et al., 2004). First, His220 that had been replaced by T4L in S1PR2-T4LΔH220 was re-introduced to the

N-terminal or C-terminal end of T4L, yielding S1PR2-T4L221 (T4L between His220 and Ala221) and S1PR2-T4L220 (T4L between Ser219 and His220), respectively. S1PR2-T4L219 was then created from S1PR2-T4L220 by two-step SDM: first, a serine was inserted at the C-terminal junction of T4L; and second, Ser219 adjacent to the N-terminus of T4L was deleted. This also yielded an intermediate construct with serines on both sides of T4L, termed S1PR2-T4L220S. SDM primers used were (insertions underlined, deletion junctions in italics): S1PR2-T4L219-SDM1-FWD, 5'-CCT ACA GCC ACG CGG ATG TTG C-3'; S1PR2-T4L219-SDM1-REV, 5'-GCG TGG CTG TAG GCA TCC CAG G-3'; S1PR2-T4L219-SDM2-FWD, 5'-GCT C*CA* ATA TCT TCG AGA TGC-3'; S1PR2-T4L219-SDM2-REV, 5'-ATA T*TG* GAG CGG ACT ACA AAG-3'; S1PR2-T4L220-SDM-FWD, 5'-CCT ACC ACG CGG ATG TTG CTG GTC CTC AGA CGC TAG C-3'; S1PR2-T4L220-SDM-REV, 5'-TCC GCG TGG TAG GCA TCC CAG GTG CCA GTA C-3'; S1PR2-T4L221-SDM-FWD, 5'-GTC CGa TCg AGC CAC AAT ATC TTC GAG ATG CTC CGC ATC G-3'; S1PR2-T4L221-SDM-REV, 5'-ATA TTG TGG CTc GAt CGG ACT ACA AAG TAG ATT CGG ACG TAC AGA GCC ACG ATA GCC-3'. In some instances, silent mutations could be introduced (lowercase) to generate restriction sites for easy mutant screening by restriction digestion. SDM products were transformed as described above, and colonies were screened for mutants by digestion or direct sequencing. Integrity of all ORFs was validated by DNA sequencing.

Evaluation of S1PR2 Expression levels

HEK293T cells [or, where indicated, HEK293S cells lacking glucose N-acetyltransferase 1, GNT1$^{-/-}$ (Reeves et al., 2002)] were maintained in Dulbecco's Modified Eagle Medium (DMEM) media containing high glucose and L-glutamine (BioConcept) containing 10% FBS at 37 °C and 5 % CO_2. Cells were seeded to 6-well plates at a density of 5x10^5 cells per well. The next day, cells were transfected with S1PR2 variants using a polyethylenimine (PEI) protocol. 3 µg of plasmid DNA were mixed with 6 µg of PEI in 1.5 ml DMEM without FBS. After 10 min of complex formation at room temperature, 900 µl DMEM and 600 µl DMEM containing 10% FBS were added, yielding a final FBS concentration of 2%. Media were aspirated from the cells, and the DNA-containing DMEM mix was added. The next day, media were replaced by fresh DMEM containing 10% FBS. 48 h after transfection, GFP fluorescence was examined under an Olympus IX81 inverted microscope. Cells were then detached with 10 mM EDTA in PBS, centrifuged at 1000 g for 5 min, resuspended in PBS, centrifuged again, and resuspended in 250 µl solubilization buffer [20 mM dodecyl maltoside (DDM), 2 mM cholesteryl hemisuccinate (CHS), Roche cOmplete EDTA-free protease inhibitors in PBS, pH 7.4]. Solubilization was achieved by rotation for 1 h at 4 °C. Finally, cellular debris was pelleted at 20'000 g for 20 min. Absorbance at 280 nm and GFP fluorescence (excitation 488 nm, emission 510 nm) were determined by fluorescence size exclusion chromatography (FSEC). For the S1PR2 homolog screen, 80 µl of the supernatant were loaded to

a Tricorn 10/200 Superdex S200 column. For the evaluation of S1PR2-T4L fusions, 10 µl were loaded to a Tosoh TSK gel Super SW3000 column. The running buffer was composed of 1 mM DDM and 0.1 mM CHS in PBS at pH 7.4. Additionally, expression levels were estimated by sodium dodecyl sulfate/polyacrylamide gel electrophoresis (SDS/PAGE), taking advantage of the fact that GFP retains fluorescence even in the presence of SDS and dithiothreitol (DTT). 16 µl of the supernatant were mixed with 4 µl of SDS/PAGE sampling buffer, loaded to a 10-20% Tris-glycine gel (Life Technologies), and run for 1 h 45 min at 125 V. GFP fluorescence was recorded in a GE Amersham RT ECL gel documentation system with blue LED epifluorescence illumination and a 510 nm long-pass emission filter. Where indicated, Coomassie staining was used as a loading control. Densitometry was performed in ImageJ (Schneider et al., 2012). In addition, GFP fluorescence of solubilized receptors was assessed on a NanoDrop 3300 (Thermo Scientific).

PNGase F Digestion of S1PR2

Peptide-N-glycosidase F (PNGase F) was recombinantly expressed and purified as described elsewhere (Grueninger-Leitch et al., 1996). Solubilized S1PR2 from *Mus musculus* and *Xenopus tropicalis* were incubated with PNGase F in SDS/PAGE buffer containing DTT at 35 °C for 2.5 h. SDS/PAGE was run as described above.

Results

Homolog screen of S1PR2

The first optimization step in S1PR2 expression was the choice of a homolog that is readily expressed in HEK293T cells. S1PR2 sequences of twelve species were considered for expression and were therefore compared in a multiple sequence alignment (Fig. 1). *Pongo abelii*, *Macaca mulatta*, and *Pan troglodytes* variants were found to share identical extracellular domains with human S1PR2 and were therefore neglected (Fig. 1A). Likewise, the homolog of *Rattus norvegicus* was nearly the same as the murine variant and was also excluded. *Danio rerio* S1PR2 featured an exceptionally long N-terminus, which would complicate any inferences on the human protein if a crystal structure were obtained (Fig. 1A). We therefore decided that an S1PR2 ensemble comprising *Bos taurus*, *Callithrix jacchus*, *Canis familiaris*, *Homo sapiens*, *Mus musculus*, *Sus scrofa*, and *Xenopus tropicalis* was sufficient to sample the S1PR2 sequence space (Fig. 1B).

We first compared expression levels of the different S1PR2 homologs as C-terminal GFP fusions in HEK293T cells. FSEC absorption profiles at 280 nm indicate that the solubilized S1PR2 homologs were loaded to the column in roughly equal protein amounts (Fig. 2A). Two major Gaussian peaks were observed in the GFP fluorescence traces of all homologs, one below 6 ml of

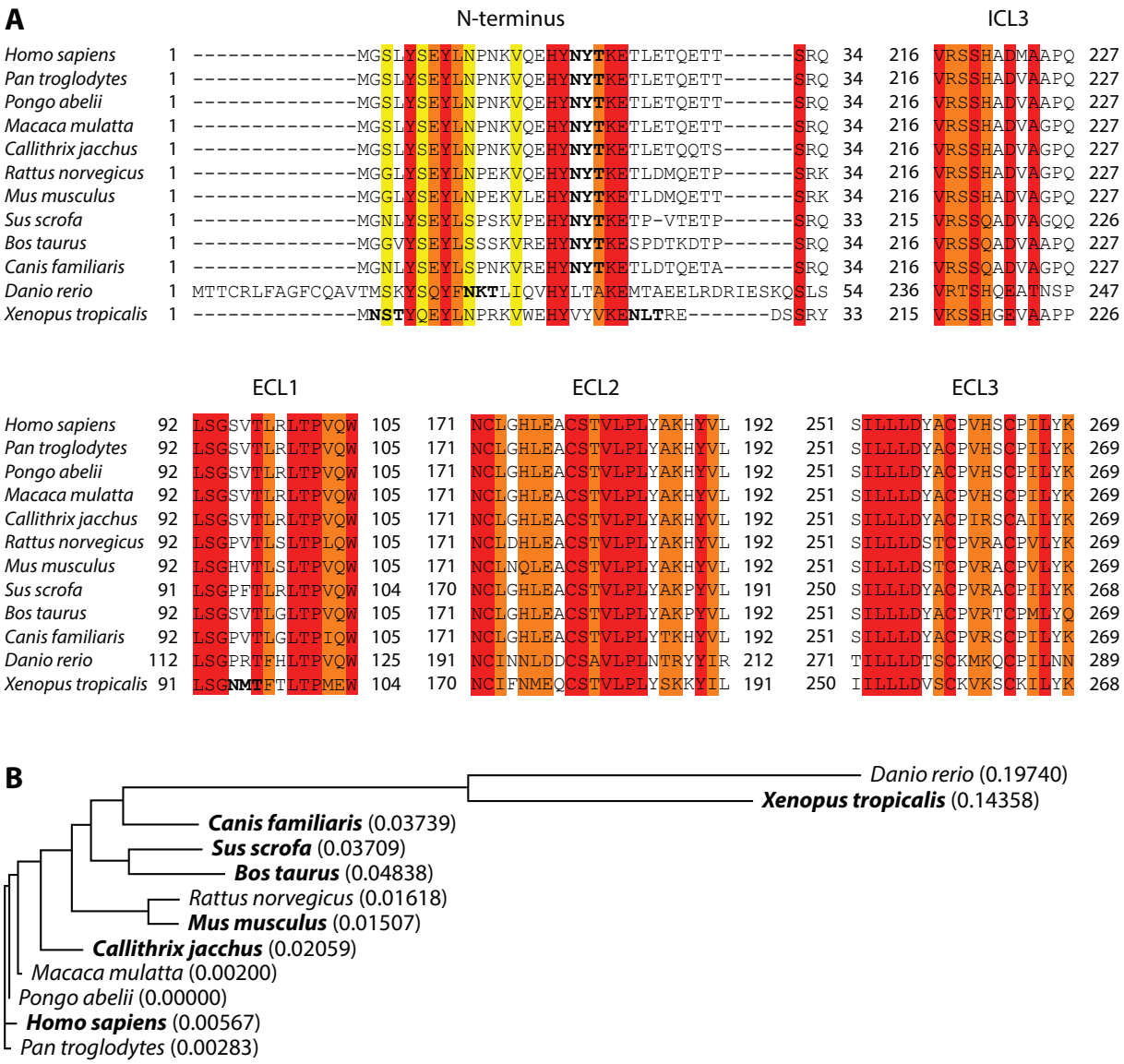

Fig. 1: S1PR2 homology across 12 species. A, Multiple sequence alignment is shown for the extracellular domains (N-terminus and ECL1-3), and for the designated T4L insertion site ICL3. N-X-S/T sequons for N-glycosylation are marked in bold type, and conserved residues are labeled (red: full conservation; orange: conservation between groups of strongly similar properties, Gonnet PAM250 score >0.5; yellow: conservation between groups of weakly similar properties, score =< 0.5). **B**, Phylogenetic tree over the whole S1PR2 sequence, indicating distances in parentheses. S1PR2 homologs chosen for expression studies are indicated in bold type.

elution volume, and one slightly above 8 ml (Fig. 2B and S3). Comparison with protein size standards suggests that the former is a void peak containing larger protein aggregates, while the latter supposedly corresponds to non-aggregated S1PR2 (Fig. S2A,B). A minor peak at ~12 ml could represent free GFP, as the constructs contain a thrombin cleavage site between S1PR2 and GFP (Fig. 2B). The S1PR2 peak was highest in constructs from *Callithrix jacchus* and *Mus musculus*, suggesting strong overexpression of these variants (Fig. 2B and Fig. S3). Among these two, the *Mus musculus* homolog exhibited a smaller void peak, which indicates a lower degree of aggregation.

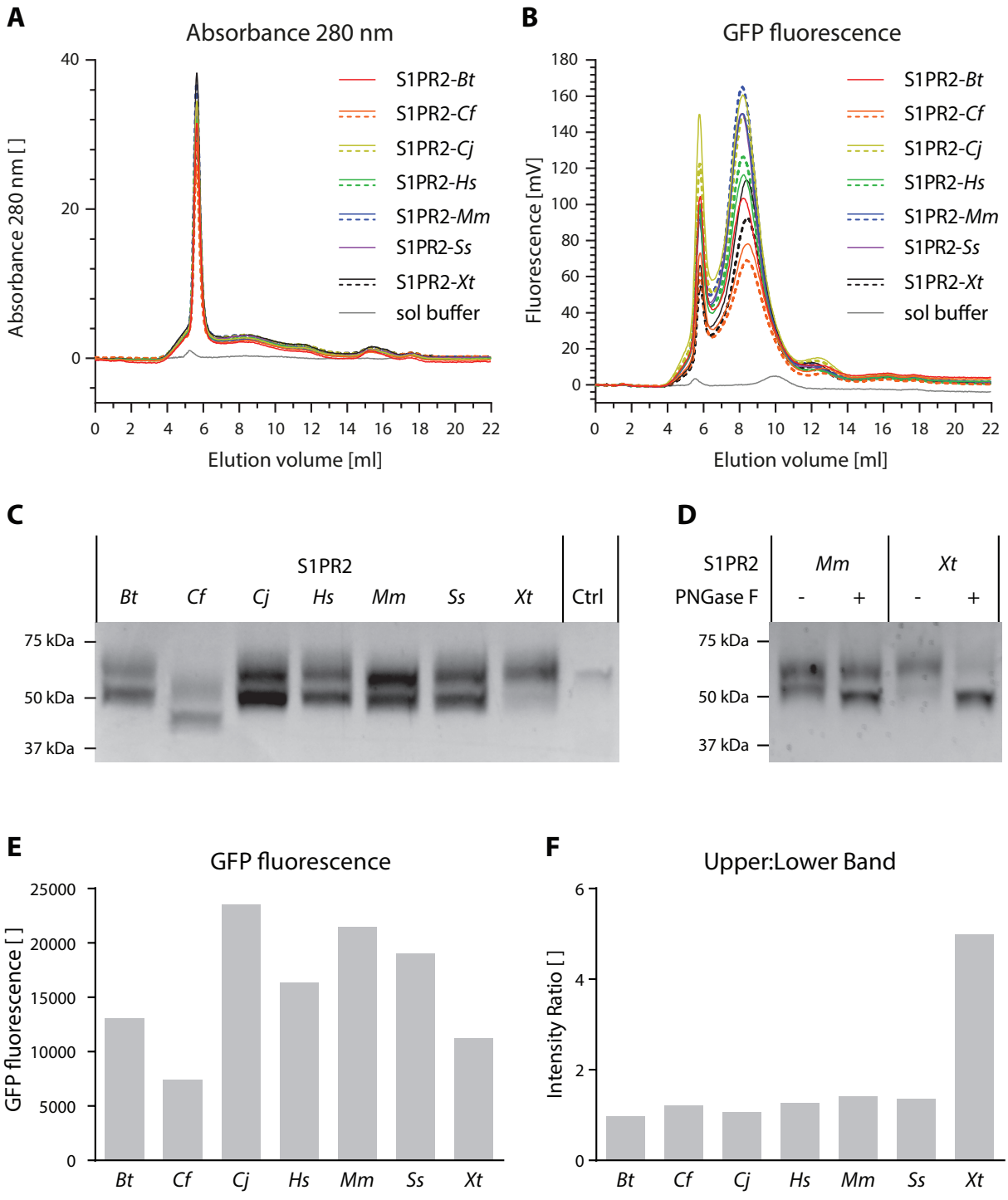

Fig. 2: Expression analysis of S1PR2 homologs. A, FSEC absorbance profiles at 280 nm indicating equal loading of S1PR2 homologs. Replicates were recorded for some homologs (dashed lines). **B**, GFP fluorescence profiles show that *Callithrix jacchus* and *Mus musculus* S1PR2 expression levels were the highest, with the latter exhibiting a smaller void peak. Replicates were recorded for some homologs (dashed lines). **C**, S1PR2 homologs produce double bands in SDS/PAGE. A different GPCR that was used as a control does not exhibit this behavior (Ctrl). The strongest bands are found in *Callitrix jacchus* and *Mus musculus* lanes. Note that *Canis familiaris* S1PR2 has a lower molecular weight than the other homologs, as its C-terminus contains a splice site. **D**, PNGase F digestion of *Mus musculus* and *Xenopus tropicalis* S1PR2 indicates N-glycosylation of the receptors. Digestion was more effective in the Xenopus tropicalis variant. **E**, Densitometry of the band doublet in C. F, Intensity ratios of the upper vs. lower bands in C. *Bt*, *Bos taurus*; *Cf*, *Canis familiaris*; *Cj*, *Callithrix jacchus*; *Hs*, *Homo sapiens*; *Mm*, *Mus musculus*; *Ss*, *Sus scrofa*; *Xt*, *Xenopus tropicalis*.

SDS/PAGE confirms that the *Callithrix jacchus* and *Mus musculus* variants of S1PR2 were expressed at the highest levels (Fig. 2C,E). *Mus musculus* S1PR2 was therefore chosen for further optimization based on its high expression as determined by FSEC and SDS/PAGE and on its relatively low void peak.

N-Linked Glycosylation of S1PR2

All S1PR2 homologs migrated as pronounced double bands with ~8 kDa separation (Fig. 2C). We therefore assessed whether this mass difference could be accounted for by differential N-linked glycosylation. All mammalian S1PR2 homologs contain one conserved N-X-S/T sequon in their N-termini (Fig. 1A). Indeed, treatment of solubilized S1PR2 from *Mus musculus* with PNGase F enhanced the intensity of the lower band, which also exhibited an even lower molecular weight than its undigested counterpart (Fig. 2D). This indicates that both bands in undigested S1PR2 contain N-glycan modifications of different molecular mass, and that the smaller N-glycan variant is more accessible to PNGase F than the larger one. In contrast to its mammalian equivalents, *Xenopus tropicalis* S1PR2 harbors two N-X-S/T consensus motifs in the N-terminus and a third one in the ECL1 (Fig. 1A). This homolog also exhibited unique behavior in SDS/PAGE, where it only produced a very faint lower band (Fig. 2C and F). Remarkably, digestion with PNGase F resulted in a complete band shift to the lower molecular size, indicating that the N-glycan is readily accessible to the enzyme in the *Xenopus tropicalis* variant (Fig. 2D).

Insertion of T4 Lysozyme

A popular strategy for crystallization of GPCRs is insertion of T4L (Ghosh et al., 2015; Piscitelli et al., 2015). This approach was also followed by Hanson et al. (2012), who inserted T4L into ICL3 of human S1PR1 (Fig. 3A). We therefore utilized sequence homology between human S1PR1 and murine S1PR2 to deduct a functional insertion site (Fig. 3B). ICL3 of S1PR2 is shorter than its S1PR1 equivalent, and the missing amino acids overlap almost perfectly with the residues replaced by T4L in the S1PR1 crystallization construct. We therefore constructed a first fusion protein termed S1PR2-T4LΔH220, where T4L was inserted at a site comparable to the insertion site in S1PR1, thereby replacing His220. Since the C-terminal junction of ICL3 is only poorly conserved among S1PR1 and S1PR2, we also cloned a chimeric fusion protein called S1PR2-T4Lchim, where the C-terminal half of ICL3 in S1PR2 was replaced with homologous S1PR1 sequence including T4L from the crystal structure. Seamless fusion cloning was used for T4L insertion, which is superior to conventional restriction endonuclease-based cloning in that it does not introduce any unwanted amino acids at the fusion junctions.

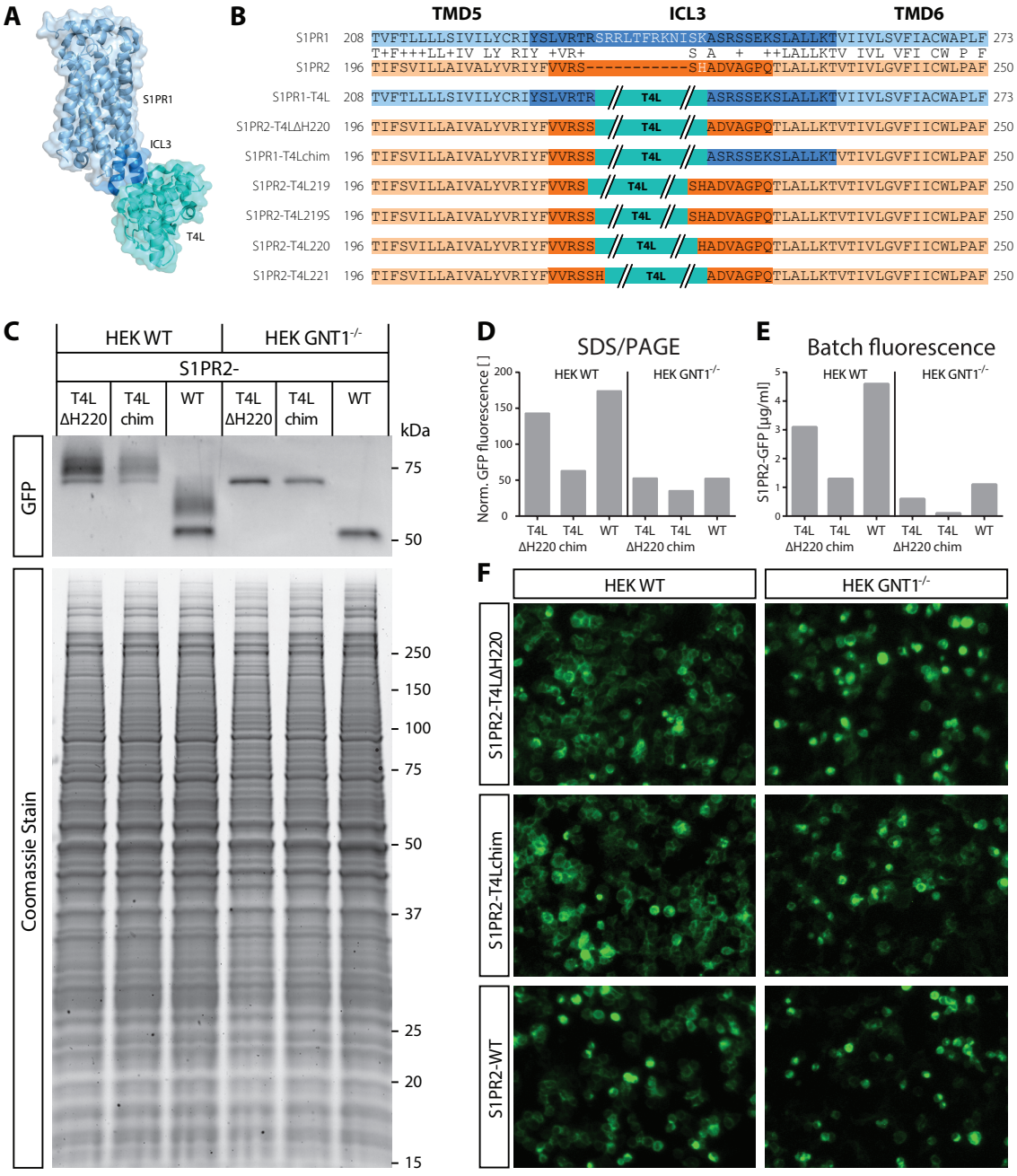

Fig. 3: S1PR2-T4L fusion proteins. A, Crystal structure of human S1PR1-T4L as determined by Hanson et al. (2012). **B**, Sequence alignment of human S1PR1 and murine S1PR2 was used to deduct functional T4L insertion sites. Identical amino acids are written between the sequences of S1PR1 and S1PR2, and + symbols indicate similar amino acids. Residues replaced by T4L in the S1PR1 crystal structure and their homologous position in murine S1PR2 are marked in white. The S1PR1-T4L construct of Hanson et al. (2012) is shown together with all S1PR2-T4L constructs used in this study. **C**, SDS/PAGE of murine S1PR2-T4LΔH220, S1PR2-T4Lchim, and S1PR2-WT expressed in wild-type (WT) or GNT1$^{-/-}$ HEK293. Higher molecular weight isoforms observed in WT cells are absent in GNT1$^{-/-}$ cells, confirming N-glycosylation of S1PR2. **D**, Densitometric quantification of C, reporting band intensities normalized to Coomassie. Expression of S1PR2-T4LΔH220 is superior to that of S1PR2-T4Lchim in both cell types, and overall expression levels are much lower in GNT1$^{-/-}$ cells compared to WT. **E**, Batch fluorescence reading of solubilized receptors confirms the findings from SDS/PAGE. **F**, Microscopy of adherent overexpressing cells prior to solubilization supports a lower overall expression level in GNT1$^{-/-}$ cells (40x magnification).

Fig. 4: Expression of the repositioned S1PR2-T4L constructs. A, FSEC profiles of S1PR2-T4L constructs using a different column than in previous experiments. Several peaks are observable, and S1PR2-T4L221 seems to be most strongly expressed. **B**, S1PR2-T4L constructs produce double bands in SDS/PAGE at higher molecular weights than WT S1PR2. Note that the lane order is different from the other panels. **C**, Densitometric analysis of B, supporting higher insertion tolerance in the C-terminal ICL3. Data from two independent experiments were normalized to WT, and means with individual data points are shown. **D**, Batch fluorescence experiments confirming superiority of more C-terminal T4L insertion sites. **E**, Microscopy of HEK293T cells before solubilization (40x magnification).

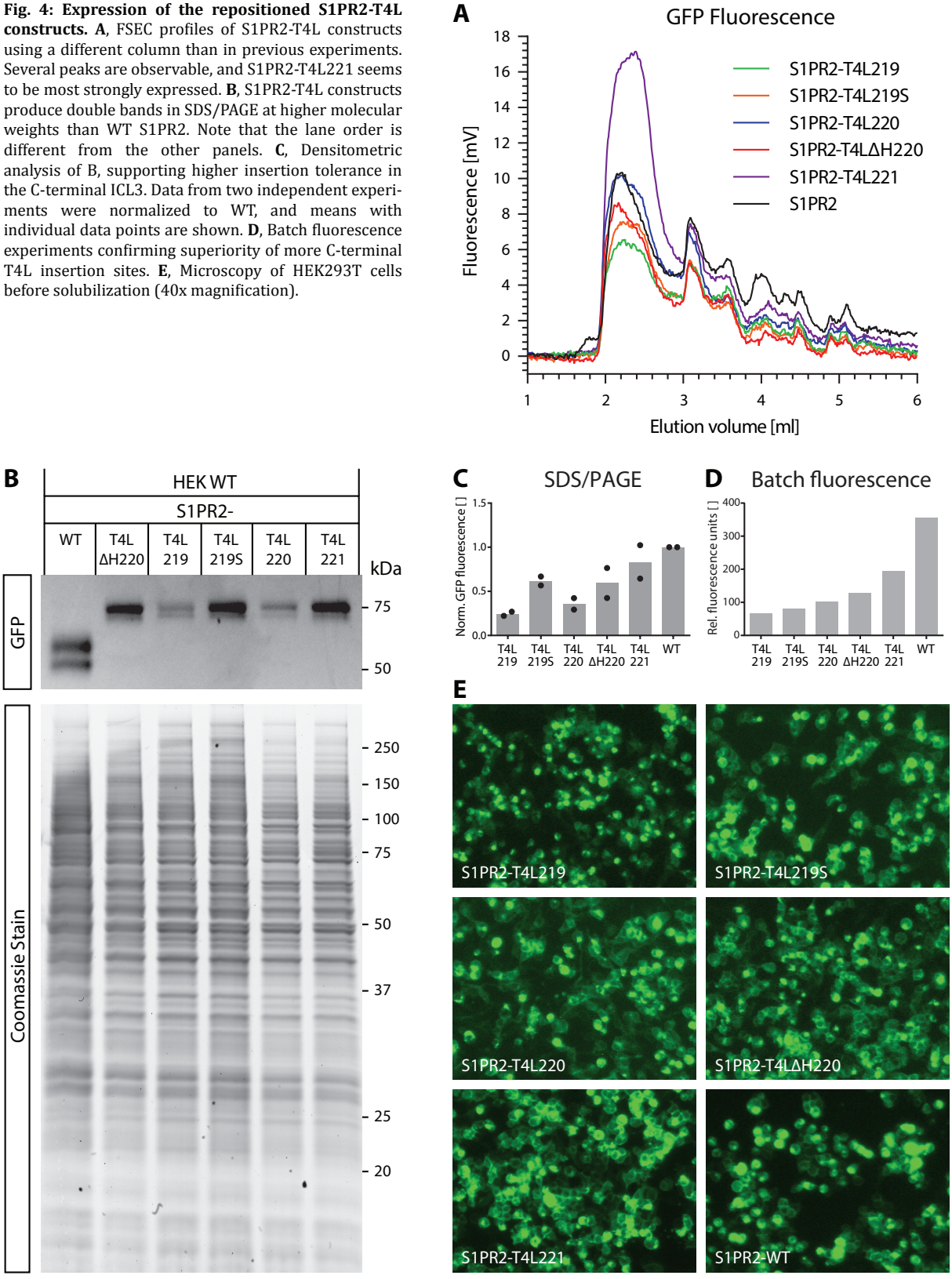

Unfortunately, due to a malfunction, no FSEC profiles could be recorded of S1PR2-T4LΔH220 and S1PR2-T4Lchim. However, SDS/PAGE and batch fluorescence readings clearly suggested superior expression of S1PR2-T4LΔH220 compared to S1PR2-T4Lchim (Fig. 3C-E). In addition, GNT1-deficient HEK293S cells were evaluated as an expression system for a homogeneous population of not N-glycosylated receptors. In line with the PNGase F digestion results, the upper bands evident in wild-type HEK293T cells were completely absent when S1PR2 was expressed in GNT1$^{-/-}$ cells (Fig. 3C). This confirms that the double bands observed in SDS/PAGE of S1PR2 originate from differential N-glycosylation. However, overall expression levels from mutant cells were much lower than those from wild-type, prompting us to continue with wild-type HEK293T (Fig. 3C-F).

As the expression levels of S1PR2-T4LΔH220 were markedly higher than those of S1PR2-T4Lchim but still lower than those of the non-T4L variant, the T4L insertion site in S1PR2-T4LΔH220 was further optimized residue by residue. Three constructs were obtained by SDM where the position of T4L corresponds to an insertion between two adjacent residues in the wild-type S1PR2 sequence: S1PR2-T4L219, S1PR2-T4L220, and S1PR2-221 (numbers denoting the position of the first T4L amino acid within the fusion sequence). In addition, an intermediate construct from step-wise SDM was evaluated where Ser219 was present on both S1PR2 moieties flanking T4L, denominated S1PR2-T4L220S (Fig. 3B).

FSEC was performed with these constructs on a different size exclusion column than during the homolog screen, yielding much more complex profiles than before (Fig. 4A). No distinct Gaussian GPCR peak was observed; instead, several peaks of declining heights were visible from ~2.2 ml to ~5 ml of elution volume. Curiously, even S1PR2-WT (wild-type), which had been used also in the homolog screen, now failed to produce a distinct GPCR peak. In addition, no shift of FSEC peaks could be observed between T4L-bearing S1PR2 and the WT construct. Overall peak heights suggested that S1PR2-T4L221 was expressed at the highest level, even compared to S1PR2-WT. In contrast, S1PR2-T4L219 expression was the lowest.

In SDS/PAGE, T4L constructs all showed higher molecular weights than the WT construct (Fig. 4B). They also exhibited double bands, though the size difference appeared to be smaller than in S1PR2-WT. Interestingly, the more C-terminally T4L had been inserted, the higher the fluorescence was as determined by SDS/PAGE, batch fluorescence measurements, and microscopy (Fig. 4B-D). Whereas microscopy supported the FSEC result that S1PR2-T4L221 was superior to S1PR2-WT, the opposite was observed in SDS/PAGE and batch fluorescence.

Discussion

Crystallization of GPCRs is a very laborious task. In our efforts toward an S1PR2 crystal structure, we therefore relied on a workflow that had been proven successful for the only S1PR family

member crystallized so far, the closely related S1PR1 (Hanson et al., 2012). In our homology screen, all the 7 S1PR2 variants analyzed were expressed at detectable levels, producing a distinct peak in the FSEC profile. It is of note that the elution volume of ~8 ml observed for this peak is larger than expected for S1PR2. In the case of *Mus musculus* S1PR2, the elution volume of the non-aggregated GPCR peak is at ~8.16 ml, which corresponds to a molecular weight of ~202 kDa (Fig. S2). The calculated molecular mass of murine GFP-tagged S1PR2 is 68.51 kDa, which is line with its migration in SDS/PAGE. This ~3x discrepancy can be explained by the unique characteristics of FSEC, which preserves molecular complexes during size separation. Solubilized S1PR2 is embedded in a detergent micelle that significantly contributes to its Stokes radius. Here, DDM was used as a detergent, which forms free micelles of ~140 molecules (Oliver et al., 2013), yielding a total molecular mass of ~71.5 kDa. In the presence of CHS, these micelles are converted to even larger, bicelle-like structures (Thompson et al., 2011). In addition, residual membrane-derived lipids and posttranslational modifications could contribute to a higher molecular weight, and dimerization of S1PR2 might further multiply the apparent size. SDS/PAGE linearizes S1PR2, which presumably causes disassembly of this complex, finally resulting in bands at the expected molecular weight range.

Murine S1PR2 was chosen for insertion of T4L, as it expressed to high levels while exhibiting relatively low aggregation. T4L is a very stable protein that is known to crystallize under various conditions (Weaver and Matthews, 1987). T4L fusions are therefore a common approach for GPCR crystallization, as they increase the polar surface area of the protein, which facilitates the formation of lattice contacts (Ghosh et al., 2015). ICL3 is a particularly attractive insertion site for T4L, as the high flexibility of this loop is problematic for crystal growth (Ghosh et al., 2015). Interestingly, our data indicate that the tolerance of ICL3 for T4L insertion increases toward the C-terminus of the loop. Whether expression levels of S1PR2-T4L221, the best expressing T4L construct, are comparable with S1PR2-WT could not be determined unambiguously.

Besides expression levels, homogeneity of GPCR conformation is an important prerequisite for crystallization (Venkatakrishnan et al., 2014). The initial finding that S1PR2 from all species produced a distinct, Gaussian-shaped peak in FSEC experiments was therefore very promising. By fractionation, this peak would be simple to separate from aggregates present in the void peak. However, later experiments with a higher-resolution size exclusion column yielded many overlapping peaks. Here, the most prominent peak was at ~2.4 ml elution volume, which is a typical value for solubilized GPCRs on this column (Fig. S2). The other peaks in the FSEC trace most likely represent an ensemble of different molecular compositions of S1PR2 complexes. Whether these assemblies are an artifact of solubilization, or whether they represent physiologically occurring clusters from the cell membrane remains elusive. Conformational ambiguity of S1PR2 could also contribute to a heterogeneous FSEC profile, and would be detrimental to crystallization. To this end, addition of a ligand can stabilize the receptor in one

conformation, which is a common approach also adopted for crystallization of S1PR1 (Deupi et al., 2012; Ghosh et al., 2015; Hanson et al., 2012).

We have identified N-glycan chains on S1PR2 of all examined species. In mammalian S1PR2 homologs, the only N-X-S/T sequon that could accommodate such an N-glycan is located at Asn19-Tyr20-Thr21. This site is conserved among S1PR1, S1PR2, and S1PR5, and glycosylation at this position is also evident in the crystal structure of human S1PR1 (Hanson et al., 2012). In S1PR2, all mammalian homologs analyzed co-exist in two N-glycosylation isomers, which correspond to a large and a small N-glycan chain at least in the case of murine S1PR2. The population with higher molecular mass was less susceptible to PNGase F digestion, suggesting lower structural flexibility. In S1PR2-T4L fusion constructs, SDS/PAGE double bands are closer together, indicating that T4L insertion influences the N-glycosylation of S1PR2. Varying degrees of glycosylation also contribute to a higher heterogeneity of receptors, which is not desirable for crystallization. Though expressing S1PR2 in GNT1$^{-/-}$ cells yielded less protein, a uniform N-glycan-free population of receptors might outweigh this disadvantage. Alternatively, mutagenesis of the N-X-S/T sequon could abolish N-glycosylation specifically in S1PR2, assumed that such a construct is properly folded and trafficked.

Our initial hypothesis that the crystallization of S1PR2 could be facilitated by closely following the protocol published for S1PR1 turned out to be too optimistic. In order to arrive at a construct suitable for crystallization, many iteration steps still need to be executed. The best-expressing T4L construct was S1PR2-T4L221, which asks for further exploration of more C-terminal insertion sites. T4L could also be added to other parts of the protein, such as the N-terminus (Zou et al., 2012) or ICL2 (Hollenstein et al., 2013). Alternatives to T4L exist that have been fused to GPCRs in order to obtain crystal structures (Chun et al., 2012). Mutagenesis of S1PR2 could further contribute to crystallization by serially truncating its termini or enhancing thermostability of the protein (Dore et al., 2011; Piscitelli et al., 2015). Antagonists of S1PR2 such as JTE-013 could be used to abolish its signaling during cell culture, which is a common strategy for enhancing the overexpression of GPCRs (Andre et al., 2006; Deupi et al., 2012). Though GPCRs expressed in mammalian cells have been successfully used in crystallography (Standfuss et al., 2007), the vast majority of GPCR crystal structures originate from baculovirus-mediated expression in insect cells (Ghosh et al., 2015). Transition to this system is another critical step which needs to be conducted carefully. Alternative expression systems used for crystallization of GPCRs are *P. pastoris* (Hino et al., 2012; Shimamura et al., 2011) or even *E. coli* (Egloff et al., 2014). Optimizing the solubilization protocol could also be essential for obtaining homogeneous S1PR2-containinc micelles. Finally, the most critical step will be the evaluation of different crystallization conditions.

In order to obtain a crystal structure of S1PR2, further systematic screening efforts are therefore necessary that go beyond the scope and timeframe of this project. However, we have learned valuable lessons on S1PR2 biology along the way.

References

Aarthi, J.J., M.A. Darendeliler, and P.N. Pushparaj. 2011. Dissecting the role of the S1P/S1PR axis in health and disease. *Journal of dental research*. 90:841-854.

Adada, M., D. Canals, Y.A. Hannun, and L.M. Obeid. 2013. Sphingosine-1-phosphate receptor 2. *The FEBS journal*. 280:6354-6366.

Altschul, S.F., W. Gish, W. Miller, E.W. Myers, and D.J. Lipman. 1990. Basic local alignment search tool. *Journal of molecular biology*. 215:403-410.

Andre, N., N. Cherouati, C. Prual, T. Steffan, G. Zeder-Lutz, T. Magnin, F. Pattus, H. Michel, R. Wagner, and C. Reinhart. 2006. Enhancing functional production of G protein-coupled receptors in Pichia pastoris to levels required for structural studies via a single expression screen. *Protein science : a publication of the Protein Society*. 15:1115-1126.

Cavasotto, C.N., and S.S. Phatak. 2009. Homology modeling in drug discovery: current trends and applications. *Drug discovery today*. 14:676-683.

Chun, E., A.A. Thompson, W. Liu, C.B. Roth, M.T. Griffith, V. Katritch, J. Kunken, F. Xu, V. Cherezov, M.A. Hanson, and R.C. Stevens. 2012. Fusion partner toolchest for the stabilization and crystallization of G protein-coupled receptors. *Structure*. 20:967-976.

Deupi, X., X.D. Li, and G.F. Schertler. 2012. Ligands stabilize specific GPCR conformations: but how? *Structure*. 20:1289-1290.

Dohlman, H.G. 2015. Thematic Minireview Series: New Directions in G Protein-coupled Receptor Pharmacology. *The Journal of biological chemistry*. 290:19469-19470.

Dore, A.S., N. Robertson, J.C. Errey, I. Ng, K. Hollenstein, B. Tehan, E. Hurrell, K. Bennett, M. Congreve, F. Magnani, C.G. Tate, M. Weir, and F.H. Marshall. 2011. Structure of the adenosine A(2A) receptor in complex with ZM241385 and the xanthines XAC and caffeine. *Structure*. 19:1283-1293.

Egloff, P., M. Hillenbrand, C. Klenk, A. Batyuk, P. Heine, S. Balada, K.M. Schlinkmann, D.J. Scott, M. Schutz, and A. Pluckthun. 2014. Structure of signaling-competent neurotensin receptor 1 obtained by directed evolution in Escherichia coli. *Proceedings of the National Academy of Sciences of the United States of America*. 111:E655-662.

Filmore, D. 2004. It's a GPCR world. *Modern Drug Discovery*. 7:24-28.

Fredriksson, R., M.C. Lagerstrom, L.G. Lundin, and H.B. Schioth. 2003. The G-protein-coupled receptors in the human genome form five main families. Phylogenetic analysis, paralogon groups, and fingerprints. *Molecular pharmacology*. 63:1256-1272.

Fredriksson, R., and H.B. Schioth. 2005. The repertoire of G-protein-coupled receptors in fully sequenced genomes. *Molecular pharmacology*. 67:1414-1425.

Ghosh, E., P. Kumari, D. Jaiman, and A.K. Shukla. 2015. Methodological advances: the unsung heroes of the GPCR structural revolution. *Nature reviews. Molecular cell biology*. 16:69-81.

Grueninger-Leitch, F., A. D'Arcy, B. D'Arcy, and C. Chene. 1996. Deglycosylation of proteins for crystallization using recombinant fusion protein glycosidases. *Protein science : a publication of the Protein Society*. 5:2617-2622.

Hanson, M.A., C.B. Roth, E. Jo, M.T. Griffith, F.L. Scott, G. Reinhart, H. Desale, B. Clemons, S.M. Cahalan, S.C. Schuerer, M.G. Sanna, G.W. Han, P. Kuhn, H. Rosen, and R.C. Stevens. 2012. Crystal structure of a lipid G protein-coupled receptor. *Science*. 335:851-855.

Hino, T., T. Arakawa, H. Iwanari, T. Yurugi-Kobayashi, C. Ikeda-Suno, Y. Nakada-Nakura, O. Kusano-Arai, S. Weyand, T. Shimamura, N. Nomura, A.D. Cameron, T. Kobayashi, T. Hamakubo, S. Iwata, and T. Murata. 2012. G-protein-coupled receptor inactivation by an allosteric inverse-agonist antibody. *Nature*. 482:237-240.

Hollenstein, K., J. Kean, A. Bortolato, R.K. Cheng, A.S. Dore, A. Jazayeri, R.M. Cooke, M. Weir, and F.H. Marshall. 2013. Structure of class B GPCR corticotropin-releasing factor receptor 1. *Nature*. 499:438-443.

Isberg, V., B. Vroling, R. van der Kant, K. Li, G. Vriend, and D. Gloriam. 2014. GPCRDB: an information system for G protein-coupled receptors. *Nucleic acids research*. 42:D422-425.

Kempf, A., B. Tews, M.E. Arzt, O. Weinmann, F.J. Obermair, V. Pernet, M. Zagrebelsky, A. Delekate, C. Iobbi, A. Zemmar, Z. Ristic, M. Gullo, P. Spies, D. Dodd, D. Gygax, M. Korte, and M.E. Schwab. 2014. The sphingolipid receptor S1PR2 is a receptor for

Nogo-a repressing synaptic plasticity. *PLoS biology*. 12:e1001763.

Kim, R.H., K. Takabe, S. Milstien, and S. Spiegel. 2009. Export and functions of sphingosine-1-phosphate. *Biochimica et biophysica acta*. 1791:692-696.

Larkin, M.A., G. Blackshields, N.P. Brown, R. Chenna, P.A. McGettigan, H. McWilliam, F. Valentin, I.M. Wallace, A. Wilm, R. Lopez, J.D. Thompson, T.J. Gibson, and D.G. Higgins. 2007. Clustal W and Clustal X version 2.0. *Bioinformatics*. 23:2947-2948.

Lescrinier, E. 2011. Structural biology in drug development. *Verhandelingen - Koninklijke Academie voor Geneeskunde van Belgie*. 73:65-78.

Marinissen, M.J., and J.S. Gutkind. 2001. G-protein-coupled receptors and signaling networks: emerging paradigms. *Trends in pharmacological sciences*. 22:368-376.

Matsumura, I. 2013. A quarter century of reaping what we SOE. *BioTechniques*. 54:127-128.

Oliver, R.C., J. Lipfert, D.A. Fox, R.H. Lo, S. Doniach, and L. Columbus. 2013. Dependence of micelle size and shape on detergent alkyl chain length and head group. *PloS one*. 8:e62488.

Overington, J.P., B. Al-Lazikani, and A.L. Hopkins. 2006. How many drug targets are there? *Nature reviews. Drug discovery*. 5:993-996.

Pham, T.C., J.I. Fells, Sr., D.A. Osborne, E.J. North, M.M. Naor, and A.L. Parrill. 2008. Molecular recognition in the sphingosine 1-phosphate receptor family. *Journal of molecular graphics & modelling*. 26:1189-1201.

Piscitelli, C.L., J. Kean, C. de Graaf, and X. Deupi. 2015. A Molecular Pharmacologist's Guide to G Protein-Coupled Receptor Crystallography. *Molecular pharmacology*. 88:536-551.

Reeves, P.J., J.M. Kim, and H.G. Khorana. 2002. Structure and function in rhodopsin: a tetracycline-inducible system in stable mammalian cell lines for high-level expression of opsin mutants. *Proceedings of the National Academy of Sciences of the United States of America*. 99:13413-13418.

Rosenbaum, D.M., S.G. Rasmussen, and B.K. Kobilka. 2009. The structure and function of G-protein-coupled receptors. *Nature*. 459:356-363.

Schneider, C.A., W.S. Rasband, and K.W. Eliceiri. 2012. NIH Image to ImageJ: 25 years of image analysis. *Nature methods*. 9:671-675.

Schwab, M.E. 2010. Functions of Nogo proteins and their receptors in the nervous system. *Nature reviews. Neuroscience*. 11:799-811.

Shimamura, T., M. Shiroishi, S. Weyand, H. Tsujimoto, G. Winter, V. Katritch, R. Abagyan, V. Cherezov, W. Liu, G.W. Han, T. Kobayashi, R.C. Stevens, and S. Iwata. 2011. Structure of the human histamine H1 receptor complex with doxepin. *Nature*. 475:65-70.

Standfuss, J., G. Xie, P.C. Edwards, M. Burghammer, D.D. Oprian, and G.F. Schertler. 2007. Crystal structure of a thermally stable rhodopsin mutant. *Journal of molecular biology*. 372:1179-1188.

Thompson, A.A., J.J. Liu, E. Chun, D. Wacker, H. Wu, V. Cherezov, and R.C. Stevens. 2011. GPCR stabilization using the bicelle-like architecture of mixed sterol-detergent micelles. *Methods*. 55:310-317.

Valentine, W.J., V.I. Godwin, D.A. Osborne, J. Liu, Y. Fujiwara, J. Van Brocklyn, R. Bittman, A.L. Parrill, and G. Tigyi. 2011. FTY720 (Gilenya) phosphate selectivity of sphingosine 1-phosphate receptor subtype 1 (S1P1) G protein-coupled receptor requires motifs in intracellular loop 1 and transmembrane domain 2. *The Journal of biological chemistry*. 286:30513-30525.

Venkatakrishnan, A.J., T. Flock, D.E. Prado, M.E. Oates, J. Gough, and M. Madan Babu. 2014. Structured and disordered facets of the GPCR fold. *Current opinion in structural biology*. 27:129-137.

Weaver, L.H., and B.W. Matthews. 1987. Structure of bacteriophage T4 lysozyme refined at 1.7 A resolution. *Journal of molecular biology*. 193:189-199.

Zheng, L., U. Baumann, and J.L. Reymond. 2004. An efficient one-step site-directed and site-saturation mutagenesis protocol. *Nucleic acids research*. 32:e115.

Zou, Y., W.I. Weis, and B.K. Kobilka. 2012. N-terminal T4 lysozyme fusion facilitates crystallization of a G protein coupled receptor. *PloS one*. 7:e46039.

Supplement

Bos taurus:

```
  1 MGGVYSEYLS SSKVREHYNY TKESPDTKDT PSRQVASALI ILLCCAIVVE NLLVLIAVAR NSKFHSAMYL FLGNLAASDL 80
 81 LAGVAFIANT LLSGSVTLGL TPVQWFAREG SAFITLSASV FSLLAIAIER HVAIAKVKLY GSDKSCRMLL LIAASWLISL 160
161 VLGGLPILGW NCLGHLEACS TVLPLYAKPY VLCVVTIFSV ILSAIVALYI RIYCVVRSSQ ADVAAPQTLA LLKTVTIVLG 240
241 VFIFCWLPAF SILLLDYACP VRTCPMLYQA HYFFAFATLN SLLNPVIYTW RSRDLRREVL RPLQCWRQAA GMQGRRDRTP 320
321 GHHLLPLRSS SSLEKGMHVP TSPTFLEGNT IV 352
```

Callithrix jacchus:

```
  1 MGSLYSEYLN PNKVQEHYNY TKETLETQQT SSRQVASAFI IILCCAIVVE NLLVLIAVAR NSKFHSAMYL FLGNLAASDL 80
 81 LAGMAFVANT LLSGSVTLRL TPVQWFAREG SAFITLSASV FSLLAIAIER HVAIAKVKLY GSDKSCRMLL LIGASWLISL 160
161 VLGGLPILGW NCLGHLEACS TVLPLYAKHY VLCVVTIFSI ILLAIVALYV RIYCVVRSSH ADVAGPQTLA LLKTVTIVLG 240
241 VFIVCWLPAF SILLLDYACP IRSCAILYKA HYFFAFATLN SLLNPVIYTW RSRDLRREVL RPLQCWRRGT GVQGRRRSGT 320
321 PGHRLLPLRS SSSLERGMHM PTSPTFLEGN TGV 353
```

Canis familiaris:

```
  1 MGNLYSEYLS PNKVREHYNY TKETLDTQET ASRQAALVII IILCFAIVVE NLLVLIAVAR NSKFHSAMYL FLGNLAASDM 80
 81 LTGVAFVANT LLSGPVTLGL TPIQWFAREG SAFITLSASV FSLLAIAIER HVAIAKVKLY GSDKSCRMLL LIGASWLISV 160
161 ALGGLPILGW NCLGHLEACS TVLPLYTKHY VLCVVTIFSV ILLAIVALYV RIYCVVRSSQ ADVAGPQTLA LLKTVTIVLG 240
241 VFIVCWLPAF SILLLDYACP VRSCPILYKA HYFFAFATLN SLLNPVIYTW RSRDLRREAQ RFGKR 305
```

Homo sapiens:

```
  1 MGSLYSEYLN PNKVQEHYNY TKETLETQET TSRQVASAFI VILCCAIVVE NLLVLIAVAR NSKFHSAMYL FLGNLAASDL 80
 81 LAGVAFVANT LLSGSVTLRL TPVQWFAREG SAFITLSASV FSLLAIAIER HVAIAKVKLY GSDKSCRMLL LIGASWLISL 160
161 VLGGLPILGW NCLGHLEACS TVLPLYAKHY VLCVVTIFSI ILLAIVALYV RIYCVVRSSH ADMAAPQTLA LLKTVTIVLG 240
241 VFIVCWLPAF SILLLDYACP VHSCPILYKA HYFFAVSTLN SLLNPVIYTW RSRDLRREVL RPLQCWRPGV GVQGRRRGGT 320
321 PGHHLLPLRS SSSLERGMHM PTSPTFLEGN TVV 353
```

Mus musculus:

```
  1 MGGLYSEYLN PEKVLEHYNY TKETLDMQET TSRKVASAFI IILCCAIVVE NLLVLIAVAR NSKFHSAMYL FLGNLAASDL 80
 81 LAGVAFVANT LLSGHVTLSL TPVQWFAREG SAFITLSASV FSLLAIAIER QVALAKVKLY GSDKSCRMLM LIGASWLISL 160
161 ILGGLPILGW NCLNQLEACS TVLPLYAKHY VLCVVTIFSV ILLAIVALYV RIYFVVRSSH ADVAGPQTLA LLKTVTIVLG 240
241 VFIICWLPAF SILLLDSTCP VRACPVLYKA HYFFAFATLN SLLNPVIYTW RSRDLRREVL RPLQCWRRGK GVTGRRGGNP 320
321 GHRLLPLRSS SSLERGMHMP TSPTFLEGNT VV 352
```

Sus scrofa:

```
  1 MGNLYSEYLS PSKVPEHYNY TKETPVTETP SRQVASVLII ILCCAIVLEN LLVLIAVARN SKFHSAMYLF LGNLAASDLL 80
 81 AGVAFIANTL LSGPFTLRLT PVQWFAREGS AFITLSASVF SLLAIAIERQ VAIAKVKLYG SDKSCRMLLL IAASWLISMV 160
161 LGGLPILGWN CLGHLEACST VLPLYAKPYV LCVVTIFSVI LSAIVALYIR IYCVVRSSQA DVAGQQTLAL LKTVTIVLGV 240
241 FIVCWLPAFS ILLLDYACPV RACPILYKAH YFFAFATLNS LLNPVIYTWR SRDLRREVLR PLQCWRRAAG GQGRRDGTPG 320
321 HRLLPLRSSS SLERGTHMPT SPTFLEGNTM V 351
```

Xenopus tropicalis:

```
  1 MNSTYQEYLN PRKVWEHYVY VKENLTREDS SRYAISIIFI IICCIIILEN LLVLTSVLRN KKFHSAMFFF IGNLAFSDFL 80
 81 TGCAYIANIL LSGNMTFTLT PMEWFIREGT AFTTLCASVL SLLAIAIERK VAIMQVEVYS SDRNCRMVLL IAACWVVSIV 160
161 IGGLPILGWN CIFNMEQCST VLPLYSKKYI LFVVTIFTII LLTIVILYVQ IYYIVKSSHG EVAAPPTLAL LKTVTIVLGV 240
241 FIICWLPAFI ILLLDVSCKV KSCKILYKAD YFFGVATLNS ALNPIIYTLR SKDMRKEFLR VLCCFNYFQK NRTPDKCMLK 320
321 LRSSSSLERC TQKHDLPTSP IMKDCTTFV 349
```

Fig. S1: S1PR2 homolog sequences. Note the shorter *Canis familiaris* isoform.

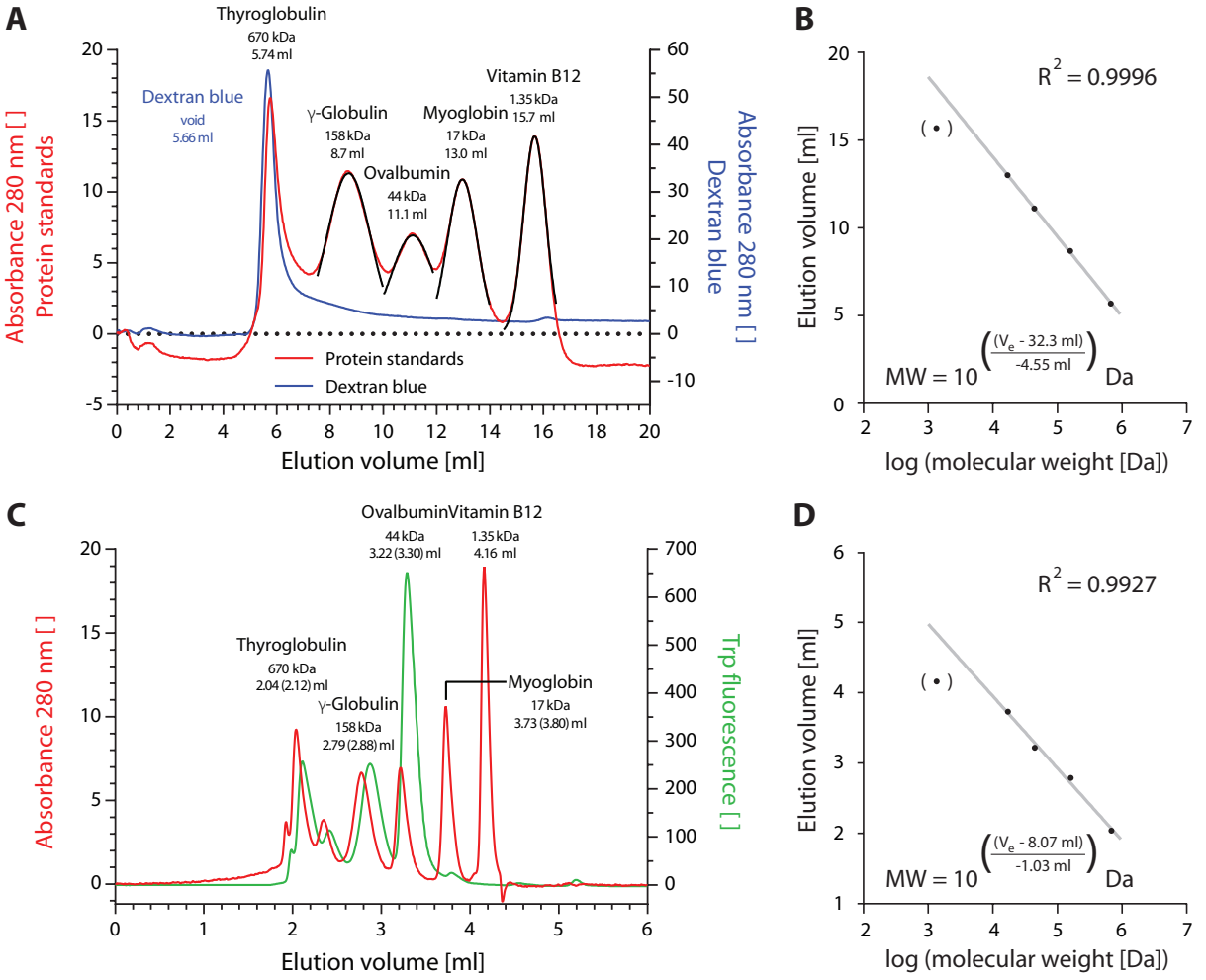

E

Construct	V_e [ml]	MW_{exp} [kDa]	MW_{pred} [kDa]	MW_{exp} : MW_{pred} [ ]
S1PR2-*Bt*	8.23	195.03	68.35	2.85
S1PR2-*Cf*1	8.46	173.69	63.37	2.74
S1PR2-*Cf*2	8.39	179.59	63.37	2.83
S1PR2-*Cj*1	8.19	198.72	68.64	2.90
S1PR2-*Cj*2	8.23	195.43	68.64	2.85
S1PR2-*Hs*1	8.23	195.43	68.55	2.85
S1PR2-*Hs*2	8.26	192.10	68.55	2.80
S1PR2-*Mm*1	8.16	202.07	68.51	2.95
S1PR2-*Mm*2	8.16	202.07	68.51	2.95
S1PR2-*Ss*	8.13	205.57	68.30	3.01
S1PR2-*Xt*1	8.39	179.59	69.52	2.58
S1PR2-*Xt*2	8.39	179.59	69.52	2.58

Fig. S2: Size calibration of FSEC profiles. A, FSEC traces for globular protein standards on the Tricorn 10/200 Superdex S200 column used for the S1PR2 homolog screen. Dextran blue was used as an indicator of the void peak. Elution volumes were estimated by Gaussian curve fitting (black). **B**, calibration curve for A. Vitamin B12 was excluded for regression (parentheses). The conversion formula from the elution volume (Ve) to the molecular weight (MW) is given. **C**, **D**, As in A and B, but using the Tosoh TSK gel Super SW3000 column employed for S1PR2-T4L construct evaluation. **C**, Note that the peaks measured by tryptophane fluorescence (parentheses) lag slightly behind the absorbance peaks due to the relative positions of the absorbance and fluorescence detectors. **E**, Difference between experimentally determined (MW_{exp}) and predicted molecular weights (MW_{pred}) in the S1PR2 homolog screen. The formula from B was used for determination of MW_{exp}. Where applicable, both replicate measurements are listed (1 and 2). *Bt*, *Bos taurus*; *Cf*, *Canis familiaris*; *Cj*, *Callithrix jacchus*; *Hs*, *Homo sapiens*; *Mm*, *Mus musculus*; *Ss*, *Sus scrofa*; *Xt*, *Xenopus tropicalis*.

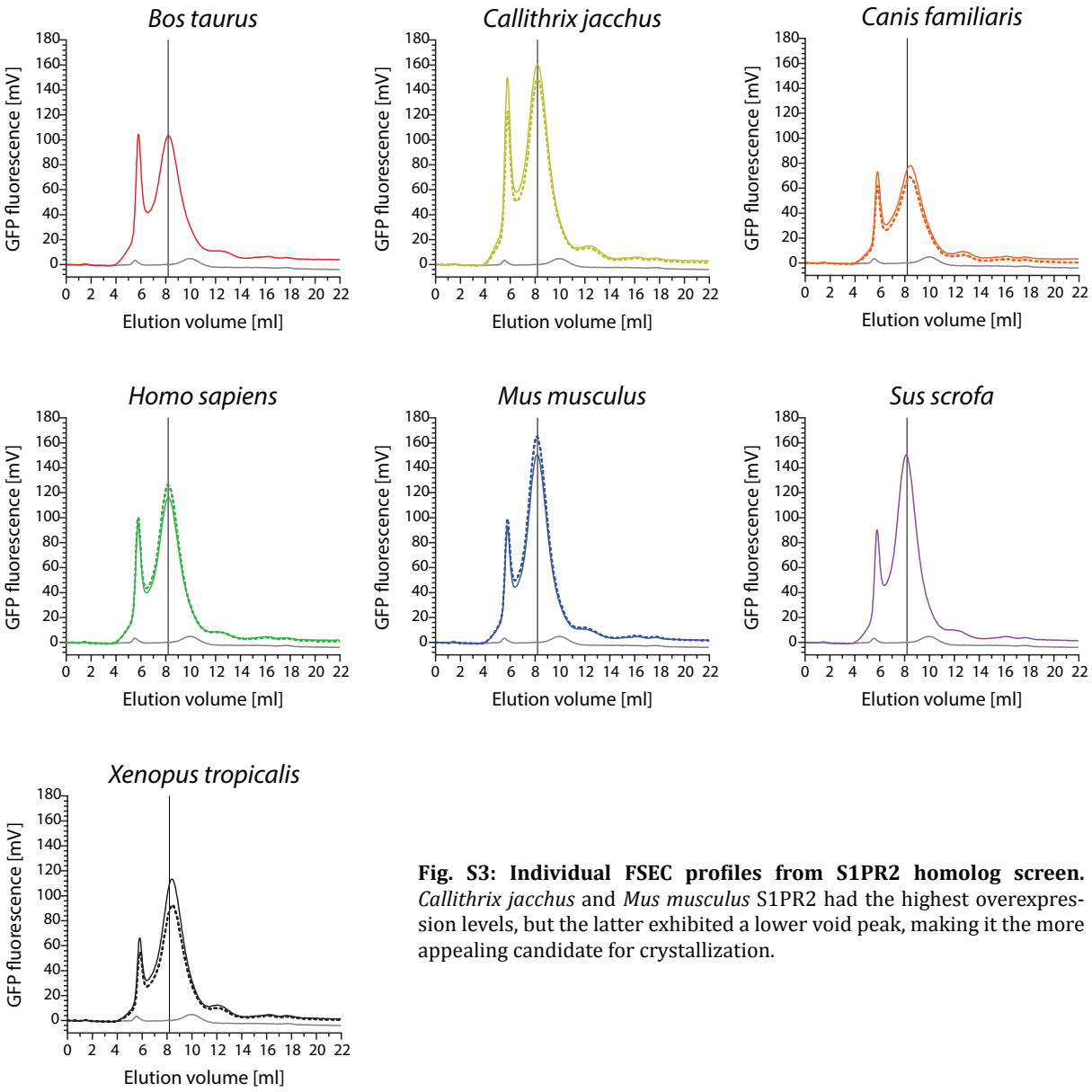

Fig. S3: Individual FSEC profiles from S1PR2 homolog screen. *Callithrix jacchus* and *Mus musculus* S1PR2 had the highest overexpression levels, but the latter exhibited a lower void peak, making it the more appealing candidate for crystallization.

CHAPTER 6

THE SPHINGOLIPID RECEPTOR S1PR2 IS A RECEPTOR FOR NOGO-A REPRESSING SYNAPTIC PLASTICITY

Anissa Kempf[1¶], Björn Tews[1¶], Michael E. Arzt[1], Oliver Weinmann[1], Franz J. Obermair[1],Vincent Pernet[1], Marta Zagrebelsky[2], Andrea Delekate[2], Cristina Iobbi[2], Ajmal Zemmar[1], Zorica Ristic[1], Miriam Gullo[1], Peter Spies[3], Dana Dodd[1], Daniel Gygax[3], Martin Korte[2], Martin E. Schwab[1]

Published in *PLoS Biol* 2014;12(1): e1001763. doi:10.1371/journal.pbio.1001763

M. E. A. conducted and analyzed microscale thermophoresis binding studies and wrote the corresponding part of the manuscript.

¶ These authors contributed equally to this work.
[1] Brain Research Institute, University of Zurich, and Dept. of Health Sciences and Technology, Swiss Federal Institute of Technology, Zurich, Switzerland
[2] Zoological Institute, Division of Cellular Neurobiology, TU Braunschweig, Braunschweig, Germany
[3] School of Life Sciences, University of Applied Life Sciences Northwestern Switzerland, Muttenz, Switzerland

Abstract

Nogo-A is a membrane protein of the central nervous system (CNS) restricting neurite growth and synaptic plasticity via two extracellular domains: Nogo-66 and Nogo-A-Δ20. Receptors transducing Nogo-A-Δ20 signaling remained elusive so far. Here we identify the G protein-coupled receptor (GPCR) sphingosine 1-phosphate receptor 2 (S1PR2) as a Nogo-A-Δ20-specific receptor. Nogo-A-Δ20 binds S1PR2 on sites distinct from the pocket of the sphingolipid sphingosine 1-phosphate (S1P) and signals via the G protein G_{13}, the Rho GEF LARG, and RhoA. Deleting or blocking S1PR2 counteracts Nogo-A-Δ20- and myelin-mediated inhibition of neurite outgrowth and cell spreading. Blockade of S1PR2 strongly enhances long-term potentiation (LTP) in the hippocampus of wild-type but not Nogo-$A^{-/-}$ mice, indicating a repressor function of the Nogo-A/S1PR2 axis in synaptic plasticity. A similar increase in LTP was also observed in the motor cortex after S1PR2 blockade. We propose a novel signaling model in which a GPCR functions as a receptor for two structurally unrelated ligands, a membrane protein and a sphingolipid. Elucidating Nogo-A/S1PR2 signaling platforms will provide new insights into regulation of synaptic plasticity.

Author Summary

Recent studies have demonstrated an important role of Nogo-A signaling in the repression of structural and synaptic plasticity in mature neuronal networks of the central nervous system. These insights extended our understanding of Nogo-A's inhibitory function far beyond its well-studied role as axonal-growth inhibitor. Repression is mediated via two different Nogo-A extracellular domains: Nogo-66 and Nogo-A-Δ20. Here, we identify the G-protein coupled receptor S1PR2 as a high-affinity receptor for Nogo-A-Δ20 and demonstrate that S1PR2 binds this domain with sites different from the recently proposed S1P binding pocket. Interfering with S1PR2 activity, either pharmacologically or genetically, prevented Nogo-A-Δ20-mediated inhibitory effects. Similar results were obtained when we blocked G_{13}, LARG, and RhoA, components of the downstream signaling pathway. These findings revealed a strong increase in hippocampal and cortical synaptic plasticity when acutely interfering with Nogo-A/S1PR2 signaling, similar to previous results obtained by blocking Nogo-A. We thus provide a novel biological concept of multi-ligand GPCR signaling in which this sphingolipid-activated GPCR is also bound and activated by the high molecular weight membrane protein Nogo-A.

Introduction

Factors inhibiting nerve fiber growth substantially contribute to the limited regenerative capacity of the adult central nervous system (CNS) after injury. They play important roles in stabilizing the complex wiring of the adult CNS of higher vertebrates and in establishing neuronal pathways in the developing nervous system [1],[2]. One of the best-studied factors is the membrane protein Nogo-A, which occurs in myelin and certain neurons, inhibiting axonal regeneration and plasticity after CNS injury [3]–[5]. Neutralization of Nogo-A has been shown to enhance axonal growth and compensatory sprouting in the adult spinal cord and brain, as well as to improve functional recovery after CNS injury [4],[6]. Recent studies have shown novel important roles of Nogo-A signaling in the repression of synaptic plasticity in mature neuronal networks, indicating an inhibitory potential of Nogo-A far beyond its well-studied restriction of axonal growth [1],[7]–[11].

Nogo-A exerts its inhibitory effects via two distinct extracellular domains: Nogo-66 (rat amino acid (aa) 1026–1091) and Nogo-A-Δ20 (rat aa544–725; part of "Amino-Nogo") [2],[12]. Nogo-66 induces growth inhibition via two membrane proteins, Nogo-66 receptor 1 (NgR1) [13], together with accessory proteins, and paired immunoglobulin-like receptor B (PirB) [14]. By contrast, the molecular identification and characterization of the receptor(s) transducing signals from the inhibitory Nogo-A-Δ20 domain has failed so far [2]. Nogo-A-Δ20 has been shown to partially mediate its inhibitory activity by interfering with integrins, but proof of a direct interaction has remained elusive [15]. Here we identified the G protein-coupled receptor (GPCR) sphingosine 1-phosphate receptor 2 (S1PR2) as a functional receptor for the Δ20 domain of Nogo-A.

S1PR2 belongs to the subfamily of five S1PRs [16]. S1PRs are known to be activated by the low molecular weight (MW) lipid ligand sphingosine 1-phosphate (S1P), which exerts diverse receptor-specific effects on various cell types, including regulation of apoptosis, cell motility and cytoskeleton dynamics [16]. In the brain and spinal cord, S1P has been shown to regulate angiogenesis and neurite outgrowth: activation of S1PR1 promotes neurite outgrowth in vitro via $G_{i/o}$ and Rac1, whereas activation of S1PR2 leads to neurite retraction, involving $G_{i/o}$, G_q, or $G_{12/13}$ and the RhoA pathway [16] –[18].

In this study we demonstrate that Nogo-A-Δ20 binds S1PR2 via extracellular receptor loops 2 and 3, which are distinct from the previously described binding site of S1P [19]. Nogo-A-Δ20 signals through the G protein G_{13}, leukemia-associated Rho guanine exchange factor (RhoGEF) LARG and RhoA. Deleting or blocking S1PR2 counteracts Nogo-A-Δ20- and myelin-mediated inhibition of neurite outgrowth and cell spreading. Acute S1PR2 blockade increases hippocampal and cortical long-term synaptic plasticity similarly to Nogo-A neutralization. These results strengthen the recently proposed physiological role of Nogo-A in restricting synaptic plasticity to

stabilize neuronal circuits [1],[9]. Further, these data support the paradigm shift for GPCR signaling from the classical "one ligand – one receptor" situation towards more dynamic models [20],[21].

Results

Nogo-A Binds to S1PR2

The GPCR S1PR2 was identified as a novel receptor candidate of the Nogo-A-Δ20 domain using a yeast two-hybrid (Y2H) screen of custom-made adult and fetal human brain libraries. In the adult CNS, S1PR2 is mainly expressed in the grey matter (Figure 1). Hippocampal pyramidal cells, cerebellar Purkinje cells, cortical neurons and spinal motoneurons, as well as retinal ganglion cells are S1PR2-positive (Figure 1A–1K). Importantly, S1PR2 is also expressed in Nogo-A-Δ20-responsive cells in vitro including 3T3 fibroblasts and immature cerebellar granule neurons (Figure S1). To validate the interaction of Nogo-A-Δ20 (Figure 2A) and S1PR2, His-tagged Nogo-A-Δ20 was co-incubated with membranes of S1PR2-overexpressing cells and subsequently immunoprecipitated (Figure 2C). S1PR2 was specifically detected in immunoprecipitation fractions (Figure 2C). Vice versa, His-tagged Nogo-A-Δ20 could be specifically probed in S1PR2 immunoprecipitated fractions, suggesting that the two proteins interact *in vitro* (Figure 2D). Co-immunoprecipitation experiments of Nogo-A or S1PR2 from whole mouse brain protein extracts further demonstrated that endogenous S1PR2 interacts with Nogo-A under physiological conditions *in vivo* (Figure 2B). To determine the binding affinity, binding of the entire Δ20-containing extracellular N-terminal domain of Nogo-A (Nogo-A-ext; Figure 2A) to biosensor-immobilized membrane preparations expressing functional full length S1PR2 protein or non S1PR2-expressing control membranes was monitored in real-time using Bio-Layer interferometry (OctetRED). Non-linear fitting revealed that Nogo-A-ext binds to S1PR2 with an apparent equilibrium binding constant (K_D) of ~142 nM (Figure 2E). The binding affinity was not influenced by the addition of S1P versus vehicle control (MeOH) (K_D MeOH~192 nM; K_D S1P~202 nM; Figure 2F). For a mapping of binding sites, individual extracellular domains (N-terminus and extracellular loops [ECLs]) of S1PR2 were synthesized as peptides and analyzed for binding to Nogo-A-Δ20 by microscale thermophoresis (Figure 2G). Nogo-A-Δ20 was found to

Figure 1. Localization of S1PR2 by immunohistochemistry in the adult mouse CNS.(A) S1PR2 expression in the hippocampus. CA, cornu ammonis; DG, dentate gyrus. **(B)** Magnification of the boxed region of CA1 depicted in (A). **(C)** S1PR2 expression in the cerebellum. GCL, granule cell layer; ML, molecular layer; PCL, Purkinje cell layer. **(D)** Magnification of the boxed region depicted in (C). **(E)** S1PR2 expression in the motor cortex. **(F)** Magnification of the boxed region depicted in (E). **(G,H)** S1PR2 expression in motoneuron cell bodies (arrows) and βIII-Tubulin-positive fibers (arrowheads) in the spinal cord. **(I,J,K)** S1PR2 expression in βIII-Tubulin-positive axons bundles (arrowheads) and cell bodies (arrows) of retinal ganglion cells. Scale bars: (A) 300 μm; (B) 30 μm; (C) 200 μm; (D) 15 μm; (E) 90 μm; (F) 30 μm; (G,H) 20 μm; (I–K) 15 μm. doi:10.1371/journal.pbio.1001763.g001

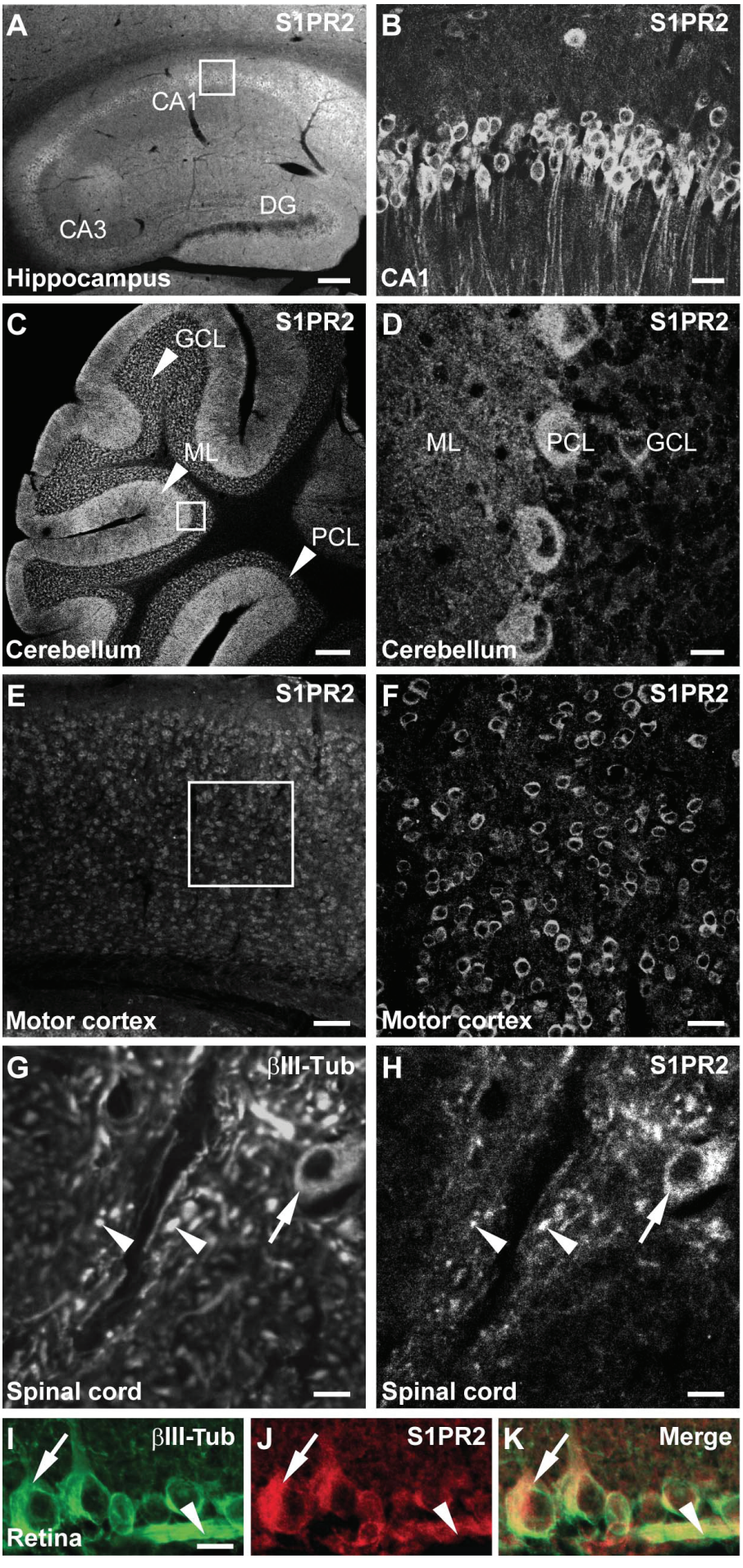
A
S1PR2
CA1
DG
CA3
Hippocampus
B
S1PR2
CA1
C
S1PR2
GCL
ML
PCL
Cerebellum
D
S1PR2
ML
PCL
GCL
Cerebellum
E
S1PR2
Motor cortex
F
S1PR2
Motor cortex
G
βIII-Tub
Spinal cord
H
S1PR2
Spinal cord
I
βIII-Tub
Retina
J
S1PR2
K
Merge

bind primarily to ECL2 (K_D~280 nM) and 3 (K_D~350 nM), less strongly to ECL1 (K_D~2 μM) and negligibly to the N-terminus of S1PR2 (K_D~11 μM) (Figure 2G). Importantly, binding analysis of the other bioactive domain of Nogo-A, Nogo-66, to S1PR2 extracellular domains revealed only unspecific binding in the high micromolar range (K_D ECL1~46 μM; K_D ECL2~7 μM; K_D ECL3~67 μM) or complete absence of binding (N-terminus) (Figure 2H). Collectively, these data show that Nogo-A-Δ20 but not Nogo-66 binds to specific extracellular domains of the GPCR S1PR2.

S1PR2 Is Internalized upon Nogo-A-Δ20 Binding

We have shown previously that Nogo-A-Δ20 is internalized into signaling endosomes upon binding, which results in RhoA activation and growth cone collapse [22]. To investigate whether S1PR2 is co-internalized upon Nogo-A-Δ20 treatment, cell surface S1PR2 expression was analyzed by immunofluorescence using a custom-made antibody (Figures 3A, S2B, and S2C). Cell surface S1PR2 levels were reduced by ~64% ($p<0.001$) 30 min after addition of Nogo-A-Δ20 (Figure 3B). To confirm this, plasma membranes of 3T3 cells were prepared 15 and 30 min post-incubation with Nogo-A-Δ20 and analyzed for S1PR2 levels by immunoblotting (Figures 3C and S2A). We found that cell surface S1PR2 levels were reduced by ~77% ($p<0.01$) and ~70% ($p<0.001$) after 15 and 30 min incubation with Nogo-A-Δ20, respectively, indicating that S1PR2 is internalized upon binding to Nogo-A-Δ20 (Figure 3C). Pulse-chase experiments revealed that the majority of internalized Nogo-A-Δ20 puncta colocalize with S1PR2 as well as with the endosomal marker EEA1 at 15 and 30 min post-incubation with Nogo-A-Δ20 (Figure 3D). Ubiquitination of GPCRs is a critical post-translational modification, which is often dispensable for initial receptor endocytosis but important for endosomal trafficking to proteasome/lysosomal degradation pathways [23],[24]. S1P has been shown to cause S1PR1 monoubiquitination and, in higher concentrations, polyubiquitination, resulting in subsequent GPCR recycling to the membrane or complete degradation, respectively [25]. S1PR2-ubiquitin conjugates were not detected upon

Figure 2. Nogo-A binds to S1PR2. (A) Schematic structure of Nogo-A showing the inhibitory domains Nogo-A-Δ20 (Δ20, orange), Nogo-66 (blue), and Nogo-A-ext. Transmembrane domains are indicated in dark grey. RHD, reticulon homology domain. **(B)** Nogo-A (~200 kDa) co-immunoprecipitated with S1PR2 (~40 kDa) and vice-versa in WT but not Nogo-A$^{-/-}$ or S1PR2$^{-/-}$ brain extracts (BE). If specified, the following controls were used in WT BE instead of the IP antibody to confirm the specificity of the interaction: IgG, control antibody; Ctrl R, resin only control; qAbR, quenched antibody (Ab) resin control. Input loading control: β-Actin (~42 kDa). **(C)** S1PR2 immunoprecipitated with His-tagged Δ20 but not heat-inactivated (hi) Δ20 in S1PR2-overexpressing membranes. Input loading control: S1PR2. **(D)** His-tagged Δ20 but not hi Δ20 immunoprecipitated with S1PR2 in S1PR2-overexpressing membranes. Input loading control: S1PR2. **(E)** Nogo-A-ext bound specifically to biosensor-immobilized S1PR2-overexpressing versus control membranes (K_D~142 nM). A Scatchard plot analysis is shown on the right. **(F)** 1 μM S1P does not modulate the interaction between Nogo-A-ext and S1PR2 when compared to the methanol (MeOH) vehicle control (MeOH, K_D~192nM; S1P, K_D~202 nM). A Scatchard plot analysis is shown on the right. **(G)** Microscale thermophoresis binding analysis of Δ20 to S1PR2 extracellular domains: ECL2 (K_D~280 nM), ECL3 (K_D~350 nM), ECL1 (K_D~1.7 μM), and N-terminus (K_D~11 μM). Scrambled ECL1 (ECL1-scr) was used as control (K_D~17 μM). Arrows indicate the identified Δ20-binding loops in S1PR2. **(H)** Nogo-66 binding to S1PR2 extracellular domains is unspecific: ECL2 (K_D~7 μM), ECL1 (K_D~46μM), ECL3 (K_D~67 μM). No binding to the N-Terminus or to ECL1-scr is observed. doi:10.1371/journal.pbio.1001763.g002

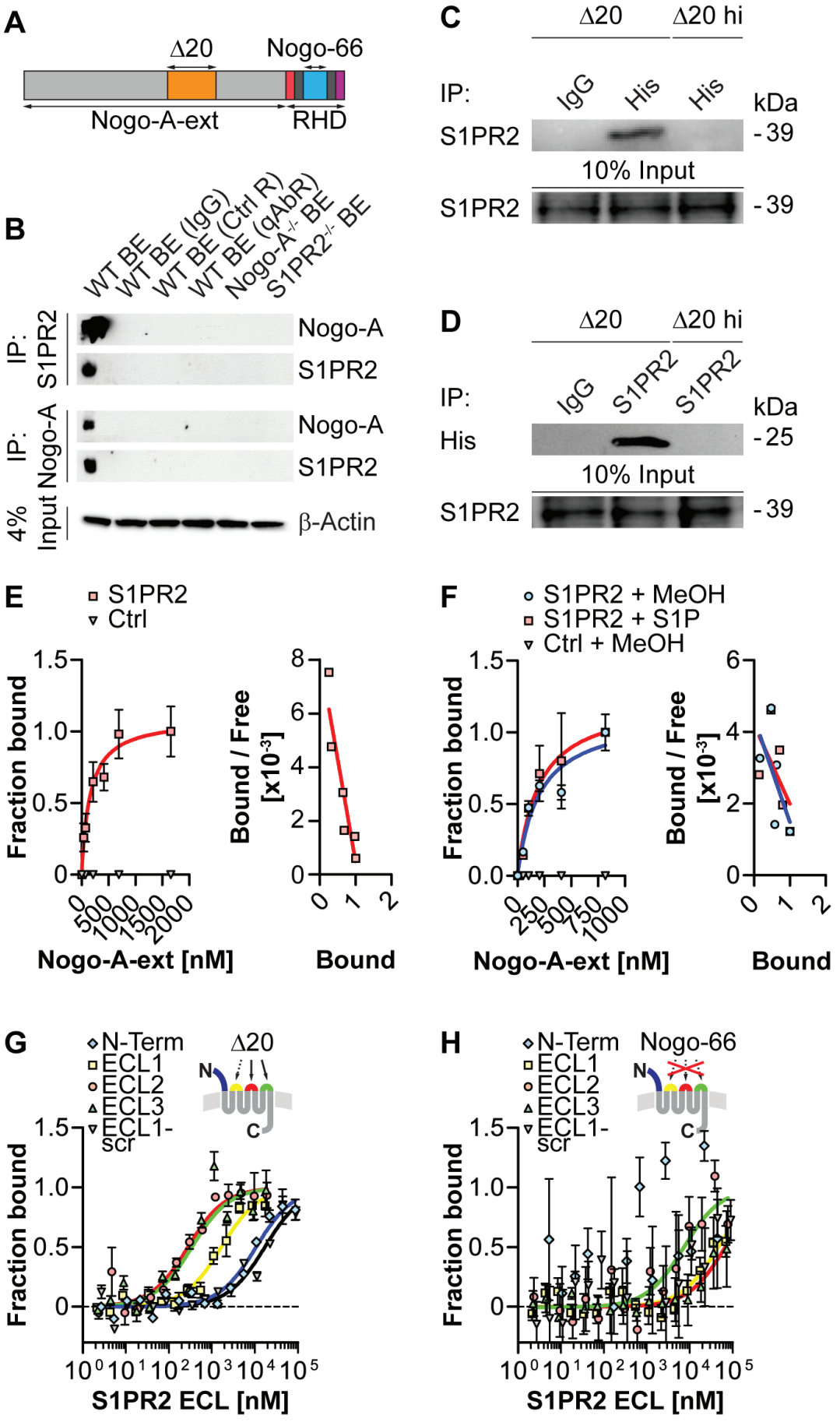
A
Δ20
Nogo-66
Nogo-A-ext
RHD
B
WT BE
WT BE (IgG)
WT BE (Ctrl R)
WT BE (qAbR)
Nogo-A-/- BE
S1PR2-/- BE
IP: S1PR2
Nogo-A
S1PR2
IP: Nogo-A
Nogo-A
S1PR2
4% Input
β-Actin
C
Δ20
Δ20 hi
IP:
IgG
His
His
kDa
S1PR2
-39
10% Input
S1PR2
-39
D
Δ20
Δ20 hi
IP:
IgG
S1PR2
S1PR2
kDa
His
-25
10% Input
S1PR2
-39
E
S1PR2
Ctrl
Fraction bound
Bound / Free [x10-3]
Nogo-A-ext [nM]
Bound
F
S1PR2 + MeOH
S1PR2 + S1P
Ctrl + MeOH
Fraction bound
Bound / Free [x10-3]
Nogo-A-ext [nM]
Bound
G
N-Term
ECL1
ECL2
ECL3
ECL1-scr
Δ20
N
C
Fraction bound
S1PR2 ECL [nM]
H
N-Term
ECL1
ECL2
ECL3
ECL1-scr
Nogo-66
N
C
Fraction bound
S1PR2 ECL [nM]

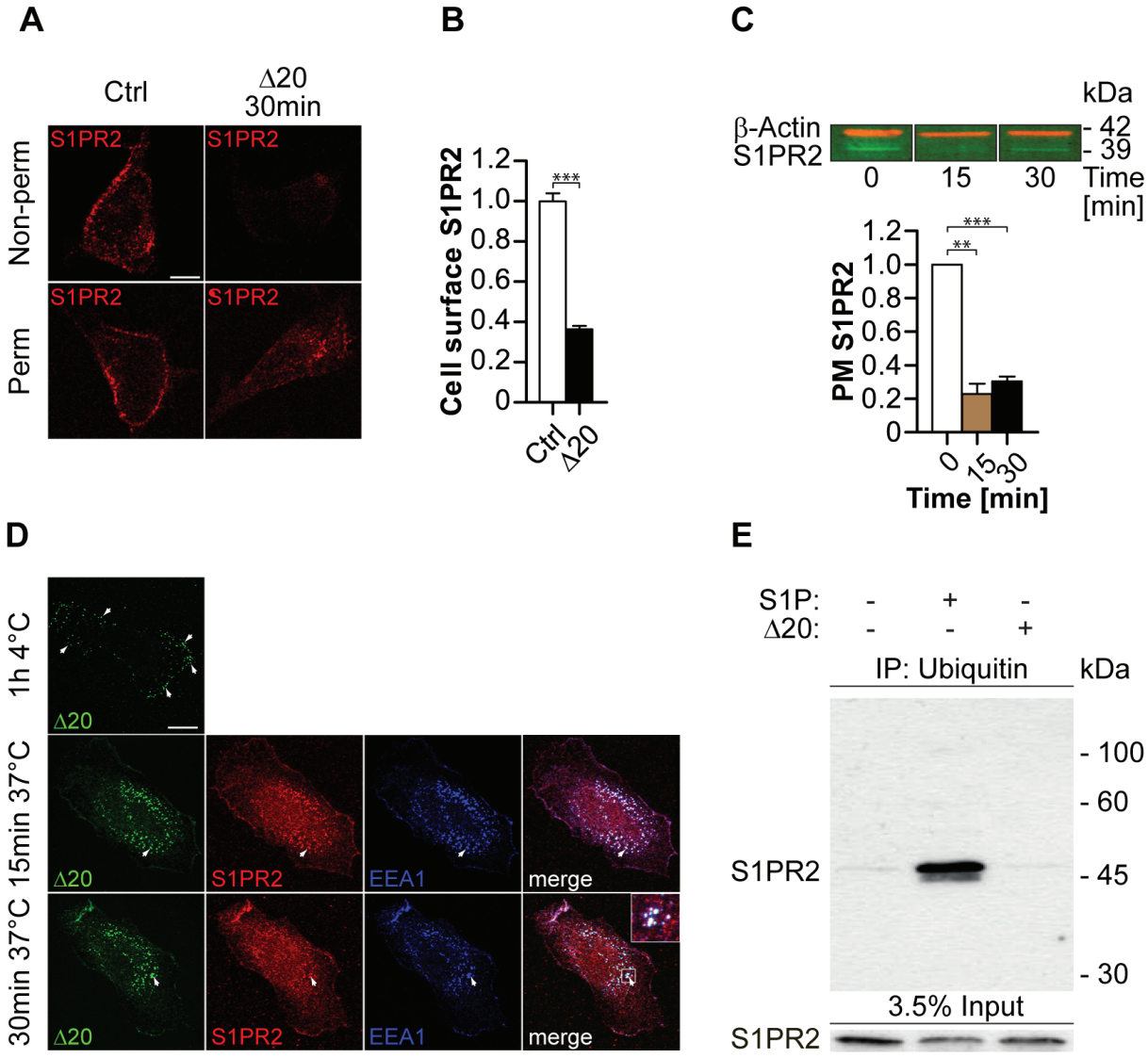

Figure 3. S1PR2 is internalized upon Nogo-A-Δ20 binding. (A) Representative confocal micrographs of 3T3 cells stained alive (Non-perm) or fixed (Perm) for S1PR2 before (control) and 30 min after Δ20 treatment at 37°C. **(B)** Mean fluorescence intensity quantification of the cell surface staining shown in (A). **(C)** Addition of Δ20 downregulates cell surface S1PR2 in 3T3 plasma membranes (PM): immunoblot and relative quantification thereof. Loading control: β-Actin. **(D)** Representative confocal micrographs of 3T3 cells incubated with 1 μM HA-tagged Δ20 for 1 h at 4°C (pulse), which were then subsequently chased for 15 and 30 min at 37°C. Cells were stained with an anti-HA (Δ20), S1PR2, or EEA1 antibody (early endosomes). Arrows indicate cell surface-bound Δ20 (top panel) or colocalization of Δ20 and S1PR2 in early endosomes (middle and bottom panel). The inset panel shows an enlarged view of the boxed region. **(E)** Western blot analysis of ubiquitinated and non-ubiquitinated protein fractions of 3T3 cells 30 min after Δ20 or S1P treatment. Data shown are means ± SEM (n = 3–6 experiments; **p<0.01, ***p<0.001). Scale bars: (A,D) 50 μm.
doi:10.1371/journal.pbio.1001763.g003

internalization of Nogo-A-Δ20 as opposed to S1P (Figure 3E), indicating that Nogo-A-Δ20 signaling is not permanently terminated in the lysosomal degradation pathway [23]–[25]. These results suggest that S1PR2 is rapidly co-internalized with Nogo-A-Δ20 into early endosomes upon binding, which is known to be a key step for Nogo-A-Δ20-mediated growth inhibition [22].

S1PR2 Mediates Nogo-A-Δ20-Induced Inhibition of Cell Spreading and Neurite Outgrowth

Nogo-A-Δ20 exerts strong inhibitory effects on growth and adhesion of different neuronal cell types and, unlike Nogo-66, also on non-neuronal cells such as 3T3 fibroblasts, which are devoid of NgR1 expression [12]. To determine the functional role of S1PR2 for Nogo-A-Δ20-mediated effects *in vitro*, the well-characterized S1PR2 blocker JTE-013 [26] was tested for its ability to reverse Nogo-A-Δ20-mediated inhibition of cell spreading. Treatment of 3T3 cells with JTE-013 significantly counteracted Nogo-A-Δ20-mediated cell spreading inhibition, resulting in an ~24% increase of spread cells when compared to vehicle (DMSO) ($p<0.05$) (Figure 4A and 4B). Similarly, on myelin, cell spreading was increased by ~56% ($p<0.001$) (Figure 4A and 4B). These effects were dose-dependent (Figure S3A) and S1PR subtype-specific (Figure S3B): blockade of S1PR1 with W146, S1PR1 and 3 with VPC-23019, S1PR1, 3, 4, and 5 with FTY-720 or S1PR5 with a function-blocking antibody [27] had no effect on Nogo-A-Δ20-mediated cell spreading inhibition (Figure S3B). In addition, no synergistic effect was observed by combining JTE-013 with any of these blocking agents (Figure S3C), suggesting that solely S1PR2 is responsible for Nogo-A-Δ20-mediated effects in 3T3 cells. To underline the functional importance of S1PR2, its expression was retrovirally silenced in 3T3 cells (sh-S1pr2; Figure S4A and S4B). Knockdown of S1PR2 resulted in a very strong increase of cell spreading on a Nogo-A-Δ20 (~51%; $p<0.001$) or myelin (~44%; $p<0.001$) substrate when compared to the control vector (sh-Vec) (Figure 4C and 4D). Similarly, primary mouse embryonic fibroblasts (MEFs) isolated from S1PR2$^{-/-}$ mice [28] were significantly less inhibited by Nogo-A-Δ20 (~41%; $p<0.01$) or myelin (~36%; $p<0.01$) when compared to wild-type (WT) MEFs (Figure 4E and 4F).

To investigate the functional importance of S1PR2 in Nogo-A-Δ20-mediated neurite outgrowth inhibition, we focused on postnatal day (P) 5–8 cerebellar granule neurons that express S1PR2 (Figure S1B). Pharmacological blockade of S1PR2 using JTE-013 led to a ~39% ($p<0.01$) and ~44% ($p<0.05$) increase in outgrowth on a Nogo-A-Δ20 and myelin substrate, respectively (Figure 4G and 4H). Similarly, knockout of S1PR2 also increased neurite outgrowth by ~51% ($p<0.001$) and ~69% ($p<0.001$) on a Nogo-A-Δ20 and myelin substrate, respectively (Figure 4I and 4J). Together, these results provide strong evidence that S1PR2 acts as a functional receptor for Nogo-A-Δ20. Importantly, application of JTE-013 had no effect on a growth-inhibitory Nogo-66 or Aggrecan substrate (Figure S5).

Nogo-A-Δ20 Signals through G_{13}, LARG, and RhoA

The G proteins G_q, G_{12}, and G_{13} were shown to interact with S1PR2 and to activate the small GTPase RhoA [16],[29]. To determine whether G_q, G_{12}, or G_{13} are implicated in Nogo-A-Δ20 mediated cell spreading inhibition, we transfected small interfering RNAs (siRNAs) targeting the

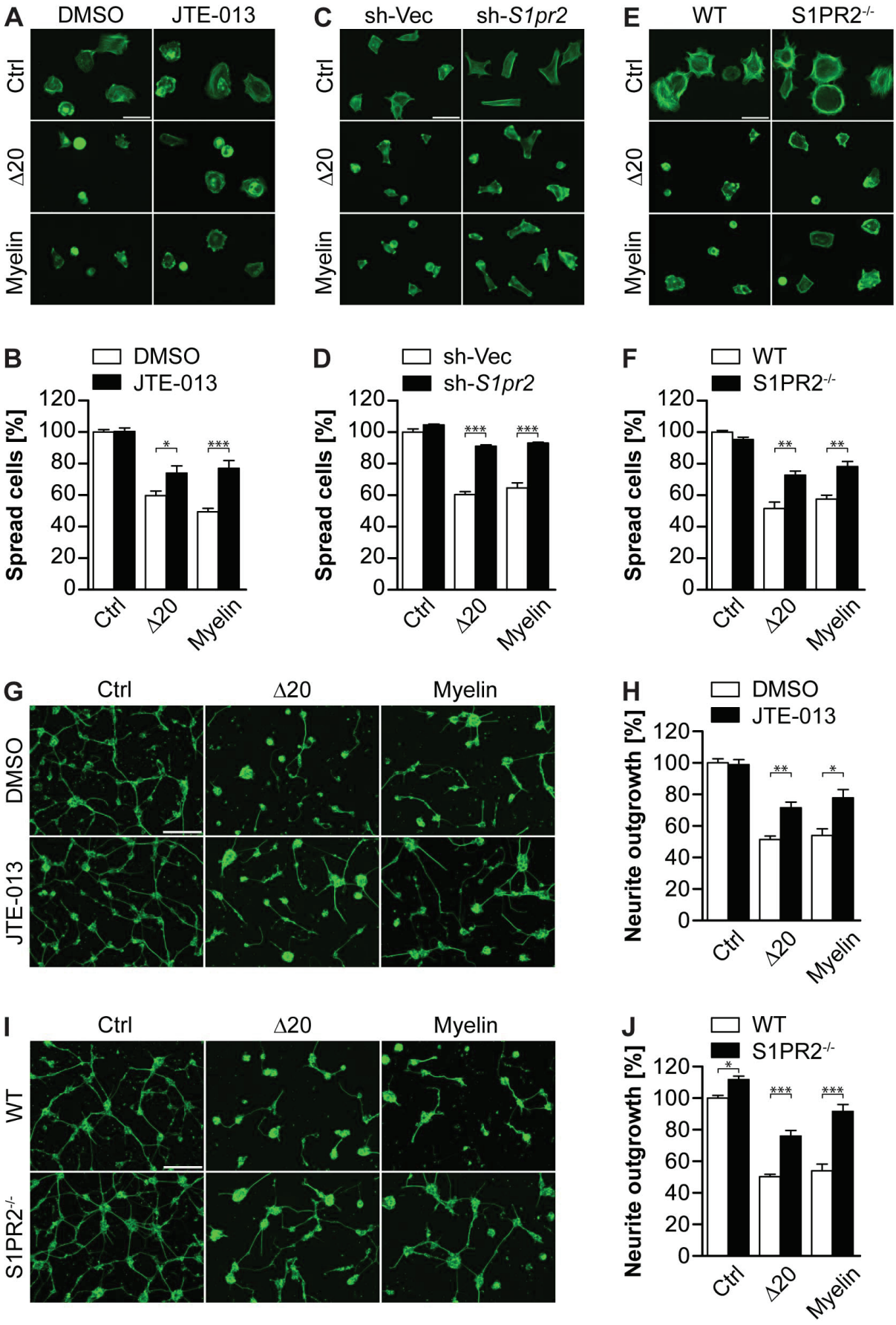
A
DMSO
JTE-013
Ctrl
Δ20
Myelin
C
sh-Vec
sh-S1pr2
E
WT
S1PR2-/-
B
D
F
Spread cells [%]
120
100
80
60
40
20
0
*
***
**
G
H
Neurite outgrowth [%]
I
J

mRNAs of the G proteins (Figure S4C and S4D). Downregulation of G_{13} but not of G_q or G_{12} fully rescued cell spreading from ~63% to ~134% on Nogo-A-Δ20 when compared to the siRNA control ($p<0.01$) (Figure 5A). No cumulative effect was observed by co-application of JTE-013, suggesting that G_{13} is a key regulator of Nogo-A-Δ20-mediated effects downstream of S1PR2 (Figure 5A). Accordingly, inhibition of the Rac1-coupled $G_{i/o}$ protein [16] with Pertussis toxin (PTX) did not have any effect on Nogo-A-Δ20-mediated cell spreading inhibition (Figure 5A). To assess whether G_{13} is also involved in Nogo-A-Δ20-mediated inhibition of neurite outgrowth, G_{13} was silenced in E19 rat cortical neurons using specific siRNAs (Figure S4E and S4F). Knockdown of G_{13} but not of G_{12} specifically rescued outgrowth from ~68% to ~87% on Nogo-A-Δ20 when compared to the siRNA control ($p<0.05$) (Figure 5B). Taken together, these results demonstrate that G_{13} is required for Nogo-A-Δ20-mediated inhibition of cell spreading and neurite outgrowth *in vitro.*

S1PR2 has been shown to couple via $G_{12/13}$ to the RhoGEF LARG to mediate various RhoA-dependent cellular effects [30]. siRNA-mediated downregulation of LARG fully rescued cell spreading from ~63% to ~103% on Nogo-A-Δ20 when compared to the siRNA control ($p<0.01$) (Figures 5A, S4C, and S4G). This is in line with LARG-mediated activation of RhoA reported for other repulsive cues such as S1P (via S1PR2 [30]), semaphorin4D (via PlexinB1 [31]), and repulsive guidance molecule RGMa (via Unc5b [32]).

To test whether Nogo-A-Δ20-induced activation of RhoA [22],[33] is S1PR2-dependent, endogenous RhoA activity was measured upon blockade or silencing of S1PR2 in 3T3 cells (Figure 5C–5F). Under control conditions, a ~2-fold increase in RhoA activation was observed after 20 min of incubation with Nogo-A-Δ20 (Figure 5C and 5D). Upon application of JTE-013 (Figure 5C and 5E) or silencing of S1PR2 (Figure 5D and 5F), RhoA activation was fully suppressed ($p<0.05$). These results suggest that S1PR2 is required for Nogo-A-Δ20-induced RhoA activation, most probably via a G_{13}-LARG signaling pathway.

Nogo-A-Δ20-Mediated Inhibition Is Modulated by Exogenous S1P

To determine possible functional interactions of Nogo-A-Δ20 and S1P at the level of S1PR2, we first investigated whether Nogo-A-Δ20 itself modulates S1P production. Extra- (EC) and

Figure 4. S1PR2 mediates Nogo-A-Δ20- and myelin-induced inhibition of cell spreading and neurite outgrowth. **(A,C)** Representative pictures of 3T3 fibroblasts treated with JTE-013 or vehicle (DMSO) (A), or stably carrying a S1pr2 shRNA (sh-S1pr2) or empty vector (sh-Vec) construct (C) and plated on control, Nogo-A-Δ20 or myelin substrates. **(B,D)** Cell spreading quantification of (A) and (C). **(E)** Representative pictures of MEFs isolated from WT or $S1PR2^{-/-}$ mice and plated on control, Nogo-A-Δ20, or myelin substrates. **(F)** Cell spreading quantification of (E). Cells were stained with Alexa488-conjugated Phalloidin in (A, C, and E). **(G,I)** Representative pictures of P5–8 cerebellar granule neurons treated with JTE-013 or DMSO (G), or isolated from $S1PR2^{-/-}$ or WT mice (I) and plated on PLL (ctrl), Nogo-A-Δ20 or myelin substrates. **(H,J)** Normalized mean neurite length per cell quantification of (G) and (I). Neurons were stained with βIII-Tubulin in (G) and (I). Data shown are means ± SEM (n = 3–6 experiments; *p<0.05, **p<0.01, ***p<0.001). Scale bars: 50 μm. doi:10.1371/journal.pbio.1001763.g004

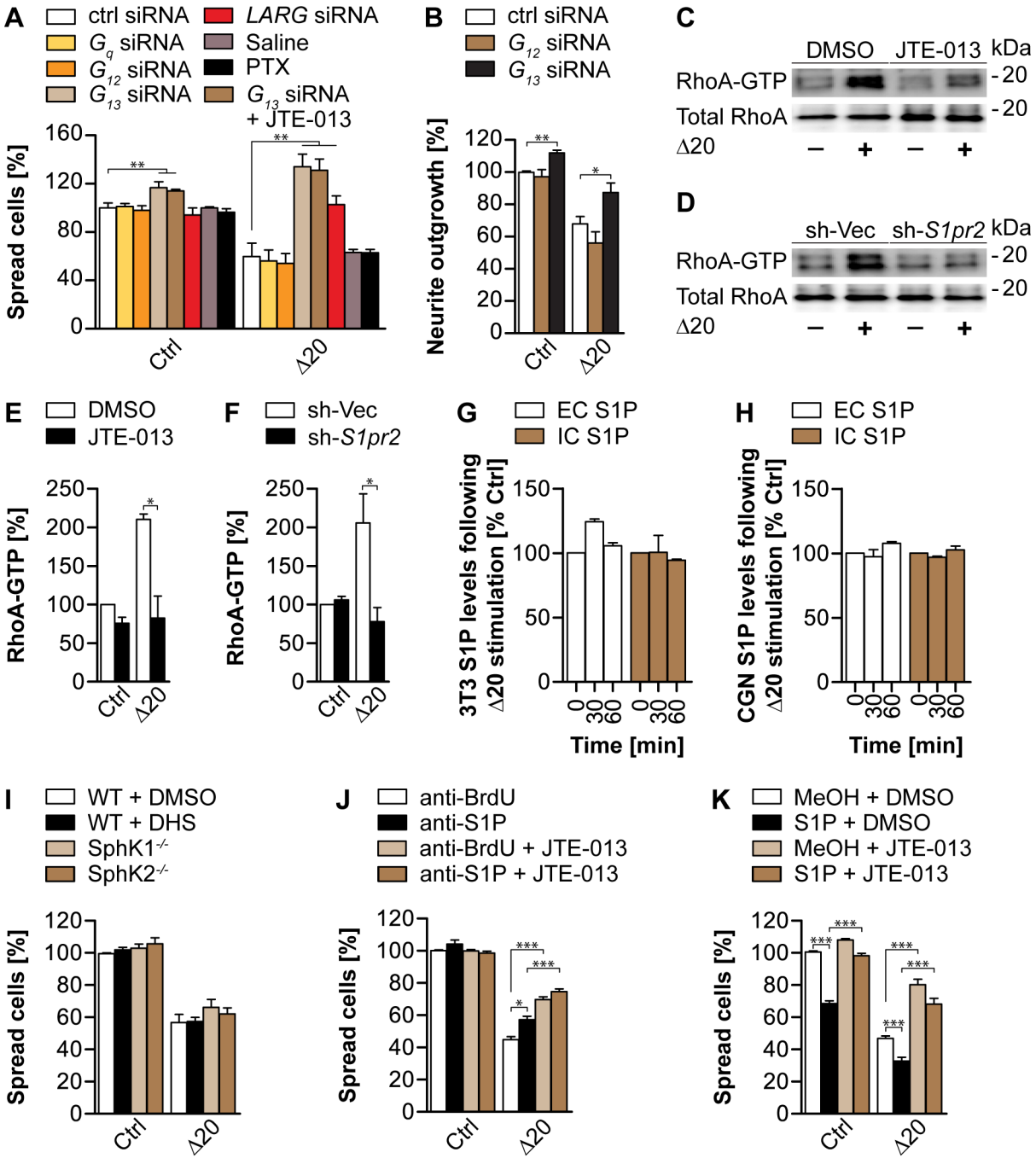

Figure 5. Nogo-A-Δ20 inhibition is mediated via the G13-LARG-RhoA signaling axis and can be modulated by exogenous S1P. (A) 3T3 cells transfected with siRNAs against G12, G13, Gq, or Larg, or control (ctrl) siRNA were replated on a Nogo-A-Δ20 substrate and assessed for cell spreading. Gi/o was blocked with Pertussis Toxin (PTX) for which saline was used as control. JTE-013 was co-applied to G13-siRNA-treated cells to investigate a cumulative effect. **(B)** Transfection of DIV4 E19 cortical neurons with siRNA against G13 but not G12 similarly rescued Nogo-A-Δ20-induced neurite outgrowth inhibition. **(C,D)** Nogo-A-Δ20-induced RhoA activation was assessed in JTE-013- versus DMSO-treated cells (C) or in cells carrying a stable knockdown of S1PR2 (sh-S1pr2) versus control vector (sh-Vec) (D). **(E,F)** Relative quantification of (C) and (D), respectively, **(G,H)** Competitive ELISA quantifications of extra- (EC) and intracellular (IC) S1P levels in 3T3 cells (G) and cerebellar granule neurons (H) before and after 30 and 60 min incubation with Nogo-A-Δ20. **(I)** Quantification of Nogo-A-Δ20-mediated cell spreading inhibition in the presence of the SphK-specific blocker D,L-threo-dihydrosphingosine (DHS) or in SphK1$^{-/-}$ or SphK2$^{-/-}$ MEFs. **(J,K)** 3T3 cells were plated on a Nogo-A-Δ20 substrate in the presence of the function blocking anti-S1P antibody Sphingomab (J) or of exogenous S1P (K) and assessed for cell spreading. Co-appliciation of JTE-013 significantly reversed the modulatory effects obtained by S1P (K) but not anti-S1P (J). Anti-BrdU antibody or methanol was used as control in (J) and (K). Data shown are means ± SEM (n = 3–6 experiments; *p<0.05, **p<0.01, ***p<0.001). doi:10.1371/journal.pbio.1001763.g005

(C)

intracellular (IC) S1P levels were quantified in 3T3 and cerebellar granule neuron cultures after a 30 and 60 min stimulation with Nogo-A-Δ20 (Figure 5G and 5H). No significant changes compared to control levels were detected, indicating that Nogo-A-Δ20 had no influence on S1P production under our experimental conditions (Figure 5G and 5H).

We then addressed the role of endogenous S1P in Nogo-A-Δ20-mediated inhibitory effects. Pharmacological blockade of the S1P-producing enzymes sphingosine kinase (SphK) 1 and 2 using D,L-threo-dihydrosphingosine (DHS) [34],[35] had no effect on Nogo-A-Δ20-mediated inhibition of cell spreading, suggesting that SphKs are not downstream elements of Nogo-A-Δ20-induced inhibition (Figure 5I). To confirm this result, MEFs isolated from SphK1$^{-/-}$ or SphK2$^{-/-}$ mice [36] were plated on a Nogo-A-Δ20 substrate. Similarly to SphK blockade, no differences in cell spreading inhibition were observed (Figure 5I).

Because S1P is found in fetal bovine serum (FBS)-containing medium [37] used in our experimental conditions, we investigated if serum-derived S1P modulates Nogo-A-Δ20-mediated inhibition. For this purpose, extracellular S1P was scavenged using the monoclonal anti-S1P antibody Sphingomab [38]. Cell spreading analysis revealed that Nogo-A-Δ20-induced inhibition was alleviated by ~28% ($p<0.05$) in the presence of the anti-S1P antibody when compared to the anti-BrdU control (Figure 5J). To exclude that disinhibition of Nogo-A-Δ20 signaling by blocking or silencing S1PR2 is mediated by an increased activation of Rac1-coupled S1PR1 through serum-derived S1P, anti-S1P was applied together with JTE-013. No differences could be observed between anti-S1P- and anti-BrdU-treated cells in the presence of JTE-013 (Figure 5J). Together, these results suggest that S1PR2-mediated inhibition by Nogo-A-Δ20 occurs independently of S1P but that S1P can modulate Nogo-A-Δ20-mediated effects. Indeed, addition of S1P to cells resulted in an ~31% ($p<0.001$) and ~28% ($p<0.001$) decrease in cell spreading inhibition on a control and Nogo-A-Δ20 substrate, respectively, when compared to the MeOH + DMSO control (Figure 5K). These results point to a modulatory function of S1P in Nogo-A-Δ20-mediated inhibition of cell spreading, presumably by independently activating RhoA-coupled cell surface S1PRs, e.g., S1PR2. Concordantly, S1P has been previously described to modulate cell adhesion and growth of different cell types [18],[27],[39]. To test this hypothesis, JTE-013 was co-applied with S1P. S1P-induced inhibition of cell spreading could be significantly reversed on a control and Nogo-A-Δ20 substrate in the presence of JTE-013 ($p<0.001$) (Figure 5K). Together, these results indicate that S1P can modulate Nogo-A-Δ20-mediated cell spreading inhibition via S1PR2. However, they also suggest that Nogo-A-Δ20 acts independently of SphK or S1P.

Nogo-A Restricts Long-Term Potentiation via S1PR2 in the Hippocampus and Motor Cortex

Growing evidence suggests that Nogo-A plays an important role in restricting synaptic plasticity [6],[9],[11]. S1PR2 is expressed in CA1 and CA3 pyramidal neurons (Figure 1A and 1B). In order to investigate the role of the Nogo-A/S1PR2 axis in long-term potentiation (LTP), hippocampal slices of WT and Nogo-A$^{-/-}$ mice were tested for LTP after acute blockade of S1PR2 using JTE-013. In WT slices, application of JTE-013 resulted in a significant increase in LTP compared with vehicle (DMSO) (~22%; $p<0.05$) (Figure 6A). In contrast, no differences in LTP were detected in Nogo-A$^{-/-}$ slices treated with JTE-013 or vehicle, suggesting that Nogo-A is required for S1PR2-mediated effects on LTP (Figure 6B). No differences in input-output (I/O) curves and paired-pulse facilitation (PPF) could be observed by application of JTE-013, suggesting that S1PR2 blockade does not alter baseline synaptic transmission or the properties of presynaptic terminals (Figure 6C–6F). In order to confirm the specificity of S1PR2, LTP was measured after blockade of the remaining S1PRs (Figure S6A and S6B). No differences in LTP and PPF could be observed upon application of VPC-23019 or FTY-720, emphasizing the specificity of a functional Nogo-A/S1PR2 interaction (Figure S6A–S6C). Next, we investigated LTP, baseline synaptic transmission as well as PPF in S1PR2$^{-/-}$ versus WT hippocampal slices. No significant changes in LTP, I/O, or PPF could be observed in S1PR2$^{-/-}$ versus WT mice (Figure S6D–S6F) as opposed to acute neutralization of S1PR2. These results mirror those obtained in Nogo-A KO [7] or NgR1 KO [8] mice and suggest that there is a strong drive for genetic compensation in this functionally very important system. [11].

Next, the outcome of a combined neutralization of the ligand Nogo-A by the function-blocking anti-Nogo-A antibody 11c7 [12] and of the receptor S1PR2 by JTE-013 was analyzed. A synergistic effect of the combined treatment as compared to either treatment alone would indicate that additional molecules, e.g., S1P are involved in S1PR2-mediated LTP restriction. A similar increase in LTP for all treated groups when compared to the IgG1 + DMSO control with no difference

Figure 6. Blockade of S1PR2 phenocopies the increase in hippocampal and cortical LTP observed upon Nogo-A neutralization. (A,B) Hippocampal WT (A) and Nogo-A$^{-/-}$ (B) slices were treated with JTE-013 or vehicle (DMSO) (WT_{DMSO}: N = 8; Nogo-$A^{-/-}{}_{DMSO}$: N = 10; $WT_{JTE\text{-}013}$: N = 11; Nogo-$A^{-/-}{}_{JTE\text{-}013}$: N = 9). 60 min after theta-burst stimulation (arrow), a significant difference in LTP could be observed between JTE-013 and DMSO treatment in WT (A) but not Nogo-A$^{-/-}$ (B) slices. **(C,D)** Input-output strength revealed no differences in JTE-013- versus DMSO-treated slices of WT (C) and Nogo-A$^{-/-}$ (D) mice (WT_{DMSO}: N = 6; Nogo-$A^{-/-}{}_{DMSO}$: N = 6; $WT_{JTE\text{-}013}$: N = 7; Nogo-$A^{-/-}{}_{JTE\text{-}013}$: N = 6). **(E,F)** PPF revealed no alterations in JTE-013- versus DMSO-treated slices of WT (E) and Nogo-A$^{-/-}$ (F) mice (WT_{DMSO}: N = 7; Nogo-$A^{-/-}{}_{DMSO}$: N = 6; $WT_{JTE\text{-}013}$: N = 5; Nogo-$A_{-/-JTE\text{-}013}$: N = 6). **(G)** LTP was measured upon simultaneous neutralization of S1PR2 using JTE-013 and of Nogo-A using 11c7 (IgG1 + DMSO: N = 7; IgG1 + JTE-013: N = 6; 11c7 + DMSO: N = 8; 11c7 + JTE-013: N = 6). **(H)** LTP was measured upon simultaneous neutralization of S1PR2 using JTE-013 and of NgR1 using anti-NgR1 (DMSO: N = 7; JTE-013: N = 9; anti-NgR1 + JTE-013: N = 8). **(I)** Rat motor forelimb area brain slices were treated with JTE-013 (N = 7) or DMSO (N = 8). Peak amplitudes were significantly larger in JTE-013- versus DMSO-treated slices upon repeated inductions of LTP (multiple arrows). **(J)** Input-output strength revealed no differences in JTE-013- (N = 8) versus DMSO-treated (N = 12) cortical slices. Insets show representative traces. Data shown are means ± SEM (*$P<0.05$). N indicates the number of mice used. doi:10.1371/journal.pbio.1001763.g006

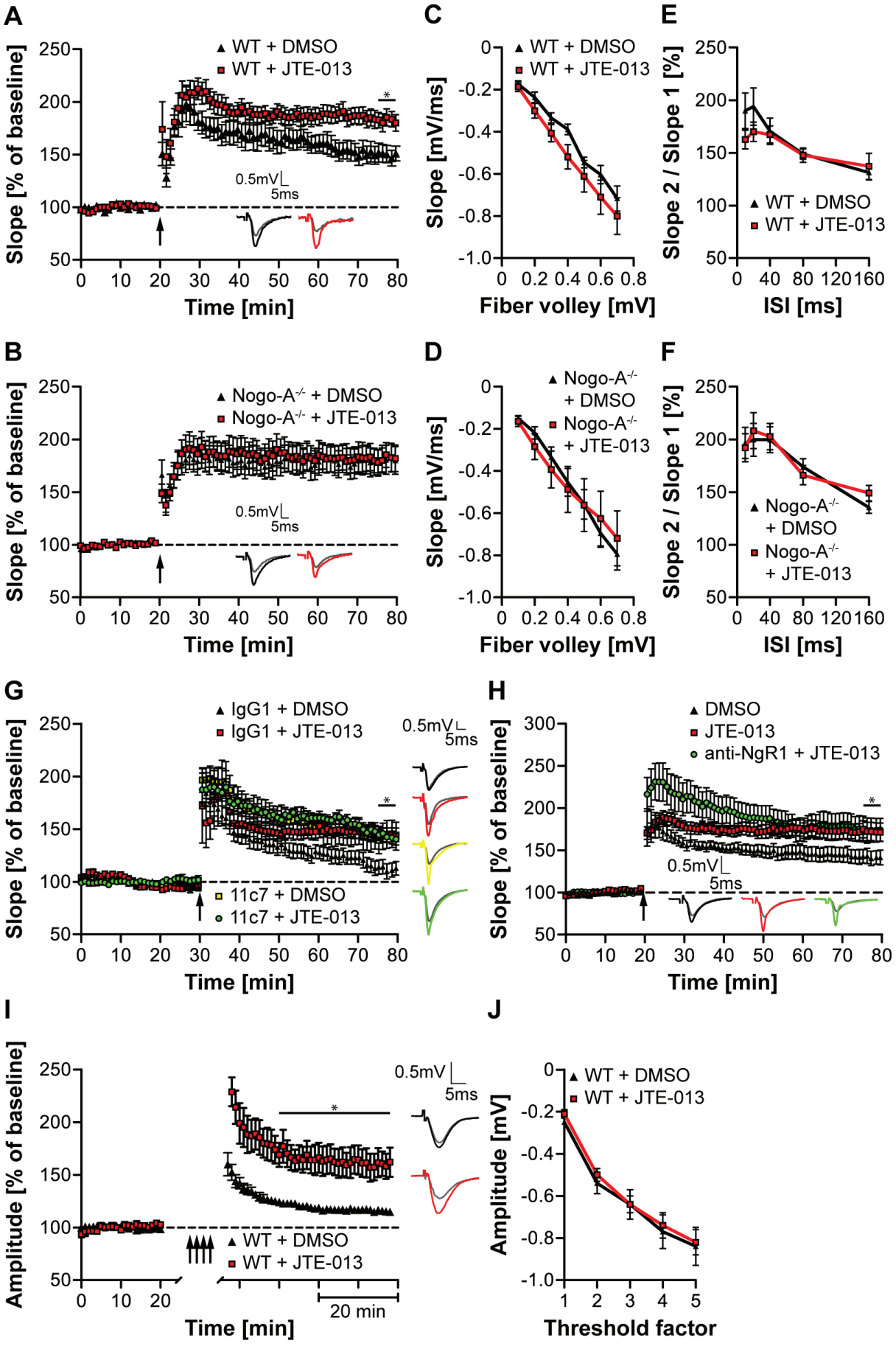
A
Slope [% of baseline]
WT + DMSO
WT + JTE-013
0.5mV
5ms
Time [min]
C
Slope [mV/ms]
WT + DMSO
WT + JTE-013
Fiber volley [mV]
E
Slope 2 / Slope 1 [%]
WT + DMSO
WT + JTE-013
ISI [ms]
B
Slope [% of baseline]
Nogo-A-/- + DMSO
Nogo-A-/- + JTE-013
0.5mV
5ms
Time [min]
D
Slope [mV/ms]
Nogo-A-/- + DMSO
Nogo-A-/- + JTE-013
Fiber volley [mV]
F
Slope 2 / Slope 1 [%]
Nogo-A-/- + DMSO
Nogo-A-/- + JTE-013
ISI [ms]
G
Slope [% of baseline]
IgG1 + DMSO
IgG1 + JTE-013
11c7 + DMSO
11c7 + JTE-013
0.5mV
5ms
Time [min]
H
Slope [% of baseline]
DMSO
JTE-013
anti-NgR1 + JTE-013
0.5mV
5ms
Time [min]
I
Amplitude [% of baseline]
WT + DMSO
WT + JTE-013
0.5mV
5ms
20 min
Time [min]
J
Amplitude [mV]
WT + DMSO
WT + JTE-013
Threshold factor

between the groups was observed (Figure 6G). To assess the relative contribution of the Nogo-A receptors NgR1 and S1PR2 onto Nogo-A-mediated restriction of synaptic plasticity, we simultaneously blocked both receptors. No significant difference could be observed between application of JTE-013 alone versus the combined application of JTE-013 and of the function-blocking anti-NgR1 antibody (Figure 6H).

Finally, we investigated the effect of S1PR2 blockade on long-term depression (LTD) in the hippocampus. In line with the results obtained after acute Nogo-A neutralization [7], JTE-013 application did neither modulate LTD induction nor maintenance compared with control conditions (Figure S6G).

Recent data indicate that Nogo-A also restricts synaptic plasticity in the primary motor cortex [11]. LTP saturation in this region was also significantly increased in JTE-013 versus DMSO-treated slices (~39%; $p<0.001$) (Figure 6I). No differences in the I/O curves were observed after S1PR2 blockade, indicating that the JTE-013-mediated increase in synaptic plasticity was not due to alterations in baseline synaptic transmission (Figure 6J). Together, these results show that Nogo-A represses synaptic plasticity in the hippocampus and motor cortex via S1PR2.

Discussion

Two distinct domains of Nogo-A can induce growth inhibition: Nogo-A-Δ20 and Nogo-66. Here, we identified the GPCR S1PR2 as the first functional receptor for the inhibitory Δ20 domain of Nogo-A. S1PR2 fulfills essential key criteria to be a Nogo-A-Δ20-specific receptor: (i) Expression in the CNS as well as in non-neuronal Nogo-A-Δ20-responsive cells; (ii) high-affinity binding to Nogo-A-Δ20; (iii) prerequisite for Nogo-A-Δ20-induced inhibition of cell spreading and neurite outgrowth; (iv) Nogo-A-Δ20-induced activation of RhoA; (v) restriction of hippocampal and cortical synaptic plasticity.

S1PR2 Is a Receptor for a Lipid and a Protein Ligand

Until very recently, GPCRs were generally thought to be activated by physical and low MW chemical stimuli [40]. However, a few adhesion GPCRs were found to also bind to membrane-bound and matrix ligands via an extended N-terminal region [41],[42]. Many of these receptors such as EGF-containing CD97, the first GPCR shown to bind to the cellular ligand decay accelerating factor, are predominantly expressed by immune cells [43]. To our knowledge, Nogo-A is the first mammalian membrane protein shown to bind to and signal through a non-orphan GPCR of the rhodopsin-like family. In contrast to adhesion GPCRs, S1PR2 does not bind Nogo-A-Δ20 via its N-terminal domain.

The recent characterization of the crystal structure of S1PR1 provided substantial structural information on its activation by S1P [19]. Access of the ligand to the binding pocket from the extracellular space is occluded by the N-terminus and the ECLs, and may be gained from within the membrane [19]. Our data provide strong evidence that Nogo-A-Δ20 primarily interacts with ECL2 and ECL3 of S1PR2, suggesting a different mechanism of activation compared to S1P. Our results also suggest that S1PR2-mediated inhibition by Nogo-A-Δ20 does not require S1P but can be exogenously modulated by the latter. Although binding of Nogo-A-Δ20 to S1PR2 does not require S1P, modulation of receptor-specific physiological outputs by binding of the bioactive lipid to its pocket within the membrane may further expand the signaling repertoire of S1PR2. It may also enable fine-tuned cellular responses depending on the ratio of ligands present under given conditions, as recently suggested for the receptor for advanced glycation endproducts (RAGE) [44]. Future biochemical and structural studies will be necessary to address this and show how binding is transferred into ligand-specific G-protein-dependent signaling. Detailed investigations will also need to determine whether the presence of additional receptors, i.e. NgR1, affects the binding properties of Nogo-A-Δ20 to S1PR2 as described for other multi-receptor systems, e.g., the viral surface glycoprotein gp120 to CD4 and the GPCR co-receptor CCR5 [45]. We could show that Nogo-A interacts with S1PR2 *in trans*. However, interaction at the surface of the same cell in cis might also be possible, similar to what has been proposed for the Nogo-A–NgR1 interaction in Purkinje cells recently [46]. Yet, such mechanisms have not been proven and their existence needs to be investigated in detail.

Multi-ligand/Multi-receptor Cross-Talk

The classic “one ligand–one receptor” paradigm has recently been challenged by an increasing number of multi-ligand/multi-receptor interactions, which could be identified in different biological systems, adding another level of complexity for fine-tuning of cellular responses [20]. Examples include neurotrophin receptors, Wnt receptors, and receptors for axonal guidance molecules such as plexins and neuropilins [20]. We propose that the Δ20 domain of Nogo-A binds to S1PR2 and the Nogo-66 loop to NgR1 and/or PirB, resulting in the formation of a multi-site/multi-ligand receptor complex. NgR1 and PirB can also interact with ligands other than Nogo-A, thereby increasing the dynamics of signal transduction [6],[9]. Additional Nogo-A co-receptors and downstream signaling components potentially located within or attached to these multi-receptor complexes might further amplify Nogo-A-mediated inhibitory effects. It was recently demonstrated that canonical GPCR signaling also occurs from endosomes for, e.g., the Wnt receptor Frizzled [47] and the β2-adrenoceptor [48]. Along this line, the Nogo-A-Δ20/S1PR2 complex is co-internalized into endosomes, from which signaling may be sustained. Currently, the concerted action and downstream trafficking of all these receptor components is still poorly

understood, in particular *in vivo*. Future studies will need to assess whether all Nogo-A (co-)receptors are found within the same complex or in different membrane microdomains, and how the receptor composition varies between different cell types, developmental stages, and pathophysiological conditions.

Interfering with Nogo-A/S1PR2 Signaling Increases Synaptic Plasticity

Nogo-A stabilizes neuronal networks by restricting CNS plasticity [2],[9]. Acute neutralization of Nogo-A or NgR1 in hippocampal slices was shown to induce an increase in LTP at CA3-CA1 synapses [7]. On the other hand, conventional knockouts of Nogo-A, PirB, or NgR1 do not show significant modulations in LTP, presumably due to compensatory mechanisms [7],[8],[10],[11],[49]. This is well in line with the lack of LTP modulation observed in S1PR2$^{-/-}$ mice. A novel transgenic rat model in which Nogo-A expression was silenced but not completely ablated by using a synthetic anti-Nogo-A microRNA leaving the genomic locus intact showed a significant increase in LTP in the hippocampus as well as in the motor cortex [11]. This underlines the strong drive for genetic compensation after complete ablation of components within this functionally very important system. Our present findings revealed an increase in hippocampal and cortical LTP when acutely interfering with S1PR2 signaling by JTE-013. Notably, no JTE-013-mediated increase in hippocampal LTP was observed in Nogo-A$^{-/-}$ mice, underlining the plasticity-restricting role of Nogo-A/S1PR2 signaling independently of S1P. Indeed, CA3–CA1 LTP was shown to be independent of SphK/S1P receptor signaling [50]. Interestingly, the blockade of both Nogo-A receptors NgR1 and S1PR2 does not show an additive effect on LTP potentiation, suggesting that both receptor-evoked responses induced by different domains of Nogo-A converge onto the same signaling pathways. However, detailed mechanisms and kinetics by which Nogo-A/S1PR2-NgR1 modify synaptic plasticity remain to be analyzed.

Conclusion

Our finding that the GPCR S1PR2 binds two structurally unrelated molecules, a low MW sphingolipid and the high MW membrane protein Nogo-A, by distinct sites contributes to and extends the paradigm shift from a classical linear model of GPCR signaling towards a more dynamic model with shared components and intramolecular cross talks [51],[52]. It will be important to understand to which extent S1P affects signaling induced by Nogo-A and vice-versa. Detailed high-resolution structural characterization of the receptor in complex with S1P, Nogo-A, or both will be required to unravel the mechanistic properties of these two signaling systems. Furthermore, the cell-specific interplay of S1PR2 with known receptors and co-receptors for Nogo-A needs to be determined in detail with regard to their corresponding physiological effects.

This information will be the basis for the design of novel molecular tools to better understand the roles of Nogo-A/S1PR2 signaling for CNS plasticity and repair.

Materials and Methods

Animals

All animal experiments were performed with the approval of and in strict accordance with the guidelines of the Zurich Cantonal Veterinary Office. All efforts were made to minimize animal suffering and to reduce the number of animals required.

S1pr2$^{-/-}$ (B6.129S6-S1pr2tm1Rlp) mice were produced by targeted mutagenesis as described previously [28] and backcrossed to C57BL/6 background.

Ensembl Accession Numbers

Accession numbers mentioned in this paper from the Ensembl Genome Browser (www.ensembl.org) are: Gna12, ENSMUSG00000000149; Gna13, ENSMUSG00000020611; Larg, ENSMUSG00000059495; RhoA, ENSMUSG00000007815; Rtn4, ENSMUSG00000020458, ENSRNOG00000004621; S1pr2, ENSMUSG00000043895.

Yeast Two-Hybrid Screen

The Nogo-A-Δ20 recombinant protein fused to the activation domain of the GAL4 transcription factor was used as bait to screen for interacting proteins from cDNAs from adult and fetal brain libraries (Clontech) using the yeast two-hybrid (Y2H) method as described previously [53]. Briefly, the cDNA encoding bait fragment was generated by PCR, cloned into pDONR201, and transferred into GATEWAY (Invitrogen)-compatible versions of pGBT9 by the LR reaction. Yeast strain CG1945 (Clontech) was transformed with the resulting vector. cDNA libraries were transformed into Y187 strain (Clontech). Bait- and prey-expressing yeasts were mated in YPDA in the presence of 10% polyethylene glycol 6000. Medium was changed to selective medium (synthetic dextrose) lacking Leu, Trp, and His with the following additives: 0.5% penicillin/streptomycin (50 μg/ml, Invitrogen), 50 μm 4-methylumbelliferyl-α-d-galactoside (Sigma), and varying concentrations of 3-amino-1, 2, 4-triazole (3-AT, Sigma). Different concentrations of 3-AT were tested in pre-screens, varying from 0–60 mM. 60 mM 3-AT produced <20% hits; 130 mM 3-AT was used in the main screen, resulting in ~0.5% strong bait-prey interactions. Mating efficiency was determined by plating of cells on selective agar plates. The cell suspension was aliquoted into microtiter plates (96 wells/plate, flat bottom, 200 μl/well) and

incubated for 3–7 days. Positive clones were screened by determining fluorescence on a SpectraFluor fluorometer (Tecan) at 465 nm (excitation at 360 nm). Wells that displayed fluorescence above background were identified and automatically collected by a Tecan Genesis 200 robot. Selected cells were passaged twice and transferred to an agar plate before PCR amplification of the library inserts. After DNA sequencing and sequence blasting, all bait-prey interactions were assessed for intrinsic prey promiscuities by comparison with in house databases containing prey information on binding frequencies obtained from previous studies [53]. Ingenuity Pathway Analysis (IPA, Ingenuity Systems) was subsequently used to identify if interaction partners signal via RhoA.

Tissue Preparation and Cell Culture

Total myelin protein extracts were prepared from the brains and spinal cords of adult Wistar rats as described previously [12]. Swiss 3T3 (ATCC), NIH 3T3 cells (ATCC), and HEK293T cells (ATCC) were maintained in DMEM containing 10% neonatal calf serum (Invitrogen). Postnatal (P5–8) cerebellar granule neurons were prepared as described previously [12]. Embryonic day (E) 19 rat cortical neurons were prepared as described previously [8]. Primary MEFs were isolated and immortalized as described previously [54]. Each primary fibroblast culture was isolated from a single E9.5 S1pr2$^{-/-}$ or WT littermate mouse.

siRNA, shRNA, and Recombinant Fusion Proteins

S1PR2 (ENST00000317726) was PCR-amplified from human blood RNA, cloned into the EcoRI/Xho sites of the pcDNA5 vector (Invitrogen) and fully sequenced. The mouse sequences of the siRNAs used are G12 (Gna12): GCGACACCAUCUUCGACAACAU, G13 (Gna13): CUGGGUGAGUCUGUAAAGUAUU, Gq (Gnaq): GCUGGUGUAUCAGAACAUC, and Larg: sc-41801 (Santa Cruz Biotechnology). The rat sequences are G12 ON-TARGETplus siRNA SMARTpool L-088001-02-0005 (Thermo Scientific) and G13 ON-TARGETplus siRNA SMARTpool L-086608-02-0005 (Thermo Scientific). A scrambled siRNA sequence was used as control (Dharmacon). NIH 3T3 cells were transfected using Lipofectamine LTX according to the manufacturer's instructions (Invitrogen). E19 cortical neurons were transfected at days in vitro (DIV) 4 using DharmaFECT 3 (Dharmacon) according to the manufacturer's instructions. Quantification of the respective mRNA knockdown was performed by qRT-PCR. Quantification of protein knockdown was performed by FACS analysis.

Silencing of S1pr2 by retroviral transduction of shRNA constructs was done by using phoenix helper-free retrovirus producer lines with pSIR delta HRCG U6 for the generation of helper-free retroviruses as described below [55]. The following shRNA construct targeting S1pr2 mRNA

transcript was used: ACCAAGGAGACGCTGGACATG [56]. Empty vector was used as control. Quantification of the respective mRNA knockdown was performed by qRT-PCR. Quantification of protein knockdown was performed by FACS analysis.

Recombinant protein Nogo-A-Δ20 (rat aa544-725) was purified as described previously [12]. Briefly, BL21/DE3 *Escherichia coli* were transformed with the pET28 expression vector (Novagen) containing His-/T7- or His-/HA-tagged Nogo-A-Δ20 and cultured at 37°C to reach an OD of 0.6 AU. Protein expression was induced by addition of 1 M IPTG for 2 h at 30°C. Fusion proteins were purified using Co_{2+}-Talon Metal Affinity Resin (Takara Bio Inc.). Nogo-A-ext (rat aa1–979) was cloned into the *Kpn*I and *Xho*I restriction sites of the pEXPR-IBA5 expression vector and the recombinant protein was purified from transiently transfected HEK293T cells using Strep-tactin chromatography (IBA).

qRT-PCR

RNA was isolated with RNeasy Micro kit (Qiagen). For synthesis of cDNA we used SuperScript III reverse transcriptase (Invitrogen). qRT-PCR was done as described before using the LightCycler 480 System (Roche, [57]). To determine the relative expression of the target genes Gna12, Gna13, Gnaq, Larg, and S1pr2 we used Tubb1 and Eef1a1 as housekeeping genes. The following primers were used: Gna12_FWD: 5′-CAT GCG ATG CTG CTA AGC TCA C-3′, Gna12_REV: 5′-TGT GTG TTC ACT CTG GGA GGT G-3′; Gna13_FWD: 5′-ACT AAC CGT GCC TCT TCA ATG GC-3′, Gna13_REV: 5′-AGG CAC CCA ACA AGA ACA CAC TG-3′; Gnaq_FWD: 5′-TGG GGA CAG GGG AGA G-3′, Gnaq_REV: 5′-TGG ATT CTC AAA AGC AGA CAC-3′; S1pr2_FWD: 5′-CAC AGC CAA CAG TCT CCA AA-3′, S1pr2_REV: 5′-TGT TCC AGA ACC TTC TCA GGA-3′; Larg_FWD: 5′-GAA TCA TCA AGG TGA ATG G-3′, Larg_REV: 5′-CTG GTG ATT CTC TCC ATA TTC-3′; Tubb1_FWD: 5′-GCA GTG CGG CAA CCA GAT-3′, Tubb1_REV: 5′-AGT GGG ATC AAT GCC ATG CT-3′; Eef1a1_FWD: 5′-TCC ACT TGG TCG CTT TGC T-3′, Eef1a1_REV: 5′-CTT CTT GTC CAC AGC TTT GAT GA-3′.

All samples were analyzed in triplicates. Melting curve analysis of PCR products followed by gel electrophoresis was performed to verify amplicons.

Antibodies and Pharmacological Blockers

The following primary antibodies were used: β Tubulin (Chemicon, MAB3408; 1:1,000), βIII Tubulin (Promega, G712A; 1:1,000), β-Actin (Sigma, A5441; 1:1,000), BrdU (AbD Serotec, function-blocking experiments: 5 µg/ml), DAPI (Invitrogen, D1306, 1:1,000), EEA1 (Cell Signaling, 2411; 1:100), GAPDH (Abcam, ab8245; 1:20,000), HA (Roche, 11867423001, 1:200), His (Santa Cruz, sc-804, 1:500), Pan-CDH (Abcam, ab6528; 1:1,000), Nogo-A (1:10,000, [58]), Nogo-A (Rb173A/Laura, 1:200), Nogo-A/B (Bianca, Rb1, 1: 20,000, [12]), Phalloidin-Alexa488

(Invitrogen; 1:500), RhoA (Cell Signaling, 2117; 1:1,000), S1PR2 (Imgenex, IMG-6135A; 1:250), S1PR2 (AbD Serotec custom made HuCAL antibody AbD14533.1 addressing extracellular S1PR2 ECL2; WB 1:1,000; IHC 1:100; TEM 1:100), S1PR2 (Santa Cruz, sc-365589; 1:500), S1PR5 (Abcam, ab13130; 1:500; function-blocking experiments: 5 μg/ml), sphingosine 1-phosphate (Funakoshi, 274594052; function-blocking experiments: 5 μg/ml), Ubiquitin (Enzo Life Sciences, UWO150; 1:1,000).

The following secondary antibodies were used: Alexa488-conjugated goat anti-mouse IgG (Invitrogen; 1:1,000), Alexa488-conjugated goat anti-rabbit IgG (Invitrogen; 1:1,000), Alexa488-conjugated goat anti-rat IgG (Invitrogen; 1:1,000), Biotin SP-conjugated AffiniPure goat anti-rabbit IgG (Jackson ImmunoResearch Laboratories; 1:250), Biotin SP-conjugated AffiniPure goat anti-human IgG F(ab′)2 fragment specific (Jackson ImmunoResearch Laboratories; 1:250), Cy3-conjugated Streptavidin (Jackson ImmunoResearch Laboratories; 1:500), Cy5 goat anti-rabbit (Invitrogen; 1:500), FITC-conjugated goat anti-human IgG (Fab specific; AbD Serotec), HRP-conjugated goat anti-human IgG (Fab specific; AbD Serotec), HRP-conjugated goat anti-rabbit IgG (Fab specific; Amersham), HRP-conjugated goat anti-mouse IgG (Fab specific; Amersham),

The following pharmacological blockers used in this study have been dissolved according to the manufacturer's instructions: W146 (Avanti Polar Lipids), VPC-23019 (Avanti Polar Lipids), JTE-013 (Tocris Bioscience), FTY-720 (Cayman Chemical), and DHS (Enzo Life Sciences). Nogo-66 was purchased from R&D Systems. Sphingosine 1-phosphate and Aggrecan were purchased from Sigma.

Binding Assays

Immobilization-based binding assays were performed on an Octet Red Instrument (fortéBIO). Recombinant S1PR2 and control membrane preparations (Millipore) were immobilized on amine-reactive biosensors (25 μg/ml; fortéO) in HBSN running buffer (BIAcore) supplemented with 10 mM $MgCl_2$. Nogo-A-ext protein was serially diluted and allowed to bind the saturated biosensor tips for 15 min at 1,000 rpm at 30°C. For experiments including S1P, 1 μM S1P was added together with Nogo-A-ext. Methanol was used as vehicle control. The binding response was normalized for baselines differences between runs and binding affinities (K_D) were calculated from a nonlinear fit according to the double-reference subtraction method in GraphPad Prism5 (GraphPad software). Data shown are the average of three to five experiments per condition.

Microscale thermophoresis ligand binding measurements were performed using a Nanotemper Monolith NT.115 (Nano Temper technologies) as previously described [59]–[60]. Briefly, recombinant Nogo-A-Δ20 was fluorescently labeled using the Amine Reactive Protein labeling kit RED (L001, Nano Temper technologies). The N-terminus and individual ECLs of S1PR2 were synthesized as peptides (JPT Peptide Technologies, sequences: N-terminus,

MGGLYSEYLNPEKVQEHYNYTKETLDMQETPSRK; ECL1, LSGHVTLSLTPVQW; ECL2, NCLNQLEAC-STVLPLYAKHYVL; ECL3, SILLLDSTCPVRACPVLYK; ECL1-scrambled negative control, VGLSQV-WTSLPTLH). A constant concentration of Nogo-A-Δ20 (~40 nM) was incubated with the different serially diluted peptides in PBS containing 0.025% Tween-20 at pH 7.4. 3–5 µl of each sample was loaded into a hydrophilic glass capillary (K004, Nano Temper technologies) and thermophoresis analysis was performed (LED 60%, IR Laser 20%) [59],[60]. MST data were normalized for baseline differences between runs and K_D values were calculated using non-linear regression assuming a Hill coefficient of 1.0 (GraphPad Prism).

Immunoprecipitation was performed with Nogo-A-Δ20 and S1PR2 membrane preparations using the His Protein Interaction Pull-Down kit following the manufacturer's instructions (Pierce). Heat-inactivated Nogo-A-Δ20 was used as control.

Co-immunoprecipitation was done using whole mouse brain tissue from P10 Nogo-$A^{-/-}$, $S1PR2^{-/-}$, and WT mice. Briefly, tissue was lysed with RIPA buffer (50 mM Tris-HCl [pH 7.2], 150 mM NaCl, 0.1% SDS, 0.5% Na.Deoxycholate, 1% NP-40) containing cOmplete Mini EDTA-free protease inhibitor cocktail tablets (Roche). Co-Immunoprecipitation was performed using the Pierce Co-IP Kit (Pierce 26149) according to the manufacturer's instructions.

In Vitro Bioassays

3T3 fibroblast spreading assays and P5-8 cerebellar granule neurons neurite outgrowth assays were performed as described previously [12]. Briefly, four-well plates (Greiner) were coated with 40 pmol/cm^2 Nogo-A-Δ20 or 5 µg/cm^2 myelin at 4°C overnight. Nogo-66 Fc was used at a concentration of 500 nM and Aggrecan at 1,000 ng/ml. In outgrowth experiments, wells were precoated with 0.3 µg/ml for 1 h at 37°C before addition of the different substrates. 3T3 cells were plated at 7,000 cells per cm^2 for 1 h at 37°C and 5% CO_2, fixed with 4% paraformaldehyde (PFA) and stained with Phalloidin-Alexa-488. Mouse P5-8 cerebellar granule neurons were plated at 7.5×10^4 cells per cm^2, cultured for 24 h at 37°C and 5% CO_2, fixed with 4% PFA and stained with anti-βIII tubulin. Each experiment was performed at least three times in four replicate wells. Spreading was quantified manually in a blinded manner and mean neurite length was quantified using the MetaMorph software (Molecular Devices). The mean neurite length is referred to as the mean total length of all neurites per cell. 3T3 cells were classified as spread cells if they bear at least two lammelipodial processes longer than one cell body diameter. Round cells were classified as non-spread. Data were normalized to baseline and plotted as average ± standard error of the mean (SEM). Cells were imaged with a Leica DM5500B microscope equipped with HCX PL FL Dry 10×/0.3 and 20×/0.5 objectives in a semi-automated way. Statistical analysis was performed in GraphPad Prism5 using a one-way ANOVA test followed by a Bonferroni post hoc test or by using

an unpaired Student's t-test. All inhibitors were used at a concentration of 100 nM if not elsewhere specified.

Internalization Assays and Flow Cytometry Analysis

Plasma membranes of 3T3 cells were prepared as described before [61] and after treatment with 1 μM T7-tagged Nogo-A-Δ20. Nogo-A-Δ20 internalization assays were performed as described previously after treatment of 3T3 cells with 1 μM HA-tagged Nogo-A-Δ20 [22]. Briefly, 3T3 cells were incubated with 1 μM Nogo-A-Δ20 for 1 h on ice (pulse) and subsequently chased for 15 and 30 min at 37°C. Flow cytometry-based quantification of S1PR2, G13, and LARG expression on 3T3 cells and CGNs, respectively, was done in a BD FACSCalibur.

Ubiquitination Assay

3T3 cells were starved in serum-free medium for 24 h. 1 μM S1P or Nogo-A-Δ20, respectively, was added to 3T3 cells for 60 min. Isolation of ubiquitinated protein fractions was done using UbiCapture-Q (Enzo Life Sciences). Finally, western blot analysis was performed to detect S1PR2 and ubiquitin.

RhoA Pulldown

3T3 cells were serum-starved overnight and treated for 20 min with 1 μM Nogo-A-Δ20 or heat-inactivated Nogo-A-Δ20 control protein. Pulldown of activated RhoA-GTP was subsequently performed using the RhoA Activation Assay Biochem Kit according to the manufacturer's instructions (Cytoskeleton, Inc.).

S1P Quantification

3T3 cells or CGNs were cultured up to 80%–85% confluence in 15 cm dishes and serum starved for 24 h prior to the experiment. Nogo-A-Δ20 was added to the cells at a concentration of 1 μM. After 15, 30, and 60 min, 3T3 cells and CGNs were lysed in 400 μl lysis buffer (20 mM PIPES, 150 mM NaCl, 1 mM EGTA, 1% v/v Triton X-100, 1.5 mM $MgCl_2$, pH 7.4). Lysates were frozen immediately at −80°C. Protein concentration was measured and cell lysates (1:10 in delipidized human sera) were analyzed with the Echelon S1P ELISA kit according to the manufacturer's instruction. Serum free cell culture medium was directly diluted 1:10 in delipidized human serum and subsequently analyzed with the S1P ELISA kit.

Immunohistochemistry

Immunohistochemistry was performed as described previously [62]. Briefly, animals were transcardially perfused with Ringer's solution, followed by 4% PFA. Prior to staining, sections were treated with 0.2% glutaraldehyde and 50 mM Tris-glycine (pH 8.0). After antigen retrieval via microwaving three times for 10 s at 600 W, the sections were treated with Kryofix (Merck) for 10 min followed by 0.3% Triton X-100 for 10 min. S1PR2 was detected with AbD14533.1 and corresponding secondary antibodies.

3T3 cells and CGNs were fixed with 4% PFA for 15 min, washed, and permeabilized with 0.1% Triton X-100. After blocking with 2% goat serum, cells were first incubated with AbD14533.1 and detected using Cy3-conjugated Streptavidin.

For cell surface immunocytochemical detection of S1PR2, 3T3 cells were incubated with 50 μg/ml AbD14533.1 in serum-free medium containing 0.02% sodium azide for 20 min on ice. Cells were washed and fixed with 0.5% PFA. After blocking (4% fetal calf serum, 2% horse serum, 0.1% cold water fish gelatine, 0.1% casein) on ice, cells were first incubated with biotinylated goat anti-human IgG, biotinylated rabbit anti-goat, and, finally, with Cy3-conjugated Streptavidin.

Electrophysiology

Hippocampus.

Acute hippocampal slices were prepared from 40–60 day old (P40–P60) WT C57BL/6 mice or Nogo-A$^{-/-}$ mice according to standard procedures. In brief, mice were anesthetized and decapitated; the brain was quickly transferred into ice-cold carbogenated (95% O_2, 5% CO_2) artificial cerebrospinal fluid (ACSF). Hippocampi were cut with a vibratome (400 μm; VT 1000S; Leica). The ACSF used for electrophysiological recordings contained 125 mM NaCl, 2 mM KCl, 1.25 mM NaH_2PO_4, 1 mM $MgCl_2$, 26 mM $NaHCO_3$, 2 mM $CaCl_2$, 25 mM glucose. Recordings were done at 32°C.

Blockade of S1PR2 was achieved by incubation of acute slices with JTE-013, blockade of S1PR1, 3, 4, 5 with FTY-720 and blockade of S1PR1, 3 with VPC-23019, respectively. The inhibitors were dissolved in DMSO and freshly added at a final concentration of 5 μM, 1 μM, and 0.1 μM, respectively, to the carbogenated ACSF. The DMSO overall concentration in the ACSF was kept at 0.01%. As control DMSO alone was added. In order to compare the data with previous experiments silicon tubing was used, and pre-washed with ACSF containing BSA (0.1 mg/ml). The slices were pre-incubated for 1 h (or 10 min for the experiments in which JTE-013 and 11c7 were combined) with the inhibitor or DMSO as control in an incubation chamber maintaining a constant flow of the solution. During the experiments the inhibitor was also around. For the

electrophysiological recordings, the perfusion rate in the recording chamber was constantly kept at 1.5 ml/min.

After placing the slices in a submerged recording chamber field, excitatory postsynaptic potentials (fEPSPs) were recorded in the stratum radiatum of the CA1 region with a glass micropipette (resistance 3–15 MΩ filled with 3 M NaCl at a depth of ~100 μm. Monopolar tungsten electrodes were used for stimulating the Schaffer collaterals at a frequency of 0.1 Hz. Stimulation was set to elicit a fEPSP with a slope of ~40%–50% of maximum for LTP recordings. After 20 min baseline stimulation LTP was induced by applying theta-burst stimulation (TBS), in which a burst consisted of four pulses at 100 Hz. These were repeated 10 times in 200 ms intervals (5 Hz). Three such trains were used to induce LTP at 0.1 Hz. Basic synaptic transmission and presynaptic properties were analyzed via I/O measurements and paired pulse facilitation. The I/O measurements were performed either by application of a defined value of current (25–250 μA in steps of 25 μA) or by adjusting the stimulus intensity to a certain current eliciting a fiber volley (FV) of desired voltage. Paired pulse facilitation was performed by applying a pair of two stimuli in different inter-stimulus-intervals (ISIs), ranging from 10, 20, 40, and 80 to 160 ms. Data were collected, stored, and analyzed with LABVIEW software (National Instruments). The initial slope of fEPSPs elicited by stimulation of the Schaffer collaterals was measured over time, normalized to baseline, and plotted as average ± SEM.

Motor cortex.

For LTP measurements in the motor cortex [11], coronal slices containing the forelimb are of M1 (1–2 mm anterior to the bregma [63]), and were prepared from adult Sprague Dawley rats (180–220 g). JTE-013 concentrations were used according to protocols used for hippocampal slices and added to the ACSF: 126 mM NaCl, 3 mM KCl, 1.25 mM NaH_2PO_4, 26 mM $NaHCO_3$, 1 mM $MgSO_4$, 2 mM $CaCl_2$, and 10 mM glucose, bubbled with a 95% O_2, 5% CO_2 mixture at 33±0.5°C). To allow optimal JTE-013 penetration, responses were recorded from the slice superface of layer II/III within M1. Basic synaptic transmission was analyzed with I/O analysis. I/O measurements were conducted by applying a value of current, which elicited a minimal (threshold) evoked response (0.2–0.3 mV). I/O curves were obtained by averaging field potential peak amplitudes of three responses to stimuli of two, three, four, and five times the threshold response. To elicit the maximum amplitude that could be evoked, we used a stimulation intensity of 25× threshold [64],[65]. For baseline measurements, stimulus intensity was adjusted to produce responses 40%–50% of the maximum amplitude. For data analysis, we computed the amplitude of the field potential response because it serves as a measure of the population excitatory synaptic response [65], reflects a monosynaptic current sink [66], and correlates well with the intracellular excitatory postsynaptic response evoked in this pathway [67]. Measurement of the field potential

slope, as routinely used, e.g., in the hippocampus, has not been used for neocortical field potential responses due to the interference of the response's initial part by variable nonsynaptic components [68]. After 20 min of baseline stimulation, focal and transient reduction of γ-aminobuturic acid-A (GABA) inhibition at the recording site was produced by applying bicuculline methiodide (3.3 mM, Tocris Bioscience) from a micropipette by touching the tip to the slice surface within 100 μm of the recording microelectrode for 15–60 s. The pipette was removed when the amplitude of test responses increased 50%–100% of baseline [66]. Immediately after bicuculline application, LTP was attempted by delivering TBS at double baseline stimulation intensity. LTP induction was attempted by using TBS, which consisted of 10 trains of stimuli at 5 Hz. Each train was composed of four pulses at 100 Hz. This sequence was delivered every 10 s for a total of five presentations. LTP was recorded for at least 20 min after it reached a stable plateau. TBS was induced until responses were saturated. Pathways were considered saturated if the difference between two subsequent states of LTP were not significantly different [68]. Maximum LTP was calculated as a percentage of baseline, plotted as average ± SEM and analyzed by a Student's t-test. Data were collected, stored, and analyzed with LABVIEW (National Instruments) and MATLAB (MathWorks) software.

References

1. Akbik FV, Cafferty WB, Strittmatter SM (2012) Myelin associated inhibitors: a link between injury-induced and experience-dependent plasticity. Exp Neurol 235: 43–52. doi: 10.1016/j.expneurol.2011.06.006
2. Schwab ME (2010) Functions of Nogo proteins and their receptors in the nervous system. Nat Rev Neurosci 11: 799–811. doi: 10.1038/nrn2936
3. Filbin MT (2003) Myelin-associated inhibitors of axonal regeneration in the adult mammalian CNS. Nat Rev Neurosci 4: 703–713. doi: 10.1038/nrn1195
4. Schwab ME (2004) Nogo and axon regeneration. Curr Opin Neurobiol 14: 118–124. doi: 10.1016/j.conb.2004.01.004
5. Yiu G, He Z (2006) Glial inhibition of CNS axon regeneration. Nat Rev Neurosci 7: 617–627. doi: 10.1038/nrn1956
6. Kempf A, Schwab ME (2013) Nogo-A represses anatomical and synaptic plasticity in the central nervous system. Physiology 28: 151–163. doi: 10.1152/physiol.00052.2012
7. Delekate A, Zagrebelsky M, Kramer S, Schwab ME, Korte M (2011) NogoA restricts synaptic plasticity in the adult hippocampus on a fast time scale. Proc Natl Acad Sci U S A 108: 2569–2574. doi: 10.1073/pnas.1013322108
8. Lee H, Raiker SJ, Venkatesh K, Geary R, Robak LA, et al. (2008) Synaptic function for the Nogo-66 receptor NgR1: regulation of dendritic spine morphology and activity-dependent synaptic strength. J Neurosci 28: 2753–2765. doi: 10.1523/jneurosci.5586-07.2008
9. Mironova YA, Giger RJ (2013) Where no synapses go: gatekeepers of circuit remodeling and synaptic strength. Trends Neurosci 36: 363–373. doi: 10.1016/j.tins.2013.04.003
10. Raiker SJ, Lee H, Baldwin KT, Duan Y, Shrager P, et al. (2010) Oligodendrocyte-myelin glycoprotein and Nogo negatively regulate activity-dependent synaptic plasticity. J Neurosci 30: 12432–12445. doi: 10.1523/jneurosci.0895-10.2010
11. Tews B, Schonig K, Arzt ME, Clementi S, Rioult-Pedotti MS, et al. (2013) Synthetic microRNA-mediated downregulation of Nogo-A in transgenic rats reveals its role as regulator of synaptic plasticity and cognitive function. Proc Natl Acad Sci U S A 110: 6583–6588. doi: 10.1073/pnas.1217665110
12. Oertle T, van der Haar ME, Bandtlow CE, Robeva A, Burfeind P, et al. (2003) Nogo-A inhibits neurite outgrowth and cell spreading with three discrete regions. J Neurosci 23: 5393–5406.
13. Fournier AE, GrandPre T, Strittmatter SM (2001) Identification of a receptor mediating Nogo-66

inhibition of axonal regeneration. Nature 409: 341–346. doi: 10.1038/35053072

14. Atwal JK, Pinkston-Gosse J, Syken J, Stawicki S, Wu Y, et al. (2008) PirB is a functional receptor for myelin inhibitors of axonal regeneration. Science 322: 967–970. doi: 10.1126/science.1161151

15. Hu F, Strittmatter SM (2008) The N-terminal domain of Nogo-A inhibits cell adhesion and axonal outgrowth by an integrin-specific mechanism. J Neurosci 28: 1262–1269. doi: 10.1523/jneurosci.1068-07.2008

16. Spiegel S, Milstien S (2003) Sphingosine-1-phosphate: an enigmatic signalling lipid. Nat Rev Mol Cell Biol 4: 397–407. doi: 10.1038/nrm1103

17. Singh IN, Hall ED (2008) Multifaceted roles of sphingosine-1-phosphate: how does this bioactive sphingolipid fit with acute neurological injury? J Neurosci Res 86: 1419–1433. doi: 10.1002/jnr.21586

18. Toman RE, Payne SG, Watterson KR, Maceyka M, Lee NH, et al. (2004) Differential transactivation of sphingosine-1-phosphate receptors modulates NGF-induced neurite extension. J Cell Biol 166: 381–392. doi: 10.1083/jcb.200402016

19. Hanson MA, Roth CB, Jo E, Griffith MT, Scott FL, et al. (2012) Crystal structure of a lipid G protein-coupled receptor. Science 335: 851–855. doi: 10.1126/science.1215904

20. Ben-Shlomo I, Hsueh AJ (2005) Three's company: two or more unrelated receptors pair with the same ligand. Mol Endocrinol 19: 1097–1109. doi: 10.1210/me.2004-0451

21. Kenakin T (2003) Ligand-selective receptor conformations revisited: the promise and the problem. Trends Pharmacol Sci 24: 346–354. doi: 10.1016/s0165-6147(03)00167-6

22. Joset A, Dodd DA, Halegoua S, Schwab ME (2010) Pincher-generated Nogo-A endosomes mediate growth cone collapse and retrograde signaling. J Cell Biol 188: 271–285. doi: 10.1083/jcb.200906089

23. Hanyaloglu AC, von Zastrow M (2008) Regulation of GPCRs by endocytic membrane trafficking and its potential implications. Annu Rev Pharmacol Toxicol 48: 537–568. doi: 10.1146/annurev.pharmtox.48.113006.094830

24. Verzijl D, Peters SL, Alewijnse AE (2010) Sphingosine-1-phosphate receptors: zooming in on ligand-induced intracellular trafficking and its functional implications. Mol Cells 29: 99–104. doi: 10.1007/s10059-010-0041-z

25. Oo ML, Thangada S, Wu MT, Liu CH, Macdonald TL, et al. (2007) Immunosuppressive and anti-angiogenic sphingosine 1-phosphate receptor-1 agonists induce ubiquitinylation and proteasomal degradation of the receptor. J Biol Chem 282: 9082–9089. doi: 10.1074/jbc.m610318200

26. Marsolais D, Rosen H (2009) Chemical modulators of sphingosine-1-phosphate receptors as barrier-oriented therapeutic molecules. Nat Rev Drug Discov 8: 297–307. doi: 10.1038/nrd2356

27. Strochlic L, Dwivedy A, van Horck FP, Falk J, Holt CE (2008) A role for S1P signalling in axon guidance in the Xenopus visual system. Development 135: 333–342. doi: 10.1242/dev.009563

28. Kono M, Mi Y, Liu Y, Sasaki T, Allende ML, et al. (2004) The sphingosine-1-phosphate receptors S1P1, S1P2, and S1P3 function coordinately during embryonic angiogenesis. J Biol Chem 279: 29367–29373. doi: 10.1074/jbc.m403937200

29. Takashima S, Sugimoto N, Takuwa N, Okamoto Y, Yoshioka K, et al. (2008) G12/13 and Gq mediate S1P2-induced inhibition of Rac and migration in vascular smooth muscle in a manner dependent on Rho but not Rho kinase. Cardiovasc Res 79: 689–697. doi: 10.1093/cvr/cvn118

30. Medlin MD, Staus DP, Dubash AD, Taylor JM, Mack CP (2010) Sphingosine 1-phosphate receptor 2 signals through leukemia-associated RhoGEF (LARG), to promote smooth muscle cell differentiation. Arterioscler Thromb Vasc Biol 30: 1779–1786. doi: 10.1161/atvbaha.110.209395

31. Swiercz JM, Kuner R, Behrens J, Offermanns S (2002) Plexin-B1 directly interacts with PDZ-RhoGEF/LARG to regulate RhoA and growth cone morphology. Neuron 35: 51–63. doi: 10.1016/s0896-6273(02)00750-x

32. Hata K, Kaibuchi K, Inagaki S, Yamashita T (2009) Unc5B associates with LARG to mediate the action of repulsive guidance molecule. J Cell Biol 184: 737–750. doi: 10.1083/jcb.200807029

33. Niederost B, Oertle T, Fritsche J, McKinney RA, Bandtlow CE (2002) Nogo-A and myelin-associated glycoprotein mediate neurite growth inhibition by antagonistic regulation of RhoA and Rac1. J Neurosci 22: 10368–10376.

34. Dragusin M, Gurgui C, Schwarzmann G, Hoernschemeyer J, van Echten-Deckert G (2003) Metabolism of the unnatural anticancer lipid safingol, L-threo-dihydrosphingosine, in cultured cells. J Lipid Res 44: 1772–1779. doi: 10.1194/jlr.m300160-jlr200

35. Liu H, Sugiura M, Nava VE, Edsall LC, Kono K, et al. (2000) Molecular cloning and functional characterization of a novel mammalian sphingosine kinase type 2 isoform. J Biol Chem 275: 19513–19520. doi: 10.1074/jbc.m002759200

36. Olivera A, Eisner C, Kitamura Y, Dillahunt S, Allende L, et al. (2010) Sphingosine kinase 1 and sphingosine-1-phosphate receptor 2 are vital to recovery from anaphylactic shock in mice. J Clin Invest 120: 1429–1440. doi: 10.1172/jci40659

37. Miller E, Yang J, DeRan M, Wu C, Su AI, et al. (2012) Identification of serum-derived sphingosine-1-phosphate as a small molecule regulator of YAP. Chem Biol 19: 955–962. doi: 10.1016/j.chembiol.2012.07.005

38. Ponnusamy S, Selvam SP, Mehrotra S, Kawamori T, Snider AJ, et al. (2012) Communication between host organism and cancer cells is transduced by systemic sphingosine kinase 1/sphingosine 1-phosphate signalling to regulate tumour metastasis. EMBO Mol Med 4: 761–775. doi: 10.1002/emmm.201200244

39. Lebman DA, Spiegel S (2008) Cross-talk at the crossroads of sphingosine-1-phosphate, growth factors, and cytokine signaling. J Lipid Res 49: 1388–1394. doi: 10.1194/jlr.r800008-jlr200

40. Liebscher I, Schoneberg T, Promel S (2013) Progress in demystification of adhesion GPCR. Biol Chem doi: 10.1515/hsz-2013-0109

41. Yona S, Lin HH, Siu WO, Gordon S, Stacey M (2008) Adhesion-GPCRs: emerging roles for novel receptors. Trends Biochem Sci 33: 491–500. doi: 10.1016/j.tibs.2008.07.005

42. Paavola KJ, Hall RA (2012) Adhesion G protein-coupled receptors: signaling, pharmacology, and mechanisms of activation. Mol Pharmacol 82: 777–783. doi: 10.1124/mol.112.080309

43. Hamann J, Vogel B, van Schijndel GM, van Lier RA (1996) The seven-span transmembrane receptor CD97 has a cellular ligand (CD55, DAF). J Exp Med 184: 1185–1189. doi: 10.1016/s0165-2478(97)85807-5

44. Sparvero LJ, Asafu-Adjei D, Kang R, Tang D, Amin N, et al. (2009) RAGE (Receptor for Advanced Glycation Endproducts), RAGE ligands, and their role in cancer and inflammation. J Transl Med 7: 17. doi: 10.1186/1479-5876-7-17

45. Lee C, Liu QH, Tomkowicz B, Yi Y, Freedman BD, et al. (2003) Macrophage activation through CCR5- and CXCR4-mediated gp120-elicited signaling pathways. J Leukoc Biol 74: 676–682. doi: 10.1189/jlb.0503206

46. Petrinovic MM, Hourez R, Aloy EM, Dewarrat G, Gall D, et al. (2013) Neuronal Nogo-A negatively regulates dendritic morphology and synaptic transmission in the cerebellum. Proc Natl Acad Sci U S A 110: 1083–1088. doi: 10.1073/pnas.1214255110

47. Niehrs C (2012) The complex world of WNT receptor signalling. Nat Rev Mol Cell Biol 13: 767–779. doi: 10.1038/nrm3470

48. Irannejad R, Tomshine JC, Tomshine JR, Chevalier M, Mahoney JP, et al. (2013) Conformational biosensors reveal GPCR signalling from endosomes. Nature 495: 534–538. doi: 10.1038/nature12000

49. Karlen A, Karlsson TE, Mattsson A, Lundstromer K, Codeluppi S, et al. (2009) Nogo receptor 1 regulates formation of lasting memories. Proc Natl Acad Sci U S A 106: 20476–20481. doi: 10.1073/pnas.0905390106

50. Kanno T, Nishizaki T, Proia RL, Kajimoto T, Jahangeer S, et al. (2010) Regulation of synaptic strength by sphingosine 1-phosphate in the hippocampus. Neuroscience 171: 973–980. doi: 10.1016/j.neuroscience.2010.10.021

51. Ghanouni P, Gryczynski Z, Steenhuis JJ, Lee TW, Farrens DL, et al. (2001) Functionally different agonists induce distinct conformations in the G protein coupling domain of the beta 2 adrenergic receptor. J Biol Chem 276: 24433–24436. doi: 10.1074/jbc.c100162200

52. Huber T, Sakmar TP (2011) Escaping the flatlands: new approaches for studying the dynamic assembly and activation of GPCR signaling complexes. Trends Pharmacol Sci 32: 410–419. doi: 10.1016/j.tips.2011.03.004

53. Albers M, Kranz H, Kober I, Kaiser C, Klink M, et al. (2005) Automated yeast two-hybrid screening for nuclear receptor-interacting proteins. Mol Cell Proteomics 4: 205–213. doi: 10.1074/mcp.m400169-mcp200

54. Todaro GJ, Green H (1963) Quantitative studies of the growth of mouse embryo cells in culture and their development into established lines. J Cell Biol 17: 299–313. doi: 10.1083/jcb.17.2.299

55. Swift S, Lorens J, Achacoso P, Nolan GP (2001) Rapid production of retroviruses for efficient gene delivery to mammalian cells using 293T cell-based systems. Curr Protoc Immunol Chapter 10: Unit 10 17C. doi: 10.1002/0471142735.im1017cs31

56. Hu W, Huang J, Mahavadi S, Li F, Murthy KS (2006) Lentiviral siRNA silencing of sphingosine-1-phosphate receptors S1P1 and S1P2 in smooth muscle. Biochem Biophys Res Commun 343: 1038–1044. doi: 10.1016/j.bbrc.2006.03.079

57. Pfaffl MW (2001) A new mathematical model for relative quantification in real-time RT-PCR. Nucleic Acids Res 29: e45. doi: 10.1093/nar/29.9.e45

58. Dodd DA, Niederoest B, Bloechlinger S, Dupuis L, Loeffler JP, et al. (2005) Nogo-A, -B, and -C are found on the cell surface and interact together in many different cell types. J Biol Chem 280: 12494–12502. doi: 10.1074/jbc.m411827200

59. Wienken CJ, Baaske P, Rothbauer U, Braun D, Duhr S (2010) Protein-binding assays in biological liquids using microscale thermophoresis. Nat Commun 1: 100. doi: 10.1038/ncomms1093

60. Zillner K, Jerabek-Willemsen M, Duhr S, Braun D, Langst G, et al. (2012) Microscale thermophoresis as a sensitive method to quantify protein: nucleic acid interactions in solution. Methods Mol Biol 815: 241–252. doi: 10.1007/978-1-61779-424-7_18

61. Whittenberger B, Glaser L (1977) Inhibition of DNA synthesis in cultures of 3T3 cells by isolated surface membranes. Proc Natl Acad Sci U S A 74: 2251–2255. doi: 10.1073/pnas.74.6.2251

62. Huber AB, Weinmann O, Brosamle C, Oertle T, Schwab ME (2002) Patterns of Nogo mRNA and protein expression in the developing and adult rat and after CNS lesions. J Neurosci 22: 3553–3567.

63. Donoghue JP, Wise SP (1982) The motor cortex of the rat: cytoarchitecture and microstimulation mapping. J Comp Neurol 212: 76–88. doi: 10.1002/cne.902120106

64. Rioult-Pedotti MS, Friedman D, Donoghue JP (2000) Learning-induced LTP in neocortex. Science 290: 533–536. doi: 10.1126/science.290.5491.533

65. Rioult-Pedotti MS, Friedman D, Hess G, Donoghue JP (1998) Strengthening of horizontal cortical connections following skill learning. Nat Neurosci 1: 230–234. doi: 10.1038/678

66. Hess G, Aizenman CD, Donoghue JP (1996) Conditions for the induction of long-term potentiation in layer II/III horizontal connections of the rat motor cortex. J Neurophysiol 75: 1765–1778. doi: 10.1007/s002210050797

67. Aroniadou VA, Keller A (1995) Mechanisms of LTP induction in rat motor cortex in vitro. Cereb Cortex 5: 353–362. doi: 10.1093/cercor/5.4.353

68. Hess G, Donoghue JP (1994) Long-term potentiation of horizontal connections provides a mechanism to reorganize cortical motor maps. J Neurophysiol 71: 2543–2547.

Supplement

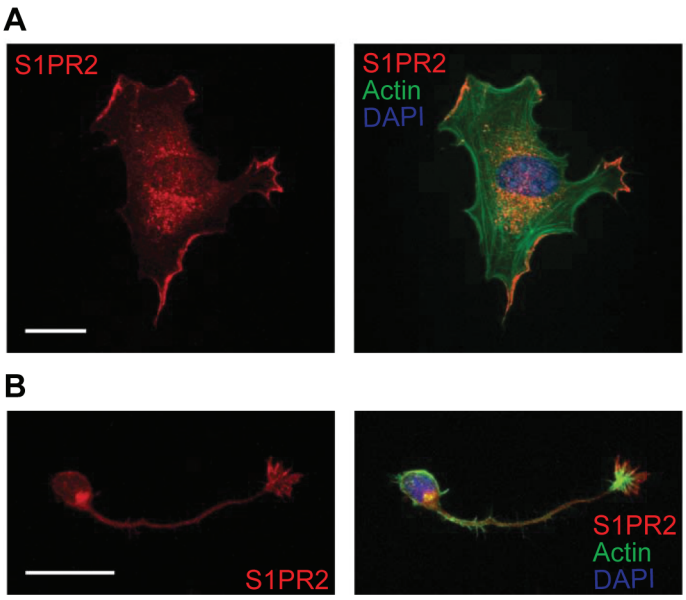

Figure S1: S1PR2 expression in 3T3 fibroblasts and immature cerebellar granule cells. (A,B) Immunofluorescence staining of 3T3 cells (A) and P8 cerebellar granule cell with neurite and growth cone (B) for S1PR2, nuclei (DAPI), and F-Actin (Phalloidin-Alexa488). Scale bars: 50 µm.

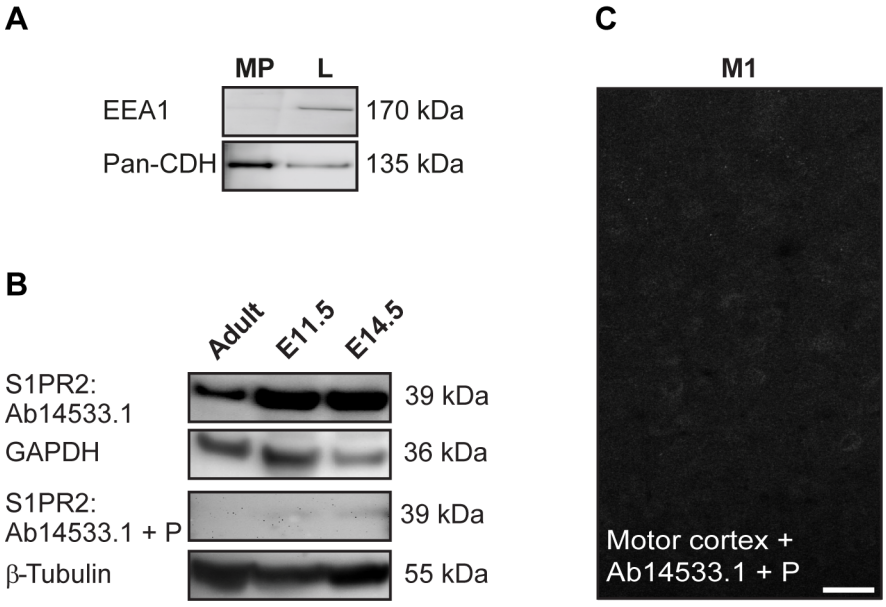

Figure S2: Purity of plasma membrane preparations and specificity of custom-made S1PR2 antibody Ab14533.1. (A) Western Blot analysis of 3T3 plasma membrane preparations reveals non-detectable amount of EEA1-positive endosomal membranes, but high content of Pan-CDH-positive plasma membrane fractions compared to whole cell lysates. MP, membrane preparations; L, whole cell lysate. **(B)** Ab14533.1 detects S1PR2 in whole brain tissue extracts. Protein expression is higher in embryonic stages (E11.5, E14.5) than in adult animals. S1PR2 signals are strongly decreased when challenged in a competition assay with the immunogenic peptide (P). **(C)** Immunohistochemical analysis of S1PR2 in the adult motor cortex (compare to Figure 1E and 1F) shows abolished S1PR2 detection using the same peptide competition assay.

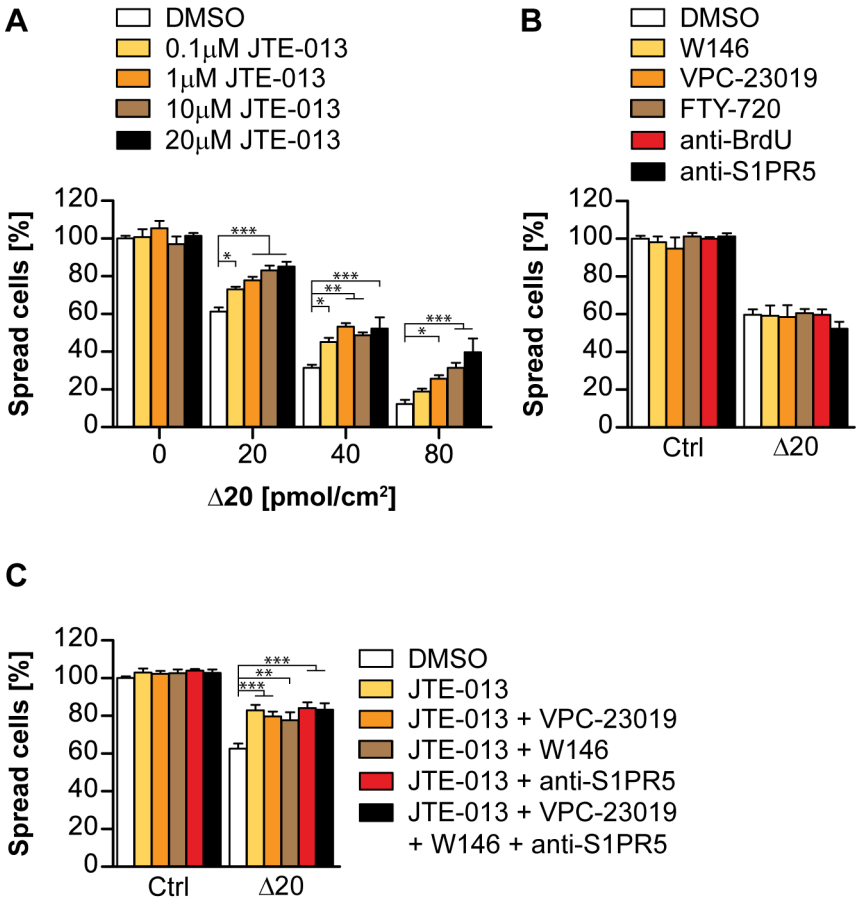

Figure S3: Blockade of S1PR1, 3, 4, and/or 5 has no effect on Nogo-A-Δ20-mediated cell spreading inhibition. (A) 3T3 fibroblasts were plated on different concentrations of a Nogo-A-Δ20 substrate in the presence of increasing concentrations of JTE-013 versus vehicle (DMSO). **(B)** 3T3 fibroblasts were plated on a Nogo-A-Δ20 substrate in the presence of the following pharmacological inhibitors: W146 for S1PR1, VPC-23019 for S1PR1 and 3, and FTY-720 for S1PR1, 3, 4, and 5. DMSO was used as control. A function-blocking anti-S1PR5 antibody had no effect on Nogo-A-Δ20-induced inhibition when compared to anti-BrdU control. **(C)** 3T3 fibroblasts were plated on a Nogo-A-Δ20 substrate in the presence of JTE-013 in different combinations with VPC-23019, W146 and/or anti-S1PR5. DMSO was used as control. Data shown are means ± SEM (n = 3–4 experiments; *p<0.05, **p<0.01, ***p<0.001).

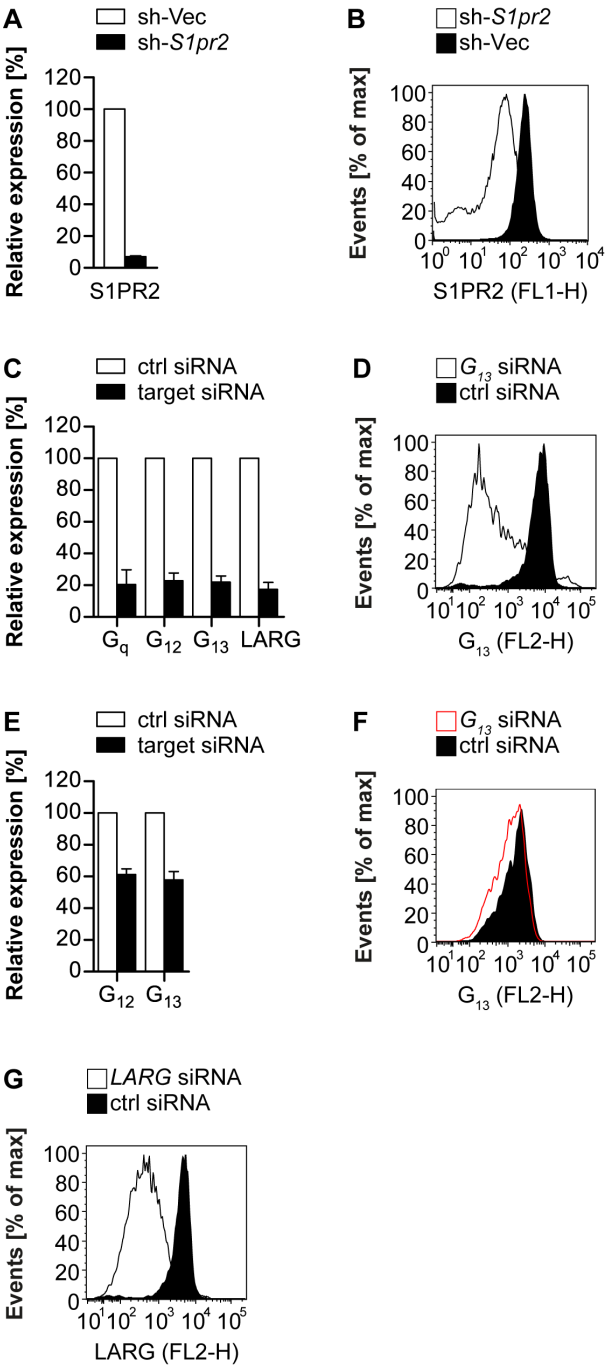

Figure S4: Knockdown efficacy of S1PR2, G_q, G_{12}, G_{13}, and LARG. (A) Quantitative RT-PCR analysis of S1PR2 expression in 3T3 cells stably expressing S1pr2 shRNA (sh-S1pr2) versus control vector (sh-Vec) revealed an ~93% knockdown. **(B)** FACS analysis of S1PR2 expression in 3T3 cells stably expressing sh-S1pr2 or sh-Vec using the Ab14533.1 antibody. **(C)** Quantitative RT-PCR analysis of 3T3 cells treated with siRNA targeting G_q, G_{12}, G_{13}, or Larg for 72 h. Scrambled siRNA (ctrl) was used as control. Relative quantification of knockdown efficacy: G_{12} (~77%), G_{13} (~78%), Gq (~79%), and Larg (83%). **(D)** FACS analysis of G_{13} expression in G13 versus ctrl siRNA-treated 3T3 cells. **(E)** Quantitative RT-PCR analysis of E19 rat cortical neurons treated at DIV4 with siRNA targeting G_{12} or G_{13} for 72 h. Scrambled siRNA (ctrl) was used as control. Relative quantification of knockdown efficacy: G_{12} (39%), G_{13} (42%). **(F)** FACS analysis of G_{13} expression in G_{13} versus ctrl siRNA-treated E19 cortical neurons. **(G)** FACS analysis of LARG expression in Larg versus ctrl siRNA-treated 3T3 cells. Histograms from one representative experiment are shown. Data shown are means ± SEM (n = 3 experiments).

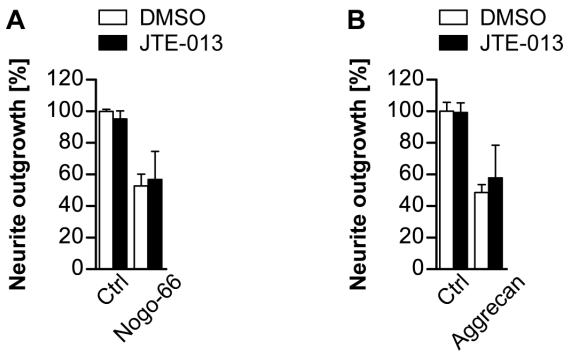

Figure S5: S1PR2 blockade has no effect on Nogo-66- and Aggrecan-mediated inhibition of neurite outgrowth. **(A,B)** Mean neurite length quantification of P5–8 CGNs treated with JTE-013 or DMSO and plated on a Nogo-66 (A) or Aggrecan (B) versus ctrl (PLL) substrate. Data shown are means ± SEM (n = 4 replicates).

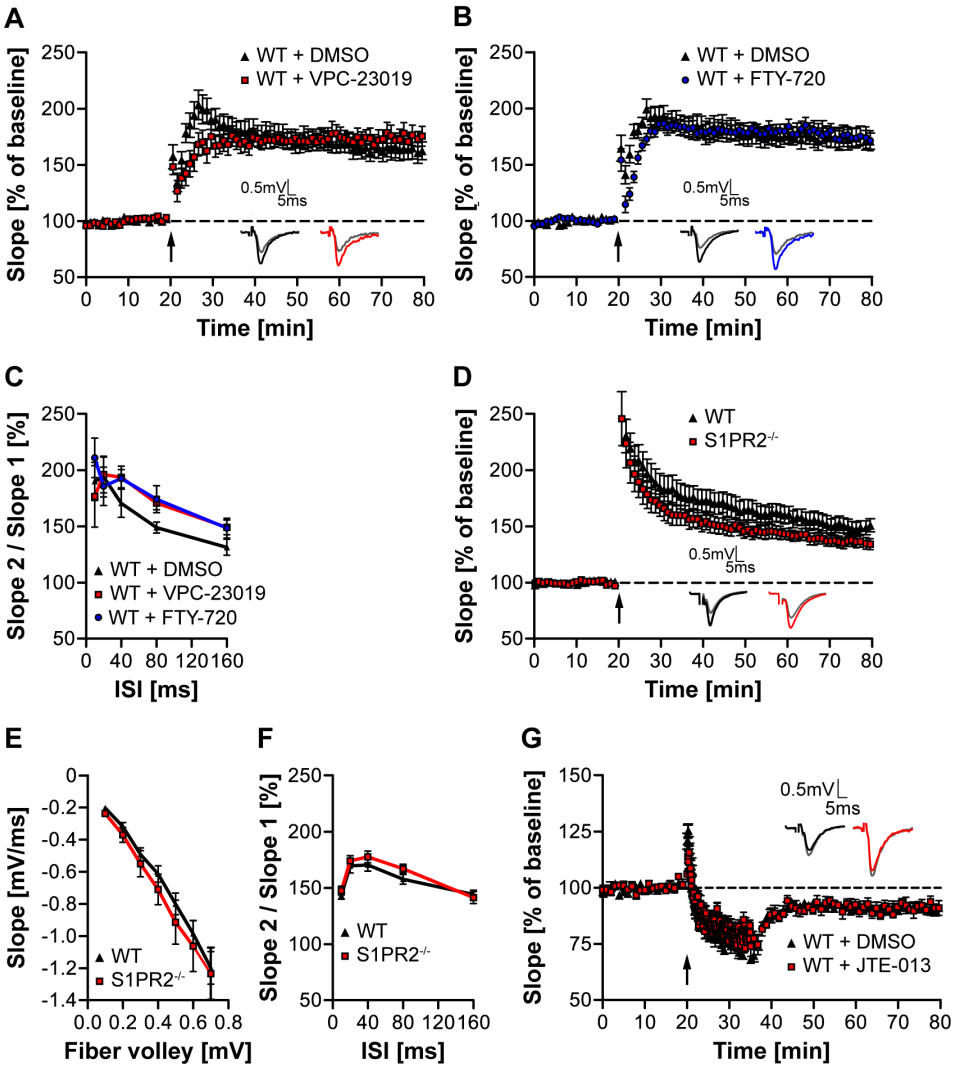

Figure S6: Pharmacological inhibition of S1PR1 and 3 or S1PR1, 3, 4, and 5 does not increase hippocampal LTP. **(A,B)** WT hippocampal slices were treated with VPC-23019 (n = 7) (A) or FTY-720 (n = 8) (B) to block S1PR1 and 3 or S1PR1, 3, 4 and 5, respectively. DMSO was used as control in (A) (n = 11) and (B) (n = 9). No significant differences in LTP could be observed between VPC-23019, FTY-720 and DMSO treatment. **(C)** PPF revealed no alterations in VPC-23019- (n = 5) or FTY-720- (n = 7) versus DMSO- (n = 7) treated slices. **(D)** No significant difference in LTP could be observed in S1PR2$^{-/-}$ (n = 11) versus WT (n = 12) mice. **(E)** Input-output strength revealed no alterations in S1PR2$^{-/-}$ (n = 8) versus WT (n = 12) mice. **(F)** PPF revealed no alterations in S1PR2$^{-/-}$ (n = 11) versus WT (n = 13) mice. **(G)** No significant difference in hippocampal long-term depression (LTD) could be observed between JTE-013- (n = 4) versus DMSO- (n = 5) treated WT slices. Arrows indicate the onset of theta-burst (A,B,D) or low frequency (G) stimulation. Data shown are means ± SEM. n indicates the number of mice used.

CHAPTER 7

SYNTHETIC MICRORNA-MEDIATED DOWNREGULATION OF NOGO-A IN TRANSGENIC RATS REVEALS ITS ROLE AS REGULATOR OF SYNAPTIC PLASTICITY AND COGNITIVE FUNCTION

Björn Tews[a,b,1], Kai Schönig[c,1], Michael E. Arzt[a], Stefano Clementi[c], Mengia-Seraina Rioult-Pedotti[d,e], Ajmal Zemmar[a], Stefan M. Berger[c], Miriam Schneider[f], Thomas Enkel[c], Oliver Weinmann[a], Hansjörg Kasper[a], Martin E. Schwab[a,2,3], and Dusan Bartsch[c,2,3]

Published in *PNAS* 2013;110(16):6583-8. DOI: 10.1073/pnas.1217665110

M. E. A. conducted, analyzed and interpreted immunofluorescence and Western blot experiments, wrote the manuscript and prepared the figures.

[1] B.T. and K.S. contributed equally to this work.
[2] M.E.S. and D.B. contributed equally to this work.
[a] Brain Research Institute, University of Zürich and Department of Health Sciences and Technology, Eidgenössiche Technische Hochschule (Switzerland), 8057 Zürich, Switzerland;
[b] Schaller Research Group at the University of Heidelberg and the German Cancer Research Center, Division of Molecular Mechanisms of Tumor Invasion, German Cancer Research Center, 69120 Heidelberg, Germany;
[c] Department of Molecular Biology, Central Institute of Mental Health, Medical Faculty Mannheim, Heidelberg University, 68159 Mannheim, Germany;
[d] Clinical Neurorehabilitation Department Neurology Clinic, University Hospital, 8008 Zürich, Switzerland;
[e] Department of Molecular Pharmacology, Physiology and Biotechnology, Brown University, Providence, RI, 02912;
[f] Research Group Developmental Neuropsychopharmacology, Institute of Psychopharmacology, Central Institute of Mental Health, Medical Faculty Mannheim, Heidelberg University, 68159 Mannheim, Germany

Abstract

We have generated a transgenic rat model using RNAi and used it to study the role of the membrane protein Nogo-A in synaptic plasticity and cognition. The membrane protein Nogo-A is expressed in CNS oligodendrocytes and subpopulations of neurons, and it is known to suppress neurite growth and regeneration. The constitutively expressed polymerase II-driven transgene was composed of a microRNA-targeting Nogo-A placed into an intron preceding the coding sequence for EGFP, thus quantitatively labeling cells according to intracellular microRNA expression. The transgenic microRNA *in vivo* efficiently reduced the concentration of Nogo-A mRNA and protein preferentially in neurons. The resulting significant increase in long-term potentiation in both hippocampus and motor cortex indicates a repressor function of Nogo-A in synaptic plasticity. The transgenic rats exhibited prominent schizophrenia-like behavioral phenotypes, such as perseveration, disrupted prepulse inhibition, and strong withdrawal from social interactions. This fast and efficient microRNA-mediated knockdown provides a way to silence gene expression *in vivo* in transgenic rats and shows a role of Nogo-A in regulating higher cognitive brain functions.

Introduction

Gene knockout (KO) technology has spurred the analysis of gene functions in mice during the past two decades (1) and has recently been expanded to other species using new genome modification technologies (2). Although germ-line gene ablation is a very powerful tool for investigating gene function *in vivo*, its most important drawback is that the complete loss of gene function often leads to molecular compensation, obscuring the role of the deleted gene. Tissue- or cell-specific KOs are more specific but are currently confined to mice as a model system. RNA interference (RNAi) is a viable alternative to the KO approach and represents a fast and powerful tool for manipulating gene expression (3). RNAi technology not only allows keeping the endogenous genomic locus intact, but it also enables the knockdown of multiple genes at the same time or the selective depletion of a specific isoform of mRNA transcripts (4). Another advantage is offered by the possibility of creating hypomorphic alleles instead of complete KOs, which can avoid embryonic lethality and better mirrors many human diseases and therapeutic interventions.

Elucidating gene functions in transgenic rats has several important advantages over using mice (5). Their larger size simplifies interventions, such as microsurgery and multiple site *in vivo* electrophysiological recordings (6). Furthermore, higher-order cognitive functions are more developed in this social rodent species than in the more solitarily living mice (7, 8). Hence, many behavioral tests are more advanced or validated for the rat species, especially regarding the behavioral assessment of complex neuropsychiatric disease phenotypes, such as negative

symptoms in schizophrenia. For the rat, only polymerase (Pol) III-controlled shRNA RNAi models have been created, but this methodology does not easily allow for tissue-specific or simultaneous expression of translated mRNAs (9). MicroRNAs (miRNAs) (10) can be efficiently expressed by Pol II promoters in eukaryotic cells and a tissue-specific manner (11). Similar to shRNAs, miRNAs bind a defined target site in an endogenous mRNA, leading to efficient knockdown of target genes (12). In mice, transgenic RNAi expression not only led to phenotypes that closely resembeled those observed in KO mice (13, 14) but also enabled the generation of hypomorphic animal models (14).

In this study, we present and investigate the potential of Pol II-driven knockdown in a rat model that quantitatively monitors the transgenic miRNA expression using EGFP as a reporter. Such cellular visualization facilitates selection and analysis of transgenic animals and targeted cell populations, opening avenues for additional cellular analysis *in vivo*. As an experimental example, we created Nogo-A (Rtn4) knockdown rats using this technology. In these rats, we found enhancement of long-term potentiation (LTP) in not only hippocampus but also cortex, and we observed behavioral phenotypes related to schizophrenia, extending those phenotypes described in the Nogo-A KO mouse (15). These findings validate the miRNA-based knockdown technology and show an important role of Nogo-A repressing neuronal plasticity. Moreover, unlike Nogo-A KO mice, which show a significant Nogo-B up-regulation, there is no such compensatory mechanism apparent in our transgenic model.

Results

Design of the miRNA Expression Unit and Generation of Nogo-A Knockdown Rats.

To determine the most efficient expression design of Pol II-driven miRNAs, we first tested two constructs, in which the miRNA was located in either the 3′ UTR of EGFP (pUTR) or an intronic sequence located 5′ of EGFP (pINTRON) (11). The intronic design enables about fourfold higher knockdown efficacy compared with 3′ design coupled with high expression of miRNA/EGFP (Fig. 1A). Different synthetic siRNAs selectively targeting Nogo-A mRNA were tested for knockdown efficiencies by transient transfections of oligonucleotides into 3T3 fibroblasts, which express Nogo-A endogenously. The most efficient RNAi sequence was chosen for the design of a miRNA targeting Nogo-A mRNA, which was then cloned into the intronic sequence of the vector pINTRON (Fig. 1A). Placing the miRNA sequences in an intron ensures effective labeling of the miRNA-expressing cells with EGFP, while at the same time, enhances and stabilizes transgenic expression (16). For strong transgenic expression of the miRNA targeting Nogo-A, we replaced the human cytomegalovirus (CMV) promoter of pINTRON with a hybrid construct comprising the CMV early

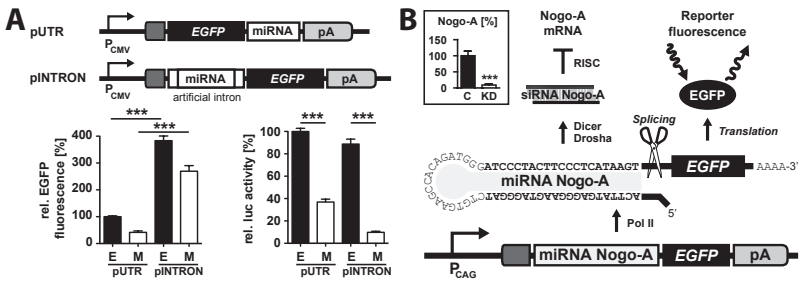

Fig. 1: Design and testing of the intronic miRNA/EGFP expression system. (A) Expression vectors pUTR and pINTRON containing a rationally designed miRNA targeting firefly luciferase (M) or no miRNA as controls (E). In pUTR, the miRNA is integrated between the 3′ end of EGFP and the polyadenylation signal (pA). In pINTRON, the miRNA is embedded within an artificial intron located 5′ of EGFP. Transient transfection experiments using miRNA/EGFP together with luciferase expression vectors show that relative EGFP activities and luciferase knockdown efficiencies are much higher for pINTRON than pUTR. Means (n = 9) and SEM are shown. **(B)** Schematic drawing of the Nogo-A miRNA insert-containing construct used for the generation of transgenic rats. Inset displays results of Nogo-A qPCR quantification relative to housekeeping genes from Nogo-A–expressing 3T3 cells transfected with either pCAG-INTRON-(miRNA Nogo-A)-EGFP (KD) or control (C) vector. ***P < 0.001.

enhancer element and the chicken β-actin (CAG) promoter (17). The miRNA is transcribed as bifunctional pre-mRNA coding for EGFP, which is processed into functional miRNA and equimolar amounts of EGFP mRNA. To test the knockdown efficiency of the final construct, we transfected 3T3 fibroblasts and quantified endogenous Nogo-A mRNA 3 d posttransfection; 91% of the Nogo-A mRNA expression was abolished compared with control conditions (Fig. 1B, Inset).

For the production of transgenic rats, the pCAG-INTRON-(miRNA Nogo-A)-EGFP DNA construct was microinjected into fertilized Sprague–Dawley rat oocytes, resulting in the generation of eight individual founders. Primary fibroblast cultures were established from ear punches of these animals (18) and tested for EGFP fluorescence.The four founders with strongest EGFP expression in fibroblasts were mated with WT Sprague–Dawley animals to establish the respective lines L2, L3, L18, and L33. From those four lines, L2, L3, and L18 transmitted the

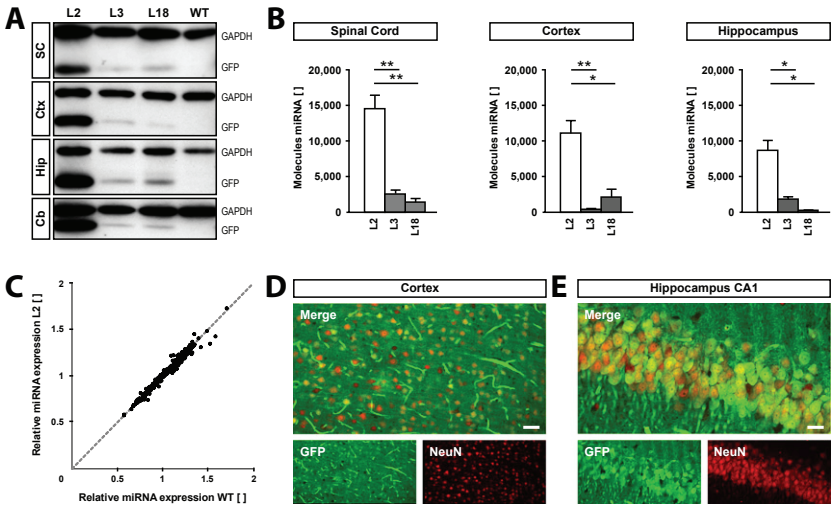

Fig. 2: Rat line L2 expresses transgenic EGFP and miRNA at the highest level without affecting the miRNA-processing machinery. (A) Western blot results of EGFP and GAPDH for different CNS regions derived from the transgenic rat lines L2, L3, and L18 as well as WT rats. Cb, cerebellum; Ctx, cortex; Hip, hippocampus; SC, spinal cord. **(B)** Absolute qPCR quantification (expressed as molecules per cell) of transgenic Nogo-A miRNA expression levels in different rat lines and CNS regions. **(C)** Scatter plot of qPCR expression levels of 359 abundantly expressed miRNAs from L2 and WT rats. Nonregulated miRNA levels of L2 vs. WT are identical and converge on the bisector of the angle. **(D and E)** Immunofluorescence of EGFP (green) and the neuronal nuclear marker neuronal nuclei (NeuN) (red) in the cortex (D) and hippocampus (E) of L2 shows a largely neuronal expression of the transgene. (Scale bar: D, 50 μm; E, 20 μm.) *P < 0.05; **P < 0.01.

transgene in Mendelian fashion and therefore were chosen for detailed analysis. To validate CAG promoter activity in the CNS, we analyzed EGFP expression in brain lysates and on histological brain sections. Western blot analyses showed expression of EGFP in all brain regions tested; the expression was strongest in line L2 (Fig. 2A). To assess functional processing of the transgenic miRNA targeting Nogo-A, we quantified the absolute number of Nogo-A miRNA copies per cell in spinal cord, cortex, and hippocampus RNA preparations by quantitative PCR (qPCR) (Fig. 2B). As expected, RNA preparations from L2 rats contained the highest concentration of transgenic miRNA, being at least fivefold above the content of all other lines in the examined regions. To ensure that overexpression of the transgenic miRNA had no influence on the overall miRNA-processing machinery (19), we compared the expression profiles of 359 abundantly expressed miRNA sequences in L2 and WT rats (Fig. 2C). The results show that the transgenic miRNA did not influence endogenous miRNA expression and thus, did not interfere with the overall miRNA-processing machinery. Histological sections of the brains of L2 rats revealed that, in the cortex, 48.8% (±7.8%, n = 5) and in the hippocampus, 72.8% (±11.2%, n = 6) of neuronal nuclei (NeuN)-positive neurons expressed EGFP (Fig. 2 D and E). Expression was also detectable in blood vessels (Fig. 2D) but absent in the vast majority of oligodendrocytes and interneurons (Fig. S1).

Nogo-A Levels Are Significantly Diminished in L2 Animals.

qPCR revealed significant reduction of Nogo-A mRNA in several CNS regions in L2 and L3 rats to about 50% and 75% of WT levels, respectively (Fig. S2). Nogo-A protein expression was assessed by Western blotting (for determination of dynamic range, see Fig. S3) and immunofluorescence analysis in different regions of the CNS of adult L2 and L3 transgenic rats. Western blots revealed a reduction of Nogo-A expression in the cortex of L2 rats to about 30% of WT mean but no detectable decrease in the cortex of L3 rats. Importantly, Nogo-B expression remained unchanged in both transgenic lines (Fig. 3A). Hippocampal Nogo-A expression was reduced by 30% in L2 rats (Fig. 3A). More detailed results were obtained from densitometric measurements of L2 histological brain sections, where Nogo-A expression was quantified by immunofluorescence. Here, the cingulate cortex of L2 rats showed a decrease of Nogo-A expression to 70%, and the motor cortex to 40% of WT levels (Fig. 3 B and C). The densitometric measurements revealed a major loss of Nogo-A expression in neurons (Fig. 3 B and C). Quantified Nogo-A levels were 40% of WT in the hippocampus, 45% of WT in the caudate-putamen, and in total, about 60% of WT in the cerebellum. In the spinal cord, Nogo-A expression decreased to 40–50% in motor neurons, whereas expression was not significantly changed in white matter oligodendrocytes of L2 animals (Fig. 3 B and C). Treatment of spinal cord slices with ethanol and acetic acid known to specifically visualize Nogo-A expression in myelin (20) confirmed retention of Nogo-A expression in oligodendrocytes of L2 rats (Fig. 3 B and C).

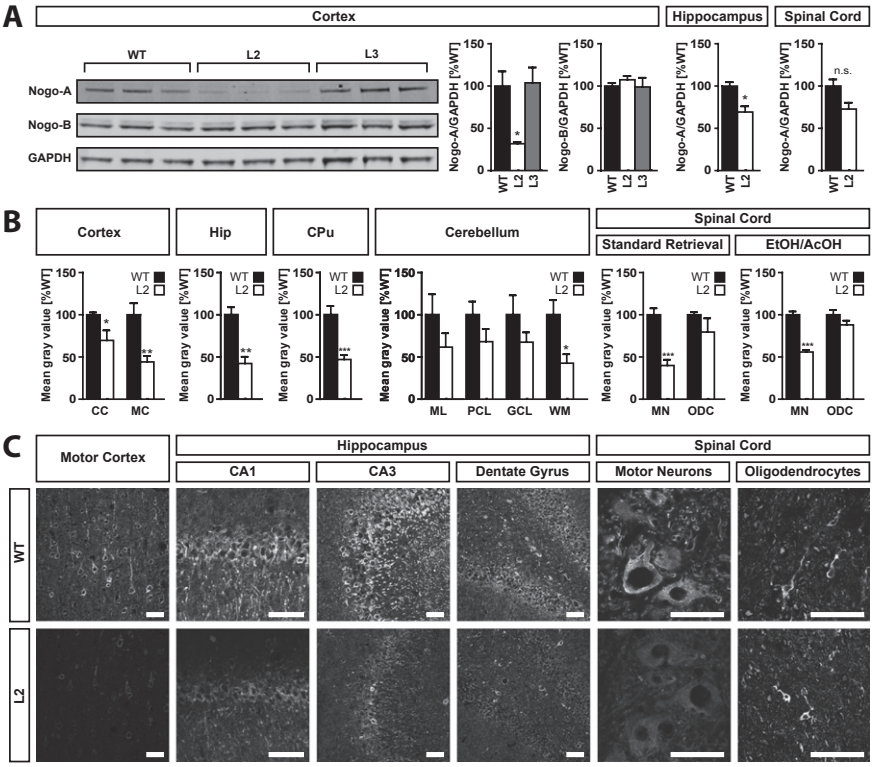

Fig. 3: Expression of Nogo-A is reduced in L2 rats. (A) Western blot analysis of Nogo-A (~200 kDa) and Nogo-B (~50 kDa) expression compared with GAPDH (~40 kDa) in different CNS tissues. Whereas Nogo-A is significantly down-regulated in the cortex of L2 rats (P = 0.0173), no cortical knockdown can be seen in animals of L3. In addition, Nogo-B remains unchanged in both L2 and L3. Nogo-A knockdown can also be observed in the hippocampus (P = 0.0195) of L2 rats, whereas only a trend is visible in whole spinal cord (P = 0.0659). Averaged Nogo-A/GAPDH ratios from three animals per transgenic line or WT are reported as a percentage of WT mean ± SEM. **(B)** Densitometric quantification of Nogo-A immunoreactivity as determined by epifluorescence microscopy in a Zeiss Axiophot microscope. Down-regulation of Nogo-A is evident in the cingulate (CC; P = 0.0499) and motor cortex (MC; P = 0.0041) of L2 rats. In addition, Nogo-A immunoreactivity is decreased in the cell layers of the hippocampus (Hip; P = 0.0080) and the caudate putamen (CPu; P = 0.0008). Down-regulation can also be observed in the cerebellar white matter (WM; P = 0.0166), whereas only a trend is seen in the molecular layer (ML; P = 0.2155), Purkinje cell layer (PCL; P = 0.1675), and granular cell layer (GCL; P = 0.2310). In the spinal cord, whereas a marked reduction of Nogo-A immunoreactivity is detected in motoneurons (MNs; P < 0.0001), no significant change can be observed in spinal oligodendrocytes (ODCs; P = 0.1135=. Similar results were obtained after ethanol/acetic acid treatment (EtOH/AcOH) of the spinal cord sections (MN, P = 0.0002; ODC, P = 0.2449). **(C)** Representative confocal images show the decrease of Nogo-A immunoreactivity in L2 rats in different CNS regions. Images of the spinal cord show sections after EtOH/AcOH treatment. (Scale bars: 50 μm.) Data are presented as mean + SEM. Asterisks represent P values obtained by comparing L2 and WT rats with unpaired t test: *P < 0.05; **P < 0.01; ***P < 0.001.

Overall, although regional variations were noted, transgenic rat line L2 with the highest miRNA expression showed about 50% reduction of Nogo-A protein expression in CNS neurons. Copy number quantification of transgenic insertions into the genome of L2 showed six copies per cell (Fig. S4). We selected L2 for additional behavioral and electrophysiological experiments.

Nogo-A–Deficient Rats Exhibit Distinct Behaviors Resembling Neuropsychiatric Phenotypes.

Cohorts of L2 and WT animals (n = 10 each) were used to investigate the consequences of reduced Nogo-A expression on behavior. We focused on the analysis of distinct neuropsychiatric intermediate phenotypes, some of which have been associated with Nogo-A function in a KO mouse model (15). Baseline behavioral parameters like locomotor activity were similar in L2 and WT rats (Fig. 4A). The two groups were indistinguishable in terms of anxiety-related behavior, deduced from the time spent in the center of the open field and the elevated plus maze task (Fig. S5A and B). However, when animals were tested for their sensorimotoric gating, a marked

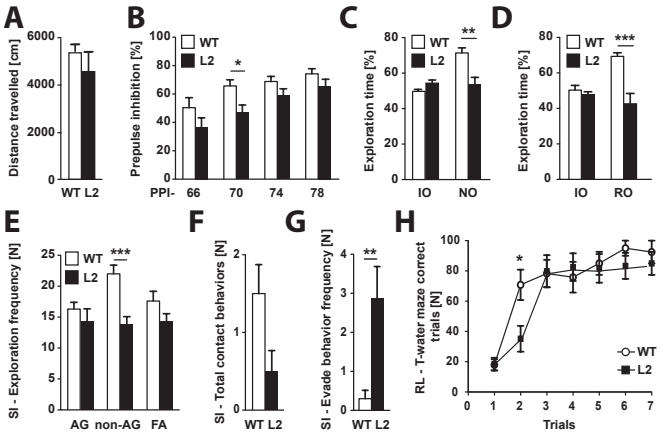

Fig. 4: L2 rats exhibit schizophrenia-like phenotypes. (A) Locomotor activity in the open field arena. No difference on distance traveled between WT and Nogo-A knockdown rats (L2). **(B)** PPI. Two-way ANOVA revealed a significant reduction in PPI in L2 rats compared with WT rats [$F_{Genotype}$ (1,54) = 4.97; P = 0.039]. However, Bonferroni posthoc testing revealed that, only at a PPI of 70 dB (PPI-70), startle amplitudes of L2 rats were significantly lower than those startle amplitudes of WT rats. **(C)** Effects of Nogo-A knockdown on novel object recognition memory in the novel object recognition task. L2 and WT rats showed no significant differences in percent of time spent in exploration of the identical objects (IOs) during the training phase of the test. In contrast, L2 rats have a significant impairment in discriminating between the novel and the familiar object during testing (NO). **(D)** Novel object relocation task. L2 and WT rats showed no significant differences in exploration of the IOs during the training phase of the test. During the test phase, L2 rats had a significant impairment in discriminating the relocated object (RO). (E–G) Behavioral performance during social interaction with an unknown social partner (social interaction). **(E)** Significant differences between WT and L2 rats were found for nonanogenital exploration (non-AG), whereas no differences were observed for anogenital exploration (AG) and following/approach (FA). **(F)** A strong trend was found for a decrease in the number of social contact behaviors (grooming/crawling). **(G)** L2 rats show significantly more social withdrawal behavior than WT littermates. **(H)** Reversal learning in the water T maze. Two-way ANOVA revealed that there was no significant difference between animals of the two genotypes in the reversal of their escape strategy in the water T maze, which was seen from their percentage of correct trails within the task [L, $F_{Genotype}$(1.108) = 1.22; P = 0.284]. In contrast, Bonferroni posthoc testing revealed that, in trial 2, L2 rats have a significant impairment in finding the escape platform. All data are mean values ± SEM. Asterisks represent P values obtained by comparing L2 and WT rats with either unpaired t or Bonferroni posthoc test after two-way ANOVA of repeated measures: *P < 0.05; **P < 0.01; ***P < 0.001.

deficit in prepulse inhibition (PPI) could be observed in L2 rats compared with WT controls [$F_{Genotype}$(1.54) = 4.97; P = 0.039] (Fig. 4B). Cognitive functions of the animals were evaluated using the novel object recognition and the object relocation paradigms. In these tasks, the animal had to distinguish a novel or relocated object from familiar objects that it had memorized. L2 animals displayed significantly decreased short-term memory capabilities compared with WT controls in discriminating both a novel object (Fig. 4C) and a relocated object (Fig. 4D) from a familiar one. No significant differences were observed between the animals of both genotypes regarding object exploration time during the training phase of the tasks. Behavioral differences between L2 rats and controls were also observed during testing of social interaction. A significant decrease in total social interaction was observed in L2 rats compared with WT (Fig. S5C). This difference originated only from a highly significant decrease in nonanogenital exploration, because no significant differences between the groups were detected for anogenital exploration and following/approach during interaction with the unfamiliar social partner (Fig. 4E). L2 rats showed a strong tendency for lower social contact behaviors compared with WT animals (P = 0.054) (Fig. 4F). Finally, L2 rats were found to withdraw significantly more often from social contact if initiated by the social partner (social evade) (Fig. 4G). No significant differences between the groups were detected for self-grooming behavior (Fig. S5D). Spatial learning and behavioral flexibility were assessed in a reversal learning paradigm using a water T maze. Performance during the initial learning of the task was indistinguishable between rats of both genotypes (Fig. S5E). However, L2 rats showed

perseveration in reversal learning, requiring one additional trial for the reversal of the escape strategy compared with WT rats (Fig. 4H and Fig. S5 F and G).

Reduced Nogo-A Expression Results in Increased Synaptic Plasticity in the Hippocampus and Motor Cortex.

Because Nogo-A expression is high in hippocampus and primary motor cortex (M1) neurons (20) (Fig. 3), we used our transgenic rat model to investigate the role of Nogo-A in regulating synaptic transmission and plasticity in these areas. To assess baseline synaptic transmission at the hippocampal CA3-CA1 Schaffer collateral pathway, input–output curves were generated by measuring evoked field excitatory postsynaptic potential (fEPSP) slopes at increasing stimulation intensities (20–100 μA). No difference was seen between the L2 and WT rats (Fig. 5A). To analyze the influence of Nogo-A on short-term plasticity, we measured paired pulse facilitation by applying two stimuli separated by a temporal interstimulus interval of 40 ms and recorded fEPSPs. We obtained slightly higher paired pulse ratios for the L2 line (Fig. 5B), which were, however, not significantly different from the ratios of control littermates (L2: 1.47 ± 0.07 SEM; WT: 1.24 ± 0.08; $P = 0.13$). To investigate the role of Nogo-A in regulating hippocampal synaptic plasticity, we induced LTP using a theta-burst stimulation (TBS) protocol after 20 min of baseline recordings. We observed a significant increase in LTP in L2 rats (157.5 ± 0.76%, $n = 4$) compared with littermate controls (132.2 ± 1.9%, $n = 4$; $P < 0.05$) (Fig. 5C). To determine whether the presence of Nogo-A in M1, a structure involved in motor skill acquisition (21), is relevant for synaptic transmission and/or synaptic plasticity, we measured evoked fEPSPs in layer II/III horizontal connections in acute brain slices containing the M1 forelimb area. Baseline synaptic transmission as determined by input–output relationships using multiples of threshold intensity was not affected in Nogo-A–deficient rats (Fig. 5D). fEPSP amplitudes were not significantly different in L2 vs. WT rats (3× threshold intensity: L2: 0.64 ± 0.035 mV; WT: 0.69 ± 0.037 mV; $P = 0.35$; $n = 15$).

The maximum potential for synaptic plasticity was determined by multiple attempts of LTP. After 20 min of baseline recordings at 50% maximum response amplitude, LTP was induced by TBS preceded by local transient application of the $GABA_A$ receptor antagonist bicuculline (22). This stimulation protocol was repeated until responses did not increase. Maximum synaptic strength (LTP saturation) was significantly increased in L2 rats (152 ± 5.9%; $n = 16$) compared with WT rats (122 ± 5.5%; $n = 15$; $P = 0.001$) (Fig. 5E), suggesting that Nogo-A is a repressor of synaptic plasticity in the motor cortex as well.

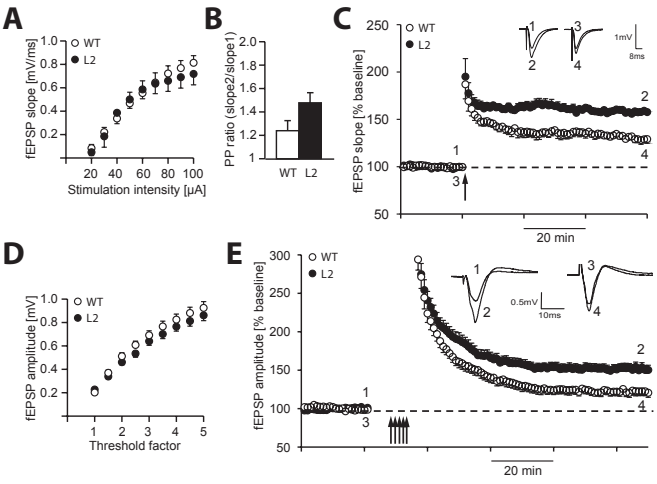

Fig. 5: Hippocampal as well as cortical LTP are increased in Nogo-A knockdown rats. (A) Input-output relationships (I/O curves) from WT (n = 6) and L2 Nogo-A knockdown rats (n = 6) recorded in the hippocampal CA3-CA1 Schaffer collateral pathway. I/O curves indicate no significant difference in synaptic strength across stimulation intensities. **(B)** Paired pulsed ratio measured at different interstimulus intervals did not significantly differ between WT and L2 (n = 6 each). **(C)** LTP was induced by TBS (arrow) in L2 and WT rats. At 60 min after TBS, a significant difference between L2 and WT rats could be observed. Inset shows original traces from representative individual experiments; numbers correspond to the time point when traces were taken. **(D)** I/O curves from WT (n = 15) and L2 Nogo-A knockdown rats (n = 15) recorded in layer II/III horizontal connections in the M1 forelimb area of brain slices. I/O curves indicate no significant difference in synaptic strength across stimulation intensities. **(E)** Maximum synaptic strength (LTP saturation) was determined by repeated induction of LTP (multiple arrows). Peak amplitudes were significantly larger in L2 (n = 16) compared with WT rats (n = 15). Each field potential trace represents an average of 10 individual responses at times indicated by numbers.

Discussion

Nogo-A is an important neurite growth inhibitory protein that stabilizes the adult CNS wiring, restricts regeneration, and also negatively regulates hippocampal plasticity (23). Recent evidence suggests that aberrant Nogo-A signaling poses an increased risk for schizophrenia (detailed review in ref. 24). We applied a Pol II-driven miRNA expression strategy for RNAi-mediated mRNA knockdown in transgenic rats, resulting in an ~50% reduction of neuronal Nogo-A protein in different regions of the CNS. The rat model that we present here extended the range of schizophrenia-like phenotypes previously reported for conventional Nogo-A KO mice and allowed for a more detailed investigation of learning and memory-related phenotypes. RNAi-mediated genetic depletion of Nogo-A significantly increased synaptic plasticity in not only the hippocampus but also the motor cortex.

Pol II-Driven Expression of Intronic Synthetic miRNA Induces Down-Regulation of the CNS Protein Nogo-A.

Traditionally, rats have been the preferred experimental animal model system in biomedical research (25), particularly for the analysis of complex neurological disorders and behavioral psychology, where they are superior to mice in many respects (26). Pol II-based miRNA expression systems are a reverse genetic strategy for overexpression of miRNAs. In our experiments, placing an miRNA sequence into an intron 5′ of a coding gene significantly enhances expression compared with 3′ insertions and at the same time, enables simultaneous expression of Pol II-controlled genes. EGFP coexpression with a similar construct in mice failed so far (14), and in rats, only shRNAs driven by a Pol III human H1 promoter have been successfully applied (9, 27).

The latter method does not allow quantitative coexpression of an interfering RNA together with a protein coding gene or tissue-specific gene expression. We inserted the Nogo-A–targeting miRNA in an intronic sequence preceding the ORF of EGFP in the vector pCAG-INTRON-EGFP (11). The CAG promoter has been shown to be well-suited for transgenic expression in rats, particularly for neurons (28–30). This construct enables labeling of miRNA-expressing cells and a quantitative measure of the amount of miRNA produced (Fig. S6), because the miRNA is spliced from the EGFP mRNA. An overall reduction of Nogo-A mRNA and protein levels by 50% in several regions of the CNS of adult rats was achieved in line L2.

Reduced Nogo-A Expression Leads to Defects in Cognition, Sensorimotor Gating, and Social Behavior.

Rat transgenic line L2 with high neuronal and not detectable oligodendrocytic EGFP reporter expression was chosen for in-depth analyses. Immunohistochemistry detecting Nogo-A confirmed the significant Nogo-A depletion in neurons. Behaviorally, these rats showed disruptions in sensorimotor gating and selective attention, and an increased perseverative behavior in reversal learning was observed. These changes are hallmarks for schizophrenia (31). Indeed, similar phenotypes were recently observed in conventional Nogo-A KO mice (15). Compared with the mouse model, unique phenotypic traits could be identified in our transgenic Nogo-A knockdown rats: they showed significantly lower exploration and reduced social contact behavior as well as much higher withdrawal from social interaction initiated by the social partner compared with their WT littermates. The presence of these negative symptoms in the rat model is of particular significance. In free social interactions, L2 rats showed normal exploratory behavior but a marked attenuation and avoidance of social contact. Although such social withdrawal behavior might be related to increased anxiety (32), we consider it unlikely, because in the open field test and the elevated plus maze task L2 rats showed no signs of anxiety and Nogo-A KO mice do not differ in anxiety-related behaviors from their WT controls (33). Social withdrawal and isolation are among the key components of negative symptoms in schizophrenia (34), and thus, social withdrawal observed in L2 rats supports a schizophrenia-like phenotype.

Current pharmacological treatments are focusing on the positive symptoms of schizophrenia in man, because genetic mouse models were quite successful in modeling these symptoms (35). In contrast, only very few mouse models exhibit the negative symptoms associated with this disease (36, 37). The Nogo-A knockdown rat with both positive and negative schizophrenia-like symptoms may provide a tool for testing compounds selective for negative symptoms, the severity of which is most predictive for poor therapeutic outcome in patients (38).

Nogo-A Is a Negative Regulator of Synaptic Plasticity in the Hippocampus and Motor Cortex.

Depletion of Nogo-A might affect the synaptic equilibrium, resulting in the observed behavioral dysfunctions. In schizophrenic patients, increased hippocampal activity at baseline and during auditory hallucinations is often observed (39, 40). We have recently found significantly increased LTP in mouse hippocampal slices treated with Nogo-A blocking antibodies and a trend for increased hippocampal LTP in Nogo-A KO mice (41). Here, we show that rats with reduced neuronal Nogo-A expression exhibit a significant increase in hippocampal LTP compared with WT littermates. To determine whether synaptic plasticity was generally changed in these animals, we measured cortical LTP induction after saturated TBS in the primary motor cortex, a region critically important for motor learning, which correlates with increased LTP (21). After TBS of horizontal connections, LTP was doubled in Nogo-A knockdown rats compared with WT littermates. These results show that neuronal Nogo-A mediates repression of synaptic plasticity in the hippocampus and the motor cortex, probably by regulating synapse maturation, size, and/or numbers (42, 43).

Inhibitory constraints on synaptic plasticity and learning and memory were shown in Aplysia, Drosophila, mice, and humans (44–46); removal of such molecular constraints can result in increased synaptic plasticity and improved learning and memory (47–49). Although generally increased hippocampal LTP correlates with improved learning and memory, pathological and prolonged increase in LTP may also lead to cognitive defects (50–54). The perseveration that we observed could indicate an effect of Nogo-A knockdown on memory, which is currently being analyzed in more detail. However, the LTP results would also be consistent with detrimental effects on cognitive functions. Nogo-A knockdown rats, KO mice, and in vivo neutralization experiments with antibodies can now be used to further analyze the roles of neuronal Nogo-A for learning, memory and cognitive functions, and neuropsychiatric diseases, particularly schizophrenia.

Specific Advantages of miRNA Knockdown Transgenic Rats.

Compensation and lethality are frequent undesirable side effects of conventional KO mice. In Nogo-A KO mice (55–57), significant up-regulation of the small splice-isoform Nogo-B was found (58), whereas Nogo-B was not affected in our transgenic Nogo-A knockdown rats. One reason might be that the miRNA-based approach targets splice form-specific mRNAs and leaves the endogenous genetic locus intact. Reducing the concentration of a target protein rather than completely removing it may also help to prevent compensation and particularly, also lethality. Importantly, partial knockdowns also mirror some human pathologic conditions more accurately, especially conditions caused by hypomorphic mutations, epigenetic silencing events, or altered

RNAi expression (59, 60) [e.g., autoimmune and neurological diseases (61)]. miRNA-based knockdown models seem ideally suited to study the disease implications of allelic (e.g., single nucleotide) mutations in disease susceptibility genes. Partial knockdown of protein function also resembles pharmacological blockade more closely than complete ablation of a given protein. Many KO phenotypes in mice are known to be strictly strain-specific because of background genes and/or compensation (58); using outbred rat strains, such as Sprague–Dawley, avoids this problem and guarantees a much more bias-free model. In addition, endogenous miRNAs can easily be studied with this technology. Finally, using polycistronic constructs for targeting multiple transcripts, replacing the CAG promoter by cell type-specific promoters, or combining the Cre/loxP or Tet system can further enlarge the spectrum of applications of this promising technology.

Materials and Methods

Detailed descriptions of experimental procedures can be found in SI Materials and Methods. A brief summary of materials and methods is give here.

Generation and Molecular Characterization of Transgenic Rats.

siRNAs targeting Nogo-A–specific exon 3 of Rtn4 were designed and cloned into the Pol II-driven vector pCAG-INTRON-EGFP. The construct pCAG-INTRON-(miRNA Nogo-A)-EGFP was tested by transfections of 3T3 cells using fluorescent microscopy and Nogo-A mRNA measurements with real-time qPCR. The linearized vector was used for the generation of transgenic Sprague–Dawley rats denominated SD-Tg(CAG-RNAi:Nogo-A,EGFP)#ZI, where # stands for the number of the transgenic line (in this work, it is abbreviated as L#). Quantification of processed miRNA and analyses of the endogenous mRNA expression levels in transgenic and WT animals were determined by qPCR. Protein levels of Nogo-A, Nogo-B, EGFP, and housekeeping genes were measured qualitatively and quantitatively by near-fluorescent Western blotting and immunohistochemistry using epifluorescence and confocal microscopy. Copy number quantification of transgenes per cell was done by genomic qPCR.

Behavioral Analysis.

For the behavioral assessment, 6-mo-old male L2 (n = 10) or WT littermate (n = 10) rats were used. The following behaviors were analyzed: basal locomotor activity, object recognition and relocation memory, reversal learning, PPI of the acoustic startle response, and social interaction (contact behavior, social exploration, and approach/following; social evade; and self-grooming behavior).

Cortical and Hippocampal LTP.

Differences in LTP were measured in hippocampal (n: L2 = 4; WT = 4) and primary motor cortical slices (n: L2 = 16; WT = 15) of L2 rats and WT littermates, respectively.

Statistical Analysis.

Statistical significance was calculated by means of unpaired, two-tailed Student t tests if not indicated otherwise.

Acknowledgments

We thank Dr. Roman Willi for discussions; Dr. Anita Buchli for management; Ariana Frömmig, Tien Nguyen, Brigitte Pesold, and Lena Wendler for technical assistance; and our colleagues Dr. Linard Filli, Miriam Gullo, Dr. Andreas Luft, Dr. Michelle Starkey, and Dr. Björn Zörner for experimental support. This work was funded by German Ministry for Education and Research (BMBF) Grant 01GQ1003B, a National Bernstein Network for Computational Neuroscience (http://www.gesundheitsforschung-bmbf.de/en/2478.php#Heidelberg) grant, a HEALTH-F2-2007-201714 DEVANX (http://devanx.vitamib.com) grant, and Swiss National Science Foundation Grant 31-122527/1 (to M.E.S.).

References

1. Glaser S, Anastassiadis K, Stewart AF. Current issues in mouse genome engineering. Nat Genet. 2005;37(11):1187–1193.
2. Tong C, et al. Rapid and cost-effective gene targeting in rat embryonic stem cells by TALENs. J Genet Genomics. 2012;39(6):275–280.
3. Hemann MT, et al. An epi-allelic series of p53 hypomorphs created by stable RNAi produces distinct tumor phenotypes in vivo. Nat Genet. 2003;33(3):396–400.
4. Volpicelli-Daley LA, Li Y, Zhang CJ, Kahn RA. Isoform-selective effects of the depletion of ADP-ribosylation factors 1-5 on membrane traffic. Mol Biol Cell. 2005;16(10):4495–4508.
5. Aitman TJ, et al. Progress and prospects in rat genetics: A community view. Nat Genet. 2008;40(5):516–522.
6. Wang D, et al. Genetic enhancement of memory and long-term potentiation but not CA1 long-term depression in NR2B transgenic rats. PLoS One. 2009;4(10):e7486.
7. Buehr M, et al. Capture of authentic embryonic stem cells from rat blastocysts. Cell. 2008;135(7):1287–1298.
8. Grant E, Mackintosh H. A comparison of the social postures of some common laboratory rodents. Behaviour. 1963;21(3/4):246–259.
9. Kotnik K, et al. Inducible transgenic rat model for diabetes mellitus based on shRNA-mediated gene knockdown. PLoS One. 2009;4(4):e5124.
10. Wienholds E, Plasterk RH. MicroRNA function in animal development. FEBS Lett. 2005;579(26):5911–5922.
11. Berger SM, et al. Quantitative analysis of conditional gene inactivation using rationally designed, tetracycline-controlled miRNAs. Nucleic Acids Res. 2010;38(17):e168.
12. Karagiannis TC, El-Osta A. RNA interference and potential therapeutic applications of short interfering RNAs. Cancer Gene Ther. 2005;12(10):787–795.
13. Kunath T, et al. Transgenic RNA interference in ES cell-derived embryos recapitulates a genetic null

phenotype. Nat Biotechnol. 2003;21(5):559–561.

14. Xia XG, Zhou H, Samper E, Melov S, Xu Z. Pol II-expressed shRNA knocks down Sod2 gene expression and causes phenotypes of the gene knockout in mice. PLoS Genet. 2006;2(1):e10.

15. Willi R, et al. Constitutive genetic deletion of the growth regulator Nogo-A induces schizophrenia-related endophenotypes. J Neurosci. 2010;30(2):556–567.

16. Brinster RL, Allen JM, Behringer RR, Gelinas RE, Palmiter RD. Introns increase transcriptional efficiency in transgenic mice. Proc Natl Acad Sci USA. 1988;85(3):836–840.

17. Niwa H, Yamamura K, Miyazaki J. Efficient selection for high-expression transfectants with a novel eukaryotic vector. Gene. 1991;108(2):193–199.

18. Schönig K, Bujard H. Generating conditional mouse mutants via tetracycline-controlled gene expression. Methods Mol Biol. 2003;209:69–104.

19. Grimm D, et al. Fatality in mice due to oversaturation of cellular microRNA/short hairpin RNA pathways. Nature. 2006;441(7092):537–541.

20. Huber AB, Weinmann O, Brösamle C, Oertle T, Schwab ME. Patterns of Nogo mRNA and protein expression in the developing and adult rat and after CNS lesions. J Neurosci. 2002;22(9):3553–3567.

21. Rioult-Pedotti MS, Friedman D, Donoghue JP. Learning-induced LTP in neocortex. Science. 2000;290(5491):533–536.

22. Hess G, Aizenman CD, Donoghue JP. Conditions for the induction of long-term potentiation in layer II/III horizontal connections of the rat motor cortex. J Neurophysiol. 1996;75(5):1765–1778.

23. Schwab ME. Functions of Nogo proteins and their receptors in the nervous system. Nat Rev Neurosci. 2010;11(12):799–811.

24. Willi R, Schwab ME. Nogo and Nogo receptor: Relevance to schizophrenia? Neurobiol Dis. 2013 10.1016/j.nbd.2013.01.011.

25. Cozzi J, Fraichard A, Thiam K. Use of genetically modified rat models for translational medicine. Drug Discov Today. 2008;13(11–12):488–494.

26. Gill TJ, 3rd, Smith GJ, Wissler RW, Kunz HW. The rat as an experimental animal. Science. 1989;245(4915):269–276.

27. Herold MJ, van den Brandt J, Seibler J, Reichardt HM. Inducible and reversible gene silencing by stable integration of an shRNA-encoding lentivirus in transgenic rats. Proc Natl Acad Sci USA. 2008;105(47):18507–18512.

28. Hakamata Y, et al. Green fluorescent protein-transgenic rat: A tool for organ transplantation research. Biochem Biophys Res Commun. 2001;286(4):779–785.

29. Michalkiewicz M, et al. Efficient transgenic rat production by a lentiviral vector. Am J Physiol Heart Circ Physiol. 2007;293(1):H881–H894.

30. Weber T, Schönig K, Tews B, Bartsch D. Inducible gene manipulations in brain serotonergic neurons of transgenic rats. PLoS One. 2011;6(11):e28283.

31. Geyer MA, Moghaddam B. Animal models relevant to schizophrenia disorders. In: Davis KL, Charney DS, Coyle JT, Nemeroff C, editors. Neuropsychopharmacology: The Fifth Generation of Progress. Philadelphia: Lippincott Williams & Wilkins; 2002. pp. 689–701.

32. File SE, Hyde JR. Can social interaction be used to measure anxiety? Br J Pharmacol. 1978;62(1):19–24.

33. Willi R, Aloy EM, Yee BK, Feldon J, Schwab ME. Behavioral characterization of mice lacking the neurite outgrowth inhibitor Nogo-A. Genes Brain Behav. 2009;8(2):181–192.

34. American Psychiatric Association . Diagnostic and Statistical Manual of Mental Disorders. 4th Ed. Washington, DC: American Psychiatric Association; 1994.

35. Kellendonk C, Simpson EH, Kandel ER. Modeling cognitive endophenotypes of schizophrenia in mice. Trends Neurosci. 2009;32(6):347–358.

36. Drew MR, et al. Transient overexpression of striatal D2 receptors impairs operant motivation and interval timing. J Neurosci. 2007;27(29):7731–7739.

37. Ward RD, Simpson EH, Kandel ER, Balsam PD. Modeling motivational deficits in mouse models of schizophrenia: Behavior analysis as a guide for neuroscience. Behav Processes. 2011;87(1):149–156.

38. Ho BC, Nopoulos P, Flaum M, Arndt S, Andreasen NC. Two-year outcome in first-episode schizophrenia: Predictive value of symptoms for quality of life. Am J Psychiatry. 1998;155(9):1196–1201.

39. Silbersweig DA, et al. A functional neuroanatomy of hallucinations in schizophrenia. Nature. 1995;378(6553):176–179.

40. Dierks T, et al. Activation of Heschl's gyrus during auditory hallucinations. Neuron. 1999;22(3):615–621.

41. Delekate A, Zagrebelsky M, Kramer S, Schwab ME, Korte M. NogoA restricts synaptic plasticity in the adult hippocampus on a fast time scale. Proc Natl Acad Sci USA. 2011;108(6):2569–2574.

42. Aloy EM, et al. Synaptic destabilization by neuronal Nogo-A. Brain Cell Biol. 2006;35(2–3):137–156.

43. Petrinovic MM, et al. Neuronal Nogo-A negatively regulates dendritic morphology and synaptic transmission in the cerebellum. Proc Natl Acad Sci USA. 2013;110(3):1083–1088.

44. Abel T, Martin KC, Bartsch D, Kandel ER. Memory suppressor genes: Inhibitory constraints on the storage of long-term memory. Science. 1998;279(5349):338–341.

45. Bartsch D, et al. Aplysia CREB2 represses long-term facilitation: Relief of repression converts transient facilitation into long-term functional and structural change. Cell. 1995;83(6):979–992.

46. Barco A, Alarcon JM, Kandel ER. Expression of constitutively active CREB protein facilitates the late phase of long-term potentiation by enhancing synaptic capture. Cell. 2002;108(5):689–703.

47. Malleret G, et al. Inducible and reversible enhancement of learning, memory, and long-term potentiation by genetic inhibition of calcineurin. Cell. 2001;104(5):675–686.

48. Chen A, et al. Inducible enhancement of memory storage and synaptic plasticity in transgenic mice expressing an inhibitor of ATF4 (CREB-2) and C/EBP proteins. Neuron. 2003;39(4):655–669.

49. Abel T, et al. Genetic demonstration of a role for PKA in the late phase of LTP and in hippocampus-based long-term memory. Cell. 1997;88(5):615–626.

50. Gerlai R, Henderson JT, Roder JC, Jia Z. Multiple behavioral anomalies in GluR2 mutant mice exhibiting enhanced LTP. Behav Brain Res. 1998;95(1):37–45.

51. Kaksonen M, et al. Syndecan-3-deficient mice exhibit enhanced LTP and impaired hippocampus-dependent memory. Mol Cell Neurosci. 2002;21(1):158–172.

52. Kim MH, et al. Enhanced NMDA receptor-mediated synaptic transmission, enhanced long-term potentiation, and impaired learning and memory in mice lacking IRSp53. J Neurosci. 2009;29(5):1586–1595.

53. Rutten K, et al. Enhanced long-term potentiation and impaired learning in phosphodiesterase 4D-knockout (PDE4D) mice. Eur J Neurosci. 2008;28(3):625–632.

54. Uetani N, et al. Impaired learning with enhanced hippocampal long-term potentiation in PTPdelta-deficient mice. EMBO J. 2000;19(12):2775–2785.

55. Kim JE, Li S, GrandPré T, Qiu D, Strittmatter SM. Axon regeneration in young adult mice lacking Nogo-A/B. Neuron. 2003;38(2):187–199.

56. Simonen M, et al. Systemic deletion of the myelin-associated outgrowth inhibitor Nogo-A improves regenerative and plastic responses after spinal cord injury. Neuron. 2003;38(2):201–211.

57. Zheng B, et al. Lack of enhanced spinal regeneration in Nogo-deficient mice. Neuron. 2003;38(2):213–224.

58. Dimou L, et al. Nogo-A-deficient mice reveal strain-dependent differences in axonal regeneration. J Neurosci. 2006;26(21):5591–5603.

59. Miller BH, Wahlestedt C. MicroRNA dysregulation in psychiatric disease. Brain Res. 2010;1338:89–99.

60. Tsankova N, Renthal W, Kumar A, Nestler EJ. Epigenetic regulation in psychiatric disorders. Nat Rev Neurosci. 2007;8(5):355–367.

61. Buckingham SD, Esmaeili B, Wood M, Sattelle DB. RNA interference: From model organisms towards therapy for neural and neuromuscular disorders. Hum Mol Genet. 2004;13(Spec No 2):R275–R288.

Supplement

Supplementary methods can be accessed online (DOI 10.1073/pnas.1217665110).

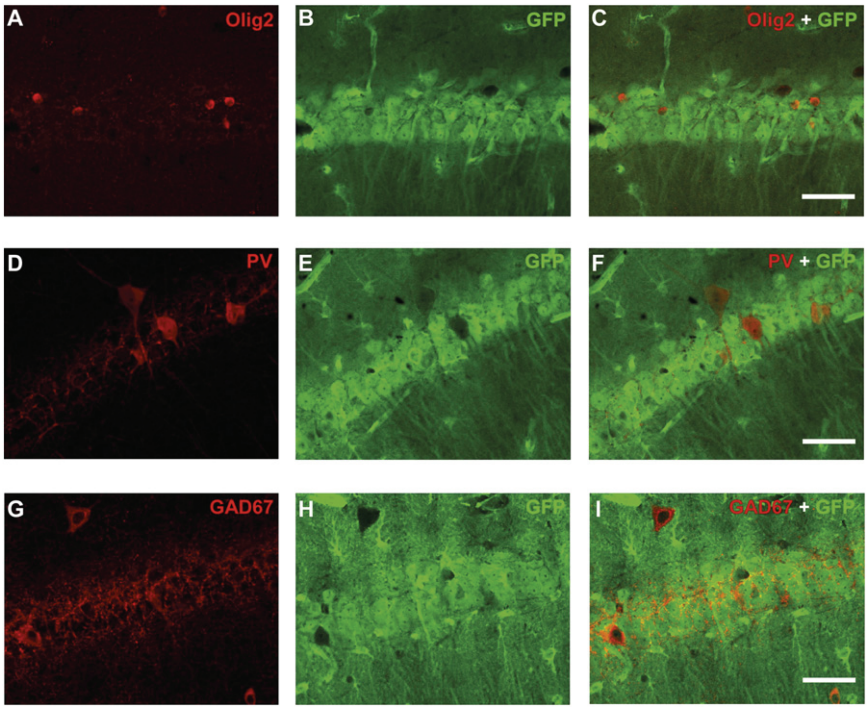

Fig. S1: Pattern of transgenic EGFP expression in L2 rat hippocampi. Immunofluorescence of the oligodendrocytic marker Oligodendrocyte transcription factor 2 (Olig2; A) or interneuronal markers Parvalbumin (PV; D) and Glutamate decarboxylase 67 (GAD67; G). EGFP expression is shown in B, E, and H.The merged pictures (C, F, and I) show the absence of transgenic expression in oligodendrocytes and interneurons. (Scale bars: 50 µm).

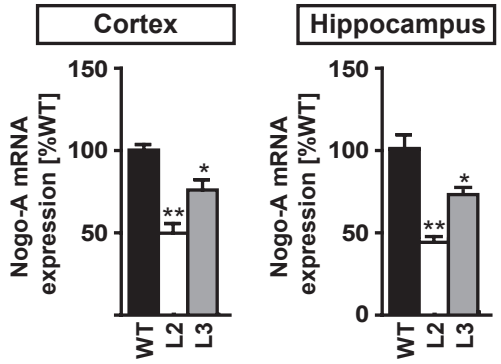

Fig. S2: Expression of Nogo-A mRNA in cortex and hippocampus. Relative expression of Nogo-A determined by qPCR in genotypes L2 and 3 as well as WT. *P<0.05; **P<0.01.

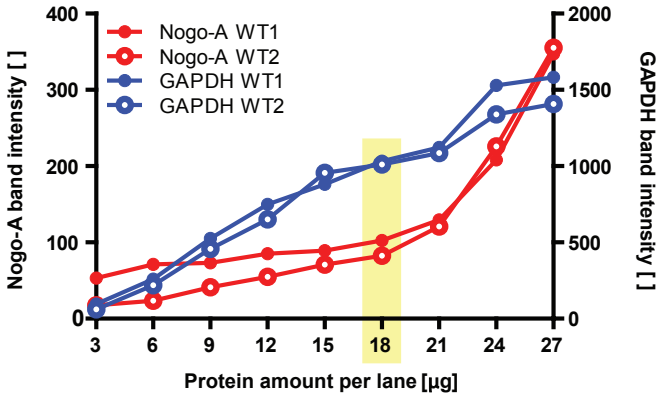

Fig. S3: Determination of the dynamic range for protein quantification by Western blotting. Serial dilutions of homogenized cortex from two WT animals were loaded on separate gels and analyzed byfluorescence Western blotting. The protein amount for subsequent experiments was selected such that differences between adjacent dilution factors were still visible (i.e., outside the saturation range of the detection system; yellow).

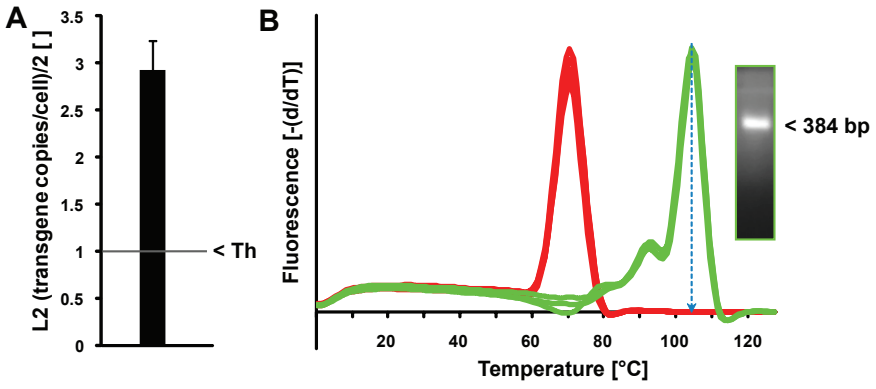

Fig. S4: Quantification of transgenic integration site. (A) qPCR copy number quantification of transgene/cell relative toTyrosine hydroxylase. **(B)** Melting curve analysis of resulting PCR products:Tyrosine hydroxylasein red and transgene in green. Inset shows an agarose gel electrophoresis of the PCR product of the transgene.

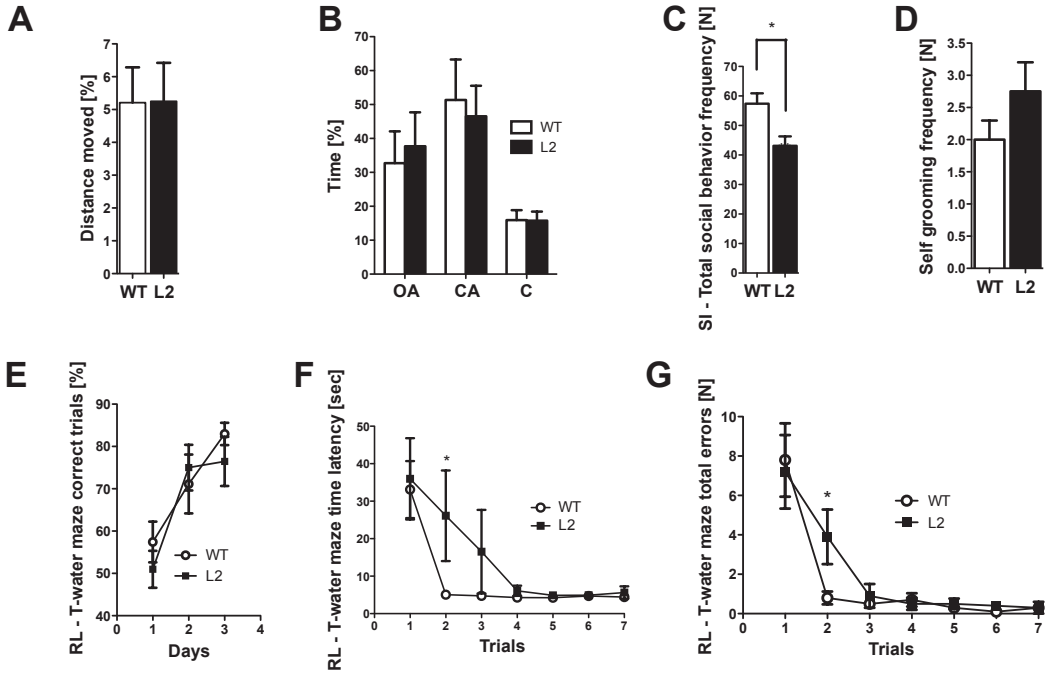

Fig. S5: Behavioral examination. (A) Percent of total distance moved in the center of the openfield arena. Nogo-A knockdown rats (L2) show no difference compared with WT control rats. **(B)** Elevated plus maze. No difference in anxiety-related behavior could be observed. The percentage of time L2 rats spend in the closed arms (COs), open arms (OAs), and center of the maze (C) is not different compared with WT animals. **(C)** Total behavioral frequency. The sum of anogenital, nonanogenital, and following/approach was significantly different between L2 and control rats. **(D)** Self-grooming during social interaction. No difference is observed between L2 and WT rats. **(E)** Learning curve for the T water maze. No difference is observed between L2 and WT rats infive trials during 3 d of learning. **(F, G)** Reversal learning in the water T maze. Two-way ANOVA revealed that there was no significant difference between animals of both genotypes in the reversal of their escape strategy in the water T maze measured as escape latencies [F;L,$F_{Genotype}(1,108)=1.53;P=0.233$] and number of total errors [G;L,$F_{Genotype}(1,108)=0.93;P=0.348$]. However, Bonferroni posthoc testing revealed that, on trial 2, L2 rats have a significant impairment infinding the escape platform (time latency and total mistakes). All data presented are mean values +SEM or mean values±SEM.Pvalues were obtained by comparing L2 and WT rats with either unpaired t or Bonferroni posthoc test after two-way ANOVA of repeated measures: *P<0.05.

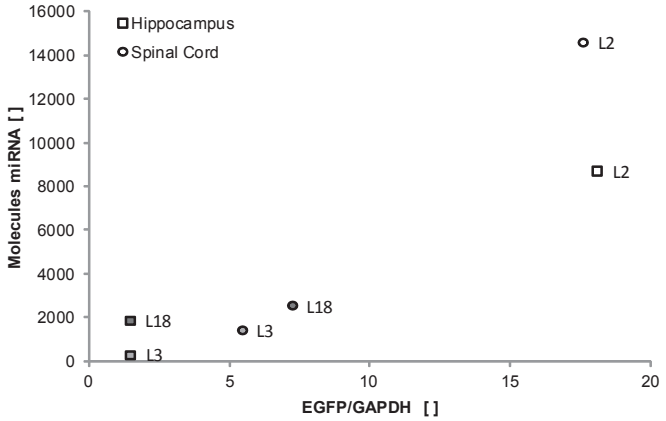

Fig. S6: Correlation of transgenic miRNA expression with EGFP expression for two exemplary regions from three transgenic rat lines.

CONCLUSIONS AND FUTURE DIRECTIONS

The findings presented in this thesis substantially contribute to our understanding of the molecular interactions that allow Nogo-A-Δ20 to impose inhibitory signals on regenerating neurons. Via direct binding to the extracellular surface of S1PR2, Nogo-A-Δ20 triggers the activation of the receptor, leading to an intracellular signaling cascade that results in actin destabilization. A single site on Nogo-A-Δ20 seems to be responsible for high-affinity binding to ECL2 and ECL3 of S1PR2. We obtained a computational homology model of S1PR2 to serve as a template for mutational mapping of the S1PR2 site that interacts with Nogo-A-Δ20. Although S1P occupies a different binding pocket that is buried inside S1PR2, signaling of these two agonists seems to be connected. An intramolecular S1PR2-FRET sensor was built to decipher the interdependence of S1P- and Nogo-A-Δ20-induced activation of S1PR2. The fact that S1PR2 is bound and activated by both a small phospholipid and a large membrane protein is also very appealing from a structural point of view. We have shown with spectroscopic techniques that Nogo-A-Δ20 is intrinsically disordered but contains some residual structure. Titration of ECL2 and ECL3 from S1PR2 did not alter the conformation of Nogo-A-Δ20. In our efforts to crystallize S1PR2, we have detected N-linked glycosylation, and a higher tolerance of the C-terminal compared to the N-terminal ICL3 for insertion of crystallization-promoting T4L.

Nogo-A-Δ20 seems to act as an allosteric modulator of S1PR2, which is an emerging concept in GPCR research (Gentry et al., 2015). Interestingly, auxiliary proteins such as tetraspanin 3 that also bind Nogo-A-Δ20 seem to facilitate this interaction, presumably by forming a multi-subunit receptor complex (Thiede-Stan et al., 2015). This observation is reminiscent of the WNT/ β-catenin pathway, where WNT and Norrin both act as ligands for a receptor complex comprising Frizzled (a GPCR) and tetraspanin proteins (Clevers, 2009; Junge et al., 2009; Niehrs, 2012). However, these two systems exhibit profound differences at the structural level. Unlike the class-A GPCR S1PR2, Frizzled receptors are the prototype of a very small class F of GPCRs, characterized by an N-terminal cysteine-rich domain (CRD) connected to the receptor by a linker sequence (Janda et al., 2012; Wang et al., 2013). WNT and Norrin, which assume unique α-helical conformations, both bind to the CRD of Frizzled (Chu et al., 2013; Janda et al., 2012; Ke et al., 2013). This contrasts with the interaction of disordered Nogo-A-Δ20 with the ECLs of S1PR2 and the

intra-membrane entry mechanism of S1P to its buried binding site. In addition, the protein domain Nogo-A-Δ20 and the small lysophospholipid S1P represent entirely different substance families binding to one common GPCR. This signaling node is therefore very unique and broadens our horizon on the capabilities of GPCR-based receptor complexes.

The wide range of functions and broad tissue distribution of S1P and S1PR2 allow for mutual influence of Nogo-A and S1P signaling in many different processes. For example, we have shown that Nogo-A restricts synaptic plasticity in the motor cortex and the CA1 region of the hippocampus via S1PR2 (Kempf et al., 2014; Tews et al., 2013). This effect is independent of S1P, as the S1PR2 antagonist JTE-013 enhanced long-term potentiation only in WT, but not in Nogo-A$^{-/-}$ mice (Kempf et al., 2014). In contrast, S1P stimulates glutamate secretion and enhances long-term potentiation in hippocampal CA3 synapses (Kajimoto et al., 2007; Kanno et al., 2010). It has been shown that S1PR1 is activated during depolymerization in these synapses (Kajimoto et al., 2007). Since S1PR1 and S1PR2 play opposite roles in many systems by activating Rac and Rho GTPases, respectively (Okamoto et al., 2000; Takuwa, 2002), the effect of S1P in synaptic plasticity might therefore be balanced by differential expression of these receptors. Nogo-A could directly influence this equilibrium by allosteric modulation of S1PR2.

Our work also poses new questions that will be approached in future experiments. Though the Nogo-A-Δ20 binding site on S1PR2 has been approximated to ECL2 and ECL3, the exact interacting residues remain elusive. S1PR2 mutants carrying alanine substitutions on the accessible surface of the receptor are therefore currently being functionally evaluated. Likewise, the minimal binding domain of Nogo-A-Δ20 is not known to date. To this end, truncation and site-directed mutagenesis experiments, as well as peptide microarrays displaying oligomer fragments of Nogo-A-Δ20 offer a promising strategy. Fragments of Nogo-A-Δ20 and S1PR2 could exhibit beneficial effects on neurite outgrowth *in vitro* and functional recovery after CNS lesions *in vivo*, as has been observed for Nogo-66 and NgR1 fragments (Fournier et al., 2002; GrandPre et al., 2002). The importance of residual α-helices for the inhibitory function of Nogo-A-Δ20 can be evaluated by mutagenesis (Rogers et al., 2014). Furthermore, the interdependence of Nogo-A-Δ20 and S1P signaling through S1PR2 will be assessed by mutations in key S1P-interacting residues.

The conformation-sensitive S1PR2-FRET biosensor can be used for a multitude of experiments. Competition assays between Nogo-A-Δ20 and JTE-013 could further corroborate binding of Nogo-A-Δ20 to a site on S1PR2 than is different from the common S1P/JTE-013 pocket. S1PR2 residues identified to abolish Nogo-A-Δ20-induced fibroblast spreading inhibition can also be mutated in S1PR2-FRET to verify their importance on the level of receptor activation. In addition, this system can be scaled up to allow high-throughput screening for novel S1PR2 ligands. Particularly, the identification of S1PR2 antagonists that selectively interfere with only one of the agonists, Nogo-A-Δ20 or S1P, would not only lead to new tools for research, but also hold great therapeutic potential.

S1PR2 inhibits the migration of neuronal progenitor cells towards stroke lesions, which underlines the potential of S1PR2 antagonists for pharmacological interventions (Kimura et al., 2008). Likewise, migration of macrophages and vascular smooth muscle cells is attenuated by S1P via S1PR2 (Michaud et al., 2010; Takashima et al., 2008). The role of S1PR2 in migration can be studied in much more detail by analyzing the spatiotemporal dynamics of its activation in migrating cells bearing S1PR2-FRET (Pertz et al., 2006). As *in-vivo* FRET imaging is just becoming available, the palette of possible applications is extended even further (Johnsson et al., 2014; Langenhan et al., 2015; Lohse, 2015; van Unen et al., 2015). S1PR2 exerts anti-migratory and anti-tumorigenic effects on glioblastoma and other cancer types, but pro-tumorigenic functions have also been described (Adada et al., 2013). Monitoring the intra-tumor heterogeneity of S1PR2 activation, as has been done for ERK (Kumagai et al., 2015), could therefore provide new insight into the ambiguous role of S1PR2 in cancer. Spatiotemporal information on S1PR2 activation can also be investigated in other systems. For example, S1PR2 activation in hippocampal neurons could be correlated with membrane depolarization, as has been done for S1PR1 by use of an S1PR1-CFP/β-arrestin-YFP FRET probe (Kajimoto et al., 2007). Transfection of S1PR2-FRET into hippocampal slices could further localize S1PR2 activation in or around individual spines, similar to the FRET biosensors of Rho and Ras GTPases (Murakoshi et al., 2011; Yasuda et al., 2006).

Further structural analysis of Nogo-A-Δ20 and S1PR2 is also important to gain a more complete understanding of their interaction. NMR is the method of choice for disordered proteins such as Nogo-A, as it does not rely on a rigid conformation. Spectral perturbations caused by interaction with, e. g., S1PR2 could be used to identify the minimal binding domain on Nogo-A-Δ20. However, we did not detect any such deviations in the spectrum upon addition of the isolated ECL peptides. Synthetic fragments of GPCRs are a popular approximation that circumvent the bottleneck of GPCR overexpression (Cohen et al., 2014; Lopes et al., 2013; Vincent et al., 2008). However, such isolated peptides lack the structural influence of adjacent hydrophobic domains, which could obscure certain aspects of their structures and binding modes. An interesting variation of this approach is the circularization of ECL peptides, which results in a loop-like conformation that supposedly resembles the physiological structure more closely (Lopes et al., 2013; Vincent et al., 2008). Another option are more sophisticated GPCR peptide mimetics comprising all ECLs and the N-terminus (Abel et al., 2014). However, the most intriguing approach would be titration of full-length S1PR2 in intact cells or micelles.

In contrast to Nogo-A-Δ20, S1PR2 is a good candidate for crystallization, a method that is becoming increasingly feasible for GPCRs owing to modern crystallographic methods (Piscitelli et al., 2015). Many parameters can be optimized to arrive at a crystal structure, including the insertion site of T4L or a similar protein, mutagenesis, ligand addition, cell culture systems, and conditions of solubilization and crystallization (Ghosh et al., 2015). The final goal of these studies would be to obtain a crystal structure of S1PR2 in complex with Nogo-A-Δ20 and/or S1P, thus

providing a framework for rational drug development. In particular, computational docking of compound libraries could be conducted on a crystal structure (Bermudez and Wolber, 2015). Identified lead substances could then be modified and screened for specificity employing high-throughput methods, such as an adapted S1PR2-FRET assay.

The work presented in this thesis therefore provides a foundation for future investigations of the structural aspects of Nogo-A-Δ20 signaling through S1PR2. Due to the complexity of this system, a combined approach using spectroscopic, crystallographic and other biochemical techniques is most likely to succeed in elucidating the particulars of this interaction. New structural insights will nourish our understanding of the underlying biology and promote our endeavor to design new treatment strategies for paralysis.

ACKNOWLEDGMENTS

First and foremost, I would like to express my gratitude to Martin Schwab. It has been a privilege to work in your group and be immersed in projects at so many levels of regenerative neurobiology. Thank you for your trust and courage giving me the freedom to pursue a project so far outside of our lab's "core business". Thanks for always keeping your door open, and for your invaluable feedback concerning lab work, teaching/presentations, and manuscripts. I would also like to thank the other members of my PhD thesis committee, Prof. Dr. Sonderegger and Prof. Dr. Suter, for their generous suggestions regarding my project.

Thanks to Björn Tews for being a great supervisor during my master thesis, and for being a constant resource of ideas during the beginning of my PhD. Björn's work has also become the foundation of my PhD project.

Frustration and repeated set-backs are an integral part of scientific everyday life. Being part of an encouraging team of colleagues/friends is therefore essential to persevere through the natural stages of a PhD. I am very grateful to all the members of the Schwab group and the Brain Research Institute, the former and the current, for providing a very supportive atmosphere. Countless discussions, scientific and non-scientific, have been a great source of joy for me and have made the recent years with you a wonderful experience.

Though any such list is bound to be incomplete, I would like to mention some individuals who were particularly important during my time at the Brain Research Institute. Regula Schneider, Roman Gonzenbach and Oliver Weinmann were my first teachers when I joined the institute for the first time during a semester project in 2007, and obviously did their job well enough to make me come back. Franziska Christ and our team of animal caretakers made it comfortably easy to obtain animals for tissue preparations whenever needed. Likewise, Tien Chau Nguyen and Zorica Ristic provided so much more than just excellent technical assistance and Nogo-A-Δ20; thank you for sharing your professional and personal experiences. Anissa Kempf has not only been a fantastic partner-in-crime concerning high-throughput fibroblast spreading assays, but also a permanent source of valuable suggestions. Thanks to my bench neighbor Stella Kramer for turning the uncountable hours of side-by-side pipetting into one of the best experiences during my PhD. I would also like to thank the Schmandke twins for their unshakable and contagious positive attitude. Thanks to Sarah Beyeler and Alice Mosberger for motivating and tolerating my

very first Swiss German sentences. Anna Guzik-Kornacka, Flora Vajda and Nina Thiede-Stan were a permanent supply of positive energy and motivation. I would like to thank Roberto Fiorelli for being my accomplice in the mission to bring music to the scientists. Thanks to Anne Engmann for being such a great sparring partner when it comes to crazy ideas. Also, thanks to Mea Holm, Martina Maibach and Michael Maurer, who have brought quite some fresh spirit into the team and who will take our *in-vitro* knowledge of Nogo-A to yet another level.

An interdisciplinary project like this would not be possible without the help of committed collaborators. To this end, I would like to thank Chayne Piscitelli and Xavier Deupi of the Paul Scherrer Institute, Villigen, for introducing me to the fascinating world of GPCR structural biology. This joint project would not have been possible without the support of Prof. Dr. Gebhard Schertler. The other fundamental collaboration that was key for this project was with the Biological NMR group of ETH Zurich centered around Prof. Dr. Roland Riek. In particular, I thank Viviane Zelenay and Stefan Bibow for their effort and patience needed for familiarizing me with the fundamentals of macromolecular NMR. Both of these groups openly shared their unpublished results with me and made me feel very welcome.

Starting a new life in a different country can be a challenge, unless you are lucky enough to end up in one apartment with the best bunch of people you could hope for. Yves, Philipp, thank you for being the brothers that I've never had. Dani, Dési, Jelena and the others, thanks for so many wonderful memories at 3F and beyond. Nora, thank you for being the heart and soul of our little "family" and for always taking good care of everyone. We miss you.

Anybody who knows me is aware that I need music to breathe. I therefore owe my gratitude to all my fellow musicians who have provided me with the constructive distraction needed to keep me mentally sane. Therefore, I would like to give a huge shout-out to my current band mates (Damaris, Fab, Pedro, Reto, Jost) and to the people who I've had the pleasure to make music with earlier in my PhD (Anina, Lesley, Helge, Julius, Louis, Martin, Monika, Patrick, Samuel, Thomas, Tristan, Yves). Thanks to my piano teachers (Marcel and Stefan) and students (Erik and Flurina). Also, thanks to the Salsa connection for repeated sore calves (mainly Celina, Celine, Edi, Jan, Maria, and Rahel).

Finally, I owe my deepest gratitude to my family, who have substantially contributed to this work with their constant love and support. I would not be who I am today without the continuing inspiration and encouragement of my parents. Thanks to Marly for being by my side no matter where each of us are in this world. Thanks to Katharina for reminding me that there are even more important things in life than science. And finally, thank you, Caro, for being the best companion (this side of the equator, or the other), and fiancée, that anyone could hope for. Konstantin Wiplinger provided internet access during a creative writing phase in paradise.

REFERENCES

Abel, S., B. Geltinger, N. Heinrich, D. Michl, A. Klose, M. Beyermann, and D. Schwarzer. 2014. Semisynthesis and optimization of G protein-coupled receptor mimics. *Journal of peptide science : an official publication of the European Peptide Society*. 20:831-836.

Adada, M., D. Canals, Y.A. Hannun, and L.M. Obeid. 2013. Sphingosine-1-phosphate receptor 2. *The FEBS journal*. 280:6354-6366.

Bermudez, M., and G. Wolber. 2015. Structure versus function-The impact of computational methods on the discovery of specific GPCR-ligands. *Bioorganic & medicinal chemistry*. 23:3907-3912.

Chen, M.S., A.B. Huber, M.E. van der Haar, M. Frank, L. Schnell, A.A. Spillmann, F. Christ, and M.E. Schwab. 2000. Nogo-A is a myelin-associated neurite outgrowth inhibitor and an antigen for monoclonal antibody IN-1. *Nature*. 403:434-439.

Chu, M.L., V.E. Ahn, H.J. Choi, D.L. Daniels, R. Nusse, and W.I. Weis. 2013. structural Studies of Wnts and identification of an LRP6 binding site. *Structure*. 21:1235-1242.

Clevers, H. 2009. Eyeing up new Wnt pathway players. *Cell*. 139:227-229.

Cohen, L.S., K.E. Fracchiolla, J. Becker, and F. Naider. 2014. Invited review GPCR structural characterization: Using fragments as building blocks to determine a complete structure. *Biopolymers*. 102:223--243.

Fincher, J., C. Whiteneck, and E. Birgbauer. 2014. G-protein-coupled receptor cell signaling pathways mediating embryonic chick retinal growth cone collapse induced by lysophosphatidic acid and sphingosine-1-phosphate. *Developmental neuroscience*. 36:443-453.

Fournier, A.E., G.C. Gould, B.P. Liu, and S.M. Strittmatter. 2002. Truncated soluble Nogo receptor binds Nogo-66 and blocks inhibition of axon growth by myelin. *The Journal of neuroscience : the official journal of the Society for Neuroscience*. 22:8876-8883.

Fournier, A.E., T. GrandPre, and S.M. Strittmatter. 2001. Identification of a receptor mediating Nogo-66 inhibition of axonal regeneration. *Nature*. 409:341-346.

Gentry, P.R., P.M. Sexton, and A. Christopoulos. 2015. Novel Allosteric Modulators of G Protein-coupled Receptors. *The Journal of biological chemistry*. 290:19478-19488.

Ghosh, E., P. Kumari, D. Jaiman, and A.K. Shukla. 2015. Methodological advances: the unsung heroes of the GPCR structural revolution. *Nature reviews. Molecular cell biology*. 16:69-81.

Gibson, C., S. Turner, and M. Donnelly. 2009. One degree of separation: paralysis and spinal cord injury in the United States. *Christopher and Dana Reeve Foundation, Short Hills*.

GrandPre, T., S. Li, and S.M. Strittmatter. 2002. Nogo-66 receptor antagonist peptide promotes axonal regeneration. *Nature*. 417:547-551.

GrandPre, T., F. Nakamura, T. Vartanian, and S.M. Strittmatter. 2000. Identification of the Nogo inhibitor of axon regeneration as a Reticulon protein. *Nature*. 403:439-444.

Janda, C.Y., D. Waghray, A.M. Levin, C. Thomas, and K.C. Garcia. 2012. Structural basis of Wnt recognition by Frizzled. *Science*. 337:59-64.

Johnsson, A.K., Y. Dai, M. Nobis, M.J. Baker, E.J. McGhee, S. Walker, J.P. Schwarz, S. Kadir, J.P. Morton, K.B. Myant, D.J. Huels, A. Segonds-Pichon, O.J. Sansom, K.I. Anderson, P. Timpson, and H.C. Welch. 2014. The Rac-FRET mouse reveals tight spatiotemporal control of Rac activity in primary cells and tissues. *Cell reports*. 6:1153-1164.

Junge, H.J., S. Yang, J.B. Burton, K. Paes, X. Shu, D.M. French, M. Costa, D.S. Rice, and W. Ye. 2009. TSPAN12 regulates retinal vascular development by promoting Norrin- but not Wnt-induced FZD4/beta-catenin signaling. *Cell*. 139:299-311.

Kajimoto, T., T. Okada, H. Yu, S.K. Goparaju, S. Jahangeer, and S. Nakamura. 2007. Involvement of sphingosine-1-phosphate in glutamate secretion in hippocampal neurons. *Molecular and cellular biology*. 27:3429-3440.

Kanno, T., T. Nishizaki, R.L. Proia, T. Kajimoto, S. Jahangeer, T. Okada, and S. Nakamura. 2010. Regulation of synaptic strength by sphingosine 1-phosphate in the hippocampus. *Neuroscience*. 171:973-980.

Ke, J., K.G. Harikumar, C. Erice, C. Chen, X. Gu, L. Wang, N. Parker, Z. Cheng, W. Xu, B.O. Williams, K. Melcher, L.J. Miller, and H.E. Xu. 2013. Structure and function of Norrin in assembly and activation of a Frizzled 4-Lrp5/6 complex. *Genes & development*. 27:2305-2319.

Kempf, A., B. Tews, M.E. Arzt, O. Weinmann, F.J. Obermair, V. Pernet, M. Zagrebelsky, A. Delekate, C. Iobbi, A. Zemmar, Z. Ristic, M. Gullo, P. Spies, D. Dodd, D. Gygax, M. Korte, and M.E. Schwab. 2014. The sphingolipid receptor S1PR2 is a receptor for Nogo-a repressing synaptic plasticity. *PLoS biology*. 12:e1001763.

Kimura, A., T. Ohmori, Y. Kashiwakura, R. Ohkawa, S. Madoiwa, J. Mimuro, K. Shimazaki, Y. Hoshino, Y. Yatomi, and Y. Sakata. 2008. Antagonism of sphingosine 1-phosphate receptor-2 enhances migration of neural progenitor cells toward an area of brain. *Stroke; a journal of cerebral circulation*. 39:3411-3417.

Kimura, A., T. Ohmori, R. Ohkawa, S. Madoiwa, J. Mimuro, T. Murakami, E. Kobayashi, Y. Hoshino, Y. Yatomi, and Y. Sakata. 2007. Essential roles of sphingosine 1-phosphate/S1P1 receptor axis in the migration of neural stem cells toward a site of spinal cord injury. *Stem cells*. 25:115-124.

Kobilka, B. 2013. The structural basis of G-protein-coupled receptor signaling (Nobel Lecture). *Angew Chem Int Ed Engl*. 52:6380-6388.

Kumagai, Y., H. Naoki, E. Nakasyo, Y. Kamioka, E. Kiyokawa, and M. Matsuda. 2015. Heterogeneity in ERK activity as visualized by in vivo FRET imaging of mammary tumor cells developed in MMTV-Neu mice. *Oncogene*. 34:1051-1057.

Langenhan, T., M.M. Barr, M.R. Bruchas, J. Ewer, L.C. Griffith, I. Maiellaro, P.H. Taghert, B.H. White, and K.R. Monk. 2015. Model Organisms in G Protein-Coupled Receptor Research. *Molecular pharmacology*. 88:596-603.

Lefkowitz, R.J. 2013. A brief history of G-protein coupled receptors (Nobel Lecture). *Angew Chem Int Ed Engl*. 52:6366-6378.

Lohse, M. 2015. In Vivo-Studies of GPCR Conformational Changes using Fluorescence-Based Assays. *Biophysical journal*. 108:358a.

Lopes, D.D., R.F. Vieira, L. Malavolta, E.F. Poletti, S.I. Shimuta, A.C. Paiva, S. Schreier, L. Oliveira, and C.R. Nakaie. 2013. Short peptide constructs mimic agonist sites of AT(1)R and BK receptors. *Amino acids*. 44:835-846.

Michaud, J., D.S. Im, and T. Hla. 2010. Inhibitory role of sphingosine 1-phosphate receptor 2 in macrophage recruitment during inflammation. *J Immunol*. 184:1475-1483.

Murakoshi, H., H. Wang, and R. Yasuda. 2011. Local, persistent activation of Rho GTPases during plasticity of single dendritic spines. *Nature*. 472:100-104.

Niehrs, C. 2012. The complex world of WNT receptor signalling. *Nature reviews. Molecular cell biology*. 13:767-779.

Oertle, T., M.E. van der Haar, C.E. Bandtlow, A. Robeva, P. Burfeind, A. Buss, A.B. Huber, M. Simonen, L. Schnell, C. Brosamle, K. Kaupmann, R. Vallon, and M.E. Schwab. 2003. Nogo-A inhibits neurite outgrowth and cell spreading with three discrete regions. *The Journal of neuroscience : the official journal of the Society for Neuroscience*. 23:5393-5406.

Okamoto, H., N. Takuwa, T. Yokomizo, N. Sugimoto, S. Sakurada, H. Shigematsu, and Y. Takuwa. 2000. Inhibitory regulation of Rac activation, membrane ruffling, and cell migration by the G protein-coupled sphingosine-1-phosphate receptor EDG5 but not EDG1 or EDG3. *Molecular and cellular biology*. 20:9247-9261.

Pertz, O., L. Hodgson, R.L. Klemke, and K.M. Hahn. 2006. Spatiotemporal dynamics of RhoA activity in migrating cells. *Nature*. 440:1069-1072.

Piscitelli, C.L., J. Kean, C. de Graaf, and X. Deupi. 2015. A Molecular Pharmacologist's Guide to G Protein-Coupled Receptor Crystallography. *Molecular pharmacology*. 88:536-551.

Prinjha, R., S.E. Moore, M. Vinson, S. Blake, R. Morrow, G. Christie, D. Michalovich, D.L. Simmons, and F.S. Walsh. 2000. Inhibitor of neurite outgrowth in humans. *Nature*. 403:383-384.

Rogers, J.M., C.T. Wong, and J. Clarke. 2014. Coupled folding and binding of the disordered protein PUMA does not require particular residual structure. *Journal of the American Chemical Society*. 136:5197-5200.

Schwab, M.E., and P. Caroni. 1988. Oligodendrocytes and CNS myelin are nonpermissive substrates for neurite growth and fibroblast spreading in vitro. *The Journal of neuroscience : the official journal of the Society for Neuroscience*. 8:2381-2393.

Schwab, M.E., and S.M. Strittmatter. 2014. Nogo limits neural plasticity and recovery from injury. *Current opinion in neurobiology*. 27:53-60.

Takashima, S., N. Sugimoto, N. Takuwa, Y. Okamoto, K. Yoshioka, M. Takamura, S. Takata, S. Kaneko, and Y. Takuwa. 2008. G12/13 and Gq mediate S1P2-induced inhibition of Rac and migration in vascular smooth muscle in a manner dependent on Rho but not Rho kinase. *Cardiovascular research*. 79:689-697.

Takuwa, Y. 2002. Subtype-specific differential regulation of Rho family G proteins and cell migration by the Edg family sphingosine-1-phosphate receptors. *Biochimica et biophysica acta*. 1582:112-120.

Tews, B., K. Schonig, M.E. Arzt, S. Clementi, M.S. Rioult-Pedotti, A. Zemmar, S.M. Berger, M. Schneider, T. Enkel, O. Weinmann, H. Kasper, M.E. Schwab, and D. Bartsch. 2013. Synthetic microRNA-mediated downregulation of Nogo-A in transgenic rats reveals its role as regulator of synaptic plasticity and cognitive function. *Proceedings of the National Academy of Sciences of the United States of America*. 110:6583-6588.

Thiede-Stan, N.K., B. Tews, D. Albrecht, Z. Ristic, H. Ewers, and M.E. Schwab. 2015. Tetraspanin-3 is an organizer of the multi-subunit Nogo-A signaling complex. *Journal of cell science*.

van Unen, J., J. Woolard, A. Rinken, C. Hoffmann, S. Hill, J. Goedhart, M. Bruchas, M. Bouvier, and M. Adjobo-Hermans. 2015. A Perspective on Studying GPCR Signaling with RET Biosensors in Living Organisms. *Molecular pharmacology*.

Vincent, B., L. Mouledous, B. Bes, H. Mazarguil, J.C. Meunier, A. Milon, and P. Demange. 2008. Description of the low-affinity interaction between nociceptin and the second extracellular loop of its receptor by fluorescence and NMR spectroscopies. *Journal of peptide science : an official publication of the European Peptide Society*. 14:1183-1194.

Wang, C., H. Wu, V. Katritch, G.W. Han, X.P. Huang, W. Liu, F.Y. Siu, B.L. Roth, V. Cherezov, and R.C. Stevens. 2013. Structure of the human smoothened receptor bound to an antitumour agent. *Nature*. 497:338-343.

Yasuda, R., C.D. Harvey, H. Zhong, A. Sobczyk, L. van Aelst, and K. Svoboda. 2006. Supersensitive Ras activation in dendrites and spines revealed by two-photon fluorescence lifetime imaging. *Nature neuroscience*. 9:283-291.